Universitat
de les Illes Balears

TESI DOCTORAL
2019

ELECTRICALLY AND THERMALLY DRIVEN TRANSPORT IN INTERACTING QUANTUM DOT STRUCTURES

Miguel Ambrosio Sierra Seco de Herrera

Universitat
de les Illes Balears

TESI DOCTORAL
2019

Programa de Doctorat de Física

ELECTRICALLY AND THERMALLY DRIVEN TRANSPORT IN INTERACTING QUANTUM DOT STRUCTURES

Miguel Ambrosio Sierra Seco de Herrera

Director: David Sánchez Martín
Tutor: Raul Toral Garcés

Doctor per la Universitat de les Illes Balears

Dr. David Sánchez Martín, profesor titular por la universidad de las Islas Baleares y

Miguel Ambrosio Sierra Seco de Herrera

DECLARAN:

Que la tesis doctoral que tiene como título *Electrically and thermally driven transport in interacting quantum dot structures* realizada por Miguel Ambrosio Sierra Seco de Herrera y dirigida por el Dr. David Sánchez Martín cumple con los requisitos necesarios para optar al título de Doctor Internacional.
Y para que quede en constancia firman este documento,

David Sánchez Martín

Miguel Ambrosio Sierra Seco de Herrera
Palma, 26. de Febrero de 2019

Papers included in this thesis

- Miguel A. Sierra and David Sánchez, Materials Today: Proceedings **2**, 483 (2015).
- Miguel A. Sierra, M. Saiz-Bretín, F. Domínguez-Adame and David Sánchez, Physical Review B, **93** 235452 (2016).
- Miguel A. Sierra, Rosa López and David Sánchez, Physical Review B **96**, 085416 (2017).
- Miguel A. Sierra, David Sánchez, Alvar R. Garrigues, Enrique del Barco, Lejia Wang and Christian A. Nijhuis, Nanoscale **10**, 3904 (2018).
- Miguel A. Sierra and David Sánchez, Journal of Physics: Conference Series **969**, 012144 (2018).
- Miguel A. Sierra, Rosa López and Jon Soo Lim, Physical Review Letters **121**, 096801 (2018).
- Miguel A. Sierra, David Sánchez, Kristen Kaasbjerg and Antti-Pekka Jauho, in preparation (2019)

Papers not included in this thesis

- Miguel A. Sierra and David Sánchez, Physical Review B **90**, 115313 (2014).

List of Symbols

Symbol	Description
Δ_C	Contact asymmetry of the heat current.
Δ_E	Electric asymmetry of the heat current.
B	Magnetic field.
C	Anihilation operator of electrons in the leads. Its creation operator will be $C^\dagger$.
D	Bandwidth energy of a reservoir or a metal.
d	Anihilation operator of electrons in the quantum dots. Its creation operator will be $d^\dagger$.
$\mathcal{G}$	Differential electrical conductance.
$\mathcal{K}$	Differential thermal conductance.
$\mathcal{L}$	Differential thermoelectrical conductance.
Π	Differential Peltier coefficient.
$\mathcal{R}$	Differential electrothermal conductance.
$\mathcal{S}$	Differential thermopower.
ε_d	Energy level of a single quantum dot or an artifitial impurity.
ε_F	Fermi energy.
f	Fermi distribution function.
$f_\alpha(\omega)$	Fermi distribution function of the reservoir α.
$\mathcal{F}$	Effective distribution function of the leads.
$\tilde{g}_0$	Quantum electric conductance.

G^a	Advanced Green's function.
Γ	Hybridation functions (or constant).
$G^{\bar{t}}$	Antitime-ordered Green's function.
$G^>$	Greater Green's function.
$G^<$	Lesser Green's function.
G^r	Retarded Green's function.
G^t	Time-ordered Green's function.
$\mathcal{H}$	General Hamiltonian.
I_{th}	Thermocurrent.
I	Electrical current.
J_{ex}	Superexchange interaction.
$\mathcal{J}$	Exchange coupling constants in the s-d model.
κ_0	Quantum thermal conductance.
$\bar{\mathcal{K}}$	Potential scattering term of the Kondo model.
$\mathcal{G}_0$	Linear electrical conductance.
$\mathcal{K}_0$	Linear heat conductance.
$\mathcal{L}_0$	Linear thermoelectrical conductance.
$\tilde{L}_0$	Lorentz number.
Π_0	Linear Peltier coefficient.
$\mathcal{R}_0$	Linear electrothermal conductance.
$\mathcal{S}_0$	Linear thermopower.
μ_α	Electrochemical potential of the lead α.
n	Occupation operator.
$\bar{n}$	Expected value of the occupation.
Q	Heat current.
Q_E	Energy current.
α	Fermionic reservoirs. Generally, there are two reservoirs: left $\alpha = L$ and right $\alpha = R$.

ρ	Density of states.
Σ	Self-energy.
σ	Spin.
T	Background temperature of the system.
T_α	Temperature of the lead α.
τ	Dot-dot tunneling amplitude.
θ	Thermal bias.
$\hat{T}$	Time-ordering operator.
$\hat{\hat{T}}$	Antitime-ordering operator.
T_K	Kondo Temperature.
$\tilde{T}_K$	Effective Kondo temperature.
$\mathcal{T}$	Transmission function of the nanosystem.
U	Intradot electron-electron interaction.
$\tilde{U}$	Interdot electron-electron interaction.
V_g	Gate voltage.
V	Applied bias voltage.
V_{th}	Thermoelectric voltage.
$\mathcal{V}$	Lead-dot tunnel amplitude.
Δ_B	Zeeman splitting energy due to a magnetic field B.
ZT	Figure of merit.

Abbreviations

Abbreviation	Description
2DEG	two-dimensional electron gas
AB	Aharonov-Bohm
AFM	atomic force microscopy
BIC	bound state in the continuum
CB	Coulomb blockade
DOS	density of states
DQD	double quantum dot
EOM	equation of motion
LED	light-emitting diode
NEGF	non-equilibrium Green's function
NRG	numerical renormalization group
QD	quantum dot
QPC	quantum point contact
QPT	quantum phase transition
RKKY	Ruderman-Kittel-Kasuya-Yosida
SAM	self-assembled molecules
SBMFT	slave-boson mean-field theory
SET	single-electron transistor
STM	scanning tunneling microscope

SW	Schrieffer-Wolf
WBL	wide band limit
WF	Wiedemann-Franz
ZBA	zero-bias anomaly

Contents

I

Introduction

II

Theory

III

Results and discussion

Acknowledgement

When I started the Phd, I had the feeling that it was never going to end. But this is it, I'm writing my final words to close this door. Lots of things happened during these four year and I have to say that it was an amazing period. For this reason, I would like to thank all the people who was part of my life during the development of my thesis.

First, I really want to thank to my supervisor: David Sánchez. If I am the researcher that I am right now, it is mainly because of you. Not only you taught me physics, you also taught me about habits, how to write, to have patience and not to give up even when it seems that everything goes wrong. After talking with other Phd students in other universities with lots of different supervisors, I can say that I was very lucky. Thank you David.

I want also to thank more people who made me grow as a researcher. All people that has been in the FISNANO group in IFISC: Rosa, Llorenç, Guillem, Maria Isabel, Javier, Jong Soo, Sun Jong... I learnt also a lot with your works, conversations and collaborations. Thank you for listening my interventions in the quantum meetings, for helping me when I needed and for the works that we made together. Additionally, I would also like to thank the people who invited me to their universities and collaborated with me: Francisco and Marta from my research stay in Madrid and Antti-Pekka and Kristen from my stay in Denmark. They were really nice experiences and I actually felt a huge progress in my scientific performance. In addition, I would like to acknowledge the government of Balearic Island for the FPI grant and for funding my research stays and my Phd.

Regarding all my friends and colleagues from IFISC, I appreciate very much our lunch talks, the company and all our mutual help. It has been really special to have so nice people around me when I come to work.

Now, my lovely family, thank you a lot for all your help. I am very happy to have all of you these years supporting me in every situation. I also appreciate all your worries, I really do. I also want to thank my closest friends: Pere, Maria del Mar, Carlos, Carla, David, Aitaren, Adrián, Christian and Vicente. Thank you for all beautiful moments, the long talks, the support, the good times and the help in bad times these years. I feel very happy of having friends like you.

Finally, it is the turn of my swing world. I am also lucky of getting to know the swing community that gave me happiness. I do not know how would I have worked in my thesis without the swing dancing but I'm sure it would have been really sad. Thank you very much Maria, Núria, Deneb, César, Joan, Ana, Jose, Sole, Laura, Mar, Rebeca, Esther, Álvaro, Gori, Mimmi, Fredrik and lots more for those beautiful moments I lived with you and made me work with a smile in my face.

Abstract

The main goal of this thesis is to study the quantum transport of quantum dot systems driven by voltage and thermal biases. Particularly, we study interacting single and double quantum dots yielding Coulomb blockade and Kondo effects giving an special emphasis at the thermally-driven response.

The first part of the thesis gives a general introduction of the main concepts of this thesis. Ch. 1 explains the fundamentals of a quantum dot and gives an overview of the most relevant experimental and theoretical works. Ch. 2 focuses on the Kondo effect, a paradigmatic many-body phenomenon which may appear in quantum dots at low temperatures. Ch. 3 summarizes the basic concepts of thermoelectrics including a discussion of state of the art involving quantum dots in the thermoelectric transport.

The models and theoretical techniques are discussed in the second part. Particularly, Ch. 4 introduces the nonequilibrium Green's function formalism which will be used in the following chapters. Ch. 5 defines the Anderson Hamiltonian and transforms it into the slave-boson and Kondo Hamiltonians. In addition, we discuss the equation of motion technique for obtaining the retarded Green's functions at several regimes and the slave-boson mean-field theory. In Ch. 6 we determine the current expressions required for the numerical calculations of the results.

Finally, the third part reveals the quantum transport results obtained for several quantum dot structures. Ch. 7 focuses on single quantum dots. First, we consider the transport across a quantum dot in the Coulomb blockade regime obtaining nonlinear thermoelectric effects such as nontrivial zeros in the thermocurrent or heat current asymmetries. Second, the Coulomb blockade theory is used to fit the results of a molecular junction experiment and, comparing with a noninteracting model, we propose the application of a magnetic field to distinguish between interacting and noninteracting molecules. The third work studies the thermally-driven response of a Kondo impurity using three different approaches covering different temperature regimes. We find that the Kondo resonance is quenched at large thermal biases implying nonlinear effects in the thermoelectric transport.

The works concerning double dot structures are explained in Ch. 8. First, the transport across a parallel-coupled double quantum dot with intradot Coulomb interactions is studied taking into account the formation of bound states in the continuum. We investigate how to detect such states using the electric and thermoelectric conductances. Second, we analyze the Coulomb drag effect in the Green's function formalism obtaining the conditions to obtain drag currents. Finally, we focus on the nonlinear transport driven by thermal biases for a two-impurity system in the Fermi liquid regime. We observe different regimes depending on the coupling between impurities. Remarkably, the system decouples at large thermal bias since one Kondo resonance vanishes.

Ch. 9 contains the general conclusions of this thesis with a discussion about the limitations of the models used and suggesting further extensions.

Resumen

El objetivo principal de esta tesis es estudiar el transporte cuántico a través de sistemas de puntos cuántico sometido a diferencias de voltaje y temperatura. Particularmente, estudiamos sistemas de un o dos puntos cuánticos interactuantes mostrando efectos de bloqueo de Coulomb y Kondo, dando un énfasis especial a la respuesta térmica.

La primera parte de la tesis da una introducción general de los conceptos principales de esta tesis. El Cap. 1 explica los fundamentos de un punto cuántico y ofrece una visión de los trabajos experimentales y teóricos más generales. El Cap. 2 trata del efecto Kondo, un fenómeno de muchos cuerpos paradigmático que puede aparece en puntos cuánticos a bajas temperaturas. El Cap. 3 resume los conceptos básicos de termoelectricidad incluyendo una discusión sobre la situación actual del transporte termoeléctrico en puntos cuánticos.

Los modelos y técnicas teóricas se discuten en la segunda parte. Concretamente, el Cap. 4 introduce el formalismo de funciones de Green de no equilibrio que serán usadas en los siguientes capítulos. El Cap. 5 define el Hamiltoniano de Anderson y lo transforma en el Hamiltoniano de bosones esclavos y Kondo. Además, comentamos la técnica de ecuación de movimiento para obtener la funcion de Green retardada en algunos regímenes y la teoría de campo medio de bosones esclavos. En el Cap. 6 determinamos las expresiones de la corriente requeridas para los posteriores cálculos númericos.

Finalmente, la tercera parte muestra los resultados de transporte cuántico obtenidos para varias estructuras de puntos cuánticos. El Cap. 7 trata de puntos cuánticos simples. Primero, consideramos el transporte a través de un punto cuántico en el régimen de bloqueo de Coulomb obteniendo efectos termoeléctricos no lineales tales como ceros no triviales en la termocorriente o asimetrías en la corriente de calor. Segundo, tomamos la teoría de bloqueo de Coulomb para ajustar los resultados a un experimento de uniones moleculares y, comparando con un modelo no interactuante, proponemos la aplicación de un campo magnético para distinguir entre moléculas interactuantes y no interactuantes. El tercer trabajo estudia la respuesta a gradientes térmicos de una impureza Kondo usando tres aproximaciones diferentes cubriendo varios rangos de temperatura. Descubrimos que la resonancia Kondo desaparece

a grandes diferencias de temperatura implicando efectos no lineales en el transporte termoeléctrico.

Los trabajos correspondientes a los puntos cuánticos dobles están explicados en el Cap. 8. Primero, se estudia el transporte a través de un doble punto cuántico acoplado paralelamente con interacciones de Coulomb internas teniendo en cuenta la formación de estados ligados en el continuo. Investigamos cómo detectar dichos estados usando las conductancias eléctrica y termoeléctrica. Segundo, analizamos el efecto de arrastre de Coulomb usando el formalismo de funciones de Green obteniendo las condiciones necesarias para encontrar corrientes de arrastre. Finalmente, nos enfocamos en el transporte no lineal debido a diferencias de temperatura en un sistema de dos impurezas en el régimen del líquido de Fermi. Observamos diferentes regímenes dependiendo del acoplo entre impurezas. Sorprendentemente, el sistema se desacopla a grandes diferencias debido a que una resonancia Kondo desaparece.

El Cap. 9 contiene las conclusiones generales de esta tesis con una discusión sobre las limitaciones de los modelos y sugiriendo posibles extensiones.

Resum

L'objectiu principal d'aquesta tesi és estudiar el transport quàntic a través d'un punt quàntic sotmès a diferències de voltatge i temperatura. Particularment, estudiam sistemes d'un o dos punts quàntics interactuants mostrant efectes de bloqueig de Coulomb i Kondo, posant un èmfasi especial a la resposta tèrmica.

La primera part de la tesi dóna una introducció general dels conceptes principals d'aquesta tesi. El Cap. 1 explica els fonaments d'un punt quàntic i ofereix una visió general dels treballs experimentals i teòrics més generals. El Cap. 2 tracta sobre l'efecte Kondo, un fenomen de molts cossos paradigmàtic que pot aparèixer en punts quàntics a baixes temperatures. El Cap. 3 resumeix els conceptes bàsics de termoelectricitat incloent una discussió sobre la situació actual del transport termoelèctric en punts quàntics.

Els models i tècniques teòriques es discuteixen en la segona part. Concretament, el Cap. 4 introdueix el formalisme de funcions de Green fora de l'equilibri que seran empleades als següents capítols. El Cap. 5 defineix el Hamiltonià de Anderson i el transforma al Hamiltonià de bosons esclaus i Kondo. A més, comentam la tècnica d'equació de moviment per obtenir la funció de Green retardada en alguns rangs i la teoria de camp mitjà de bosons esclaus. En el Cap. 6 determinam les expressions de les corrents requerides pels posteriors càlculs numérics

Finalment, la tercera part mostra els resultats de transport cuàntic obtinguts per vàries estructures de punts cuàntics. El Cap. 7 tracta de punts quàntics simples. Primer, consideram el transport a travès d'un punt quàntic en el règim de bloqueig de Coulomb obtenint efectes termoeléctrics no lineals com zeros no trivials en la termocorrent o asimetries en el corrent de calor. Segon, tornam el bloqueig de Coulomb per ajustar els resultats a un experiment d'unions moleculars i, comparant amb un model no interactuant, proposam l'aplicació d'un camp magnètic per distingir entre molècules interactuant i no interactuant. El tercer treball estudia la resposta a gradients tèrmics d'una impuresa Kondo emprant tres aproximacions diferents cobrint diversos rangs de temperatura. Descobrim que la ressonància Kondo desapareix a grans diferències de temperatura implicant efectes no lineals al transport termoeléctric.

Els treballs corresponents als punts quàntics dobles estan explicats al Cap. 8. Primer, s'estudia el transport a través d'un punt quàntic doble acoblat paral·lelament amb interaccions de Coulomb internes tenint en compte la formació d'estats lligats en el continu. Investigam com detectar aquests estats emprant les conductàncies elèctrica i termoelèctrica. Segon, analitzam l'efecte d'arrossegament de Coulomb emprant el formalisme de funcions de Green obtenint les condicions necessàries per encontrar corrents d'arrossegament. Finalment, ens enfocam al transport no lineal a causa de diferències en la temperatura en un sistema de dues impureses en el règim de líquid de Fermi. Observam diferents règims depenent de la connexió entre impureses. Sorprenentment, el sistema es desacobla a grans diferències, ja que una ressonància Kondo desapareix.

El Cap. 9 conté les conclusions generals d'aquesta tesi amb una discussió sobre les limitacions dels models i suggerint possibles extensions.

I

Introduction

1. Quantum dots

Nanoscience has an important impact in our society both directly and indirectly. One of the main reasons that makes nanoscience a relevant topic is the fact that the scale of electronic systems such as transistors is reducing very fast. We have almost arrived to the critical dimensions where transistors can not efficiently operate because quantum effects begin to play a crucial role and a quest for different systems is urged.

Nanotechnology is a cross-disciplinary field involving branches of science like physics, engineering or chemistry, and delves with devices which have a typical length of few nanometers. This thesis considers nanoeletronic systems, which have been traditionally treated within condensed matter physics. These systems are called nanostructures or mesoscopic devices, the latter because they are large enough to be considered complex and interacting, but small enough such that quantum effects are not negligible as in the macroscopic world. Nanophysics uses techniques borrowed from quantum mechanics, electromagnetism and statistical physics in order to explain theoretically and experimentally the properties of nanodevices.

One of the most paradigmatic examples of mesoscopic physics, which is also the main system of interest for this thesis, is the quantum dot (QD) [1]. In principle, conduction electrons in a metal behave as free-motion particles in all dimensions of space. This motion can be restricted by quantum confinement, yielding low dimensional systems. Hence, when electrons are confined in the three spatial directions, a QD is formed, characterized by a discrete spectrum of bound states. QDs are atomic-like condensed-matter systems with effectively 0 spatial dimensions.

There are different types of quantum dots depending on the fabrication process: self-assembled [2], electrochemicaly assembled [3], QDs in heterostructured nanowires [4], etc. However, in this thesis we mostly focus on semiconductor QDs created via lateral confinement. Basically, they are built in a two-dimensional electron gas (2DEG), a free-electron layer located at the interface of two semiconductors with different energy gap (typically GaAs, InAs, etc). On top of the 2DEG (see the sketch of Fig. 1.1a and the scanning tunneling microscope of Fig. 1.1b for comparison) electrodes are deposited acting as electron barriers when an

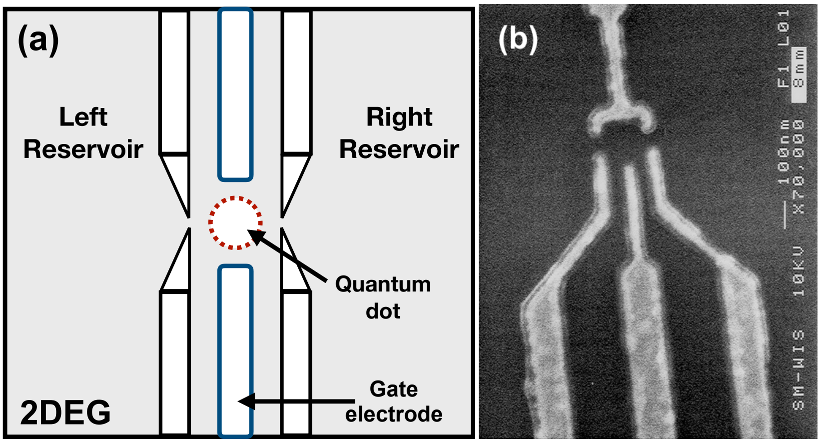

Fig. 1.1. (a) Sketch of a lateral quantum dot built upon a semiconductor 2DEG (gray area) and white electrodes (white parts). Due to doping in the semiconductor, we consider that the 2DEG is a fermionic reservoir with a large number of electrons. The QD is created by applying electrostatic potentials at the electrodes. However, they still allow electron tunneling in and out the reservoirs. Between both electrodes, the QD is created at the center (red circle) with whose electronic occupation may be tuned using a gate electrode (blue rectangle). (b) Electron tunneling microscope image of a real QD device. In comparison with (a) one may easily identify each part of the system. Image extracted from D. Goldhaber-Gordon *et al.* [7].

electrical potential is applied. Thus, with a proper configuration of electrodes, one may confine electrons in a small region of space (red dashed circle in Fig.1.1a) that displays discrete levels in the density of states (DOS). Notwithstanding, electrons may tunnel through the tunnel barriers in or out of the QD from or to the electronic reservoirs (massive regions to the left and right of Fig. 1.1a). Tunneling allows us to investigate electron transport across the dot giving us valuable information about the QD electronic properties. Additionally, another electrode is used as a gate which is able to tune the QD electronic levels. Therefore, internal properties of the QD can be easily manipulated with electric fields, which represents a huge advantage over real atoms. Thus, QDs are now a well established area in experimental physics. Regarding the details of the fabrication process, these are beyond the scope of our theoretical thesis. The interested reader is referred to, e. g., Refs. [5, 6].

The study of electron transport eases the characterization of the main properties of semiconductor QDs. In a macroscopic system, carriers moving in a metal collide with atoms changing their direction and velocity (Drude model). The typical length between collisions is called *mean free path* l_e. When the length scales are larger than the mean free path ($L > l_e$), as happens in macroscopic devices, transport is diffusive. In the case of QDs (and nanostructures, in general), the lengths of the conductor does not overtake the mean free path ($L < l_e$) and carrier directions are modified only through boundary scattering. This is the *ballistic transport* regime, the main behavior of the vast majority of mesoscopic systems, including the QD structures analyzed in this thesis.

The mean free path l_e is not the only relevant length in the physics of electronic transport in QDs. Additional scales must be taken into account [8, 9]. Firstly, the mean distance for an electron to remain in a definite quantum state without losing its phase coherence is called *phase-relaxation length* l_φ or *coherence length*. Furthermore, the length associated with the diffusion due to the temperature T of the system is the *thermal length* l_T. This covers the distance traveled by an electron before it gets diffused in the system. Consequently, l_T is proportional to the inverse of T. QDs are confined systems at low temperature, therefore we expect thermal lengths larger than the coherence length $l_T \gg l_\varphi$.

Some interesting applications of QDs have arisen in the last decades. We highlight their implementation in quantum computation because the electron spin in the QD can operate as a *qubit* (quantum bit) [1]. A combination of several QDs makes it possible to implement different logical gates to control the qubits. Additionally, their optoelectronic properties (not discussed in this thesis) facilitate the use of QDs as photovoltaic devices or light-emitting diodes (LEDs). Finally, the three terminal configuration of QDs (see Fig. 1.1a) brings up the creation of single-electron transistors (SETs) [1, 7, 10] which, in contrast with conventional transistors, show a regime where transport is controlled by the flow of electrons one by one. This operation mode is called *sequential tunneling* and will be further explained in Sec. 1.1.

In the following sections, we will discuss phenomena and systems highly related with QDs. First, Sec. 1.1 introduces the Coulomb blockade (CB) effect, a phenomenon characteristic in small confined systems with strong electron-electron interactions. We will explain different experiments where the CB effect is present. Later, we consider the molecular junctions in Sec. 1.2. These are hybrid systems where transport occurs through a molecule instead of a QD, but with similar characteristics. Finally, in Sec. 1.3 we study in detail the DQD system, focusing closely on the parallel and serial configurations and giving special emphasis to the Coulomb drag effect.

1.1 Coulomb blockade

The usual size of semiconductor QDs is around 100 nm [6]. In addition, we recall that electrons are charged particles which interact between them via Coulomb potentials. This potential becomes more relevant in small-sized devices because the electrostatic energy of the confined particles can not be neglected, $U \propto 1/r$. On the other hand, we must take into account that the level spacing Δ of the dot also increases substantially when the size is decreased $\Delta \propto 1/r^2$. Small dots satisfy $\Delta \gg U$ and transport is thus limited to one single level which can be filled with only one or two electrons. Another energy scale plays an important role in the transport through the QD: the temperature of the system. As known, large temperatures destroy the quantum behavior of particles and reduce the impact of Coulomb interactions. Therefore, temperature has to be a small energy scale of the system $\Delta \gg U \gg k_B T$.

Charging effects are crucial in the study of transport through nanostructures because the electrostactic potential is able to create an energy gap in the distribution of the discrete states of the DOS. In other words, conduction electrons need to overcome the intradot Coulomb interaction energy U between charged particles occupying the nanodevice. This phenomenon is called *Coulomb blockade* and appears in a large number of mesoscopic systems. This effect was first observed by Scott-Thomas *et al.* [11]. They reported a periodic oscillation of resonances in the linear conductance $\mathcal{G}_0$ as a function of a voltage gate V_g. The effect is unique to small conductors since fermionic reservoirs have good screening properties and strong interactions can be neglected.

The essence of the Coulomb blockade effect can be easily described by means of the *orthodox* or *electrostatic model*. As it is necessary to deeply understand the physics of this effect, we will now discuss the electrostatic model in detail. The structure of a QD system is depicted with an electrical circuit (Fig. 1.2) in which each part of the configuration is represented as an element in the circuit. First, the QD is indicated as an island at the center of the circuit (brown rectangle in Fig. 1.2) . This island will accumulate a charge proportional to the number of the electrons confined inside ($Q = Ne$, N being the number of electrons and e, the elementary electron charge). The tunnel junction that couples the reservoir and the QD consists of a capacitor C_α, where $\alpha = \{L, R\}$ labels left of right, and a resistance $R_{t\alpha}$ (blue rectangles). The tunnel resistance R_t is required to be large enough in order to obtain opaque barriers. Thus, we can estimate a lower bound of the resistance by applying the energy-time uncertainty relationship [5, 6]

$$\Delta E \Delta t > h \, , \tag{1.1}$$

where $\Delta E \approx U = e^2/C$, C being the total capacitance of the system and $\Delta t \approx R_{t\alpha} C$ is the charging time of the QD junction. The uncertainty principle requires that the tunnel resistance has to be $R_{t\alpha} \gg h/e^2 = 25.813$ kΩ. Otherwise, charging effects will not be visible experimentally. The gate (pink rectangle) is connected capacitively to the dot. In this case there

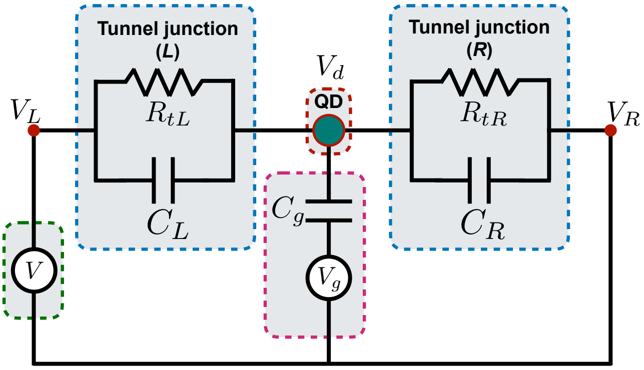

Fig. 1.2. Equivalent circuit of a QD system or single electron transistor. The blue rectangles represent the tunnel junctions between the reservoirs and the quantum dot (see also Fig. 1.1).The tunnel junctions consist of a resistance $R_{t(\alpha)}$ and a capacitance C_α with $\alpha = \{L, R\}$ indicating the left or right reservoir. The gate (pink rectangle) is composed of the gate voltage V_g and a capacitor C_g. The quantum dot is located at the node between tunnel junctions (red rectangle) characterized by a potential V_d. The other red nodes correspond to voltages V_L and V_R. Finally, both reservoirs are controlled with an applied voltage V.

is no tunnel resistance R_t because electron flow is not allowed between the gate and the dot. This gate terminal is used to tune the QD levels with the application of a voltage V_g. Finally, we apply between reservoirs a bias voltage V (green rectangle) to induce a current through the dot.

First, we compute the charge of the island

$$Q = Q_R + Q_L + Q_g \, , \tag{1.2}$$

where $Q_R = C_R(V_d - V_R)$, $Q_L = C_L(V_d - V_L)$ and $Q_g = C_g(V_d - V_g)$ denote the charge induced in the left, right and gate capacitors, respectively. V_L, V_R, V_g and V_d are the voltage set at the nodes indicated in Fig. 1.2. For simplicity, in this model we assume negligible tunnel resistances and the charge is thus an integer number of electrons. We would like to mention that real systems can contain random charges trapped at the junctions generating an additional polarization charge Q_p [5]. Nevertheless, this term is also neglected in the model. After a straightforward calculation, one can determine the voltage at the island V_d as a function of the charge:

$$V_d(Q) = \frac{Q}{C} + \frac{C_L V_L + C_R V_R + C_g V_g}{C} \, , \tag{1.3}$$

where $C = C_L + C_R + C_g$ is the total capacitance. The electrostatic energy of the QD is defined as the integral of Eq. (1.3) over the charge

$$W_d(Q) = \frac{Q^2}{2C} + \frac{C_L V_L + C_R V_R + C_g V_g}{C} Q \, . \tag{1.4}$$

The total energy $E_t(N)$ of the QD is obtained by adding the kinetic term to the electrostatic energy

$$E_t(N) = \sum_{i=1}^{N} \varepsilon_N + \frac{N^2 e^2}{2C} + \frac{C_L V_L + C_R V_R + C_g V_g}{C} Ne \, . \tag{1.5}$$

In Eq. (1.5) we replaced $Q = Ne$ where N is the number of electrons confined in the island. Now, we should define the addition energy $\mu_d(N) = E_t(N) - E_t(N-1)$ which reads

$$\mu_d(N) \quad = \quad \varepsilon_N + \frac{(2N-1)e^2}{2C} + \frac{C_L V_L + C_R V_R + C_g V_g}{C} e \, . \tag{1.6}$$

The addition energy μ_d will give the position of the resonances along the local DOS (see Ch. 5). Eq. (1.6) shows appealing physics. The distance between consecutive resonances is $\Delta\mu_d(N) = \Delta_N + e^2/C$ where $\Delta_N = \varepsilon_{N+1} - \varepsilon_N$. This means that adding a new electron to the island always requires that such electron has to reach at least an energy $U = e^2/C$ even for degenerate levels $\Delta_N = 0$.

Now, the goal is to find the conditions for transport to be allowed. This will happen when the addition energy is in between the lead electrochemical potentials ($\mu_L > \mu_d > \mu_R$ and $\mu_R > \mu_d > \mu_L$). Applying $\mu_\alpha = \varepsilon_F + eV_\alpha$, we obtain the following requirements

$$0 > \varepsilon_N + (2N-1)U - \varepsilon_F - \frac{C_R + C_g}{C} eV_L + \frac{C_R}{C} eV_R + \frac{C_g}{C} eV_g \, , \tag{1.7a}$$

$$0 < \varepsilon_N + (2N-1)U - \varepsilon_F + \frac{C_L}{C} eV_L - \frac{C_L + C_g}{C} eV_R + \frac{C_g}{C} eV_g \, , \tag{1.7b}$$

for the condition $\mu_L > \mu_d > \mu_R$. The $\mu_R > \mu_d > \mu_L$ case is obtained by replacing > by < in Eq. (1.7) and viceversa. We remark that the tuning parameters are the applied voltage V and the gate voltage V_g. In order to satisfy the relation $V = V_L - V_R$, we set $V_L = -V_R = V/2$ and then we depict the boundary lines denoting the conditions of Eqs. (1.7a) and (1.7b) in a V versus V_g plot forming the stability diagram shown in Fig. 1.3a.

We have set the capacitances at $C_R = C_g = C_L = C_0$ and $\varepsilon_N = \varepsilon_F$ for simplicity. Dashed lines in Fig. 1.3a denote the boundary lines. Notice that at low applied voltages these boundaries form a diamond shape. Inside the diamond the tunneling conditions are not satisfied and, consequently, transport is prohibited. This characteristic forbidden region

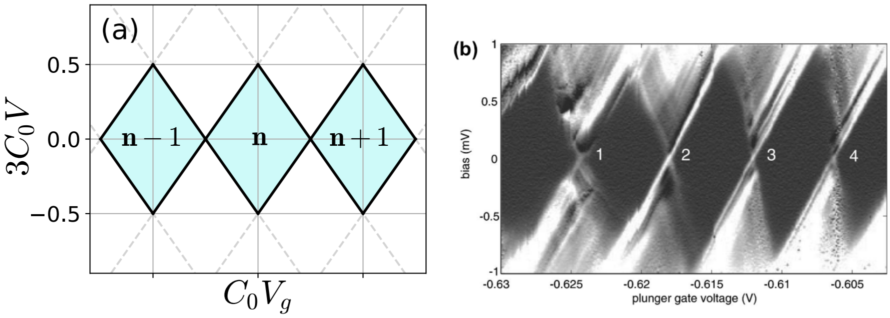

Fig. 1.3. (a) Stability diagram of a QD in the case in which the capacitances $C_R = C_g = C_L = C_0$ and for $\varepsilon_N = \varepsilon_F$. Turquoise areas represent forbidden tunneling across the QD at $T = 0$. Therefore, transport is not possible for electrons inside these regions. Each of these regions is associated a certain number of electrons occupying the QD. These regions are called *Coulomb diamonds*. (b) Differential electrical conductance $\mathcal{G}$ in a logarithmic scale as a function of the gate and applied voltages in a QD. Dark colors indicate absence of transport while the scale of grays denotes the strength of the carrier flow. This illustrates the fact that the QD clearly is in the Coulomb blockade regime. Figure (b) is taken from Lindermann *et al.* [12].

is called *Coulomb diamond* and is visible in a large variety of systems. In experimental setups, the stability diagram is obtained by measuring the differential conductance $\mathcal{G} = dI/dV$ i. e., the variation of electrical current due to a change in the applied voltage. An illustrative example is given in Fig. 1.3b where $\mathcal{G}$ is shown as a function of both gate and bias voltages in a QD. The dark regions in the plot correspond to the turquoise areas in the stability diagram of Fig. 1.3a. Hence, this QD works in the Coulomb blockade regime. In this tesis, we will study QDs and molecular junctions which show these particular patterns in the conductance.

If we measure the linear electrical conductance [the conductance at zero bias $\mathcal{G}_0 = \mathcal{G}(V = 0)$], we observe a series of equidistant resonances. Generally, when $U \gg \Delta E$ the separation between peaks is given by the electrostatic energy $U = e^2/C$. At finite but low temperatures, the width of the resonances is related with the background temperature $k_B T$ [13]. Furthermore, we highlight that Eq. (1.6) implies that the resonances of the dot may be tuned easily by applying a gate voltage V_g. Eq. (1.6) is also valid for molecular junctions and it will be crucial in the description of these systems in Secs. 5.1.1 and 7.2.

The straightforward fabrication and implementation of QDs gives rise to a plethora of quantum transport experiments. Y. Meir *et al.* [14] compared experimental data obtained by Meirav *et al.* [15] with a theoretical model of a QD which shows a sequence of narrow equidistant peaks in the linear conductance $\mathcal{G}_0$ as a function of the gate voltage

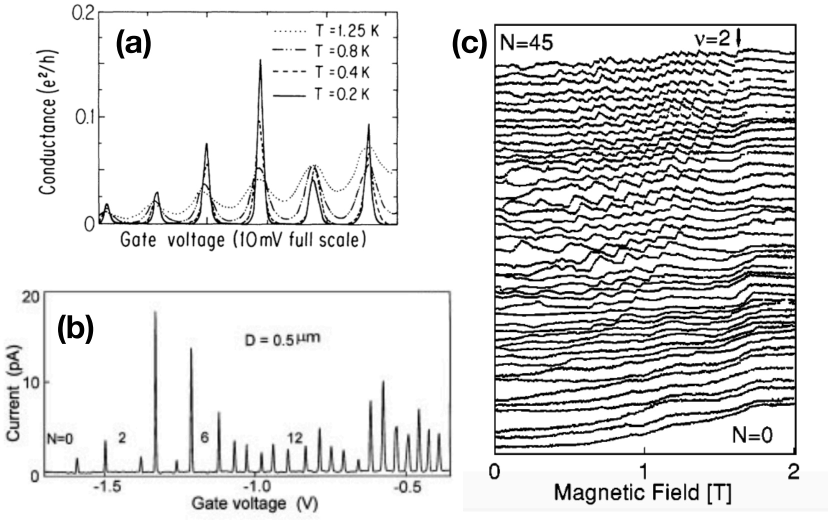

Fig. 1.4. Experiments related to the Coulomb blockade effect. In (a) the electrical conductance is plotted as a function of the gate voltage applied in a QD setup showing a series of equidistant resonances which smear out at higher temperatures. This picture is taken from Y. Meir *et al.* [14]. In (b), Kouwenhoven *et al.* [16] found the same series of peaks separated due to the electron-electron interactions. Finally, (c) shows the evolution of the peaks maxima as function of a magnetic field reported by Ciorga *et al.* [19].

V_g with a smearing at higher temperatures (Fig. 1.4a). Kouwenhoven *et al.* [16] also reported CB oscillations as shown in Fig. 1.4b and applied the *orthodox model* to explain this phenomenon . Additionally, they found a staircase in the current I due to the addition of electrons to the discrete levels of the QD. Nagamune *et al.* [17] observed similar results in a QD which also exhibits Coulomb oscillations. Tarucha *et al.* [18] studied the modification of these oscillations when a magnetic field is applied. The CB resonances shift in pairs when a magnetic field is applied. The latter is strongly related with the results of Sec. 7.2. Ciorga *et al.* [19] studied the transport in a lateral QD under magnetic fields (Fig. 1.4c) obtaining a spin-blockade effect making it possible to find the spin state by measuring the current. These are just a few representative examples. The list we provide is by no means exhaustive.

The CB effect is a main topic of this thesis and we will discuss it properly in the results. First, we analyze the CB effect and the thermoelectric properties (see Sec. 3 for more information about thermoelectricity) of a single QD model in Sec. 7.1. Later, we closely examine the difference between interacting and noninteracting molecular junctions (more information about these systems in Sec. 1.2) in Sec. 7.2. Finally, we investigate the role of interactions in parallel-coupled DQD in Sec. 8.1.

1.2 Molecular junctions

As explained previously, QDs are not the only system exhibiting CB features. This section concerns molecular junctions, systems where a molecule controls the electronic transport between metallic reservoirs. Additionally, these systems have characteristics similar to QDs. We can classify these devices within a branch of science called *molecular electronics* [20], which investigates electrical and thermal transport of individual molecules or combination of them. This area emerged several decades ago with a change of the perspective for molecules: They were not only part of bulk materials, but they might also be useful components for the electronic industry. Nowadays, the analytical tools and device architectures have motivated many scientists from different disciplines to join efforts in this interesting field.

Molecular electronics is important mainly for two different reasons. First, the implementation of molecular devices into nanoelectronic systems serves as a complementary tool due to their novel functionalities out of the scope of solid state devices. On the other hand, it offers new fascinating physics in the description of how molecules behave out of equilibrium. Concerning technological aspects of molecular electronics, it has good advantages in comparison with the technology of regular transistors [21]: To start with, the size of the molecules is around 1 or 10 nanometers and provides good benefits in terms of cost and efficiency. Another advantage is the speed of the molecules because conduction may be favored in well-fabricated molecular wires. Additionally, the fruitful improvement in the technology of nanodevice manipulation makes both the self-assembly of molecular structures and the tuning of its electrical properties easier. Finally, the large number of molecule structures yield new technological insights which a usual silicon-based technology may not achieve.

The first notion of molecular electronics appeared in the 1950's by Arthur von Hippel introducing the basis of bottom-up approach as *molecular engineering* [22]. However, molecular electronics really started in the late 1960's when several groups studied experimentally the electric transport through molecular monolayers. During the 1970's Aviram started the theory of electron transfer in single molecules. In fact, he gave the first proposal of using a single molecule as an electronic component called *molecular rectifiers* [23]. A huge progress occurred in the 1980's with the invention of the scanning tunneling microscope (STM). In fact, the first molecular electronic device appeared in 1985 [24]. More recently, two different groups reported the first transport experiment in single molecule junctions [25] in 1997, which helped molecular electronics to become a well-established field.

The fabrication process of molecular junctions is based on the creation of an atomic-sized contact into a metallic layer. In such contact the molecule shall be placed allowing transport through it. There are different ways to perform it: Employing an STM or an atomic force microscopy (AFM) in which the gap is created using a tip and they move electrons via tunnel currents or electrical forces, respectively. Notwithstanding, one of the most used fabrication processes is the electromigration technique. The method consists of the assembly of a wire between metals which is burnt by applying strongly electrical currents (see Fig. 1.5c). Then, the wire breaks yielding a nanoscale gap inside which the molecule may be stacked.

The fabrication of tunnel junctions explained previously provide setups where the molecule acts as a SET. The molecule energy levels permit a sequential tunneling in the transport where only a single electron may flow though the system at the same time. Nevertheless, there are different molecular systems in tunnel junctions. For example, we highlight the STM break-junctions [26, 27]: the molecule is attached to a metal reservoir and the tip of a STM. A voltage difference is applied between components giving rise to an electrical current through the molecule. Finally, self-assembled molecules (SAM) are also common examples of systems composed of molecular tunnel junctions [28, 29, 30, 31, 32, 33]. They consist of domains where molecules spontaneously organize on top of a metal generating a surface. To induce currents, another metallic material is connected on top of these SAMs.

1.2.1 Transport in molecular junctions

We now briefly review the state of the art in transport experiments concerning molecular junctions. First, H. Park *et al.* [34] reported transport measurements in molecular SETs. The current through the molecule presented quantization of the molecular levels and at low voltages the conductance was surpressed obeying the Coulomb blockade effect (see Fig. 1.4b). Later, J. Park *et al.* [35] showed additional results for SET for two different molecules. They also observed CB effects as the previous work. For strong interactions, a zero-bias anomaly appeared in the electrical conductance as a signature of Kondo correlations (for more information about the Kondo effect, see Ch. 2). The conformation of a molecule in a tunnel junction has been demostrated to modify the shape of the electrical conductance. Venkatamaran *et al.* [26] reported that the conductance decreases as the twist angle between phenyl units in a biphenyl molecule increases. They also observed a decrease of conductance with the number of phenyl units in the molecule. Similar results were found by Ho Choi *et al.* [36] (Fig. 1.5a). They studied the

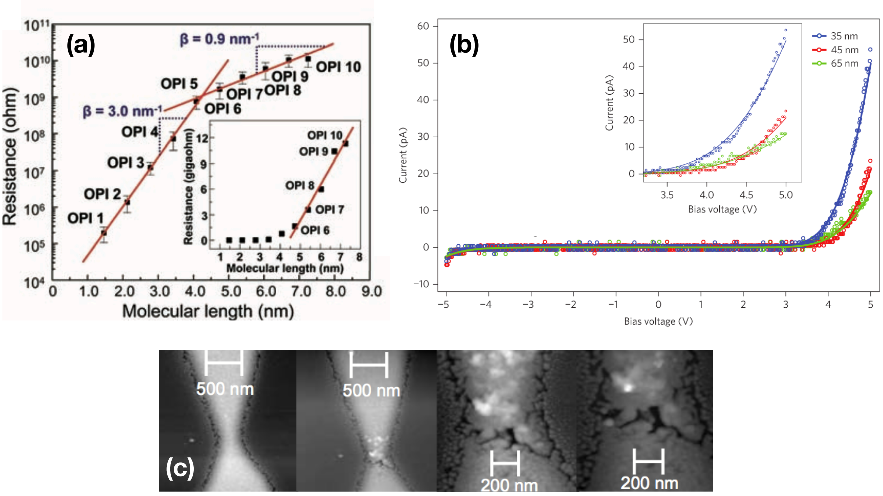

Fig. 1.5. (a) Resistance versus the length of a molecular wire. Increasing the length of molecule will increase its resistance and, consequently, the electrical conductance will decrease. Figure extracted from Ho Choi *et al.* [36]. (b) Current as a function of the voltage bias of a DNA molecule with different lengths. This is a clear example of a molecule diode. This image is a slight modification of Livshifts *et al.* [39]. (c) Images showing a junction during an electromigration process. Clearly, in the fourth image the junction is broken and a small constriction has been created. This image is taken from Cuevas *et al.* [20].

resistance of a molecule dependent on its length finding an increase at higher lengths. More concretely, they found transport regimes for short and long molecules. For each of these regimes, the resistance increases with different exponential trends. The length dependence of the electrical conductance was also studied by Lafferentz *et al.* [37]. Interestingly, the $I - V$ characteristics exhibit a molecular diode shape. Graphene nanoribbons seems to show a similar length dependence in transport than previous works as Koch *et al.* reported [38]. Surprisingly, DNA molecules also exhibit molecular diode characteristics as explained by Livshifts *et al.* [39] (see Fig. 1.5b).

In addition to the molecular diode characteristics, Yan *et al.* identified three different regimes depending on the thickness of a molecule. At low thickness, the coherent tunneling controls the electrical current. On the other hand, strong temperature dependence and hopping transport appear for large thickness. Finally, for intermediate thicknesses (around $3 - 20$ nm) the electric current is tuned mainly by the voltage bias. Yuan *et al.* [40] concluded that control of the coupling between molecules and electrodes is essential to the fabrication of molecular junctions. They found high rectification ratios when a ferrocene

SAM is strongly coupled to the electrodes. Similar rectification effects were also detected by Chen *et al.* [31]. They attributed the rectification to Coulomb interactions which permits to switch electrostatically the coupling between molecules and electrodes. Concerning thermal effects, Garrigues *et al.* [41] investigated the temperature dependence of a Ferrocene molecule. They identified several transport regimes which behave quite differently when temperature is increased. They fit the results using a model which does not take into account electron-electron interactions.

A more detailed explanation of the work of Garrigues *et al.* [41] is found in Sec. 7.2.1. We will compare such work with an interacting model which is also able to fit the experimental results (Sec. 7.2.2). In Sec. 7.2.3, we will discuss the possibility of distinguish between noninteracting and interacting cases. Finally, for a more general overview of molecular junctions one can read Refs. [20, 33, 42].

1.3 Double quantum dots

Since QDs can be considered as artificial atoms, the condensed matter analogue of the molecule is the DQD. They consist of a combination of two QDs which can be connected between them with a tunnel amplitude or capacitively (via Coulomb interactions). DQDs are fascinating devices which exhibit rich physics to be still understood and, consequently, they are one of the pillars of this thesis.

Applying the fabrication techniques explained previously, the creation and manipulation of DQDs are as straightforward as the single QD becoming a suitable device to investigate quantum coherence and superposition states. In addition, there are multiple DQD structures depending on the tunnel configuration between the different parts of the setup (the reservoirs and the dots). Generally, we can distinguish two clear configurations: Parallel-coupled DQDs (Fig. 1.6a) where the QDs are connected to the same reservoirs, usually with a low dot-dot tunnel amplitude, and serially-coupled DQDs (Fig. 1.6b) where each dot is coupled to only one reservoir and electrons have to cross both dots in order to generate transport.

In addition to the Coulomb blockade effect caused by *intradot* couplings, we find that the electron-electron interaction between the dots (*interdot*) may be also significant in the electronic transport. An electrostatic model similar to the Sec. 1.1 is used in order to obtain the stability diagram of the system, i. e. , the regions of (V_{g1}, V_{g2}) where the number of electrons occupying the dots is increased or decreased by one unit ($n_i \to n_i \pm 1$ where $i = 1, 2$ is the subindex determining the QDs). Fig. 1.6c shows the most general electrostatic model for a DQD system, each dot

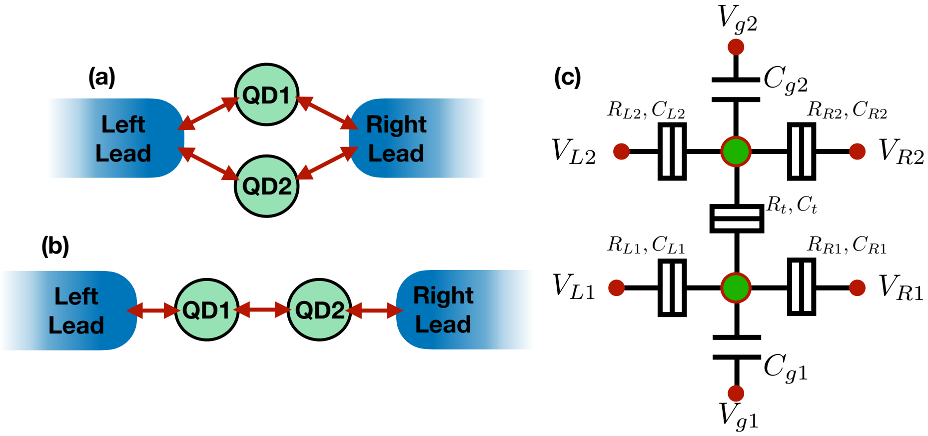

Fig. 1.6. Schematics of the structure of a parallel-coupled DQD (a) and a serially-coupled DQD (b). The former consists of two QDs coupled to the left and right electronic reservoirs while in the latter each dot is attached to a single reservoir and the opposite QD. (c) General sketch of a DQD electrostatic circuit: The tunnel coupling between the reservoir $\alpha = L, R$ and the dot $i = 1, 2$ is modelled with a resistance $R_{\alpha i}$ and a capacitor $C_{\alpha i}$. The dot-dot coupling is represented by R_t and C_t. Additionally, the QD levels may be tuned by applying gate voltages V_{gi}.

attached to two reservoirs with tunnel and capacitive couplings characterized by a resistance $R_{\alpha i}$ and a capacitance $C_{\alpha i}$ where $\alpha = L, R$ denotes the reservoir. Besides, a voltage $V_{\alpha i}$ may be applied to each reservoir of the system. The tunnel barrier between dots is characterized by R_t and C_t. For interacting dots without tunneling, the resistance is assumed to be large $R_t \to \infty$. Finally, the QDs level positions are tuned with the gate voltages V_{gi}. With this model one can switch from the serial to the parallel configuration just with an appropriate change of the parameters of the system.

1.3.1 Parallel configuration

When both dots are connected to the reservoirs but with small tunneling between dots such as $R_t \ll R_{L1}, R_{L2}, R_{R1}, R_{R2}$ in Fig. 1.6c, we deal with the parallel configuration (Fig. 1.6a). In an electrostatic circuit the system is usually described when $V_{L1} = V_{L2}$ and $V_{R1} = V_{R2}$ (see Fig. 1.6c). The stability plot of the parallel DQD clearly shows hexagonal shape (Fig. 1.7a) [43, 44]. Generally, the occupation of the QDs only varies by one electron in sequential tunneling (gray lines in Fig. 1.7a). However, cotunnel transitions are also possible in which two electron transitions take place simultaneously (red lines in Fig. 1.7a).

This configuration is interesting because electrons may take multiple possible paths the transport leading to a coherent superposition of them.

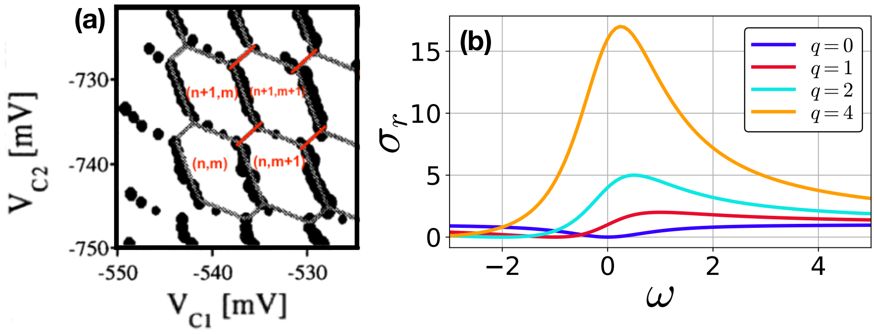

Fig. 1.7. (a) Stability diagram for a typical DQD, V_{C1}, V_{C2} are the gate voltages applied to the dot 1 and 2, respectively. The plot data represent experimental values while the solid lines display the expected diagram computed from an electrostatic model. The solid red lines show the region where a cotunnel transition may occur modifying $(n+1, m) \to (n, m+1)$, n and m being the occupation of the first and second QD. This is a simultaneous two-electron transition. This plot is a slight modification of a figure taken from Hofmann *et al.* [43]. (b) Ratio of transitions probabilities of a particle between the unperturbed path of a continuum state and the perturbed path due to a discrete level as a function of the energy ω and different values of the Fano parameter q [Eq. (1.8)] in a DQD setup.

We now briefly discuss coherence induced effects:

- **Aharonov-Bohm (AB) Interferometer.** DQDs can act as AB interferometers [45]. These devices [46] are systems where an electron can travel in two different ways (in a DQD setup, each possible path crosses a QD) from left to right reservoir. Electrons display an interference pattern dependent on the phase difference between paths. The coherence strongly depends on the singlet or triplet states of a pair of electrons flowing through the AB interferometer [47]. Due to the AB phase, the electric conductance of the system exhibits oscillations when the magnetic field is tuned [45, 48, 49].
- **Fano resonances**. Among the interference phenomena which may manifest themselves in DQDs, we highlight the appearance of Fano resonances [50, 51]. They are produced due to the existence of a coupling between continuum and discrete quantum states [52]. Therefore, particles may perform two different transitions during transport: a path which starts at the continuum, moves to the discrete state and then returns to the continuum and a second one where carriers are not perturbed by the discrete state. The interference between these two amplitudes creates asymmetric line shapes in the total density of states or transmission of the system. In order to observe the asymmetric lineshape, we calculate the ratio σ_r between the total and the unperturbed transition probabili-

ties as a function of the energy ω and the Fano parameter q obtaining,

$$\sigma_r = \frac{(\omega + q)^2}{1 + \omega^2} \, . \tag{1.8}$$

We plot this ratio for different Fano parameters q in Fig, 1.7b. We observe that when $q = 0$ the curve is symmetric and has an antiresonance at $\omega = 0$. As q increases, the shape of the curve becomes more asymmetric. These antiresonances will be also shown in the transmission function of a DQD denoting the existence of a bound state in the continuum (BIC). The DOS $\rho(\omega)$ is now split into two different components: a continuum function of the global spectrum and a discrete state indicated as a Dirac delta centered at the BIC position ω_0: $\rho(\omega) \approx f(\omega) + \delta(\omega - \omega_0)$. In Ch. 8.1, we will explain how BICs are influenced by Coulomb interactions and will discuss their electric and thermoelectric effects.

- **Dicke effect**: Following with the coherence related effects, the Dicke effect resembles the Fano effect in similar ways [53]. This effect was first explained in the context of collisions of atoms in a solid [54]. Dicke states that Doppler resonances which result from the change of momentum due to spontaneous emission of a photon in a pair of atoms generate a resonance in the DOS which narrows in the absence of collisions. In comparison with the Fano effect, the Dicke effect is its optics analogue. Since impurities in metals and QDs can be treated as artificial atoms, the Dicke effect is also expected to arise [55, 56].

Additional effects can be found in parallel-coupled DQDs. For instance, Coulomb drag in QDs, a topic which will be deeply explained in Sec. 1.3.2, is a very appealing effect which has attracted lots of attention nowadays. Furthermore, an experiment was performed by Holleitner *et al.* [57]. They reported that cotunnel effects between dots occur without Coulomb charging energies (strongly related with Fig. 1.7a) and they found that by increasing the interdot tunneling the conductance resonances start to merge. Fuhrer *et al.* [58] reported Fano effect mesurements due to magnetic fluxes and high temperatures. They discovered vanishing Fano resonances at high temperatures. They were able to tune the asymmetry with a magnetic field. Additionally Gustavsson *et al.* [59] were able to detect in real-time electrons interfering in DQDs using a quantum point contact (QPC) as a charge detector. A promising application of DQD setups is their functionality to work as qubits in a quantum computer [60, 61, 62] due to their entanglement properties and easy manipulation using quantum gates.

1.3.2 Coulomb drag

A special case of a parallel DQD structure is described by $V_{L1} = V_{R1} = 0$ and $R_t \to \infty$ in Fig. 1.6c yielding the Coulomb drag effect [63]. In this setup we distinguish two different subsystems coupled to each other via an interdot Coulomb interaction between electrons occupying the QDs described by the capacitance C_t in the electrostatic model. Coulomb drag is just one particular case of a broader topic known as the frictional drag. The phenomenon consists of two isolated conductors with a small separation: one conductor is driven out of equilibrium by an applied voltage V which induces an electric current through this active conductor. However, the passive system is also affected by the bias V of the active layer although this second system is at equilibrium. An interaction between the carriers of the passive and active layers triggers the generation of current at the equilibrium system. In other words, carriers in the biased system drag carriers in the equilibrium system exchanging energy and momentum. The interaction can be of any kind: electron-phonon [64], plasmon [65] or Coulomb interactions, the latter being the main interest in this thesis. Concerning conductors, the Coulomb drag appears in a variety of systems such as 2DEGs [66], nanowires [67], graphene heterostructures [68], etc.

We focus our attention on a capacitive-coupled DQD as sketched in Fig. 1.8a: each layer is composed of a QD attached to two reservoirs. The reservoirs of the active layer (drive system) are at different electrochemical potential generating a voltage bias V. In contrast, the leads of passive layer (drag system) remain at the Fermi energy ε_F. The interaction between layers is basically an interdot electron-electron interaction $\tilde{U}$. The main cause of the induced current in this nanodevice is an asymmetry in the drag system as reported by Sánchez *et al.* [69]. They showed that the detailed balance condition has to be broken in order to find mesoscopic drag in the DQD system. This prediction was confirmed experimentally by Shinkai *et al.* [70] and later by Bischoff *et al.* [71]. In essence, the asymmetry arises from different tunnel coupling of the drag QD to the leads ($R_{L1} \neq R_{R1}$ and $C_{L1} \neq C_{R1}$ in Fig. 1.6.). Recent theoretical and experimental works [71, 72, 73] reveal that cotunnel processes, in addition to sequential tunneling, are crucial to characterize the generation of drag currents.

Several theoretical discussions of the drag effect have recently appeared. Jauho and Smith [74] analyzed the mesoscopic drag current between two 2D conductors for diverse background temperatures. They solved the Boltzmann equation with the goal of examining the change of momentum between layers. They found that the momentum transfer depends on T^2, in good agreement with previous experimental works

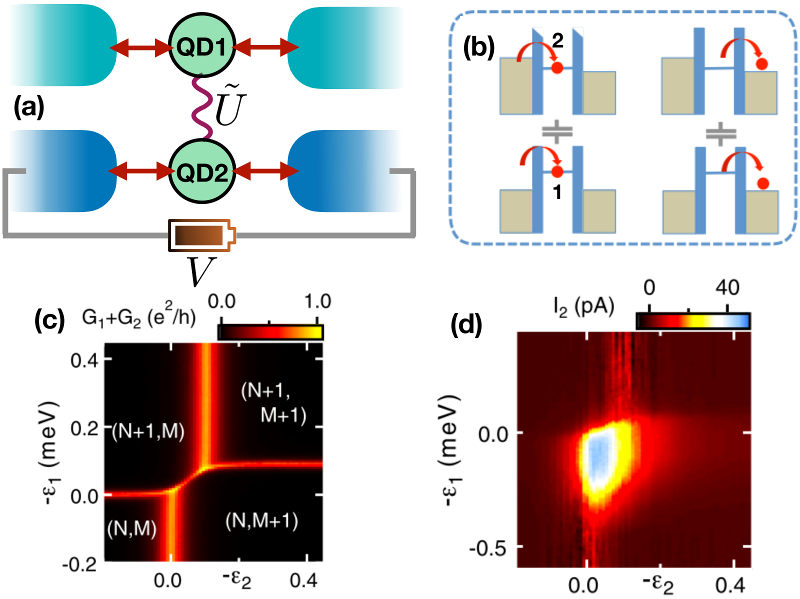

Fig. 1.8. (a) Scheme of a capacitive-coupled DQD acting as a Coulomb drag system. QD1 is attached to the top reservoirs at equilibrium while the QD2 is attached to leads with a voltage difference V. The QDs are linked with an electron-electron interaction $\tilde{U}$ when both dots are filled with one electron. The top system reacts to the applied bias of the bottom system with an induced current at a preferential direction depending on the tunneling amplitudes. (b) Energy diagram of the dominant cotunnel processes yielding drag currents. The height is associated to energy values. Left and right brown squares indicate the lead density of states denoted as Fermi seas controlled by the eletrochemical potentials. The lines in the middle represent the QD energy level taking place in the cotunnel process. Image extracted and slightly modified from Keller *et al.* [72]. (c) Experimental stability diagram portraying the number of electrons of the drive N and drag M QDs. (d) Experimental measurements of drag current as a function of the drive ε_1 and drag ε_2 levels for a given electrical bias. One can observe a regime where the drag takes place around the triple points indicated at (c). Images (b), (c) and (d) are extracted from Keller *et al.* [72].

[75]. Kamenev and Oreg [76] reported results of drag physics in 2D nanodevices finding a rectification of the thermal fluctuations due to the electric fields of the drive system. Levchenko and Kamenev [77] examined exhaustively the drag mechanism in a quantum circuit formed by two QPCs coupled capacitively. The drag is produced by asymmetries in the energy-dependent transmission probabilities of the QPCs. In the linear regime of voltage bias, they observed that the device behaves like a bulk 2D system and in the nonlinear regime, the drag is attributed to the shot noise of the active layer. Later, Sanchez *et al.* [69] studied fluctuation-dissipation relations emphasizing that they are still satisfied

despite the violation of the detailed balance condition.

We want to stress two papers published almost simultaneously: Kaasbjerg and Jauho [73] and Keller *et al.* [72]. Both of them used a master equation approach (for more information about the theoretical model see Segal [78]) obtaining similar theoretical results. They reported that lowest order cotunnel transitions, i. e. , transitions for one electron going out of (into) the drive QD while simultaneously another electron goes into (out of) the drag dot (Fig. 1.8b), play an important role in the Coulomb drag of DQDs. In accordance with previous reports, energy-dependent transition probabilities are also needed in order to generate drag. Particularly, Keller *et al.* showed measurements of a capacitively DQD setup for interdot interactions larger than the lead tunnel rates. They observed that the drag current is higher around the triple points (Fig. 1.8c) corresponding with the range of parameters where the cotunnel transitions take place.

In Sec. 8.2, we also investigate theoretically the Coulomb drag effect in a DQD setup using the Keldysh nonequilibrium Green's function formalism (Ch. 4). We obtain good agreement with the previous experimental results. We connect the Coulomb drag effect with the orbital Kondo effect (for more information see Sec. 8.2) giving some qualitative predictions. Finally, we would like to emphasize the applicability of the Coulomb drag in the current technology. Since DQDs are good candidates for quantum information and quantum computing, the drag effect allows us to analyze deeply and detect the transport mechanism through qubits.

1.3.3 Serial configuration

Now, we consider the case of $R_{L1}, R_{R2} \to \infty$ and $C_{L1}, C_{R2} \to 0$ in the circuit of Fig. 1.6. Notice that carriers need to cross both dots in order to generate non-vanishing currents. Thus, for disconnected dots ($R_t \to \infty$), transport is prohibited. This corresponds to the serial configuration of QDs. At low voltage bias, the stability diagram for serial DQDs is similar to the one shown in Fig. 1.7a also exhibiting an hexagonal shape when tuning the gate voltage of the dots [79].

For dots with a single level $\varepsilon_{1,2}$ contributing to transport, the energy levels of the artificial molecule can be expressed in a more convenient form for negligible interdot Coulomb interactions ($\tilde{U} \to 0$). Thus, we obtain a superposition of bonding and antibonding states:

$$\varepsilon_\pm = \frac{\varepsilon_1 + \varepsilon_2}{2} \pm \sqrt{\left(\frac{\varepsilon_1 - \varepsilon_2}{2}\right)^2 + |\tau|^2}\,, \tag{1.9}$$

where ε_- (ε_+) is the bonding (antibonding) energy level and τ is the tunneling amplitude for an electron to hop between QDs. Notice that we have two energy levels separated at least by τ. Therefore, unless the DQD is decoupled (which makes no sense because we would be dealing with two single QDs systems), the bonding and antibonding levels will never cross. Anyway, for separated energy levels $\Delta\varepsilon = \varepsilon_1 - \varepsilon_2 \gg \tau$ the tunnel amplitude would be negligible.

Another intriguing effect may be encountered when we include spin effects in a highly interacting serial DQD system with also high tunneling amplitudes. At large intradot interactions such that only one electron is occupying each dot, the system yields a superexchange interaction $J_{\text{ex}} \approx \tau^2/U$ which connects the electron spin of the dots. In this situation, the DQD states turns out to be singlet and triplet states. The former would be the ground state [61, 80] which allows the detection and control of the electron spin with a simple detuning the dot energy levels [81]. This result has fundamental importance for quantum computation [60] because serially-coupled DQDs are prototypical examples of entangled qubits. In fact, a large variety of discussions about quantum computation in serial DQDs have been reported [62, 82, 83]. Furthermore, electrons in a serial DQD may also interact with the electron spins at the leads yielding two-impurity Kondo systems. This topic will be explained carefully in Ch. 2.

In the thesis we discuss transport in serially-coupled DQDs in Sec. 8.3 for low temperatures leading to the Kondo effect. We study the thermoelectric and heat transport of a two-impurity Kondo system observing that the thermal bias is able to decouple the DQD. We also investigate how the superexchange interaction J_{ex} is modified by these thermal differences.

2. Kondo effect

Condensed matter physics harbors mysteries and unknown questions yet to discover. It deals with structures embedded in metals, which contain a large number of particles. Since these particles are charged, interactions take place over the whole structure. Therefore, although some effects may be well understood with statistical and mean-field methods, the evidence that there exists complexity in metals is indisputable. The field is thus a part of many-body physics. As an example, a many-body physics problem might be the Coulomb blockade already explained in Sec. 1.1 because even though Coulomb interactions involve two particles, the screening effect of an occupied QD clearly influences all electrons flowing through the leads. On the other hand, when we consider spin and magnetic impurities, metals may experience a very intriguing phenomenon: The Kondo effect [84].

We understand magnetic impurities as the ones which contribute with a Curie-Weiss term to the susceptibility $\mathcal{X} = C(T + \tilde{\theta})^{-1}$ where C is the Weiss constant and $\tilde{\theta}$ is a constant temperature. Basically, the impurities have localized spins which may interact with free conduction electrons in the metal. The spin interactions are responsible of multiple transport phenomena. The most clear manifestation is the appearance of a minimum in the resistance at low temperatures. The first observation of this phenomenon was made by de Haas *et al.* [85] in 1934. However, no rigurorous theoretical explanation appeared until 30 years later when Kondo published his theory [86]. After Kondo's work, the effect behind the resistance minimum was still a topic of discussion for 30 more years since the effect was not totally understood in all regimes of temperature.

It turns out that the birth of nanotechnology inspired a revival of the subject during the last decades [87]. The possibility of simulating the behaviour of magnetic impurities using a QD [7] opens a new window to test the Kondo effect experimentally, spurring a growing interest in theoretical research. Additionally, the easy manipulation of the relevant parameters of a nanodevice enables features and phenomena that would be unfeasible to examine with normal metals.

In this chapter, we explain what the Kondo effect is and discuss the state of the art of this paradigmatic effect. More concretely, we describe

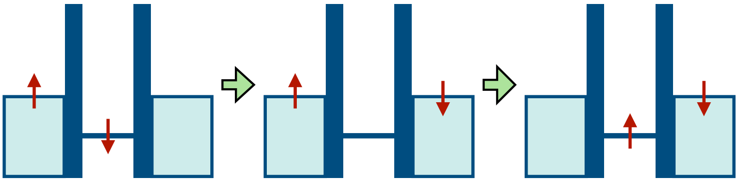

Fig. 2.1. Spin-flip process in an energetic diagram. Light blue rectangles represent Fermi seas of a metal (reservoir) while the dark blue solid line symbolizes the energy level of the magnetic impurity (QD). The electron spin is denoted with red arrows. We observe how the electron flips due to two tunneling processes which empty the localized state and then fill it with an electron of opposite spin.

in detail the effect in Sec. 2.1. We start explaining the appearance of the resistance minimum (Sec. 2.1.1) and then we formulate the Kondo problem (Sec. 2.1.2). We distinguish the typical energies of the problem and we explain the most widely used models which are able to explain the phenomenon (Sec. 2.1.3). Then, we focus on the case when the Kondo effect appears in a QD paying attention of the response to an electric field and we introduce relevant experiments in Sec. 2.2. In the last section, we focus on two concrete cases concerning DQDs: The orbital Kondo effect (Sec. 2.3.1) and the two-impurity Kondo system (Sec. 2.3.2).

2.1 Magnetic impurities in metals

The Kondo effect arises from the screening of a magnetic moment (or a spin in a singly-occupied QD) due to the itinerant electrons in a metal (fermionic reservoirs). An antiferromagnetic interaction results in the emergence of a many-body singlet between the electrons in the conduction band of the metal and the electrons occupying the localized state. High order spin-flip processes are essential to generate such antiferromagnetic correlations. Additionally, strong electron-electron interactions U and low temperatures T are also crucial for this effect to arise.

An example of a spin-flip process is depicted in Fig. 2.1. We observe the metallic Fermi seas at the left and right sides of the diagram and a discrete level with an energy lower than the Fermi energy $\varepsilon_d \ll \varepsilon_F$ (dark blue solid line of the diagram). At the topmost occupied state (Fermi energy ε_F), an electron with spin $\sigma = \uparrow$ is found in one side while an electron of $\sigma = \downarrow$ is situated in the localized level. The spin-flip process takes place via two tunnel hoppings: First, the electron occupying the localized state travels to the right Fermi sea. Afterwards, the electron with opposite spin located at the left reservoir tunnels into the impurity. Since both hopping are virtual transitions, we deal with a spin-flip cotunneling process which is dominant in the regime where the Kondo effect arises.

2.1.1 Resistance Mininum

As temperature is decreased, the resistivity of a metal is expected to diminish. Phonons are almost absent and the resistivity is generally dominated by the electronic collisions with the impurities of the material. For nonmagnetic impurities, the low-temperature resistance is proportional to the concentration of impurities in the metal. In this case, the total resistance gets lower with temperature until it becomes constant at $T \approx 0$. Nonetheless, it was shown experimentally in the 30s that metals doped with magnetic impurities exhibit a fascinating difference: the resistance reaches a minimum and starts to grow at lower temperatures [85]. More experiments were reported in the following years after its discovery. For instance, Sarachik *et al.* [88] clearly showed a resistance minimum for dilute Fe alloys of $\mathrm{Nb}-\mathrm{Mo}$ alloys. Previous results were convincing enough to ensure that magnetic impurities play an important role in metals at low temperatures. Additionally, the minimum depth is proportional to the concentration of magnetic impurities meaning that this effect comes from the combination of the interactions of each single impurity with conduction electrons in the metal.

Kondo [86] explained the resistance minimum using a perturbation expansion of the s-d model up to third order in the antiferromagnetic coupling amplitude $\mathcal{J}$ of the Heisenberg exchange interaction between the localized level and the conduction electrons. He found that the resistance of a metal increases logarithmically as

$$R_{\mathrm{K}}(T) = c_{\mathrm{imp}} R_1 \log \frac{k_B T}{D} , \tag{2.1}$$

where c_{imp} is the concentration of impurities, R_1 a resistance which depends of intrinsic parameters of the system i. e., the antiferromagnetic coupling ($R_1 \propto \mathcal{J}$), and D is the energy bandwidth of the metal assumed to be larger than temperature $D \gg k_B T$. Remarkably, Eq. (2.1), including the phonon term and the constant impurity resistance, accurately agrees with previous experimental results [89].

2.1.2 Fermi liquid and the Kondo Problem

Kondo's prediction correctly describes the resistance minimum and the increasing resistance at lower temperatures. Nonetheless, it has an important drawback: The resistance diverges at $T \to 0$. This unphysical result reveals that the theory is only valid at some regime, even after taking into account higher order terms in the perturbation expansion of the susceptibility [90]. In fact, the logarithmic terms of the expansion may overcome the constant terms yielding a non-physical result in which one can identify a characteristic energy scale

$$k_B T_K \approx D \exp\left(-\frac{1}{2\mathcal{J}\rho}\right), \tag{2.2}$$

where ρ is the density of states of the metal. This energy scale limits the validity of the Kondo model: For $T > T_K$, the Kondo theory is valid and gives reliable results but for $T < T_K$ a nonpertubative approach is needed to understand the physics behind this Kondo problem. In this temperature regime, we can classify the metal to be in a Fermi liquid state.

We understand Fermi liquid as the regime where the properties of the conduction electrons can be described within the Landau-Fermi liquid theory [91]. This theory assumes that the low-energy excitations are equivalent to the excitations of a non-interacting system with renormalized parameters. The effect of interactions depends directly on temperature and at $T = 0$ the metal behaves as a non-interacting system. Now, excitations act as noninteracting quasiparticles with a lifetime which tend to infinity as the energy approaches the Fermi level ε_F due to the Pauli exclusion principle [92]: We consider a metal at $T = 0$ with an excited electron in an energy state $\omega_1 > \varepsilon_F$. The electron interacts with another electron in the Fermi sea with energy $\omega_2 < \varepsilon_F$. The energy of the interacting electrons is exchanged while the total energy has to be conserved $\omega_1 + \omega_2 = \omega_3 + \omega_4$. Due to the Pauli exclusion principle, the resulting states should be above the Fermi sea $\omega_{3,4} > \varepsilon_F$. However, for excitations at the Fermi energy $\omega_1 = \varepsilon_F$, all energies has to be the same yielding infinite lifetimes for such excitations.

Therefore, an important advantage of the Fermi liquid theory is that the Kondo problem can be understood with the noninteracting quasiparticles at low temperatures. Good agreement with experiment is found in the numerical renormalization group (NRG) calculations of Wilson [93]. The NRG method consists of the recursive diagonalization of the model Hamiltonian separated in a finite number of intervals. Each step of the recursive calculation takes a new interval which should be diagonalized to find the resulting eigenenergies. When applying the Fermi-liquid correspondence of the NRG calculation, the local DOS of the Kondo model when $T \to 0$ can be obtained in the particle-hole symmetry point:

$$\rho_{\mathrm{K}}(\omega) = \frac{1}{\pi}\frac{\Gamma}{(\omega - \varepsilon_F)^2 + \Gamma^2}, \tag{2.3}$$

where Γ is the hybridation between the impurity and the excitations in the metal. We observe that the DOS contains a resonance centered at

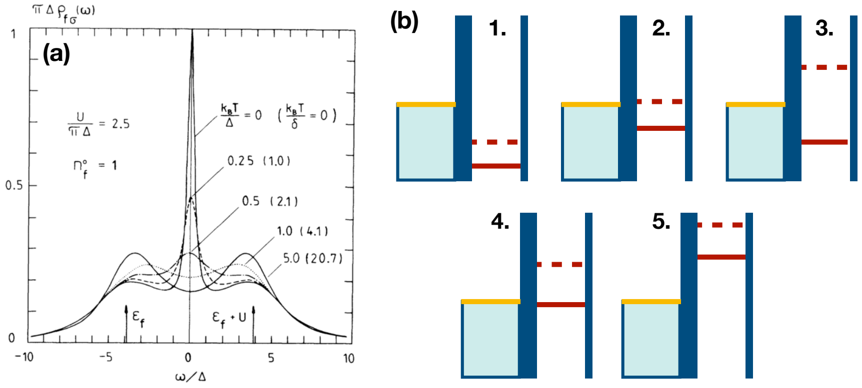

Fig. 2.2. (a) Theoretical DOS of a Kondo impurity as a function of the energy ω for different temperatures showing the Abrikosov-Suhl resonance at the Fermi energy, in this case $\varepsilon_F = 0$. Image taken from Horvatik *et al.* [94]. (b) Energy scheme of the different regimes which are found in the Anderson model. The orange line represents the Fermi energy ε_F while the impurity states are described with red lines at the energy level ε_d (solid line) and the interacting resonance $\varepsilon_d + U$ (dashed line). Diagram 1 corresponds to the full orbital regime. Unlike 1, the scheme 5 shows the empty orbital regime. Schemes 2 and 4 describe the intermediate valence regimes. Finally, the localized moment regime is represented with diagram 3.

the Fermi energy ε_F instead of at the impurity energy level ε_d which is located below the Fermi level. The new peak in the DOS is named Abrikosov-Suhl resonance or Kondo resonance and will be broadly discussed in Secs. 7.3 and 8.3. NRG calculations relate the hybridation function Γ at $T = 0$ with the Kondo temperature $\pi\Gamma = 4k_BT_K/w$ [84] where w is the Wilson number [93]. For this reason, the width of the Kondo resonance can be understood as an effective Kondo temperature T_K at different background temperatures, which will be useful to study the Kondo effect for systems outside the equilibrium. Due to the low value of the Kondo temperature, we expect a very narrow peak in the DOS of the impurity in comparison with the tunnel width of the discrete state resonances. We remark that multiple methods are able to exhibit Abrikosov-Suhl resonances such as Refs. [94] or [95] (Fig. 2.2a). The disadvantage is that the models generally predict a good qualitative, but not quantitative, Kondo temperature.

Furthermore, in the Fermi liquid theory, the Friedel sum rule for interacting electrons is also verified. The Friedel sum rule [96] associates the electronic variations in the metal with the occupation of the impurity. Mathematically, it takes the form [84]

$$\bar{n}_{\mathrm{imp}} = \frac{\eta(\varepsilon_F)}{\pi}\,, \tag{2.4}$$

where $\eta(\varepsilon_F)$ is the phase shift of the system at the Fermi level and can be calculated by evaluating the DOS of the impurity. Since the Kondo models should obey the Friedel sum rule, Eq. (2.4) will be useful in this thesis and will be redefined in Ch. 4 within the non-equilibrium Green's function (NEGF) formalism.

2.1.3 Models and regimes

We will now briefly introduce the theoretical models relevant for this thesis which are broadly used to explain the Kondo effect. First, the exchange s-d model characterizes the impurity as a magnetic moment [97]. In other words, a spin operator $\hat{S}$ gives us the information of the impurity while the conduction electrons moving inside the metal are described with creation and annihilation operators. The local spin and the conduction electrons experience a Heisenberg interaction term whose amplitude is denoted by a coupling constant $\mathcal{J}_{k,k'}$ where k, k' are carrier wavenumbers. This is the model used by Kondo [86] in which he applied a perturbative expansion until third order in $\mathcal{J}_{k,k'}$ finding the logarithm dependence of the resistance.

Another model which describes a magnetic impurity is the so-called Anderson model [98, 99]. In this model, one considers free conduction electrons and a localized state ε_d in which electrons can tunnel out and in with amplitude $\mathcal{V}$. The Pauli exclusion principle only allows two electrons occupying the localized state due to the spin degree of freedom. Additionally, we need to consider the intradot electron-electron interactions U when both electrons occupy ε_d. This model is the key to this thesis and will be fully explained in Ch. 5.

Concerning the energies of the impurity, we can identify several parameter regimes in the Anderson model where the system behaves differently:

- **Localized moment**: when the energy of the localized state is lower than the Fermi energy of the metal $\varepsilon_d < \varepsilon_F$, cotunnel transitions through the impurity are more favorable. On the other hand, the Coulomb interaction U is large enough to prevent the level ε_d from being doubly-occupied, meaning that $\varepsilon_d + U > \varepsilon_F$. Finally, the hybridation constants Γ should be smaller than the distance between the resonances and the Fermi level $\Gamma \ll |\varepsilon_d + U - \varepsilon_F|, |\varepsilon_d - \varepsilon_F|$ in order to clearly obtain discrete levels (Fig. 2.2b, diagram 3). In this regime of energies, the impurity is singly-occupied and the spin-flip processes of Fig. 2.1 are not negligible. Furthermore, the parameter regime is also consistent with the s-d model enabling the conversion from the Anderson model into the s-d model by applying an Schrieffer-Wolf (SW) transformation [100] (see Ch. 5).

- **Intermediate valence**: If the hybridization constant Γ is comparable to $|\varepsilon_d + U - \varepsilon_F|$ and $|\varepsilon_d - \varepsilon_F|$ (Fig 2.2b, diagrams 2 and 4), charge fluctuations are possible and the impurity occupation is no longer constant. Therefore, this regime is not appropriate for applying the SW transformation. This range of energies is also termed the mixed-valence regime.
- **Empty and full orbital regime**: For a level far away from the Fermi energy ε_F, the impurity has no electrons in the localized state ($\varepsilon_d \gg \varepsilon_F$ and $\varepsilon_d + U \gg \varepsilon_F$), as in Fig. 2.2b diagram 5, or is doubly-occupied ($\varepsilon_d \ll \varepsilon_F$ and $\varepsilon_d + U \ll \varepsilon_F$), as in diagram 1. In both cases, if charge fluctuations are negligible, i. e., a constant occupation, virtual transitions are not possible and the impurity does not affect the quantum transport.

The SW tranformation permits to associate the parameters of the s-d model to those of the Anderson model [100]. In fact, Haldane [101] redefines the Kondo temperature of Eq. (2.2) including the intrinsic parameters of the Anderson model for $U \gg \Gamma$.

$$k_B T_K = \sqrt{U\Gamma} \exp\left(\pi \frac{\varepsilon_d(\varepsilon_d + U)}{2\Gamma U}\right) . \tag{2.5}$$

Notice that in the localized moment regime the term inside the exponential in Eq. (2.5) has to be negative. Otherwise, the Kondo temperature would take large values and the model would not be valid.

Although the previous models are widely used in the literature concerning the Kondo effect, we still mention that there exist alternative models decribing magnetic impurities in metals: When considering electrons in d of f shells, the ionic model [102] would be ideal to describe the physics correctly. The ionic model relates the interactions with the low-lying configurations of an isolated ion in the metal. Additionally, there exists a generalization of the s-d model called Coqblin-Schrieffer model [103] which is important for impurities with a large quantity of spin localized levels.

2.2 Artificial Impurities

As stated previously, QDs offer the possibility of revisiting the Kondo physics because they can act as artificial impurities in a 2DEG [87]. In fact, Glazman and Raikh [95] suggested theoretically that transistor-like structures with a resonant tunneling barrier may exhibit a Kondo singlet.

The easy manipulation of artificial impurities provides a new arena to explore the Kondo effect. The QDs as shown in Fig. 1.1 offer a way to test the energy regimes by appropiately tuning the gate with an electric field. Nonetheless, a few distinctions should be pointed out: the levels of the QD are tuned with a gate voltage and we may distinguish regions of an even or odd number of confined electrons. As a result, the total spin of the discrete levels will be determined by the parity and only for odd number of electrons the QD may have a free spin able to display Kondo features [7]. The novelty of this property is that we can turn the QD from a nonmagnetic to a magnetic artificial impurity. Another difference concerns the resistance minimum: the connection of the QD and the electrodes mixes both states through the Kondo resonance. In other words, electrons should cross the impurity to induce currents. In bulk systems, electrons can travel without going through the impurity and the localized state is thus blocking the transport. Consequently, in QDs the linear conductance $\mathcal{G}_0$, instead of the resistance, exhibits a logarithmic increase [104, 105, 106].

2.2.1 Transport and non-equilibrium behavior

Apart from the equilibrium properties, the application of voltage (or thermal) bias between electrodes allows one to study the properties of artificial impurities in conditions out of equilibrium. When the differential conductance is evaluated, a clear sharp resonance emerges at zero voltage ($V = 0$) at low temperatures [7, 105, 107]. Thus, a new channel of transport has been generated due to spin-flip processes between the QD and the fermionic reservoirs. The new resonance in $\mathcal{G}$ is called zero-bias anomaly (ZBA) and is a hallmark of the Kondo effect in QDs. Actually, $\mathcal{G}$ mimics the local DOS and the ZBA can be identified with the Abrikosov-Suhl resonance mentioned above. We remark that the ZBA might also be a signature of other diverse effects such as Majorana fermions [108, 109], so one needs to analyze the system carefully in order to know if the resonance arises from Kondo correlations. Additionally, a magnetic field B is able to split the ZBA in two different resonances at $V \propto \pm B$ [35, 107]. However, as the magnetic field increases, the resonances also smear out and, at sufficiently large B, the Kondo channels disappear (see Fig. 2.3a).

The differential conductance is also a convenient tool to detect regions of odd and even number of electrons. As we explained in Sec. 1.1, the conductance presents a diamond structure when depicted as a function of the gate V_g and bias V voltage. Each of these diamonds represents a different number of electrons and the transport is forbidden inside. When Kondo correlations appear, the ZBA emerges and a nonzero conductance line at $V = 0$ is shown inside the Coulomb diamond only for an odd number of electrons [112, 113, 114] as shown in Fig. 2.3c-

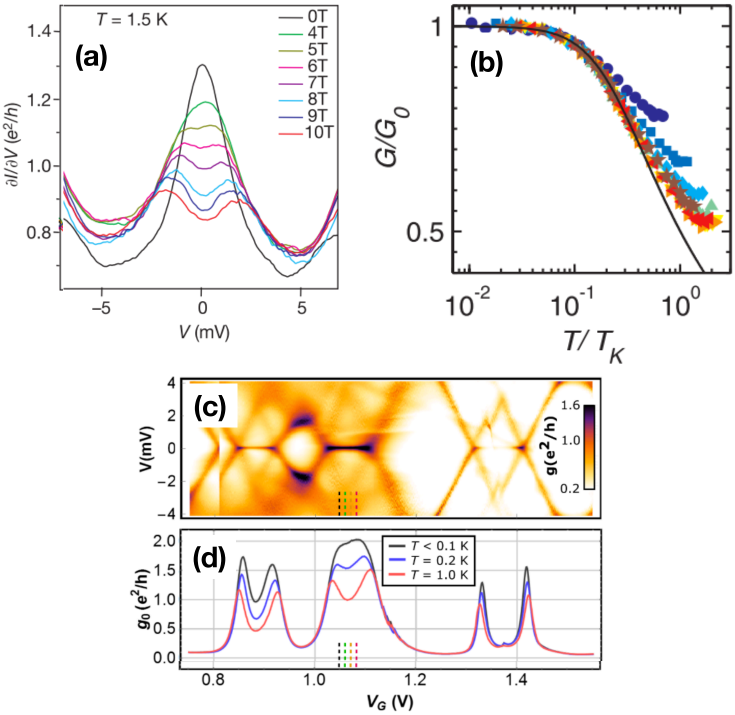

Fig. 2.3. (a) Differential conductance $\mathcal{G}$ of a real QD acting as a Kondo impurity as a function of the bias voltage V and for different magnetic fields showing a splitting of the ZBA. Image extracted from Park *et al.* [35]. (b) Differential conductance measurements of a Kondo impurity as a function of temperature normalized by the Kondo temperature T_K. The solid line represents theoretical calculations. Importantly, all curves seem to coincide showing an universal behaviour. Image extrated from Kretinin *et al.* [110]. (c) Differential conductance as a function of both gate V_g and bias V voltages. We observe lines of transport at $V = 0$ inside the diamond structures of the Coulomb blockade corresponding to the ZBA, alternatively indicating that the QD level is singly-occupied. Therefore, the Kondo effect allows transport at low voltages. (d) Linear electric conductance as a function of the gate voltage V_g for different background temperatures. One can notice how the CB peaks converge in a plateau yielding the ZBA at low temperatures. Plots (c) and (d) taken from Svilans *et al.* [111]

d. At $T > T_K$, the ZBA vanishes and we obtain the typical diamond of the Coulomb blockade effect.

The presence of a voltage bias also modifies the local DOS of the QD. In fact, the Abrikosov-Suhl resonance at the Fermi energy splits into two peaks at finite bias [115, 116]. The reason behind the splitting is that the lead DOSs consist of Fermi seas at unequal eletrochemical potential μ_α. In addition to the resonance separation, the Kondo peaks also weaken at higher voltages due to dephasing destroying the Kondo resonances [117]. Experimentally, it is possible to observe splitting and dephasing in $\mathcal{G}$ of a QD using a third weakly-coupled terminal [113].

A remarkable consequence of the application of a voltage bias is that the conductance $\mathcal{G}$ also obeys a logarithmic dependence [105, 116]

$$\mathcal{G} \approx \frac{e^2}{\hbar} \frac{1}{\ln^2 \frac{eV}{k_B T_K}} . \tag{2.6}$$

Hence, Kondo correlations gradually disappear at high temperatures and voltage biases. Previous works reported that the scaling properties of the Kondo effect are universal [105, 116] with respect to T/T_K and $eV/k_B T_K$. Such universal features can be obtained by applying theoretical and numerical renormalization group techniques. Later, Kretinin *et al.* [110] reported measurements of an experiment with QDs confirming the universality in $\mathcal{G}$ (Fig. 2.3b).

In Sec. 7.3 we investigate the case of a single artificial impurity and we revisit the non-equilibrium features observed and measured previously. Additionally, we explore the case when the single impurity is in contact to a hot and a cold reservoir simultaneously applying three different methods. Finally, we also analyze these effects in the electrical and heat current transport.

2.3 Kondo effect in DQDs

The fabrication of DQDs provides insights of the Kondo effect in new possible ways. Theoretically, the two-impurity Anderson model suggests that the interdot coupling $\tilde{U}$ is also able to create Kondo features [118, 119, 120]. In order to explain this, we return to the DQD structures sketched in Figs. 1.6a, 1.6b and 1.7a when tunneling is not allowed between electrons. For large intradot eletron-electron interactions U, the QDs can only be singly occupied and if the DQD presents a non-negligible interdot interaction, the energy level of the QDs may be treated as a pseudo-spin which also causes Kondo correlations. This is the so-called orbital Kondo effect. On the other hand, both dots may exhibit Kondo features at low temperatures and, in combination with the dot-dot tunnel and intradot couplings, a quantum phase transition (QPT) between the Kondo effect and an antiferromagnetic singlet in the DQD is possible [121, 122, 123]. These setups are part of the two-impurity Kondo systems.

2.3.1 Orbital Kondo effect

The orbital Kondo effect, in comparison with the regular spin Kondo effect, does not vary significantly in a theoretical manner. However, it offers fascinating experimental advantages that are not totally feasible

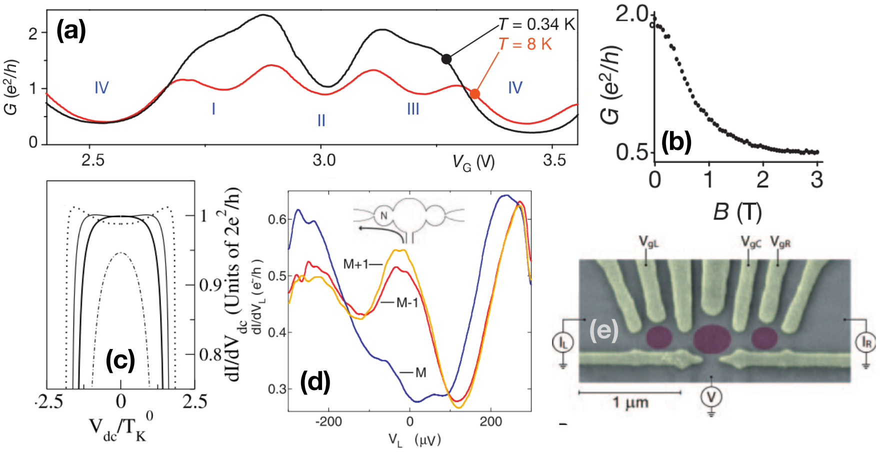

Fig. 2.4. (a) Linear conductance $\mathcal{G}_0$ as a function of the gate voltage of a DQD. An enhancement is shown at lower temperatures indicating Kondo correlations. (b) Differential conductance $\mathcal{G}$ at zero bias as a function of the magnetic field. The intensity of the exponencial decay determines whether the correlations comes from the orbital Kondo effect or not. (c) Theoretical differential conductance as a function of the applied voltage for different values of $J_{\text{ex}}/k_B T_K$ showing a QPT between the antiferromagnetic singlet and the Kondo effect in a serial DQD (d) Experimental differential conductance of an individual dot in a serial DQD system whose STM image is shown in (e). Each curve represents different occupations of the second dot. Plots (a) and (b) extracted from Jarillo-Herrero *et al.* [127], (c) from López *et al.* [128] and (d) and (e) from Craig *et al.*[129].

in the regular Kondo effect. Explicitly, it provides new experimental methods to investigate the phenomenon. Assuming a setup similar to Fig. 1.6a, each QD may experience voltage or temperature biases. In comparison with a regular Kondo impurity, the voltage-dependent situation would be equivalent to apply spin-dependent voltage biases to the electrodes, which is a hard task to accomplish experimentally with real spins but still achievable with ferromagnetic contacts which generate spin-polarized currents [124, 125, 126]. However, the induced spin-dependent tunneling rates may also alter Kondo correlations. Hence, these systems are unable to perfectly describe such situation and a different experimental setup is necessary. For the thermally-biased case, it is not achievable in the regular Kondo effect because the heating affects all conduction electrons indistinctively. Furthermore, in an orbital Kondo impurity, the pseudo-spin may be controlled and measured by using gates at the QDs which in a spin Kondo impurity only can be possible to obtain with magnetic fields .

When the orbital Kondo effect is combined with the regular Kondo effect, novel transport properties are possible. In particular, it has been shown that the regular Kondo temperature T_K may be enhanced for larger interdot interactions [130, 131, 132]. As a consequence, one may observe Kondo features with higher symmetry due to the entanglement between the orbital and spin degrees of freedom (simultaneous spin and pseudospin flips). This combined effect was studied experimentally in carbon nanotubes by Jarillo-Herrero *et al.* [127]. In Fig. 2.4a the linear conductance of the system exhibits an enhancement when the temperature is lowered as expected with the Kondo effect. They distinguish the orbital Kondo resonances from the regular spin Kondo effect by evaluating the exponential decay at applied magnetic fields (Fig. 2.4b). Recently, Amasha *et al.* [133] reported interesting experimental results. They found the usual ZBA for strong interdot coupling proving that the system is in the orbital Kondo regime. When a pseudo-spin Zeeman splitting is present, the individual conductances exhibit Kondo resonances at the spin-dependent voltages. Nevertheless, the width of the Kondo peaks are equal demonstrating that a general characteristic Kondo temperature T_K may be deduced.

In this thesis we investigate theoretically an orbital Kondo system in which the Kondo correlations induce the Coulomb drag effect in Sec. 8.2.

2.3.2 Two-impurity Kondo system

In addition to the orbital Kondo effect, other effects may arise in DQD systems. Here, we highlight the competition in a DQD at low temperatures between the Kondo effect and the Ruderman-Kittel-Kasuya-Yosida (RKKY) interaction [134]. The latter was first described by Ruderman [135] and consists of the interaction between nuclear magnetic moments in metals. The work was extended later by Kasuya [136] and Yosida [137]. The RKKY interaction is also visible in DQDs with large intradot and tunnel couplings [138]. As explained in Sec. 1.3.3, both couplings may result in an effective antiferromagnetic interaction J_{ex} between dot spins. When the antiferromagnetic interaction is large enough, a spin singlet between the electrons of the localized dots is created.

Notice that the interaction between the localized spin states of the QDs competes with the Kondo effect and, consequently, yields a QPT as explained by Craig *et al.* [129]. As shown in Fig. 2.4d, they depicted the differential conductance of the left dot of the serial DQD system of Fig. 2.4e. A Kondo resonance arises for even occupations of the right QD when the left QD is filled with an odd number of electrons. Nevertheless, the resonance is absent when the right dot has odd number of electrons (blue curve in Fig. 2.4d). The reason behind this effect is the generation of a spin singlet from the RKKY interaction. López *et al.* [128] studied theoretically such QPT, finding that is visible in the conductance due to the splitting of the ZBA at larger J_{ex} (Fig. 2.4c). Such peak separation is also visible in the work of Aono *et al.* [139]. Additionally, a QPT between ferromagnetic to antiferromagnetic coupling is visible in the occupation of the system depending on the spin degrees of freedom as reported by Zitko *et al.* [140].

We emphasize the amount of experimental work related to the characteristic QPT. In addition to Schroer *et al.*. [134] and Jeong *et al.* [138], DQDs in carbon nanotubes also display the transition between Kondo and the antiferromagnetic spin singlet as reported by Chorley *et al.* [141]. On the other hand, Chen *et al.* [142] studied how the system is affected by tuning the tunneling coupling τ. They observed a single Kondo peak at low values of τ and a splitting of the resonance at large dot-dot tunneling.

In Sec. 8.3 we investigate theoretically the role of the tunneling amplitude finding similar results as in Chen *et al.* [142] and study how the system responds when a thermal bias is applied. Furthermore, the electric and heat currents are calculated finding nonlinear characteristics. Finally, we discuss the Kondo-to-antiferromagnetic-singlet QPT and how the critical value of the antiferromagnetic coupling J_{ex} can be modified with a temperature gradient.

3. Quantum Thermoelectrics

So far, we have focused on how electric currents are induced by applying electric fields and have discussed experiments and theoretical works concerning intriguing transport properties of QDs. For a more complete understanding, different driving forces can be applied such as magnetic fields, mechanical perturbations or additional electric potentials to observe and compare the response of nanodevices. Generally, temperature plays an important role. For example, nanostructured setups are not able to operate at high temperatures because quantum coherence decays with increasing temperatures. Besides, in the previous chapter we have explained how low temperatures contributes to many-body phenomena such as the Kondo effect. Furthermore, nanodevices can be attached to more than one fermionic reservoir at different temperatures. In such case, an electric current can also be induced even in the absence of a voltage bias.

On the other hand, we remark that heat may additionally be transferred along a conductor (or the nanostructured device) yielding heat currents Q. In fact, thermal gradients are able to cause heat flows via phonons, photons or transfer of particles. In comparison with the electric current, applied voltages can be also responsible for generating heat currents in the system. In summary, voltage biases V may induce heat currents Q and thermal biases θ may produce electric currents I. These effects are at the core of the field called *thermoelectrics* [143, 144].

The field of thermoelectrics was born in 1821 with an experiment realized by T. J. Seebeck. He showed that when a junction connecting two dissimilar metallic wires is heated, an electromotive force is produced [145]. This effect yields a finite voltage induced in open circuit conditions. Therefore, wires forming a thermocouple exhibits thermoelectric voltages proportional to the temperature applied at the junction. This effect is called Seebeck effect (more details in Sec. 3.1). Later, a second discovery was made by J. Peltier in 1834. He found that the direction of the electric current applied to a thermocouple may produce a small cooling or heating [145]. This phenomenon is called Peltier effect. We shall remark that this is a different effect from the Joule heating characteristic of metals which quickly dominates in the system. The main difference is that the Peltier effect comes from a reversible process while the Joule effect is an irreversible process which always dissipates energy at the system. The nontrivial reciprocal relation between Seebeck and Peltier effects was revealed by W. Thompson in 1855. The coefficients which characterize both effects are related theoretically using the Onsager relations derived from the microreversibility principle [146].

Hence, a thermocouple can act as a heat engine or a refrigerator if we apply a temperature difference or a voltage bias, respectively. More recently, Joffe reported that doped semiconductors are materials with relatively high efficiency [147]. Such efficiency is often evaluated by the figure of merit ZT in which normal devices are usually characterized by $ZT \approx 1$. Nevertheless, figures of merit of $ZT > 3$ are necessary to obtain competitive heat-to-work converters.

Nanotechnology offered new prospects in the thermoelectrics field. Hicks and Dresselhaus [148, 149] reported theoretical results showing that low dimensionality systems might present high values of ZT. Particularly, Mahan and Sofo [150] demonstrated that narrow resonances may give $ZT \to \infty$ Therefore, nanodevices such as QDs are promising setups to fabricate efficient converters of waste heat to work. Nowadays, a large amount of works can be found about thermoelectric properties of nanostructures [151, 152].

This chapter summarizes the physics and the state of the art of thermoelectrics. First, we explain the basic concepts in Sec. 3.1 which are crucial to understand the theoretical works of this thesis: we introduce linear transport coefficients and the Onsager reciprocal relations in Sec. 3.1.1, following a discussion of the connection with nanodevices in Sec. 3.1.2 and finishing with a summary of the heat transport properties in Sec. 3.1.3. Later, an overview of rectification, asymmetries and nonlinear transport is given in Sec. 3.2. Finally, in Sec. 3.3 we review recent theoretical and experimental works on thermoelectrics in QDs.

3.1 Basic Concepts

Although the physics of thermoelectrics can be qualitatively understood, we need to learn the basic concepts in order to properly analyze the QD systems of this thesis. For this reason, we focus on the main parameters concerning thermoelectrics and its relations in transport theory. Let us now consider a system as skecthed in Fig. 3.1. It consists of a QD coupled to two reservoirs at different temperatures T_α and electrochemical potentials μ_α. Consequently, we define a voltage bias $V = \mu_L - \mu_R$ and a thermal difference $\theta = T_L - T_R$ for the system. We remark that even though Fig. 3.1 is depicted with a QD, the definitions of the following sections are general for conductors and other nanodevices.

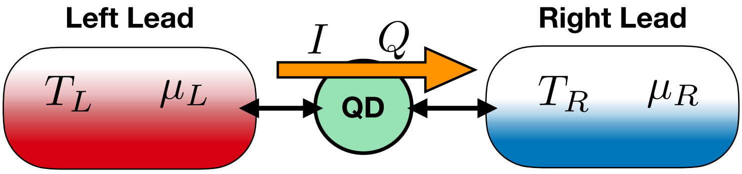

Fig. 3.1. (a) Scheme of a QD structure connected to two leads under non-equilibrium conditions $\mu_L > \mu_R$ and $T_L > T_R$. We illustrate the case when the electric (I) and heat Q currents flow from the left to the right lead.

3.1.1 Linear Transport. Onsager relations

We begin with the definitions of the linear transport coefficients. We identify two different flows through a conductor: the electronic flux determined by the electric current I and the heat flow characterized by the heat current Q.

It is well known that after applying a voltage bias V an electric current will flow obeying the Ohm's law $I = \mathcal{G}_0 V$, where

$$\mathcal{G}_0 = \left.\frac{\partial I}{\partial V}\right|_{eq}, \tag{3.1}$$

with eq denoting $V = 0$ and $\theta = 0$ (equilibrium). In this case, $\mathcal{G}_0$ is the *linear electrical conductance*. In analogy with the Ohm's law, the heat current Q of a conductor increases linearly with a temperature gradient θ following the Fourier's law $Q = \mathcal{K}_0\theta$:

$$\mathcal{K}_0 = \left.\frac{\partial Q}{\partial \theta}\right|_{eq}, \tag{3.2}$$

$\mathcal{K}_0$ being the *linear thermal conductance*. However, there still exist two more cases. When a thermal bias θ is applied to the system, an electric current is also induced. In the absence of applied electric fields, this current is regarded as thermocurrent $I_{\text{th}}(\theta) = I(V = 0, \theta)$ from which the *linear thermoelectric conductance* $\mathcal{L}_0$ is derived:

$$\mathcal{L}_0 = \left.\frac{\partial I_{\text{th}}}{\partial \theta}\right|_{eq}. \tag{3.3}$$

Eq. (3.3) represents the changes in the electric current due to small thermal differences. The last case is the generation of heat current due to the application of a voltage bias to the system obtaining $Q = \mathcal{R}_0 V$. Now, the coefficient which governs the linear transport is the *linear electrothermal conductance*,

$$\mathcal{R}_0 = \left.\frac{\partial Q}{\partial V}\right|_{eq}. \tag{3.4}$$

Therefore, we have defined four different responses which fully determine the linear transport through the system. Near equilibrium, one can express the currents as a function of both biases (a voltage V and a thermal bias θ) simultaneously:

$$I = \mathcal{G}_0 V + \mathcal{L}_0 \theta \,, \tag{3.5a}$$

$$Q = \mathcal{R}_0 V + \mathcal{K}_0 \theta \,. \tag{3.5b}$$

With a proper manipulation of the parameters, the conductances form the Onsager matrix [151, 153]. In addition, the second law of thermodynamics imposes the conditions that the electrical and thermal conductances should be always positive ($\mathcal{G}_0 > 0$ and $\mathcal{K}_0 > 0$) [151]. The reason behind these requirements can be understood with the power $P = IV$ which has to be always positive in the linear regime. Therefore following Eq. (3.5a) for $\theta = 0$ we observe that $\mathcal{G}_0 V^2 > 0$ yielding the previous condition. Similar arguments can be made for $\mathcal{K}_0$.

Additional relations may be established after applying the Onsager-Casimir conditions [146]. When applying a magnetic field B, microreversibility relates the thermoelectric and electrothermal conductances:

$$\mathcal{R}_0(-B) = T\mathcal{L}_0(B) \,. \tag{3.6}$$

Notice that for a zero magnetic field $T\mathcal{L}_0 = \mathcal{R}_0$. For the electric and thermal conductances, a symmetry condition with the magnetic field is demanded from microreversibility

$$\mathcal{G}_0(B) = \mathcal{G}_0(-B) \,, \tag{3.7}$$

$$\mathcal{K}_0(B) = \mathcal{K}_0(-B) \,. \tag{3.8}$$

Although $\mathcal{L}_0$ and $\mathcal{R}_0$ are good quantities to theoretically study the thermoelectric properties of small conductors, experimentally it is customary to work with different thermoelectric coefficients. First of all, let us consider again the setup of Fig. 3.1. After applying a temperature difference θ, one may tune the electrochemical potentials μ_α in order to compensate the electric flows obtaining zero net current $I(V,\theta) = 0$. The voltage corresponding to this situation is called *thermovoltage* $V = V_{\text{th}}$. Using Eq. (3.5a), the thermovoltage can be written in terms of the conductances allowing us to obtain the Seebeck coefficient or *thermopower* $\mathcal{S}_0$:

$$\mathcal{S}_0 \equiv -\frac{V_{\text{th}}}{\theta} = \frac{\mathcal{L}_0}{\mathcal{G}_0} \,, \tag{3.9}$$

where the sign of $\mathcal{S}_0$ is chosen by convention. The Peltier effect is described by the generation of heat currents due to applied electric currents, in the absence of thermal bias ($\theta = 0$). Therefore, we define the

Peltier coefficient Π_0 as

$$\Pi_0 = \left.\frac{Q}{I}\right|_{\theta=0} = \frac{\mathcal{R}_0}{\mathcal{G}_0}\,. \tag{3.10}$$

The Peltier coefficient can also be understood as the transported entropy by the electron flow of the system [151] because the entropy current depends linearly on the heat current proportional to Π_0/T. Note that the Onsager reciprocal relation of Eq. (3.6) provides a correspondence between the Seebeck and Peltier coefficients.

$$\Pi_0(B) = T\mathcal{S}_0(-B) \tag{3.11}$$

All previous relations are derived by using the standard thermodynamics for irreversible processes. Nevertheless, results obtained within transport theory, i. e., Boltzmann equation or the Landauer formalism, give us additional relations for conductors at low temperatures. The approximations would be generally valid for macroscopic conductors. However, they also offer good qualitative behavior for small devices. Firstly, the thermal and electric conductances are related by the Wiedemann-Franz (WF) law [154, 155]

$$\frac{\mathcal{K}_0}{\mathcal{G}_0} = \tilde{L}_0 T\,, \tag{3.12}$$

where $\tilde{L}_0 = \pi^2(e/k_B)^2/3$ is the Lorentz number. Generally, the WF law can not always be applied and has a very specific range of validity. On the other hand, the *Mott's formula* [156] establishes a relation between the thermopower and the electric conductance.

$$\mathcal{S}_0 = \frac{\pi^2}{3}\frac{k_B}{e}k_B T\frac{d}{d\mu}\ln\mathcal{G}_0(\mu)\,, \tag{3.13}$$

where μ denotes the chemical potential of the conductor ($\mu = \varepsilon_F$). These relations are of fundamental interest for the study of thermoelectric properties of metals and are generally violated when considering nonlinear effects (Sec. 3.2).

3.1.2 Connection with internal properties of nanodevices

An important advantage of the thermoelectric properties in nanodevices is that we deal with measurable physical magnitudes. Other quantities such as, the spectral ρ or the transmission $\mathcal{T}$ function, are internal properties of the system and, only under specific conditions, it is possible to find relations between internal quantities and the conductances of the system. For the case of the transmission function, we highlight the Landauer formula [155]

$$\mathcal{G}_0 = \frac{2e^2}{h}\mathcal{T}(\varepsilon_F) \ . \tag{3.14}$$

This corresponds to the conductance of a quantum channel inside a nanodevice. The transmission $\mathcal{T}$ is the probability for an electron to cross the system. Eq. (3.14) is valid at $T \to 0$. After applying the Landauer formalism to the thermal conductance $\mathcal{K}_0$, a similar result is obtained leading to the expression of the WF law (Eq. 3.12). Additionally, Eq. (3.14) has two different terms that are essentially positive which gives $\mathcal{G}_0 > 0$. One is the already explained transmission function of the electrons at the Fermi energy and the second is twice (due to spin degree of freedom) the quantum of electric conductance $\tilde{g}_0 = e^2/h$.

On the other hand, the thermoelectric coefficients give us new opportunities for the study of the internal properties of nanodevices. The Mott formula [Eq. (3.13)], also obtained from Landauer formalism, states that the Seebeck coefficient is dependent on the first derivative of the transmission function $\mathcal{T}'(\varepsilon_F)$ after replacing Eq. (3.14) into Eq. (3.13). Hence, the Seebeck coefficient offers additional information about the internal characteristic of the system. In this case, we observe that now $\mathcal{S}_0$ may also give negative values. The sign of the thermopower determines if the flow is dominated by electrons (positive) or holes (negative) [151]. To clarify, holes mean electrons traveling below the Fermi energy.

The previous results lead us to the discussion of the differences between the electric currents $I(V)$ and thermocurrents $I_{\text{th}}(\theta)$. First, the electric current will present in single QDs a staircase shape as a function of the applied voltage V and can not present sign reversals since the disspated power IV must be positive. In contrast, the thermocurrent may exhibit several changes of sign since the flow of holes and electrons may be modified at higher gradients. Such sign reversals give points of finite thermal biases θ and zero net currents. We call these points *nontrivial zeros* of the thermocurrent and they were already predicted and observed (see Sec. 3.3.2 for more details). Another difference concerns the theoretical range of V and θ. The electrical current can be obtained at all values of V whereas the thermocurrent gives unphysical values when $\theta < -T$ because the temperature can not cross the absolute zero $T_\alpha = 0$. We may solve this problem in two terminal system by considering that negative θ denotes a heating of the second reservoir with $\theta_R = -\theta$. Generally, with this definition we also expect symmetric shapes of thermocurrent around $\theta = 0$ as happens with electrically-biased currents.

3.1.3 Heat transport

Here, we discuss general aspects of heat transport. Typically, the heat current behaves essentially different from the electric current. For this reason, theoretical heat transport approaches may not be as straightforward as electric current models. Experimentally, measurements require more stringent techniques in order to probe thermal properties of nanodevices and employ indirect methods [145]. This is related to the quantum of thermal conductance κ_0 [157, 158, 159] which takes the form

$$\kappa_0 = \frac{\pi}{6\hbar} k_B^2 T \,. \tag{3.15}$$

In contrast with $\tilde{g}_0$ which take values around $38.7\ \mu\text{A}/V$, the thermal quantum conductance is dependent on the background temperature. This implies a disadvantage for measurement since nanodevices work at very low temperatures, where the thermal quantum may range from $\kappa_0 = 3.35$ pW/K at 4 K to $\kappa_0 = 84.9$ pW/K at 100 K.

Furthermore, the thermal conductance has two different contributions in small-scaled systems: $\mathcal{K}_{\text{ph}}$ associated to vibrations of the lattice and $\mathcal{K}_0$ related to the carriers. In the former case, the vibrations correspond to collective oscillations whose excitations are described with bosonic quasiparticles called phonons. The phonon behavior is usually studied with the Debye model [160]. From a thermoelectric perspective, the goal is to reduce considerably the phonon contribution inside the conductor in order to only deal with the carrier conductance. An additional Peltier coefficient may emerge as a result of the energy exchange between phonons and electrons leading to the phonon drag effect [153]. Consequently, a Seebeck coefficient arises due to Eq. (3.11) yielding new thermoelectric effects. Nevertheless, thermoelectric devices commonly operate in a regime of parameters where the phonon drag effect is negligible.

The systems considered in this thesis work at very low temperature. As a consequence, the motion of carriers governs the thermal conductance and, therefore, the phonon thermal conductance is assumed to be negligible $\mathcal{K}_{\text{ph}} \to 0$. Thus, we focus our attention on studying the effects related to the electronic thermal conductance. Using first law of thermodynamics, the heat current may be separated in two different terms [161]

$$Q = Q_E + IV \,, \tag{3.16}$$

where Q_E is the energy current associated to the internal energy rate of change in the system and IV is the Joule term coming from the dissipation of energy due to a flow of particles in the conductor. We remark that at low voltages the Joule term of Eq. (3.16) is second order in V. This implies that the electrothermal conductance, and consequently the Peltier coefficient, is originated from the energy current Q_E. Hence, the thermal conductance $\mathcal{K}_0$ is determined from the energy current since the first order in θ of the Joule term would also lead to a term proportional to $V\theta$. Therefore, the linear transport of heat is basically dominated by the internal energy flow Q_E and corresponds to a reversible term whereas the Joule effect is an irreversible process which dominates at high applied voltages.

3.2 Rectification and nonlinear effects

When working with bulk systems, the applied gradients can not be strong since the distances in the conductor are usually large. In this case, the system properties are restricted to the linear regime. Nevertheless, nanodevices are characterized for their small size and, in this case, the nonlinear effects are accessible. Additionally, such systems are characterized by a transmission function highly dependent on the energy $\mathcal{T}(\omega)$, a feature that induces nonlinear transport phenomena.

Far from equilibrium, it is convenient to study the differential transport coefficients of the system. They are defined in the following way

$$\mathcal{G} = \frac{\partial I}{\partial V}\,,\ \mathcal{L} = \frac{\partial I}{\partial \theta}\,,\ \mathcal{R} = \frac{\partial Q}{\partial V}\,,\ \mathcal{K} = \frac{\partial Q}{\partial \theta}\,, \tag{3.17}$$

which are the differential electrical, thermoelectrical, electrothermal and thermal conductances, respectively. The electrical conductance was already explained in Ch. 1. The rest of conductances were less studied in literature, despite the fact that they became variables of interest during the last decades [162]. In addition to the conductance, differential Seebeck and Peltier coefficients can also be defined:

$$\mathcal{S} = \frac{\partial V_{\mathrm{th}}}{\partial \theta}\,,\ \Pi = \frac{\partial Q}{\partial I}\,. \tag{3.18}$$

Generally, the currents are measured at the fermionic reservoirs connected to the nanodevices and we are not only restricted to the case of two reservoirs. For this reason, we now consider the multiterminal setup of Fig. 3.2. A QD system attached to N reservoirs denoted with $\alpha = \{1, 2, \dots, j \dots, N\}$ (for $N = 2$ reservoirs $\alpha = \{L, R\}$) and each of them characterized by an electrochemical potential $\mu_\alpha = \varepsilon_F + eV_\alpha$ and a local temperature $T_\alpha = T + \theta_\alpha$ where ε_F is the Fermi energy and T the background temperature. Therefore, the electric I_α and heat Q_α flows are dependent on α and need to obey conservation laws: The conservation

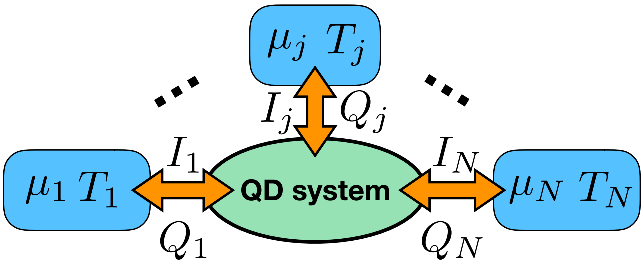

Fig. 3.2. Sketch of the most general QD system attached to N fermionic reservoirs denoted as $\alpha = \{1, 2, \dots, j \dots, N\}$ and characterized by an electrochemical potential of $\mu_\alpha = \varepsilon_F + eV_\alpha$ and a temperature $T_\alpha = T + \theta_\alpha$. Each of these reservoirs experiences electric I_α and heat Q_α currents.

of charge demands the following condition to the electrical currents in the steady state:

$$\sum_\alpha^N I_\alpha = 0\,. \tag{3.19}$$

and the energy conservation law requires that in the long time limit

$$\sum_\alpha^N Q_\alpha = \sum_\alpha^N I_\alpha V_\alpha\,. \tag{3.20}$$

Every model must satisfy Eqs (3.19) and (3.20) even in the nonlinear regime of transport. In the following sections we will briefly discuss the present knowledge about nonlinear transport in nanostructures.

3.2.1 Second order conductances. Violation of linear relations

The most straightforward extension of the transport theory to the nonlinear regime is to include the second order corrections to the currents. In this section we introduce the second order conductances and review the most relevant works regarding this topic

Expanding the currents I_i and Q_i as a function of each applied voltage and thermal bias one obtains

$$I_i = \sum_j \left(\mathcal{G}_{ij} V_j + \mathcal{L}_{ij}\theta_j\right) + \sum_{jl}\left(\mathcal{G}_{ijl} V_j V_l + \mathcal{L}_{ijl}\theta_j\theta_l + \mathcal{M}_{ijl} V_j \theta_l\right), \tag{3.21a}$$

$$Q_i = \sum_j \left(\mathcal{R}_{ij} V_j + \mathcal{K}_{ij}\theta_j\right) + \sum_{jl}\left(\mathcal{R}_{ijl} V_j V_l + \mathcal{K}_{ijl}\theta_j\theta_l + \mathcal{B}_{ijl} V_j \theta_l\right). \tag{3.21b}$$

Notice that now in addition to the diagonal second order conductances ($\mathcal{G}_{ijl}$, $\mathcal{L}_{ijl}$, $\mathcal{R}_{ijl}$ and $\mathcal{K}_{ijl}$), Eq. (3.21) has two crossed contributions $\mathcal{M}_{ijl}$ and $\mathcal{B}_{ijl}$ which appear in the case of simultaneous thermal and voltage

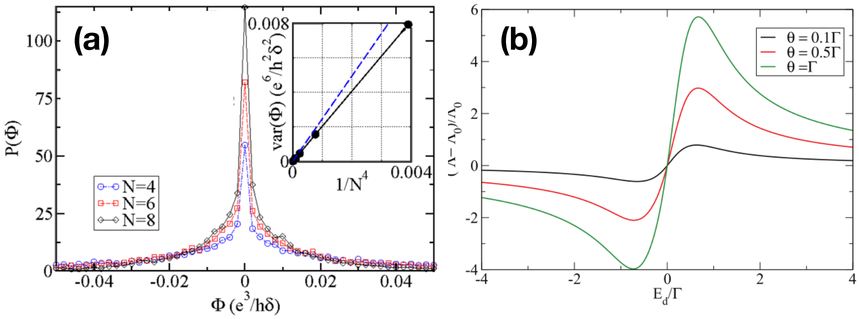

Fig. 3.3. (a) Probability distribution for the departures from the Onsager relation of the electrical conductance of chaotic cavity connected to N conductor channels. Image taken from Sánchez and Büttiker [163]. (b) Departures from the WF law as a function of the energy of the discrete level of an interacting QD attached to two reservoirs at different temperatures. Image taken from López and Sánchez [168].

biases in the electrical and heat currents, respectively. The first terms in the expansions still obey the linear transport relations of Sec. 3.1 and departures will only be visible in the second order conductances. Consequently, we are interested in the violation of the relations for the differential conductances.

Firstly, the electric nonlinear transport and its deviations from Eq. (3.7) were studied by Sánchez and Büttiker [163]. They theoretically investigated the electrical current under a voltage bias for a finite magnetic field and they calculated for the specific case of a quantum Hall bar the Onsager asymmetry of the second order conductance ($\Phi = [\mathcal{G}_{111}(B) - \mathcal{G}_{111}(-B)]/2$ in Fig. 3.3a) finding that the nonlinear conductance is indeed asymmetrical due to electron-electron interactions. Spivak and Zyurin [164] found similar results with a different approach. Later, Marlow *et al.* [165], Zumbühl *et al.* [166] and Leturcq *et al.* [167] confirmed previous predictions with experimental measurements of phase-coherent billiards, chaotic QDs and AB interferometers, respectively.

Thermal and thermoelectric rectification effects may also be present in mesoscopic conductors. Kulik [169] investigated the thermoelectric generation and cooling in metallic constrictions. He discussed the possibility of having nonlinear thermoelectric cooling (nonlinear Peltier effect). Dzurak *et al.* [170] reported measurements of the thermopower in a one-dimensional constriction. They were able to approximate the results with a linear-response model. Bogachek *et al.* [171] studied the thermal transport and Peltier effect in the nonlinear regime. They uncovered that the Kelvin-Onsager relation given by Eq. (3.11) and the WF law are not satisfied in the nonlinear regime. Thermal rectification effects were also modelled in a mesoscopic conductor by Terraneo *et al.* [172].

Additional experiments were realized by Chang *et al.* [173] in carbon nanotubes and by Scheibner *et al.* [174] in QDs. Furthermore, Whitney [175] analyzed theoretically refrigeration and heat engine circuits in the nonlinear regime of transport for a QPC with electron-electron interactions. He discussed the parameter regimes where ZT is no longer a good variable to describe thermoelectric transport and one needs to resort to the nonlinear transport calculations.

Very recently, Sánchez and López [176] used scattering theory in order to compute the second order thermoelectric coefficients for mesoscopic systems with electron-electron interactions. They applied their approach to an interacting QD structure finding good agreement with the full numerical calculations. They obtained high sensitivities of the nonlinear thermopower and rectification effects in the second order conductances. Similar results were provided by Meair and Jacquod [177]. Further results were discussed by López and Sánchez [168] concerning heat current and Peltier effect. Applying scattering theory they also found rectification effects in the heat flow and a highly nonlinear behavior of the Peltier coefficient. Finally, they investigated the WF law observing departures from the Lorentz number (Fig. 3.3b).

Finally, we would like to mention that broken Onsager relations were also experimentally observed by Mathews *et al.* [178]. In addition, they also analyzed the deviation from the multiterminal transport relations predicted theoretically by Butcher [179].

3.2.2 Transport asymmetries

The previously discussed Onsager reciprocity relations and WF law gives us information about the symmetries in transport. However, additional transport symmetries are also interesting to investigate. Here, we return to the two-terminal configuration of Fig. 3.1 and consider the following asymmetries that may occur in the heat transport:

$$\Delta_C = \mathcal{Q}_L(V_L, V_R) - \mathcal{Q}_R(V_L, V_R) \, , \tag{3.22a}$$

$$\Delta_E = \mathcal{Q}_L(V_L, V_R) - \mathcal{Q}_L(V_R, V_L) \, . \tag{3.22b}$$

We identify two different asymmetries: Δ_C is the contact asymmetry which describes the difference of heat flow between terminals. Δ_E is the electric asymmetry and corresponds to the heat current difference for reversed electric fields. These heat asymmetries were first measured in molecular juctions by Lee *et al.* [180]. In the linear regime, such asymmetries are related to electric and thermoelectric coefficients:

$$\Delta_C \approx 2\mathcal{G}_0\mathcal{S}_0 TV \, , \tag{3.23a}$$

$$\Delta_E \approx 2\mathcal{G}_0\mathcal{S}_0 TV \, . \tag{3.23b}$$

These relations help the experimental measurement of heat transport since $\mathcal{G}_0$ and $\mathcal{S}_0$ are accessible parameters. Following the previous experimental result, Argüello-Luengo *et al.* [181] explored theoretically the role of inelastic and dephasing processes by including a probe terminal. Deviations from Eq. (3.23) were found leading to nonlinear effects. Additionally, they observed a breaking of the particle-hole symmetry in the contact asymmetry in contrast with the electric asymmetry, which is conserved. Inelastic and dephasing effects were also studied by Sánchez and Serra [182] and Benenti *et al.* [151] in the thermoelectric transport. They discovered asymmetries in the Seebeck coefficient under the influence of a magnetic field. In addition, they found an expression for the quantum fluctuations of the thermopower.

In our thesis we investigate such relations in detail for the case of an artificial Kondo impurity in the Fermi-Liquid regime (see Sec. 7.3.2). We will also compare the results with the symmetries found in the energy current and the Joule term.

3.3 Thermoelectrics in quantum dots

As mentioned, the interest in quantum thermodynamics has rapidly grown during the last few decades and a vast number of works can be found in the literature (see representative works in Refs. [151, 152, 162]). In this section we focus on the theoretical and experimental research of thermoelectric transport in QD structures which is, by itself, a broad topic.

3.3.1 Linear response

Research on the thermoelectric properties of a QD was first considered with the linear response. Beenakker and Staring [183] proposed a theory to evaluate the thermopower. The theory, which was based on the orthodox model, predicted that the Seebeck coefficient oscillates with the Fermi energy with the same periodicity as the CB resonances, but displaying a sawtooth shape. This prediction was confirmed experimentally in the work of Staring *et al.* [184] and Molenkamp *et al.* [185] showing good agreement with the theory (Fig. 3.4a). Additional measurements were reported by Dzurak *et al.* [186] finding similar results.

Later, Blanter *et al.* [188] studied theoretically the thermopower of a QD embedded in an AB interferometer. They observed strong oscillations in the thermopower with changs of sign when tuning the AB flux. Godjin *et al.* [189] measured the thermopower of a chaotic QD and compared the results with Monte Carlo simulations. They proved that the fluctuations of the thermopower does not show a Gaussian dis-

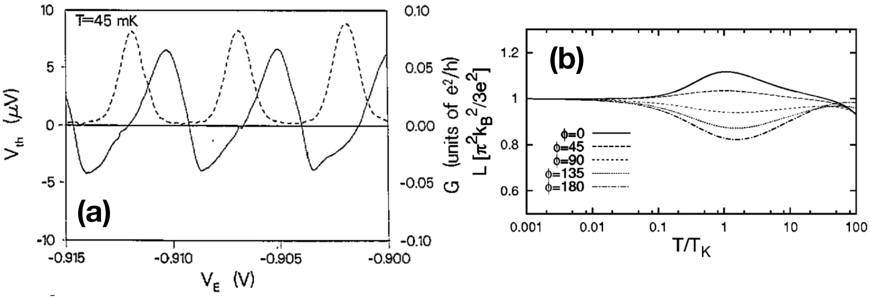

Fig. 3.4. (a) Thermovoltage (solid line) and electric conductance (dashed line) measurements of a semiconductor QD as a function of the gate voltage. The sawtooth lineshape of the thermovoltage is noticeable and the comparison with the electrical conductance shows clearly CB periodicity. Image taken from Molenkamp *et al.* [185]. (b) Lorentz function [Eq. (3.12)] showing the departures of the WF law for a Kondo-correlated QD embedded in an AB interferometer. The WF law starts to deviate for values of the temperature around T_K. Picture extracted from Kim and Hershfield [187].

tribution. The thermoelectric response of the Kondo effect was studied theoretically by Boese and Fazio [190] in the linear and nonlinear regime (for discussion on the nonlinear results, see the following section). Logarithmic dependences were found in the thermopower at the Kondo regime. The case of an AB interferometer under the presence of Kondo correlations was investigated by Kim and Hershfield [187]. Besides the crossover where the Kondo effect appears, they explained that the AB oscillation amplitudes are enhanced for temperatures near the Kondo temperature T_K. Additionally, the WF law is not satisfied around the crossover (Fig. 3.4b). Thermopower measurements in the Kondo regime were presented by Scheibner *et al.* [114]. They observed departures to the Mott formula and their results nicely agree with the previous theoretical results. Krawiec and Wysokinski [191] discussed the case when a QD is coupled to ferromagnetic leads in the Kondo regime. They found suppression of the thermopower at low temperatures and violation of the WF law. NRG calculations were performed by Costi and Zlatic [192] in order to understand the thermoelectrics of a QD. They studied departure of the linear relations, the figure of merit and efficiencies at every regime of energies concerning Kondo.

Reddy *et al.* [193] experimentally found in a molecular junction the sawtooth lineshape of the thermopower as in experiments with QDs. The figure of merit of a DQD was investigated by Liu and Yang [194] finding high values at room temperature. High ZT was also found around the Fano resonances of a DQD by Zheng *et al.* [195]. Strong thermopower was found in Kondo-correlated molecular junctions by Cornaglia *et al.* [196]. The charge and spin thermopower in addition to the figure of merit was studied theoretically in a QD acting as a Kondo impurity by Weymann and Barnas [197]. They discovered that both thermopowers are influenced by spin polarization. A similar system was also studied by Ye *et al.* [198] for both spin and orbital Kondo regimes.

Finally, we emphasize that this is only a short selection of relevant works about linear thermoelectric transport in QDs. For further information, we refer the reader to Refs. [151, 152, 162].

3.3.2 Nonlinear response

In comparison to the linear response, the literature concerning nonlinear thermoelectrics is less extensive. Nevertheless, progress has been made in the last decades, both experimentally and theoretically.

The experiment of Staring *et al.* [184] also included nonlinear transport measurements. They observed that the thermovoltage as a function of the thermal difference had a nonlinear trend with an intriguing result: There exists a specific value of thermal bias where the thermovoltage is zero. Afterwards, Boese and Fazio [190] also calculated the differential thermopower observing that for several level positions $\mathcal{S}$ is also able to change its sign as the thermal difference θ is increased. In addition, they found that the Onsager reciprocity relation of Eq. (3.11) is broken for differential Seebeck and Peltier coefficients at finite θ. Krawiec and Wysokinski [199] presented theoretical calculations showing also that the thermopower crosses the $V_{\text{th}} = 0$ line with almost unnoticeable dependence on the tunneling asymmetry between leads. Azema *et al.* [200] discussed the enhancement of the efficiency and power in the nonlinear regime of a Kondo-correlated QD predicting an experimental optimal operation point. As explained above, the second-order thermoelectric response of a QD was also analyzed by Sánchez and López in Refs. [168, 176] finding departures from the Onsager reciprocal relations and the WF law.

A very intriguing experiment was reported by Svensson *et al.* [201]. They measured the thermocurrent and thermovoltage of three different nanowire QDs (Fig 3.5a). In addition to the sawtooth behavior in the thermovoltage as function of the energy for several thermal biases, they found that both the thermovoltage and the thermocurrent are absent for an appropriate tuning of the thermal difference between reservoirs (Fig. 3.5b). They fitted the experimental results with a simple model which exhibits these nontrivial zeros. However, a complete understanding of the behavior was still missing. Later, a CB model was employed to explain this fascinating phenomenon [202]. As expected, we obtained theoretically nontrivial zeros in I_{th} and V_{th} and we attributed them to a compensation between electron and hole flows. For the sake of com-

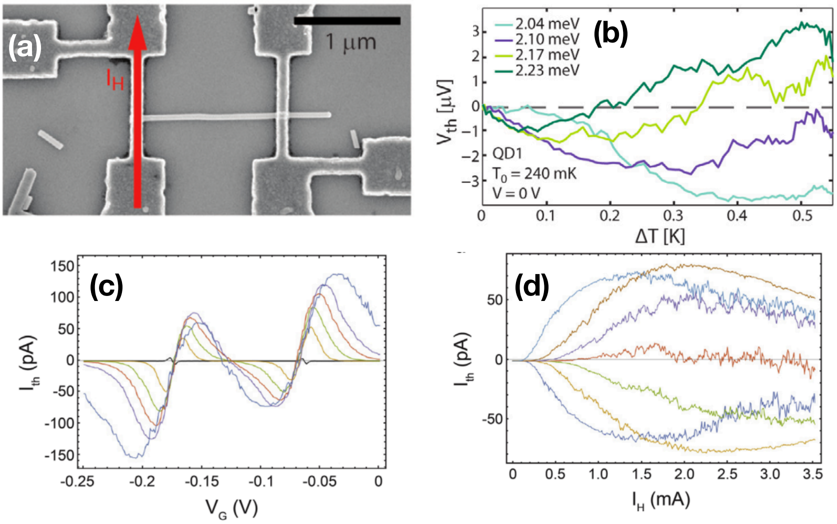

Fig. 3.5. (a) STM image of a QD embedded in a nanowire. The red arrow represents an electric current used with the goal of heating the left reservoir. (b) Thermovoltage of the QD showed in (a) as a function of the thermal bias. We may identify nontrivial zeros in the thermovoltage for some values of the gate voltage. (c) Experimental values of the thermocurrent of a QD as a function of the gate voltage at a finite thermal bias. We observe that a plateau is formed at increasing thermal difference. (d) Thermocurrent as a function of the temperature difference for the same system as (c). We remark that nontrivial behaviour is visible at large biases. (a) and (b) are taken from Svensson *et al.* [201] while (c) and (d) are taken from Svilans *et al.* [205].

pleteness, we discuss in detail such results in Sec. 7.1 although this work is not included in this thesis. At the same time, Zimbovskaya [203] reported similar theoretical results and she extended the work by applying crossed gradients (both V and θ) [204] using scattering theory. Furthermore, we highlight the experimental work of Svilans *et al.* [205]. They also measured the thermocurrent as a function of an applied thermal bias of a QD obtaining similar results. The agreement of the experiment with our theoretical results was surprisingly accurate showing that our model is able to explain the thermoelectric properties of a QD. Very recently, Svilans *et al.* [111] also reported thermoelectric experiments of a Kondo-correlated QD. They found that a sawtooth shape can be induced in the Kondo region at low background temperatures.

Additionally, different aspects and configurations of the thermoelectric transport through a QD was also investigated. Koch *et al.* [206] studied the thermoelectric properties of a molecular QD attached to two leads and coupled to an optical phonon mode. At low thermal bias, the Pauli blockade makes the phonon contribution negligible in the thermovoltage. Hwang *et al.* [207] studied the spin-polarized thermoelectric transport of an antidot coupled to normal and ferromagnetic leads. They found a change of sign in the charge and spin currents with finite thermal biases. A subsequent work proposed that such system may work as a spin thermoelectric diode [208]. The nonlinear efficiency and electric power was also studied by Wang *et al.* [209] stating that a Zeeman splitting is able to improve the performance of a QD engine. Such engine properties were also studied by Gomez-Silva *et al.* [210] in a QD with a T-shaped configuration predicting that their system can be an efficient thermolectric device.

To conclude, we want to emphasize that one of the aims of this thesis is indeed to investigate the nonlinear thermoelectric features of QD structures. First, the heat current and Peltier effect of an interacting QD is studied in Sec. 7.1. Later, we calculate the thermal effects of a molecular junction under the influence of electron-electron interactions and fit the results with previous measurements in Sec. 7.2. Such work will be compared with a noninteracting model which also exhibits good agreement with experiments. The thermal and thermoelectric responses of a Kondo impurity at all regimes is discussed with detail in Sec. 7.3. The role of interactions and its thermoelectric effects of DQDs are the main topics of Sec. 8.1. Finally, the thermal and thermoelectric transport of an artificial Kondo impurity is analyzed in Sec. 8.3.

II

Theory

4. Green's Functions Formalism

We recall that nanoscience usually faces complex many-body problems in which interactions between electrons may play an important role and the tools coming from the usual statistical physics are not enough to describe the fascinating effects that nanodevices hide. In previous chapters we have already mentioned several of the most used theoretical techniques in quantum transport physics, i. e., scattering theory which describes the transport with wave fluxes [211] or the NRG calculations introduced by Wilson [93] among others. In this thesis, our main technique is the NEGFs formalism, which is based on the computation of Green's function related to the Hamiltonian $\mathcal{H}$ which models the system.

In mathematics, Green's functions $G(t,t')$ are solutions of inhomogeneous differential equations of the form $\hat{L}(t)G(t,t') = \delta(t-t')$ where $\hat{L}(t)$ is a linear operator and $\delta(t-t')$ is the Dirac delta. In quantum mechanics, they have a more particular definition but still obeying a similar type of differential equation. In fact, Green's functions have complicated expressions depending on the Hamiltonian.

Since most of the calculations of this thesis employ NEGFs, a proper description of the formalism is needed in order to fully understand the mathematical steps behind the physical models. For this reason, this chapter is still an introduction of the current theory which summarizes the most important concepts within the NEGFs formalism. Particularly, in Sec. 4.1 we briefly explain the dynamical pictures of quantum mechanics giving an especial emphasis to the interaction picture. The equilibrium Green's functions are defined in Sec. 4.2 and the theory will be extended to the nonequilibrium case in Sec. 4.3, which includes a discussion of the Dyson's equation (Sec. 4.3.1) and the Langreth rules definition required (Sec. 4.3.2) for the calculation of NEGFs integrals and products.

4.1 Quantum mechanics pictures

In quantum mechanics, the dynamics of a physical system is described with a Hamiltonian $\mathcal{H}$. In the models of this thesis, we consider closed systems described by $\mathcal{H}_0$ while interactions between the different parts of the isolated systems like the Coulomb interactions or the tunneling transitions are represented by a perturbation $\mathcal{W}$.

$$\mathcal{H} = \mathcal{H}_0 + \mathcal{W}(t) \ . \tag{4.1}$$

Fundamentally, the parameters of interest are the expected values of observables $\hat{\mathcal{O}}$. Those expected values portray the physics of real systems even when they evolve in time. Mathematically, we are free to include the time evolution in the observables or in the quantum states. For this reason, we are allowed to apply different representations (or pictures) when we solve quantum mechanical problems.

The most basic concepts of quantum mechanics are normally expressed in the *Schrödinger picture*. In this case, wavefunctions, or quantum states, represented by $|\phi(t)\rangle$ evolve in time obeying the Schrödinger equation.

$$i\hbar\partial_t|\phi(t)\rangle = \mathcal{H}|\phi(t)\rangle \ . \tag{4.2}$$

Eq. (4.2) is valid when the Hamiltonian is independent of time, that means $\partial_t\mathcal{H} = 0$. At this moment, we define the evolution operator $\hat{U}(t)$ in order to include the time dependencies of the system. This operator is an unitary transformation which turns the initial state $|\phi_0\rangle$ into the resulting state at time t following

$$|\phi(t)\rangle = \hat{U}(t)|\phi_0\rangle \ . \tag{4.3}$$

Taking into account Eq. (4.2), we remark that $\hat{U}(t)$ depends on the total Hamiltonian of the system. Therefore, in this picture quantum states evolve with time with $\hat{U}(t)$ whereas the operators are independent of time.

Another possible representation is the *Heisenberg picture*. In this case, $\hat{U}(t)$ is applied to the operators, which now evolve in time following $\hat{\mathcal{O}}(t) = U^{\dagger}(t)\hat{\mathcal{O}}(0)U(t)$. Accordingly, operators in this picture obey

$$i\hbar\frac{d\hat{\mathcal{O}}}{dt} = \left[\hat{\mathcal{O}}, \mathcal{H}\right] \ , \tag{4.4}$$

which is the Heisenberg equation of motion. In contrast to the Schrödinger picture, operators now contain all the evolution of the system whereas the states $|\phi_0\rangle$ are time independent.

Although the Heisenberg and Schrödinger representations are broadly used to solve quantum physics problems, for Hamiltonians like Eq. (4.1) it may be more convenient to use a mixture of both interpretations: the *interaction picture*. Now, both states and operators will evolve in time following different unitary transformations.

First, we assume that the Hamiltonian $\mathcal{H}_0$ of Eq. (4.1) is well-known and is perturbed by $\mathcal{W}$ in such a way that the complete diagonalization of $\mathcal{H}$ can not be found straightforwardly. Hence, we split the time operator $\hat{U}(t)$ properly following the terms of Eq. (4.1). Consequently, in this representation, operators evolve with $\mathcal{H}_0$

$$\hat{O}(t) = e^{i\mathcal{H}_0 t/\hbar}\hat{O}e^{-i\mathcal{H}_0 t/\hbar} , \tag{4.5}$$

On the other hand, states depend on time as follows

$$|\Psi(t)\rangle = e^{i\mathcal{H}_0 t/\hbar}e^{-i\mathcal{H}t/\hbar}|\Psi(0)\rangle . \tag{4.6}$$

Therefore, Eq. (4.6) allows us to define a new operator $\bar{U}(t)$ characteristic from interaction picture. Its equation of motion reads

$$i\hbar\frac{d\bar{U}}{dt} = \mathcal{W}(t)\bar{U}(t) , \tag{4.7}$$

whose solution depends explicitly on the perturbation Hamiltonian.

$$\bar{U}(t) = \hat{T}e^{-\frac{i}{\hbar}\int_0^t dt_1 \mathcal{W}(t_1)} , \tag{4.8}$$

where $\hat{T}$ is a time-ordering operator which redistributes the product of operators in increasing time:

$$\hat{T}\hat{\mathcal{O}}_1(t_1)\hat{\mathcal{O}}_2(t_2) = \theta(t_1 - t_2)\hat{\mathcal{O}}_1(t_1)\hat{\mathcal{O}}_2(t_2) + \theta(t_2 - t_1)\hat{\mathcal{O}}_2(t_2)\hat{\mathcal{O}}_1(t_1) . \tag{4.9}$$

Using the evolution operator $\bar{U}(t)$, the change of a quantum state from the time t' to t is given by the S-matrix $S(t,t') = \bar{U}(t)\bar{U}^\dagger(t')$. Applying Eq. (4.8), the S-matrix also takes an exponential form in terms of the perturbation.

$$S(t,t') = \hat{T}e^{-\frac{i}{\hbar}\int_{t'}^t dt_1 \mathcal{W}(t_1)} . \tag{4.10}$$

Eq. (4.10) yields the property $S(t,t'')S(t'',t') = S(t,t')$ which will be used in the following section. We remark that $S(t,t')$ is a key element for the NEGF formalism and the time-dependent perturbation methods.

4.2 Equilibrium Green's functions

Green's functions are very powerful when many-particle systems are considered for both thermal and nonthermal equilibrium. For the moment, we restrict ourselves to the $T = 0$ equilibrium case, which will be extended in Sec. 4.3 to the nonequilibrium case. The single-particle Green's function is defined as

$$G(x,t;x't') = -\frac{i}{\hbar}\frac{\langle\Psi_0|\hat{T}\psi(t)\psi^\dagger(t')|\Psi_0\rangle}{\langle\Psi_0|\Psi_0\rangle} , \tag{4.11}$$

where $|\Psi_0\rangle$ is the ground state of the total Hamiltonian [Eq. (4.1)] and ψ and $\psi^\dagger$ are operators in the Heisenberg picture. Eq. (4.11) obeys an equation of motion which takes the form of an inhomogeneous Schrödinger equation [212, 213].

We consider that at $t \to -\infty$ the system is in a nonperturbed state $|\phi_0\rangle$ of $\mathcal{H}_0$. Afterwards, the system evolves to the ground state $|\Psi_0\rangle$ of the total Hamiltonian at $t = 0$. Therefore, following the Gell-Mann and Low theorem, the ground state obeys $|\Psi_0(-\infty)\rangle = S(0, -\infty)|\phi_0\rangle$ [213]. Similarly, the final state (at $t \to \infty$) is assumed to return to the unperturbed state $\langle\Psi_0| = \langle\phi_0|S(\infty, t)$. Then, we apply the properties of the S-matrix to express Eq. (4.11) in the following way

$$G(x,t;x,t') = -\frac{i}{\hbar}\frac{\langle\phi_0|\hat{T}\psi(x,t)\psi^\dagger(x',t')S(\infty,-\infty)|\phi_0\rangle}{\langle\phi_0|S(\infty,-\infty)|\phi_0\rangle} \,. \qquad (4.12)$$

Interestingly, a series expansion of Eq. (4.10) gives us the possibility of studying the perturbation expansion for the Green's function and, consequently, any operator in orders of $\mathcal{W}$. The terms of the expansion encompass expected values of more than three or four field operators $\psi(t_i)$ which may be split in pairs by using the Wick's theorem [214]. Additionally, each term of this separation can be intuitively understood with Feynman diagrams [213, 215]. Actually, only the fully-connected diagrams play a role in the perturbation expansion because the disconnected diagrams cancels the normalization condition.

$$\begin{aligned} G(x,t;x't') &= -\frac{i}{\hbar}\sum_{j=0}^{\infty}\left(-\frac{i}{\hbar}\right)^n \int_{-\infty}^{\infty} dt_1 \ldots dt_n \times \qquad (4.13) \\ &\quad \langle\phi_0|\hat{T}\psi(t)\psi^\dagger(t')\mathcal{W}(t_1)\ldots\mathcal{W}(t_n)|\phi_0\rangle_{\text{con}} \,. \end{aligned}$$

This relation will be used in the evaluation of the current by using a perturbative expansion up to third order in Sec. 6.2 .

Another important issue is the consideration of finite temperatures in the system. A typical method for including temperatures is the use of Matsubara Green's functions [216]. Instead, we will employ Keldysh Green's functions (Sec. 4.3) because they take into account simultaneously thermal and nonequilibrium effects. Regarding temperature, the Green's function is redefined [213, 216]

$$G(x,t;x',t') = -\frac{i}{\hbar}\mathrm{Tr}\left[\varrho\hat{T}\psi(x,t)\psi^\dagger(x',t')\right] \,, \qquad (4.14)$$

where ϱ is the equilibrium density matrix coming from statistical physics. From now on, the expected values of any operator $\mathcal{O}(t)$ will be computed in the following form

$$\langle\mathcal{O}(t)\rangle = \mathrm{Tr}\left[\varrho\hat{T}\mathcal{O}_H(t)\right] \qquad (4.15)$$

where $\mathcal{O}_H$ is the operator in the Heisenberg picture.

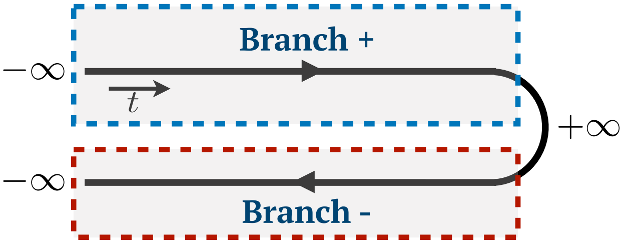

Fig. 4.1. Sketch of the Keldysh contour. The time path starts at the + branch from $t \to -\infty$ to $t \to \infty$. At that point, the contour now returns along the − branch going back in time until $t \to -\infty$.

4.3 Non-equilibrium Green's functions

When we deal with non-equilibrium processes, we face with the problem that the final state of the perturbed system at $t \to \infty$ may not be the same as the initial one and the formalism of Sec. 4.2 is not valid. Consequently, we need a more complete method to calculate the Green's functions of the system. Fortunately, the resulting theory is almost equivalent to the equilibrium Green's function formalism. In this case, we need to extend the Hamiltonian of Eq. (4.1) with an additional transient term $\mathcal{H}'(t)$ dependent on time which takes place at t_0. Nevertheless, we neglect the transient dynamics, which are beyond the scope of the topic of this thesis, taking the perturbation time at $t_0 \to -\infty$. In such case, the Green's function of Eq. (4.11) is transformed into

$$G(1,1') = -\frac{i}{\hbar}\left\langle \hat{T}_C \psi(1)\psi^\dagger(1')\right\rangle \,, \tag{4.16}$$

where (1) denotes (x,t) for simplicity. We stress that now the time-ordering operator $\hat{T}$ is transformed into contour-ordered operator $\hat{T}_C$ which may take a more general path. Particularly, we choose the Keldysh contour sketched in Fig. 4.1.

The Keldysh path starts at $t_0 \to -\infty$ and continues with increasing times along the + branch. When the time $t \to \infty$ is reached, the path returns to lower times along the − branch until it ends in $t \to -\infty$ again. In such case, the S-matrix corresponding to this contour becomes

$$S_c(-\infty,-\infty) = S_-(-\infty,\infty)S_+(\infty,-\infty)\,. \tag{4.17}$$

Notice that now the final state is again the initial unperturbed state of the system allowing us to properly calculate the expected value of the nonequilibrium process. Importantly, one shall take care of the branches when applying the perturbation expansion of the S-matrix. Actually, we deal with different types of Green's function since t and t' may be located in different branches. For this reason, we are now going to define each of them: When both operators are at the + branch, the contour-ordering operator becomes a time-ordering operator $\hat{T}_C \to \hat{T}$ and we obtain a Green's function similar to Eq. (4.11)

$$G^t(1,1') \equiv G^{++}(1,1') = -\frac{i}{\hbar}\left\langle \hat{T}\psi(1)\psi^\dagger(1')\right\rangle \ , \tag{4.18}$$

which is referred as the *time-ordered* (or *casual*) *Green's function*. If the operators act in the negative branch instead, Eq. (4.16) results in the *antitime-ordered Green's function*

$$G^{\bar{t}}(1,1') \equiv G^{--}(1,1') = -\frac{i}{\hbar}\left\langle \hat{\bar{T}}\psi(1)\psi^\dagger(1')\right\rangle \ , \tag{4.19}$$

where $\hat{\bar{T}}$ is the antitime-ordering operator. We also can obtain Green's function whose operators are in different branches. For t located at the + branch and t' at the − branch, we define the *lesser Green's function*

$$G^<(1,1') \equiv G^{+-}(1,1') = +\frac{i}{\hbar}\left\langle \psi^\dagger(1')\psi(1)\right\rangle \ , \tag{4.20}$$

and in the opposite case, we encounter the *greater Green's function*

$$G^>(1,1') \equiv G^{-+}(1,1') = -\frac{i}{\hbar}\left\langle \psi(1)\psi^\dagger(1')\right\rangle \ . \tag{4.21}$$

Following Eq. (4.9), a relation between the Green's function is satisfied,

$$G^t + G^{\bar{t}} = G^< + G^> \ , \tag{4.22}$$

meaning that the four Green's function are not totally independent. For the aim of this thesis, it is convenient to define two additional Green's function which are essential for the description of transport processes. These are the *retarded Green's function*

$$\begin{aligned} G^r(1,1') &= -\frac{i}{\hbar}\theta(t-t')\left\langle\left[\psi(1),\psi^\dagger(1')\right]_+\right\rangle \\ &= \theta(t-t')\left[G^>(1,1') - G^<(1,1')\right] \ , \end{aligned} \tag{4.23}$$

where $[\ldots]_+$ denotes the anticommutator; and the *advanced Green's function*

$$\begin{aligned} G^a(1,1') &= \frac{i}{\hbar}\theta(t'-t)\left\langle\left[\psi(1),\psi^\dagger(1')\right]_+\right\rangle \\ &= \theta(t'-t)\left[G^<(1,1') - G^>(1,1')\right] \ . \end{aligned} \tag{4.24}$$

Notice that now these Green's functions obey

$$G^r - G^a = G^> - G^< \ . \tag{4.25}$$

Depending on the physics we want to investigate, some Green's functions are more appropriate than others. First, G^t and $G^{\bar{t}}$ are useful for computing a perturbative expansion. In fact, such expansion may be performed using diagrammatics, which is a powerful tool. On the other hand, $G^<$ and $G^>$ describe correlations and other physical properties in the system. For instance, the lesser Green's function is related with the occupation density of a system in which the operators ψ and $\psi^\dagger$ represent annihilation or creation of particles following $\langle n \rangle = -i\hbar G^<(1,1)$. In the Fourier space, it obeys

$$\langle n \rangle = \frac{1}{2\pi i} \int d\omega G^<(\omega) \ . \tag{4.26}$$

Integrals like Eq. (4.26) will be solved in this thesis. The last pair of Green's functions, G^r and G^a, have the advantage of describing internal properties of the system such as its local DOS defined as

$$\rho(\omega) = -\frac{1}{\pi} \mathrm{Im}[G^r(\omega)] \ , \tag{4.27}$$

where $G^r(\omega)$ is just the Fourier transform of the retarded Green's function. We highlight that ρ acts as a probability density and, consequently, obeys the sum rule

$$\int_{-\infty}^{\infty} d\omega \rho(\omega) = 1 \ . \tag{4.28}$$

Using the fluctuation-dissipation relation and Eq. (4.26), we can prove that Eq. (4.28) corresponds to the Friedel sum rule of Eq. (2.4). Furthermore, the retarded and advanced Green's functions are the essential ingredient to theoretically investigate the transport properties and other physical magnitudes of mesoscopic conductors. For this reason, the retarded Green's function will be evaluated for the Anderson model in Sec. 5.2 using the equation-of-motion technique and later their relation with the currents will be discussed in Sec. 6.1.

4.3.1 Dyson's Equation

The goal of this section is to derive the Dyson's equation and explain its applications. First, we separate the Hamiltonian $\mathcal{W} = \mathcal{W}^{(1)} + \mathcal{W}^{(2)}$ where $\mathcal{W}^{(1)}$ describes an external potential and $\mathcal{W}^{(2)}$ accounts for interaction between particles in the system. Then, the Hamiltonian can be expressed in the following way [212]

$$
\begin{aligned}
\mathcal{H} &= \int d1 \psi^{\dagger}(1)\mathcal{H}_0(1)\psi(1) + \int d1 \psi^{\dagger}(1)\mathcal{W}^{(1)}(1)\psi(1) \\
&\quad + \int d1d2 \psi^{\dagger}(1)\psi^{\dagger}(2)\mathcal{W}^{(2)}(2,1)\psi(2)\psi(1) \,. \qquad (4.29)
\end{aligned}
$$

When pair interactions $\mathcal{W}^{(2)}$ are absent in the system, we may identify the equation of motion of the Green's functions as

$$
\begin{aligned}
[i\hbar\partial_t - \mathcal{H}_0(1)]g(1,1') &= \delta(1'-1) \,, \qquad (4.30) \\
[i\hbar\partial_t - \mathcal{H}_0(1) - \mathcal{W}^{(1)}(1)]G(1,1') &= \delta(1'-1) \,, \qquad (4.31)
\end{aligned}
$$

where $g(1,1')$ is the unperturbed Green's functions fully governed by $\mathcal{H}_0$. Combining Eqs. (4.30) and (4.31) with a little bit of algebra one obtains

$$
G(1,1') = g(1,1') + \int d2 g(1,2)\mathcal{W}^{(1)}(2)G(2,1') \,, \qquad (4.32)
$$

which is regarded as the *Dyson's equation*. Actually, Eq. (4.32) may be generalized adding two-body interactions $\mathcal{W}^{(2)}$ with the Feynmann diagramatic technique to Eq. (4.16) yielding

$$
\begin{aligned}
G(1,1') &= g(1,1') + \int d2 g(1,2)\mathcal{W}^{(1)}(2)G(2,1') \\
&\quad + \int d2d3 g(1,2)\Sigma(2,3)G(3,1') \,, \qquad (4.33)
\end{aligned}
$$

where $\Sigma(2,3)$ is the so-called *self-energy* and includes all possible combination of virtual interactions. Mathematically, such virtual interactions can be understood as irreducible Feynman diagrams coming from $\mathcal{W}^{(2)}$. Along this thesis we will encounter equations similar to Eq. (4.33) and different expressions for the self-energy Σ depending on dot-lead tunnel couplings or electron-electron interactions.

4.3.2 Langreth Rules

Dyson's equation [Eq. (4.33)] is composed of convolutions of several Green's functions or self-energies following in time

$$
C(t,t') = \int_{C_0} d\tau A(t,\tau)B(\tau,t') \,, \qquad (4.34)
$$

where C_0 represents the time contour we consider. Eq. (4.34) is valid when each term is a casual Green's functions. We ensure that the Dyson's equation [Eq. (4.33)] is indeed expressed with casual Green's function. The problem arises when it is necessary to find a different type of Green's

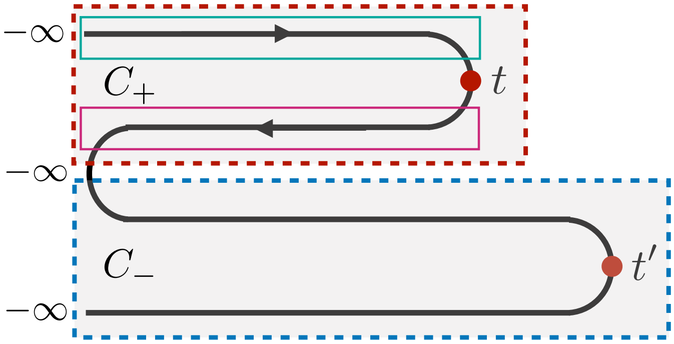

Fig. 4.2. Deformation of the Keldysh contour of Fig. 4.1. Each rectangle corresponds to a time segment of the path integral. The path C_+ is defined from the first $\tau \to -\infty$ to the second one (red dashed rectangle) while the remaining path corresponds to C_- (blue dashed rectangle). The solid green rectangle represents the path from $\tau \to -\infty$ to $\tau = t$ and the solid pink rectangle indicates the contour which goes from $\tau = t$ to $\tau \to -\infty$.

function. Evidently, one may compute a similar equation following the procedure of Sec. 4.3.1. Nevertheless, the Langreth rules [217] offer us a straightforward method to find an equivalent equation for noncasual Green's functions.

The Langreth rules are derived by deforming the Keldysh contour (Fig. 4.1). This deformation is feasible because the initial and final states are not modified and, for this reason, the expected values are strictly the same. We proceed with the calculation of the Langreth rule for a lesser Green's function $C^<$. The path becomes the one shown in Fig. 4.2. In this case, the path starts at $\tau = -\infty$ and increases until it reaches $\tau = t$. Afterwards, the time decreases to $\tau \to -\infty$ and increases again. At $\tau = t'$, the path follows decreasing times until it ends at $\tau = -\infty$. For a better comprehension, we define two different contours: C_+ goes from the first $\tau \to -\infty$ to the second one. Right after, C_- starts and follows the path until the end. Therefore, Eq. (4.34) is split into two terms taking into account the different contours

$$C^<(t,t') = \int_{C_+} d\tau A(t,\tau)B^<(\tau,t') + \int_{C_-} d\tau A^<(t,\tau)B(\tau,t') \,. \qquad (4.35)$$

We observe that in the first integral $B^<$ is a lesser function because τ travels along C_+ and t' is contained in C_-. Similar arguments are applied for $A^<$ in the C_- integral. Now, we split both paths again.C_+ is separated in the path between $\tau \to -\infty$ and $\tau = t$ (green solid rectangle in Fig. 4.2) and the contour which goes from $\tau = t$ to $\tau \to -\infty$ (pink solid rectangle in Fig. 4.2). Thus, the first integral of Eq. (4.35) reads

$$\begin{aligned}\int_{C_+} d\tau A(t,\tau)B^<(\tau,t') &= \int_{-\infty}^{t} d\tau A^>(t,\tau)B^<(\tau,t') \\ &\quad + \int_{t}^{-\infty} d\tau A^<(t,\tau)B^<(\tau,t') \\ &= \int_{-\infty}^{\infty} d\tau A^r(t,\tau)B^<(\tau,t')\;, \qquad (4.36)\end{aligned}$$

where A^r is obtained applying Eq. (4.23). A similar procedure is done in order to derive the solution of the C_- integral. Finally, the Langreth rule for $C^<$ is

$$C^<(t,t') = \int_{-\infty}^{\infty} d\tau[A^r(t,\tau)B^<(\tau,t') + A^<(t,\tau)B^a(\tau,t')]\;. \qquad (4.37)$$

The greater function $C^>$ takes a similar form to Eq. (4.37) with the replacement of $<$ by $>$. By replacing Eq. (4.37) into Eqs. (4.23) and (4.24), we are able to get the retarded and advanced functions of C.

$$C^{r,a}(t,t') = \int_{-\infty}^{\infty} d\tau A^{r,a}(t,\tau)B^{r,a}(\tau,t')\;. \qquad (4.38)$$

We remark that the pair-interaction term of the Dyson's equation is a convolution of three functions. Therefore, we shall also define the Langreth rules for $D = ABC$. Using repeatedly Eq. (4.37) and (4.38), the Green's functions of D read

$$\begin{aligned} D^< &= A^rB^rC^< + A^rB^<C^a + A^<B^aC^a \qquad (4.39)\\ D^r &= A^rB^rC^r\;. \qquad (4.40)\end{aligned}$$

Importantly, we have not written the integrals in time for simplicity but one should be aware that they should be taken into account. In addition to the convolution, we will also face in this thesis with products of Green's functions evaluated at opposite times $C(t,t') = A(t,t')B(t',t)$. Therefore, we compute its Langreth rules with the same method as above:

$$\begin{aligned} C^<(t,t') &= A^<(t,t')B^>(t',t)\;, \qquad (4.41)\\ C^r(t,t') &= A^r(t,t')B^<(t',t) + A^<(t,t')B^a(t',t)\;. \qquad (4.42)\end{aligned}$$

As an illustrative example, we now evaluate the Dyson's equation for the lesser Green's function when the perturbation is only due to pair interactions. We substitute Eq. (4.39) into Eq. (4.33) and, ignoring the integrals, we obtain the following Dyson's equation:

$$G^< = g^< + g^r\Sigma^rG^< + g^r\Sigma^<G^a + g^<\Sigma^aG^a\;. \qquad (4.43)$$

An iterative replacement of $G^<$ provides us an useful relation which will be used in following chapters of this thesis:

$$G^< = (1 + G^r \Sigma^r) g^< (1 + G^a \Sigma^a) + G^r \Sigma^< G^a \ . \tag{4.44}$$

We identify the first term as a transient component which will be generally neglected [213]. The lesser Green's function is thus written as $G^< = G^r \Sigma^< G^a$.

Finally, we want to emphasize that the NEGFs formalism is very broad and we have only focused on the properties and methods of relevance for this thesis. For instance, this formalism may be extended by considering Green's functions for bosonic particles as phonons or photons. For a more complete explanation, we refer the reader to Refs. [212, 213, 214].

5. Anderson Model

One of the most relevant theories describing QD systems is the *Anderson model*. It was introduced by P. W. Anderson with the aim of defining localized magnetic states in metals [98]. He proposed a Hamiltonian whose terms represent different parts of the setup such as the leads and the dots as well as the tunnel hoppings or the interaction between electrons. Anderson's theory was extended by the work of Alexander and Anderson [218] in which they added two neighboring localized states which interact with each other. They found that the exchange processes leading to ferromagnetic and antiferromagnetic interactions are relevant in the system. Recalling that QDs may act as artificial localized magnetic states, the Anderson Hamiltonian is thus an important model to discuss the physics in these nanoscaled systems.

We emphasize that the Anderson Hamiltonian is not the only model which can address QD physics. As explained in Sec. 2.1.3, many models exist in the literature able to describe the electronic properties of quantum impurities. For instance, the s-d Hamiltonian proposed by Zener [97] characterizes the spin-spin interactions between particles in the localized state with free carriers in the metal. In fact, we recall that this last model was used by Kondo [86] to obtain theoretically the logarithmic trend of the resistance with temperature. Nevertheless, it can be demonstrated that any of these alternative models can be derived from the Anderson Hamiltonian with an appropriate manipulation in the right parameter regime, as is carried out with the Schrieffer-Wolff transformation [100].

The solution of the Anderson model can be explored with the aid of the NEGF formalism explained in Ch. 4. Actually, Anderson's papers [98, 218] used this tool to find relevant physical magnitudes, i. e., the occupation or the DOS. Importantly, the application of the equation of motion (EOM) technique to the NEGF is widely used in order to find the analytical expression of the Green's function in different regimes. In addition, the series expansion of the S-matrix may be also performed although its validity reduces to small perturbations. Moreover, different techniques can be found in the literature such as the NRG which is able to correctly derive the DOS in the Kondo limit showing the Abrikosov-Suhl resonance [219].

The properties of the systems considered in this thesis are studied with the Green's functions computed from Anderson Hamiltonian via either the EOM technique or a perturbation expansion. In Sec. 5.1 we present the general Hamiltonian and transform it into different types of Hamiltonian for more concrete cases and regimes. Later, we introduce the EOM technique in Sec. 5.2 to obtain the expression of the retarded Green's functions using several approximations. Finally, we explain the slave-boson mean-field theory (SBMFT) in Sec. 5.3 and compute the mean-field equations for single and double QDs in the Fermi liquid regime. This chapter introduces the models and techniques employed for the results of this thesis and develops the theoretical calculations needed for evaluating the Green's functions, leading to the local DOS, transmission functions and other interesting physical properties. Therefore, it contains both well known results (Secs. 5.1, 5.2.1, 5.2.2 and introductory parts of Secs. 5.2 and 5.3) and original calculations (Secs. 5.2.3, 5.2.4, 5.3.1 and 5.3.2).

5.1 The general Hamiltonian

Since this thesis encompasses a large variety of QD setups, we first consider the most general scenario to write its corresponding Anderson Hamiltonian. Therefore, we revisit the structure sketched in Fig. 3.2. The QD system is formed by N_d QDs which may be attached to N fermionic reservoirs characterized with a given electrochemical potential μ_α and a temperature T_α. Conduction electrons of the reservoirs thus follow the Fermi distribution function of energies

$$f_\alpha(\omega) = \frac{1}{1 + \exp\left(\frac{\omega - \mu_\alpha}{k_B T_\alpha}\right)} \,. \tag{5.1}$$

Now, we proceed with the definition of the model Hamiltonian. We identify three different terms in the general Anderson model

$$\mathcal{H} = \mathcal{H}_{\text{leads}} + \mathcal{H}_{\text{QDs}} + \mathcal{H}_{\text{tun}} \,. \tag{5.2}$$

The first term is the Hamiltonian of the leads

$$\mathcal{H}_{\text{leads}} = \sum_{\alpha k \sigma} \varepsilon_{\alpha k \sigma} C^\dagger_{\alpha k \sigma} C_{\alpha k \sigma} \,, \tag{5.3}$$

where $C^\dagger_{\alpha k \sigma}$ ($C_{\alpha k \sigma}$) is the creation (annihilation) operator of electrons located at the lead α with energy $\varepsilon_{\alpha k \sigma}$ with k being the wavenumber and σ the spin of such electrons. Notice that Coulomb interactions between electrons inside the reservoirs are considered negligible, implying that electrons will behave as free particles. This approximation is valid when the reservoirs are metals with good screening properties, which is the experimentally relevant situation in most of the cases.

The second part corresponds to the Hamiltonian of the QDs which may be split in three additional terms

$$\begin{aligned}\mathcal{H}_{\text{QDs}} &= \mathcal{H}_{\text{nint}} + \mathcal{H}_{\text{intra}} + \mathcal{H}_{\text{inter}} \\ &= \sum_{\mu\nu\sigma} H_{\mu\sigma,\nu\sigma} d^{\dagger}_{\mu\sigma} d_{\nu\sigma} + \sum_{\mu} U_{\mu} n_{\mu\uparrow} n_{\mu\downarrow} \\ &\quad + \frac{1}{2} \sum_{\mu\neq\nu,\sigma_\mu\sigma_\nu} \tilde{U}_{\mu,\nu} n_{\mu\sigma_\mu} n_{\nu\sigma_\nu} \ . \end{aligned} \tag{5.4}$$

$\mathcal{H}_{\text{nint}}$ is the Hamiltonian of the QD array in the absence of electron-electron interactions. We identify $d^{\dagger}_{\mu\sigma}$ ($d_{\mu\sigma}$) as the operator which creates (annihilates) electrons with spin σ at the dot μ. $H_{\mu\sigma,\nu\sigma}$ are the energy matrix elements of the noninteracting Hamiltonian whose diagonal terms represent the energy levels of the dots defined as $H_{\mu\sigma,\mu\sigma} = \varepsilon_{\mu\sigma}$. The nondiagonal terms correspond to tunneling transitions between levels (e. g., for a DQD with $\mu \neq \bar{\mu}$: $H_{\mu\sigma,\bar{\mu}\sigma} = \tau$). Furthermore, we assume spin-conserved tunneling meaning that $H_{\mu\sigma_1,\nu\sigma_2} \propto \delta_{\sigma_1\sigma_2}$.

The two additional terms of Eq. (5.4) are the intradot ($\mathcal{H}_{\text{intra}}$) and interdot ($\mathcal{H}_{\text{inter}}$) interacting Hamiltonians. The former depends on the occupation operators ($n_{\mu\sigma} = d^{\dagger}_{\mu\sigma} d_{\mu\sigma}$ for the dot μ) at different spins with amplitude U_{μ}. This is a consequence of the Pauli principle because we assume that there exists only one level in each dot in which the spin degeneracy permits double occupation allowing electron-electron interactions inside. On the other hand, the latter includes occupations of two distinct QDs with Coulomb strength $\tilde{U}_{\mu,\nu}$ (for interactions between the dots μ and ν). Note that we have inserted $1/2$ in order to avoid double counting.

So far, Eqs. (5.3) and (5.4) define two distinctive isolated subsystems, namely, the reservoirs and the dots. The connection between them is performed by including the tunneling Hamiltonian $\mathcal{H}_{\text{tun}}$

$$\mathcal{H}_{\text{tun}} = \sum_{\alpha k\sigma\mu} \left(\mathcal{V}_{\alpha k\sigma,\mu} C^{\dagger}_{\alpha k\sigma} d_{\mu\sigma} + \mathcal{V}^{*}_{\alpha k\sigma,\mu} d^{\dagger}_{\mu\sigma} C_{\alpha k\sigma} \right) \ , \tag{5.5}$$

where $\mathcal{V}_{\alpha k\sigma,\mu}$ is the tunnel hopping amplitude for an electron with spin σ between the μ QD and the α reservoir.

If we compare Eq. (5.2) with Eq. (4.1), we can identify $\mathcal{H}_{\text{leads}}$ and $\mathcal{H}_{\text{nint}}$ as the unperturbed Hamiltonians while $\mathcal{H}_{\text{tun}}$, $\mathcal{H}_{\text{intra}}$ and $\mathcal{H}_{\text{inter}}$ could be treated, in principle, as perturbations of the system. Therefore, in the NEGF formalism, from the Hamiltonians given by Eq. (5.3) and $\mathcal{H}_{\text{nonint}}$ in Eq. (5.4) we obtain the unperturbed Green's functions

(App. A) and our goal here is to find valid NEGFs which comprise such perturbations.

5.1.1 Single quantum dots and molecular junctions

In the previous section, we have defined the Hamiltonian for a QD system with any number of dots N_d. However, we now focus first on a simpler case: a single QD ($N_d = 1$). For this particular system, the most significant modification is made to the dot Hamiltonian, which reduces to

$$\mathcal{H}_{\mathrm{QD}} = \sum_{\sigma} \varepsilon_{d\sigma} d_{\sigma}^{\dagger} d_{\sigma} + U n_{\uparrow} n_{\downarrow} , \tag{5.6}$$

where $\varepsilon_{d\sigma}$ is the energy level of the QD for an electron with spin σ. The spin dependence may be originated from a Zeeman splitting due to a magnetic field $\varepsilon_{d\sigma} = \varepsilon_d + \sigma \Delta_B$, where $\Delta_B = g\mu_B B$ is the Zeeman energy coming from B. Since we deal with a single QD, the μ label is unnecessary and the interdot interactions do not exist. We may classify several energies depending on the number of electrons occupying the QD: $\omega = 0$ for an empty dot, $\omega = \varepsilon_{d\sigma}$ when the QD is occupied by an electron of spin σ and $\omega = 2\varepsilon_d + U$ when the dot is doubly occupied. This fact shows that electrons have to overcome the intradot interaction energy U in order to have two electrons inside the dot. We will observe below that the local DOS will indeed exhibit resonances located at these energies yielding the CB effect introduced in Sec. 1.1. The transport through a QD in the CB regime will be studied in the nonlinear regime in Sec. 7.1.

For a Kondo system in the absence of magnetic fields B, we should take into account several parameter regimes as explained in Sec. 2.1.3. We will explain below that high Coulomb interactions, low temperatures and strong couplings lead to Kondo correlations. Their impact on transport will be analyzed in Sec. 7.3 for a QD attached to leads out of equilibrium.

In order to compare with experiments, it is convenient to establish a relation between the gate voltage V_g and the QD energy level ε_d. For this reason, we resort to the orthodox model following Eq. (1.6):

$$\varepsilon_d = \varepsilon_N - \frac{C_L V_L + C_R V_R + C_g V_g}{C} e \, . \tag{5.7}$$

Moreover, the Coulomb interaction depends on the total capacitance of the circuit $U = e^2/C$. These relations will be used in Sec. 7.2 with the goal of fitting temperature-dependent experiments performed with molecular junctions.

5.1.2 The slave-boson Hamiltonian

The Kondo problem can be described in the Fermi liquid regime by considering low temperatures T and strong interactions U as explained in Sec. 2.1.2. Although the Anderson Hamiltonian is a useful model to illustrate the Kondo effect, some methods are not valid enough for temperatures below the Kondo temperature $T < T_K$. For instance, the perturbation expansion and the EOM technique also applied in this thesis provide Green's functions that exhibit charge fluctuations in the system. That implies that the results are restricted to $T > T_K$. For the Fermi liquid regime represented by $T < T_K$, these fluctuations should be negligible (spin fluctuations are still allowed) and a different formalism is thus needed.

With this goal in mind, we now discuss the slave-boson Hamiltonian, which can be derived from the Anderson Hamiltonian. The procedure, introduced by Coleman [220], inspired by Barnes [221, 222], begins with the transformation of Eqs. (5.4) and (5.5) into a Hamiltonian with Hubbard operators $X_{\mu\sigma,\nu\sigma} = |\mu\sigma\rangle\langle\nu\sigma|$ where $|\mu\sigma\rangle = d^\dagger_{\mu\sigma}|0\rangle$ is the quantum state of an electron with spin σ occupying the μ dot. After this transformation, we find

$$\mathcal{H}_{\text{QDs}} = \sum_{\mu\nu\sigma} H_{\mu\sigma,\nu\sigma} X_{\mu\sigma,\nu\sigma} \,, \tag{5.8}$$

$$\mathcal{H}_{\text{tun}} = \frac{1}{\sqrt{N_s}} \sum_{\alpha k\sigma\mu} \left(\mathcal{V}_{\alpha k\sigma,\mu} C^\dagger_{\alpha k\sigma} X_{0\mu,\mu\sigma} + \mathcal{V}^*_{\alpha k\sigma,\mu} X_{\mu\sigma,0\mu} C_{\alpha k\sigma} \right) \,, \tag{5.9}$$

where the subindex 0 in $X_{0\mu,\mu\sigma} = |0\rangle\langle\mu\sigma|$ and $X_{\mu\sigma,0\mu} = |\mu\sigma\rangle\langle 0|$ denotes tunneling transitions involving an empty QD. This is an N_s-fold degenerate model where N_s is the degeneracy of the angular momentum (for our setups $N_s = 2$). We remark that we have assumed large intradot interactions $U \to \infty$ and small interdot interactions $\tilde{U} \to 0$ even though this model can be extended to a more general situation.

A substantial disadvantage of the Hubbard operators is that they do not obey fermionic or bosonic commutation rules:

$$\left[X_{\mu_1\sigma_1,\nu_1\sigma_1}, X_{\mu_2\sigma_2,\nu_2\sigma_2}\right] = \delta_{\sigma_1\sigma_2} \left(\delta_{\nu_1\mu_2} X_{\mu_1\sigma_1,\nu_2\sigma_1} - \delta_{\nu_2\mu_1} X_{\mu_2\sigma_1,\nu_1\sigma_1}\right) \,. \tag{5.10}$$

Hence, its perturbation expansion has to be implemented without employing the Wick's theorem [84], a very arduous task when dealing with more than one QD in the system. For this reason, Coleman [220] proposed to transform the Hubbard operators $X_{\mu\sigma,\nu\sigma}$ into a combination of bosonic and fermionic operators

$$X_{0\mu,\mu\sigma} = b^\dagger_\mu f_{\mu\sigma} \,, \tag{5.11a}$$

$$X_{\mu\sigma,0\mu} = f^\dagger_{\mu\sigma} b_\mu \ , \tag{5.11b}$$

$$X_{\mu\sigma,\nu\sigma} = f^\dagger_{\mu\sigma} f_{\nu\sigma} \ , \tag{5.11c}$$

$$X_{0\mu,0\mu} = b^\dagger_\mu b_\mu \ , \tag{5.11d}$$

where $b^\dagger_\mu$ (b_μ) is a bosonic operator which creates (destroys) an empty state in the μ QD and $f^\dagger_{\mu\sigma}$ ($f_{\mu\sigma}$) is a pseudofermion operator which creates (annihilates) a single-electron occupied state with spin σ in the μ QD. After this transformation, Eqs. (5.8) and (5.9) become

$$\mathcal{H}_{\text{QDs}} = \sum_{\mu\nu\sigma} H_{\mu\sigma,\nu\sigma} f^\dagger_{\mu\sigma} f_{\nu\sigma} \ , \tag{5.12}$$

$$\mathcal{H}_{\text{tun}} = \frac{1}{\sqrt{N_s}} \sum_{\alpha k\sigma\mu} \left(\mathcal{V}_{\alpha k\sigma,\mu} C^\dagger_{\alpha k\sigma} b^\dagger_\mu f_{\mu\sigma} + \mathcal{V}^*_{\alpha k\sigma,\mu} f^\dagger_{\mu\sigma} b_\mu C_{\alpha k\sigma} \right) . \tag{5.13}$$

The infinite-U slave-boson forbids double-occupancy. Hence, we need to include Lagrange multipliers λ_μ which restrict the system to a subspace of singly-occupied QDs.

$$\mathcal{H}_{\text{Lag}} = \sum_\mu \lambda_\mu \left(1 - b^\dagger_\mu b_\mu - \sum_\sigma f^\dagger_{\mu\sigma} f_{\mu\sigma} \right) . \tag{5.14}$$

Later in this chapter, we will introduce the mean-field version of the slave-boson theory (SBMFT) which gives reliable results for the systems considered in this thesis. Particularly, we will employ this model in Sec. 7.3.2 with the goal of analyzing the Kondo effect and transport properties of a single artificial impurity in the Fermi liquid regime. Additionally, we will also study thermal effects in a two-impurity system in Sec. 8.3.

5.1.3 The Kondo Hamiltonian

As explained in Sec. 2.1.3, magnetic impurities can be modelled with the so-called s-d model, which treats the impurity as a spin interacting antiferromagnetically to the conduction electrons. This model was introduced by Zener [97] and its relation with the Anderson Hamiltonian was explained by Schrieffer and Wolff [100]. This section will focus on the transformation of the Anderson Model into the s-d or Kondo model.

For the sake of simplicity, we perform the calculation for the case of a single QD [Eqs. (5.3), (5.5) and (5.6)]. Firstly, we define the conditions for a valid transformation: The QD should be filled with only one electron, meaning $\varepsilon_d < 0$ and $\varepsilon_d + U > 0$. Hence, the doubly-charged state is not allowed in the QD. Additionally, we assume narrow resonances such that $\Gamma/|\varepsilon_d| \ll 1$ and $\Gamma/|\varepsilon_d + U| \ll 1$ with Γ being the hybridization constant

$$\Gamma_{\alpha\sigma} = 2\pi \sum_k \rho_\alpha(\varepsilon_{\alpha k\sigma}) \left|\mathcal{V}_{\alpha k\sigma}\right|^2 \ , \tag{5.15}$$

where ρ_α is the local DOS of the lead. The hybridization constant is also understood as the lifetime of an electron occupying the QD. Under these limits, the system is dominated by high-order tunneling transitions $\mathcal{V}$. For this reason, we apply an unitary transformation $e^{-\bar{\mathcal{S}}}$ which eliminates the first order in $\mathcal{V}$ of the Anderson model [Eq. (5.5)]. The resulting Hamiltonian $\bar{\mathcal{H}} = e^{\bar{\mathcal{S}}}\mathcal{H}e^{-\bar{\mathcal{S}}}$ approximately becomes

$$\bar{\mathcal{H}} \approx \mathcal{H}_0 + \mathcal{H}_{\text{tun}} + [\bar{\mathcal{S}}, \mathcal{H}_0] + [\bar{\mathcal{S}}, \mathcal{H}_{\text{tun}}] + \frac{1}{2}[\bar{\mathcal{S}}, [\bar{\mathcal{S}}, \mathcal{H}_0]] \,, \tag{5.16}$$

where $\mathcal{H}_0 = \mathcal{H}_{\text{leads}} + \mathcal{H}_{\text{QDs}}$. Eq. (5.16) suggests that, for removing the first order in $\mathcal{V}$, the unitary transformation has to obey

$$\mathcal{H}_{\text{tun}} = [\mathcal{H}_0, \bar{\mathcal{S}}] \,. \tag{5.17}$$

With this condition in mind, we apply a transformation of the form:

$$\bar{\mathcal{S}} = \sum_{\alpha k \sigma} \left[w^{(1)}_{\alpha k \sigma} n_{\bar{\sigma}} C^\dagger_{\alpha k \sigma} d_\sigma + w^{(2)}_{\alpha k \sigma} (1 - n_{\bar{\sigma}}) C^\dagger_{\alpha k \sigma} d_\sigma - \text{H.c.} \right] \,, \tag{5.18}$$

where $\bar{\sigma}$ denotes the opposite spin of σ. $w^{(1)}_{\alpha k \sigma}$ and $w^{(2)}_{\alpha k \sigma}$ are functions of the parameters of the Anderson model which can be found solving Eq. (5.17) (more details given in App. B) and read

$$w^{(1)}_{\alpha k \sigma} = \frac{\mathcal{V}_{\alpha k \sigma}}{\varepsilon_{\alpha k \sigma} - \varepsilon_{d \sigma} - U} \,, \tag{5.19a}$$

$$w^{(2)}_{\alpha k \sigma} = \frac{\mathcal{V}_{\alpha k \sigma}}{\varepsilon_{\alpha k \sigma} - \varepsilon_{d \sigma}} \,. \tag{5.19b}$$

Once the linear term in $\mathcal{V}$ is eliminated, Eq. (5.16) contains two terms: the Hamiltonian $\mathcal{H}_0$ and the first nonzero component of the unitary transformation $\mathcal{H}_{\text{SW}} = (1/2)[\bar{\mathcal{S}}, \mathcal{H}_{\text{tun}}]$. In App. B we carefully compute $\mathcal{H}_{\text{SW}}$ finding four parts: the s-d Hamiltonian

$$\mathcal{H}_{\text{sd}} = \sum_{\alpha k \sigma_\alpha \beta q \sigma_\beta} \mathcal{J}_{\alpha\sigma_\alpha, \beta\sigma_\beta} \hat{S}_l s^l_{\sigma_\alpha \sigma_\beta} C^\dagger_{\alpha k \sigma_\alpha} C_{\beta q \sigma_\beta} \,, \tag{5.20}$$

where $s^l_{\sigma_\alpha \sigma_\beta}$ are the matrix coefficients proportional to the Pauli matrices $2\hat{s}^l = \hat{\sigma}^l$ (with $l = \{x, y, z\}$) while $\hat{S}_l$ is the l-component of Pauli spin operator of the QD. $\mathcal{J}_{\alpha\sigma_\alpha, \beta\sigma_\beta}$ is the amplitude of the antiferromagnetic interaction between the electron occupying the QD and the conduction electrons of the reservoirs:

$$\mathcal{J}_{\alpha\sigma_\alpha, \beta\sigma_\beta} = \left(w^{(2)}_{\alpha k \sigma_\alpha} - w^{(1)}_{\alpha k \sigma_\alpha} \right) \mathcal{V}^*_{\beta q \sigma_\beta} + \left([w^{(2)}_{\beta q \sigma_\beta}]^* - [w^{(1)}_{\beta q \sigma_\beta}]^* \right) \mathcal{V}_{\alpha k \sigma_\alpha} \,. \tag{5.21}$$

The second term of the SW Hamiltonian describes simultaneous hopping of two electrons inside or outside the QD:

$$\mathcal{H}_{\text{ch}} = \frac{1}{4}\sum_{\alpha k\sigma} \tilde{\mathcal{J}}_{\alpha\sigma,\beta\bar{\sigma}} C^{\dagger}_{\beta q\bar{\sigma}} C^{\dagger}_{\alpha k\sigma} d_{\sigma} d_{\bar{\sigma}} + \text{H.c.} \,, \tag{5.22}$$

where now $\tilde{\mathcal{J}}$ is

$$\tilde{\mathcal{J}}_{\alpha\sigma_\alpha,\beta\sigma_\beta} = \left(w^{(2)}_{\alpha k\sigma_\alpha} - w^{(1)}_{\alpha k\sigma_\alpha}\right)\mathcal{V}_{\beta q\sigma_\beta} + \left(w^{(2)}_{\beta q\sigma_\beta} - w^{(1)}_{\beta q\sigma_\beta}\right)\mathcal{V}_{\alpha k\sigma_\alpha} \,. \tag{5.23}$$

The following term is a direct s-d interaction with no spin exchange

$$\mathcal{H}_{\text{dir}} = \sum_{\alpha k\sigma\beta q}\left(\bar{\mathcal{W}}_{\alpha\sigma,\beta\sigma} - \frac{1}{4}\mathcal{J}_{\alpha\sigma,\beta\sigma}\left[n_\sigma + n_{\bar{\sigma}}\right]\right) C^{\dagger}_{\alpha k\sigma} C_{\beta q\sigma} \,, \tag{5.24}$$

where

$$\bar{\mathcal{W}}_{\alpha\sigma,\beta\sigma} = \frac{1}{2}\left(w^{(2)}_{\alpha k\sigma_\alpha}\mathcal{V}^{*}_{\beta q\sigma_\beta} + [w^{(2)}_{\beta q\sigma_\beta}]^{*}\mathcal{V}_{\alpha k\sigma_\alpha}\right) \,. \tag{5.25}$$

Finally, the last term only depends on the QD operators

$$\mathcal{H}_0' = -\sum_{\alpha k\sigma}\left(\bar{\mathcal{W}}_{\alpha\sigma,\alpha\sigma} - \frac{1}{2}\mathcal{J}_{\alpha\sigma,\alpha\sigma} n_{\bar{\sigma}}\right) n_\sigma \,. \tag{5.26}$$

The next step is to reduce the Hilbert space by eliminating the subspace of the QD operators. Consequently, we transform $\mathbf{1} = n_\sigma + n_{\bar{\sigma}}$ and neglect the two-electron contribution to end up with the Kondo Hamiltonian

$$\mathcal{H}_{\text{Kon}} = \sum_{\alpha k\sigma\beta q} \bar{\mathcal{K}}_{\alpha\sigma,\beta\sigma} C^{\dagger}_{\alpha k\sigma} C_{\beta q\sigma} + \sum_{\alpha k\sigma_\alpha\beta q\sigma_\beta} \mathcal{J}_{\alpha\sigma_\alpha,\beta\sigma_\beta} \hat{S}_l s^{l}_{\sigma_\alpha\sigma_\beta} C^{\dagger}_{\alpha k\sigma_\alpha} C_{\beta q\sigma_\beta} \,, \tag{5.27}$$

where $\bar{\mathcal{K}}$ is the amplitude of the potential scattering term [84]

$$\bar{\mathcal{K}}_{\alpha\sigma,\beta\sigma} = \bar{\mathcal{W}}_{\alpha\sigma,\beta\sigma} - \frac{1}{4}\mathcal{J}_{\alpha\sigma,\beta\sigma} \,. \tag{5.28}$$

The potential scattering term is not significant around the particle-hole symmetry point $\varepsilon_d = -U/2$ but is necessary for a correct computation of the cotunneling processes taking place in the QD. Kaminski *et al.* [105] used a modified Kondo Hamiltonian where the amplitude of the potential scattering term turns into $\bar{\mathcal{K}} \to \mathcal{J}/4$ yielding

$$\mathcal{H}_{\text{Kam}} = \sum_{\alpha k\sigma_\alpha\beta q\sigma_\beta} \mathcal{J}_{\alpha\sigma_\alpha,\beta\sigma_\beta}\left(\frac{1}{4}\delta_{\sigma_\alpha\sigma_\beta} + \hat{S}_l s^{l}_{\sigma_\alpha\sigma_\beta}\right) C^{\dagger}_{\alpha k\sigma_\alpha} C_{\beta q\sigma_\beta} \,. \tag{5.29}$$

Both Eqs. (5.27) and (5.29) will be employed along this thesis. In Sec. 7.3.1 we will study how Kondo correlations vanish due to increasing thermal gradients.

5.2 Equation of motion

Once the Hamiltonian of the system is determined, a mathematical technique is needed to obtain its physical properties as the local DOS or the currents. Here, the goal is to calculate the Green's functions for the Hamiltonian given by Eq. (5.2) in the Keldysh NEGFs formalism. To achieve that, we employ the EOM technique, which consists of calculating the dynamics of the Green's functions via a system of differential equations. Generally, it is necessary to truncate such equations in order to obtain a closed set. Such truncation needs to be valid in some parameter regime because the solution has to properly model the physical phenomenon we want to study.

Basically, the technique starts considering a retarded Green's function [Eq. (4.23)]

$$\langle\langle \psi_{\vec{a}}(t), \psi^{\dagger}_{\vec{b}}(t') \rangle\rangle \equiv G^{r}_{\vec{a},\vec{b}}(t,t') = -\frac{i}{\hbar}\theta(t-t')\left\langle \left[\psi_{\vec{a}}(t), \psi^{\dagger}_{\vec{b}}(t')\right]_{+}\right\rangle , \qquad (5.30)$$

where $\psi_{\vec{a}}(t)$ are operators of the Anderson Hamiltonian (C or d) and $\vec{a}$ and $\vec{b}$ represent sets of quantum numbers. In this case, the Green's function of Eq. (5.30) can be understood as a coefficient of a matrix which collects of all possible individual Green's functions. At this stage, the next step consists of finding the EOM of Eq. (5.30) by calculating the partial derivative in t such that

$$\begin{aligned} i\hbar\partial_t G^{r}_{\vec{a},\vec{b}}(t,t') &= \delta(t-t')\left\langle \left[\psi_{\vec{a}}(t), \psi^{\dagger}_{\vec{b}}(t')\right]_{+}\right\rangle \\ &\quad +\theta(t-t')\left\langle \left[\partial_t\psi_{\vec{a}}(t), \psi^{\dagger}_{\vec{b}}(t')\right]_{+}\right\rangle . \end{aligned} \qquad (5.31)$$

Eq. (5.31) has a term which depends on the anticommutator at equal times and a second term which involves the evolution of the operator $\psi_{\vec{a}}(t)$. Such operators will obey the Heisenberg equation [Eq. (4.4)] which transforms Eq. (5.31) into

$$\begin{aligned} i\hbar\partial_t G^{r}_{\vec{a},\vec{b}}(t,t') &= \delta(t-t')\left\langle \left[\psi_{\vec{a}}(t), \psi^{\dagger}_{\vec{b}}(t')\right]_{+}\right\rangle \\ &\quad +\frac{i}{\hbar}\theta(t-t')\left\langle \left[[\mathcal{H}, \psi_{\vec{a}}(t)], \psi^{\dagger}_{\vec{b}}(t')\right]_{+}\right\rangle . \end{aligned} \qquad (5.32)$$

Clearly, we observe that the EOM of $G^{r}_{\vec{a},\vec{b}}$ contains a function of additional Green's functions depending on the form of the Hamiltonian $\mathcal{H}$ and we will typically deal with an infinite set of coupled differential equations. Due to this difficulty, we will truncate the set in the following sections by applying physical arguments.

Since one of our goals is finding the local DOS, we proceed to the calculation of the EOM for the QD retarded Green's function

$$G^r_{\mu\sigma,\nu\sigma}(t,t') = -\frac{i}{\hbar}\theta(t-t')\left\langle\left[d_{\mu\sigma}(t), d^\dagger_{\nu\sigma}(t')\right]_+\right\rangle , \tag{5.33}$$

whose EOM, applying the Anderson Hamiltonian of Eq. (5.2), reads

$$\begin{aligned} i\hbar\partial_t G^r_{\mu\sigma,\nu\sigma} &= \delta_{\mu\nu}\delta(t-t') + \sum_\lambda H_{\mu\sigma,\lambda\sigma}G^r_{\lambda\sigma,\nu\sigma} \\ &+ \sum_{\alpha k}\mathcal{V}^*_{\alpha k\sigma,\mu}G^r_{\alpha k\sigma,\nu\sigma} + U_\mu\langle\!\langle d_{\mu\sigma}n_{\mu\bar{\sigma}}, d^\dagger_{\nu\sigma}\rangle\!\rangle \\ &+ \sum_{\lambda\neq\mu,\sigma_\lambda}\tilde{U}_{\mu,\lambda}\langle\!\langle d_{\mu\sigma}n_{\lambda\sigma_\lambda}, d^\dagger_{\nu\sigma}\rangle\!\rangle . \end{aligned} \tag{5.34}$$

As expected, the retarded Green's function depends on higher order correlators: $\langle\!\langle d_{\mu\sigma}n_{\mu\bar{\sigma}}, d^\dagger_{\nu\sigma}\rangle\!\rangle$ and $\langle\!\langle d_{\mu\sigma}n_{\lambda\sigma_\lambda}, d^\dagger_{\nu\sigma}\rangle\!\rangle$ due to intradot and interdot interactions, respectively. Eq. (5.34) is key to the results of this thesis and we thus devote the following sections to solve it properly taking into account different regimes.

5.2.1 Non-interacting solution

The simplest assumption is to consider that the Coulomb interactions are negligible ($U_\mu = \tilde{U}_{\mu,\nu} = 0$). In this situation, the unknown functions of Eq. (5.34) are only the dot and tunneling retarded Green's function. Since Eq. (5.34) corresponds to the former , we also compute the EOM of the latter:

$$i\hbar\partial_t G^r_{\alpha k\sigma,\nu\sigma} = \varepsilon_{\alpha k\sigma}G^r_{\alpha k\sigma,\nu\sigma} + \sum_\lambda \mathcal{V}_{\alpha k\sigma,\lambda}G^r_{\lambda\sigma,\nu\sigma} . \tag{5.35}$$

Our next step is resorting to Fourier space, which transforms $i\hbar\partial_t \to \omega$. Additionally, the Green's functions become energy-dependent $G(t,t') \to G(\omega)$. After such transformation, Eq. (5.35) reads

$$G^r_{\alpha k\sigma,\nu\sigma}(\omega) = \sum_\lambda \frac{\mathcal{V}_{\alpha k\sigma,\lambda}}{\omega - \varepsilon_{\alpha k\sigma}}G^r_{\lambda\sigma,\nu\sigma}(\omega) . \tag{5.36}$$

In this case, we encounter a closed system of algebraic equations whose size depends on the number of QDs in the device. Combining Eq. (5.34) in the Fourier space and Eq. (5.36) we obtain

$$G^r_{\mu\sigma,\nu\sigma} = \left[\mathbf{1}\omega - \mathcal{H}_{\text{nint}} - \Sigma^r\right]^{-1}_{\mu\sigma,\nu\sigma} , \tag{5.37}$$

which is a very straightforward solution. As expected, the dot retarded Green's function depends in a trivial way on the noninteracting Hamiltonian $\mathcal{H}_{\text{nonint}}$ and the retarded tunneling self-energy Σ^r which is defined as

$$\Sigma^r_{\mu\sigma,\nu\sigma} = \sum_{\alpha k} g^r_{\alpha k\sigma}\mathcal{V}^*_{\alpha k\sigma,\mu}\mathcal{V}_{\alpha k\sigma,\nu} = \sum_{\alpha k}\frac{\mathcal{V}^*_{\alpha k\sigma,\mu}\mathcal{V}_{\alpha k\sigma,\nu}}{\omega - \varepsilon_{\alpha k\sigma}} \tag{5.38}$$

In the wide band limit (WBL), Eq. (5.38) can be approximated to the hybridization functions of Eq. (5.15) following

$$\Sigma^r_{\mu\sigma,\nu\sigma} \approx -i\frac{\Gamma_{\mu\sigma,\nu\sigma}}{2} \ . \tag{5.39}$$

Now, we discuss the case of a DQD with a dot-dot tunneling τ. The Green's function takes the following form

$$G^r_{\mu\sigma,\nu\sigma} = \frac{(\omega - \varepsilon_{\bar{\mu}} - \Sigma^r_{\bar{\mu}\sigma,\bar{\mu}\sigma})\delta_{\mu\nu} + (\tau + \Sigma^r_{\bar{\mu}\sigma,\mu\sigma})\delta_{\bar{\mu}\nu}}{(\omega - \varepsilon_{\mu} - \Sigma^r_{\mu\sigma,\mu\sigma})(\omega - \varepsilon_{\bar{\mu}} - \Sigma^r_{\bar{\mu}\sigma,\bar{\mu}\sigma}) - (\tau + \Sigma^r_{\mu\sigma,\bar{\mu}\sigma})(\tau + \Sigma^r_{\bar{\mu}\sigma,\mu\sigma})} \ , \tag{5.40}$$

where ε_μ is the spin-independent energy of the μ QD [$H_{\mu\sigma,\mu\sigma}$ in Eq. (5.4)] and $\bar{\mu}$ denotes $\{2,1\}$ for $\mu = \{1,2\}$ the DQD being as sketched in Fig. 1.6a or Fig. 1.6b. Eq. (5.40) will generate two resonances in the local DOS which represent broadened bonding and antibonding states [223].

If we consider a single QD, G^r reduces to a function with a single pole

$$G^r_{\sigma,\sigma} = \frac{1}{\omega - \varepsilon_{d\sigma} - \Sigma^r_{\sigma,\sigma}} \ . \tag{5.41}$$

If we insert Eq. (5.41) into Eq. (4.27), we obtain a Lorentzian resonance in the DOS, which corresponds to the Breit-Wigner approximation.

5.2.2 Hartree Approximation

A common way to include the role of interactions is assuming that electrons feel a mean-field potential which comprises all possible pair interactions. Within this approach, we may approximate the higher order correlators of Eq. (5.34) replacing the number operator to its mean occupation:

$$\langle\!\langle d_{\mu\sigma} n_{\lambda\sigma_\lambda}, d^\dagger_{\nu\sigma} \rangle\!\rangle \approx \langle n_{\lambda\sigma_\lambda} \rangle G^r_{\mu\sigma,\nu\sigma} \ . \tag{5.42}$$

This is called *Hartree approximation* and is widely used in the literature [94, 104, 223, 224]. Considering this approach, Eq. (5.37) turns out to be

$$G^r_{\mu\sigma,\nu\sigma} = [\mathbf{1}\omega - \mathcal{H}_{\text{nonint}} - \mathcal{N}^{\text{Har}} - \Sigma^r]^{-1}_{\mu\sigma,\nu\sigma} \ , \tag{5.43}$$

where $\mathcal{N}^{\text{Har}}$ is a diagonal matrix whose elements correspond to the mean-field values of the intradot and interdot interactions

$$\mathcal{N}^{\text{Har}}_{\mu\sigma,\mu\sigma} = U_\mu \bar{n}_{\mu\bar{\sigma}} + \sum_{\lambda\neq\mu,\sigma'} \tilde{U}_{\mu,\lambda}\bar{n}_{\lambda\sigma'} \ , \tag{5.44}$$

where, from now on, we apply the notation $\bar{n} = \langle n \rangle$ for simplicity. Due to the diagonal form of $\mathcal{N}$, the mean-field interactions only shift the energy levels of the QD. For the single QD case, we clearly observe that the level of the resonance [Eq. (5.41)] is changed by $\varepsilon_d \rightarrow \varepsilon_d + U\bar{n}_{\bar{\sigma}}$

$$G^r_{\sigma,\sigma} = \frac{1}{\omega - \varepsilon_{d\sigma} - U\bar{n}_{\bar{\sigma}} - \Sigma^r_{\sigma,\sigma}} \; . \tag{5.45}$$

Notice that now Eq. (5.45) depends on $\bar{n}_{\bar{\sigma}}$ which is, at the same time, dependent on the retarded Green's function [see Eqs. (4.26) and (4.44)]. Consequently, we have to deal with a self-consistent calculation in order to find the final solution. For the DQD case, we obtain

$$G^r_{\mu\sigma,\nu\sigma} = \frac{(\omega - \Omega^r_{\bar{\mu}\sigma,\bar{\mu}\sigma} - \mathcal{N}_{\mu\bar{\sigma}})\delta_{\mu\nu} + \Omega^r_{\bar{\mu}\sigma,\mu\sigma}\delta_{\bar{\mu}\nu}}{(\omega - \Omega^r_{\mu\sigma,\mu\sigma} - \mathcal{N}_{\mu\sigma})(\omega - \Omega^r_{\bar{\mu}\sigma,\bar{\mu}\sigma} - \mathcal{N}_{\mu\bar{\sigma}}) - \Omega_{\mu\sigma,\bar{\mu}\sigma}\Omega_{\bar{\mu}\sigma,\mu\sigma}} \, , \tag{5.46}$$

where $\Omega_{\mu\sigma_\mu,\nu\sigma_\nu} = H_{\mu\sigma_\mu,\nu\sigma_\nu} + \Sigma^r_{\mu\sigma_\mu,\nu\sigma_\nu}$ and $\mathcal{N}_{\mu\sigma} \equiv \mathcal{N}^{\mathrm{Har}}_{\mu\sigma,\mu\sigma}$. Despite its simplicity, this approach is unable to show characteristic features of CB, i. e., the Coulomb Diamonds; or even the Kondo effect. Therefore, we take an additional step in the EOM technique with the goal of finding a more accurate approximation.

5.2.3 Hubbard-I Approximation

The next step consists of computing the EOM of the correlators involving the intradot and interdot interactions [last two terms of Eq. (5.34)]. Applying Eq. (5.32) to such correlators we obtain

$$\begin{aligned}
i\hbar\partial_t\langle\langle d_{\mu\sigma}n_{\lambda\sigma_\lambda}, d^\dagger_{\nu\sigma}\rangle\rangle \;\; = \;\; & \delta_{\mu\nu}\bar{n}_{\lambda\sigma_\lambda}\delta(t-t') + \sum_\eta H_{\mu\sigma,\eta\sigma}\langle\langle d_{\eta\sigma}n_{\lambda\sigma_\lambda}, d^\dagger_{\nu\sigma}\rangle\rangle \\
& + \sum_\eta H_{\lambda\sigma_\lambda,\eta\sigma_\lambda}\langle\langle d_{\mu\sigma}d^\dagger_{\lambda\sigma_\lambda}d_{\eta\sigma_\lambda}, d^\dagger_{\nu\sigma}\rangle\rangle \\
& - \sum_\eta H_{\eta\sigma_\lambda,\lambda,\sigma_\lambda}\langle\langle d_{\mu\sigma}d^\dagger_{\eta\sigma_\lambda}d_{\lambda\sigma_\lambda}, d^\dagger_{\nu\sigma}\rangle\rangle \\
& + \sum_{\alpha k} \mathcal{V}^*_{\alpha k\sigma,\mu}\langle\langle C_{\alpha k\sigma}n_{\lambda\sigma_\lambda}, d^\dagger_{\nu\sigma}\rangle\rangle \\
& + \sum_{\alpha k} \mathcal{V}^*_{\alpha k\sigma_\lambda,\lambda}\langle\langle d_{\mu\sigma}d_{\lambda\sigma_\lambda}C_{\alpha k\sigma_\lambda}, d^\dagger_{\nu\sigma}\rangle\rangle \\
& - \sum_{\alpha k} \mathcal{V}_{\alpha k\sigma_\lambda,\lambda}\langle\langle d_{\mu\sigma}C^\dagger_{\alpha k\sigma_\lambda}d_{\lambda\sigma_\lambda}, d^\dagger_{\nu\sigma}\rangle\rangle \\
& + \sum_{\eta\neq\mu,\sigma_\eta} \tilde{U}_{\eta,\mu}\langle\langle d_{\mu\sigma}n_{\eta\sigma_\eta}n_{\lambda\sigma_\lambda}, d^\dagger_{\nu\sigma}\rangle\rangle \\
& + U_\mu\langle\langle d_{\mu\sigma}n_{\mu\bar{\sigma}}n_{\lambda\sigma_\lambda}, d^\dagger_{\nu\sigma}\rangle\rangle \; .
\end{aligned} \tag{5.47}$$

This lengthy equation covers three simultaneous virtual transitions and higher order interaction processes. We proceed with the truncation of Eq. (5.47) by applying physical arguments to obtain a valid result [225].

First, we neglect correlators involving hopping transitions among three different states (thus neglecting Kondo correlations). These terms are

$$\langle\!\langle d_{\mu\sigma} d^{\dagger}_{\lambda\sigma_\lambda} d_{\eta\sigma_\lambda}, d^{\dagger}_{\nu\sigma} \rangle\!\rangle \approx 0 \,, \tag{5.48a}$$

$$\langle\!\langle d_{\mu\sigma} d^{\dagger}_{\eta\sigma_\eta} d_{\lambda\sigma_\lambda}, d^{\dagger}_{\nu\sigma} \rangle\!\rangle \approx 0 \,, \tag{5.48b}$$

$$\langle\!\langle d_{\mu\sigma} d_{\lambda\sigma_\lambda} C_{\alpha k\sigma_\lambda}, d^{\dagger}_{\nu\sigma} \rangle\!\rangle \approx 0 \,, \tag{5.48c}$$

$$\langle\!\langle d_{\mu\sigma} C^{\dagger}_{\alpha k\sigma_\lambda} d_{\lambda\sigma_\lambda}, d^{\dagger}_{\nu\sigma} \rangle\!\rangle \approx 0 \,, \tag{5.48d}$$

$$\langle\!\langle d_{\mu\sigma} n_{\eta\sigma_\eta} n_{\lambda\sigma_\lambda}, d^{\dagger}_{\nu\sigma} \rangle\!\rangle \approx 0 \,, \tag{5.48e}$$

when $\{\mu,\sigma\} \neq \{\lambda,\sigma_\lambda\} \neq \{\eta,\sigma_\eta\}$. Now, we take Hartree-like approximations for the remaining unknown correlators in order to avoid the calculation of additional EOMs:

$$\langle\!\langle d_{\eta\sigma} n_{\lambda\sigma_\lambda}, d^{\dagger}_{\nu\sigma} \rangle\!\rangle \approx \langle n_{\lambda\sigma_\lambda} \rangle G^{r}_{\eta\sigma,\nu\sigma} \,, \tag{5.49a}$$

$$\langle\!\langle C_{\alpha k\sigma} n_{\lambda\sigma_\lambda}, d^{\dagger}_{\nu\sigma} \rangle\!\rangle \approx \langle n_{\lambda\sigma_\lambda} \rangle G^{r}_{\alpha k\sigma,\nu\sigma} \,, \tag{5.49b}$$

$$\langle\!\langle d_{\mu\sigma} n_{\eta\sigma_\eta} n_{\lambda\sigma_\lambda}, d^{\dagger}_{\nu\sigma} \rangle\!\rangle \approx \langle n_{\eta\sigma_\eta} \rangle \langle\!\langle d_{\mu\sigma} n_{\lambda\sigma_\lambda}, d^{\dagger}_{\nu\sigma} \rangle\!\rangle \,. \tag{5.49c}$$

when again $\{\mu,\sigma\} \neq \{\lambda,\sigma_\lambda\} \neq \{\eta,\sigma_\eta\}$. The approximation of Eq. (5.49c) is only performed in the equation involving $\langle\!\langle d_{\mu\sigma} n_{\lambda\sigma_\lambda}, d^{\dagger}_{\nu\sigma} \rangle\!\rangle$. Otherwise, we follow Eq. (5.48e). Finally, we achieve a closed set of differential equations which can be solved. Now, Eq. (5.47) in the Fourier space becomes

$$\left(\omega - \varepsilon_\mu - U_\mu(1 - n_{\mu\bar{\sigma}}) - \mathcal{N}^{\text{Har}}_{\mu\sigma\mu\sigma}\right) \langle\!\langle d_{\mu\sigma} n_{\mu\bar{\sigma}}, d^{\dagger}_{\nu\sigma} \rangle\!\rangle = \bar{n}_{\mu\bar{\sigma}} \Xi_{\mu\nu} \,, \tag{5.50a}$$

$$\left(\omega - \varepsilon_\mu - \tilde{U}_{\mu,\lambda}(1 - n_{\lambda\sigma_\lambda}) - \mathcal{N}^{\text{Har}}_{\mu\sigma\mu\sigma}\right) \langle\!\langle d_{\mu\sigma} n_{\lambda\sigma_\lambda}, d^{\dagger}_{\nu\sigma} \rangle\!\rangle = \bar{n}_{\lambda\sigma_\lambda} \Xi_{\mu\nu} \,, \tag{5.50b}$$

with

$$\Xi_{\mu\nu} = \left(\delta_{\mu\nu} + \sum_{\eta \neq \mu} H_{\mu\sigma,\eta\sigma} G^{r}_{\eta\sigma,\nu\sigma} + \sum_{\alpha k} \mathcal{V}^{*}_{\alpha k\sigma,\mu} G^{r}_{\alpha k\sigma,\nu\sigma} \right) \,, \tag{5.51}$$

Here, we have distinguished between the correlators of the intradot and the interdot interactions [$\lambda \neq \mu$ in Eq. (5.50b)]. Now, Eq. (5.34) in the Fourier space reads

$$(\omega - \varepsilon_\mu) G^{r}_{\mu\sigma,\nu\sigma} = \mathcal{N}^{\text{Hub}}_{\mu\sigma,\mu\sigma} \Xi_{\mu\nu} \,, \tag{5.52}$$

where

$$\begin{aligned} \mathcal{N}^{\text{Hub}}_{\mu\sigma,\mu\sigma} &= 1 + \frac{U_\mu \bar{n}_{\mu\bar{\sigma}}}{\omega - \varepsilon_\mu - U_\mu(1 - n_{\mu\bar{\sigma}}) - \mathcal{N}^{\text{Har}}_{\mu\sigma\mu\sigma}} \\ &\quad + \sum_{\lambda \neq \mu, \sigma_\lambda} \frac{U_{\mu,\lambda} \bar{n}_{\lambda\sigma_\lambda}}{\omega - \varepsilon_\mu - \tilde{U}_{\mu,\lambda}(1 - n_{\lambda\sigma_\lambda}) - \mathcal{N}^{\text{Har}}_{\mu\sigma\mu\sigma}} \,. \end{aligned} \tag{5.53}$$

We remark that $\mathcal{N}^{\text{Hub}}$ is also a diagonal matrix and contains all the contribution of the electron-electron interactions. With a proper manipulation of Eq. (5.52), we end up with the following result

$$G^r_{\mu\sigma,\nu\sigma} = \left[\omega[\mathcal{N}^{\text{Hub}}]^{-1} - \Omega - \left([\mathcal{N}^{\text{Hub}}]^{-1} - 1\right) \text{diag}[\mathcal{H}_{\text{nint}}]\right]^{-1}_{\mu\sigma,\nu\sigma} . \tag{5.54}$$

where $\text{diag}[\mathcal{O}]$ denotes the diagonal matrix of $\mathcal{O}$. For the single QD case, we may rewrite the Green's function as a two-pole solution

$$G^r_{\sigma,\sigma} = \frac{1 - \bar{n}_{\bar{\sigma}}}{\omega - \varepsilon_d - \Sigma^r_{\sigma,\sigma}\left(1 + \frac{U\bar{n}_{\bar{\sigma}}}{\omega - \varepsilon_d - U}\right)} + \frac{\bar{n}_{\bar{\sigma}}}{\omega - \varepsilon_d - U - \Sigma^r_{\sigma,\sigma}\left(1 - \frac{U(1-\bar{n}_{\bar{\sigma}})}{\omega - \varepsilon_d}\right)} \tag{5.55}$$

This is the Hubbard-I approximation. However, it is more convenient to solve the single dot Green's function by applying a different approximation. Instead of applying Eq. (5.49b), we compute the EOM of $\langle\!\langle C_{\alpha k\sigma} n_{\bar{\sigma}}, d^\dagger_{\nu\sigma} \rangle\!\rangle$ neglecting correlators involving hoppings with more than two particles. Interestingly, we now obtain a simpler solution

$$G^r_{\sigma,\sigma} = \frac{1 - \bar{n}_{\bar{\sigma}}}{\omega - \varepsilon_d - \Sigma^r_{\sigma,\sigma}} + \frac{\bar{n}_{\bar{\sigma}}}{\omega - \varepsilon_d - U - \Sigma^r_{\sigma,\sigma}} . \tag{5.56}$$

Eq. (5.56), in comparison with Eq. (5.55), has numerical advantages which facilitates the self-consistent calculation of the occupations offering similar results for the parameter regime considered in this thesis. We observe that Eq. (5.56) consists of two resonances, one centered at ε_d and a second (Coulomb) one located at $\varepsilon_d + U$, weighted by $1 - \bar{n}_{\bar{\sigma}}$ and $\bar{n}_{\bar{\sigma}}$, respectively. Hence, one resonance will be more relevant than the other depending on the QD occupation. Eq. (5.56) will be employed for studying the transport properties of an interacting single QD in Sec. 7.1 and a molecular junction in Sec. 7.2.

Concerning DQDs, when interdot interactions are negligible, the two-resonance Green's function reads

$$\begin{aligned} G^r_{\mu\sigma,\nu\sigma} &= h_{\mu\nu}\left[\frac{1 - \bar{n}_{\mu\bar{\sigma}}}{\omega - \varepsilon_\mu - \tilde{\Sigma}^r_{\mu\sigma}\left(1 - \frac{U_\mu \bar{n}_{\mu\bar{\sigma}}}{\omega - \varepsilon_\mu - U_\mu}\right)}\right. \\ &\qquad \left. + \frac{\bar{n}_{\mu\bar{\sigma}}}{\omega - \varepsilon_\mu - U_\mu - \tilde{\Sigma}^r_{\mu\sigma}\left(1 - \frac{U_\mu(1-\bar{n}_{\mu\bar{\sigma}})}{\omega - \varepsilon_\mu}\right)}\right] , \end{aligned} \tag{5.57}$$

where

$$h_{\mu\nu} = \delta_{\mu\nu} + \delta_{\bar{\mu}\nu} \frac{\mathcal{N}^{\text{Hub}}_{\bar{\mu}\sigma,\bar{\mu}\sigma} \Sigma^r_{\bar{\mu}\sigma,\mu\sigma}}{\omega - \varepsilon_{\bar{\mu}} - \mathcal{N}^{\text{Hub}}_{\bar{\mu}\sigma,\bar{\mu}\sigma} \Sigma^r_{\bar{\mu}\sigma,\bar{\mu}\sigma}} , \tag{5.58}$$

$$\tilde{\Sigma}^r_{\mu\sigma} = \Sigma^r_{\mu\sigma,\mu\sigma} + \frac{\Sigma^r_{\bar{\mu}\sigma,\mu\sigma} \Sigma^r_{\mu\sigma,\bar{\mu}\sigma}}{\omega - \varepsilon_{\bar{\mu}} - \mathcal{N}^{\text{Hub}}_{\bar{\mu}\sigma,\bar{\mu}\sigma} \Sigma^r_{\bar{\mu}\sigma,\bar{\mu}\sigma}} \mathcal{N}^{\text{Hub}}_{\bar{\mu}\sigma,\bar{\mu}\sigma} . \tag{5.59}$$

Notice that Eq. (5.57) is the two-particle extension of Eq. (5.55). It is able to describe accurately the DQD system of Sec. 8.1 and will be used to analyze the role of intradot interactions in the generation of BICs and studying its transport properties.

5.2.4 Beyond Hubbard-I

Although the Hubbard-I approximation correctly describes CB effects, it is unable to exhibit Kondo features. For this reason, an approach beyond Hubbard-I is required. From now on, we restrict ourselves to the single QD setup in view of the complexity of the problem. We follow Lacroix [226] and Kashcheyevs *et al.* [227] and compute the remaining correlators of Eq. (5.47)

$$\begin{aligned}(i\hbar\partial_t - \varepsilon_{\alpha k\sigma})\langle\langle C_{\alpha k\sigma} n_{\bar{\sigma}}, d_\sigma^\dagger\rangle\rangle &= \mathcal{V}_{\alpha k\sigma}\langle\langle d_\sigma n_{\bar{\sigma}}, d_\sigma^\dagger\rangle\rangle \\ &+ \sum_{\beta q}\mathcal{V}^*_{\beta q\bar{\sigma}}\langle\langle C_{\alpha k\sigma} d_{\bar{\sigma}}^\dagger C_{\beta q\bar{\sigma}}, d_\sigma^\dagger\rangle\rangle \\ &- \sum_{\beta q}\mathcal{V}_{\beta q\bar{\sigma}}\langle\langle C_{\alpha k\sigma} C^\dagger_{\beta q\bar{\sigma}} d_{\bar{\sigma}}, d_\sigma^\dagger\rangle\rangle\ , \end{aligned} \tag{5.60a}$$

$$\begin{aligned}(i\hbar\partial_t - \varepsilon_{\alpha k\sigma})\langle\langle d_\sigma d_{\bar{\sigma}}^\dagger C_{\alpha k\bar{\sigma}}, d_\sigma^\dagger\rangle\rangle &= \langle d_{\bar{\sigma}}^\dagger C_{\alpha k\bar{\sigma}}\rangle\delta(t-t') + \mathcal{V}_{\alpha k\bar{\sigma}}\langle\langle d_\sigma n_{\bar{\sigma}}, d_\sigma^\dagger\rangle\rangle \\ &+ \sum_{\beta q}\mathcal{V}^*_{\beta q\sigma}\langle\langle C_{\beta q\sigma} d_{\bar{\sigma}}^\dagger C_{\alpha k\bar{\sigma}}, d_\sigma^\dagger\rangle\rangle \\ &- \sum_{\beta q}\mathcal{V}_{\beta q\bar{\sigma}}\langle\langle d_\sigma C^\dagger_{\beta q\bar{\sigma}} C_{\alpha k\bar{\sigma}}, d_\sigma^\dagger\rangle\rangle\ , \end{aligned} \tag{5.60b}$$

$$\begin{aligned}(i\hbar\partial_t + \delta\varepsilon_{\alpha k})\langle\langle d_\sigma C^\dagger_{\alpha k\bar{\sigma}} d_{\bar{\sigma}}, d_\sigma^\dagger\rangle\rangle &= \langle C^\dagger_{\alpha k\bar{\sigma}} d_{\bar{\sigma}}\rangle\delta(t-t') - \mathcal{V}^*_{\alpha k\bar{\sigma}}\langle\langle d_\sigma n_{\bar{\sigma}}, d_\sigma^\dagger\rangle\rangle \\ &+ \sum_{\beta q}\mathcal{V}^*_{\beta q\sigma}\langle\langle C_{\beta q\sigma} C^\dagger_{\alpha k\bar{\sigma}} d_{\bar{\sigma}}, d_\sigma^\dagger\rangle\rangle \\ &+ \sum_{\beta q}\mathcal{V}^*_{\beta q\bar{\sigma}}\langle\langle d_\sigma C^\dagger_{\alpha k\bar{\sigma}} C_{\beta q\bar{\sigma}}, d_\sigma^\dagger\rangle\rangle\ , \end{aligned} \tag{5.60c}$$

where $\delta\varepsilon_{\alpha k} = \varepsilon_{\alpha k\sigma} - 2\varepsilon_d - U$. Again, higher order correlators are found in the EOMs. Hence, we close the system of equations by assuming the relation proposed by Mattis [228] which follows the Wick theorem for the case of a retarded Green's function obtaining

$$\langle\langle A^\dagger BC, D^\dagger\rangle\rangle \approx \langle A^\dagger B\rangle\langle\langle C, D^\dagger\rangle\rangle - \langle A^\dagger C\rangle\langle\langle B, D^\dagger\rangle\rangle \tag{5.61}$$

After some mathematical arrangements, the retarded Green's function of the QD reads

$$\begin{aligned} G^r_{\sigma,\sigma}(\omega) &= \frac{1-\tilde{n}_{\bar{\sigma}}}{\omega - \varepsilon_d - \Sigma_0 + \frac{U\Sigma_1}{\omega-\varepsilon_d-U-\Sigma_0-\Sigma_3}} \\ &+ \frac{\tilde{n}_{\bar{\sigma}}}{\omega - \varepsilon_d - U - \Sigma_0 - \frac{U\Sigma_2}{\omega-\varepsilon_d-\Sigma_0-\Sigma_3}}\ , \end{aligned} \tag{5.62}$$

where $\Sigma_0 = \Sigma^r_{\sigma,\sigma}$, $\tilde{n}_\sigma = \bar{n}_\sigma + \delta n_\sigma$ and

$$\delta n_\sigma = \sum_{\alpha k} \frac{\mathcal{V}^*_{\alpha k\sigma}}{\omega - \varepsilon_{\alpha k\sigma}} \langle d^\dagger_\sigma C_{\alpha k\sigma} \rangle - \sum_{\alpha k} \frac{\mathcal{V}_{\alpha k\sigma}}{\omega - \delta\varepsilon_{\alpha k}} \langle C^\dagger_{\alpha k\sigma} d_\sigma \rangle \;, \tag{5.63a}$$

$$\Sigma_1 = \sum_{\alpha k\beta q} \frac{\mathcal{V}^*_{\alpha k\bar\sigma} \mathcal{V}_{\beta q\bar\sigma}}{\omega - \varepsilon_{\alpha k\bar\sigma}} \langle C^\dagger_{\beta q\bar\sigma} C_{\alpha k\bar\sigma} \rangle + \sum_{\alpha k\beta q} \frac{\mathcal{V}_{\alpha k\bar\sigma} \mathcal{V}^*_{\beta q\bar\sigma}}{\omega + \delta\varepsilon_{\alpha k}} \langle C^\dagger_{\alpha k\bar\sigma} C_{\alpha k\bar\sigma} \rangle - \Sigma_0 \delta n_{\bar\sigma} \;, \tag{5.63b}$$

$$\Sigma_2 = \Sigma_3 - \Sigma_1 \;, \tag{5.63c}$$

$$\Sigma_3 = \sum_{\alpha k} \left[\frac{|\mathcal{V}_{\alpha k\bar\sigma}|^2}{\omega - \varepsilon_{\alpha k\bar\sigma}} + \frac{|\mathcal{V}_{\alpha k\bar\sigma}|^2}{\omega + \delta\varepsilon_{\alpha k}} \right] . \tag{5.63d}$$

This solution was already derived by Meir *et al.* [14]. In their work they assumed for the expected values inside Eqs. (5.63) that

$$\langle d^\dagger_\sigma C_{\alpha k\sigma} \rangle \approx 0 \tag{5.64}$$

$$\langle C^\dagger_{\beta q\bar\sigma} C_{\alpha k\bar\sigma} \rangle \approx \delta_{\alpha\beta} \delta_{kq} f_\alpha(\varepsilon_{\alpha k}) \;, \tag{5.65}$$

which is a valid approach for describing cotunneling at temperatures $T \gg T_K$. However, at lower temperatures the model may display unphysical results. For this reason, we will employ instead a modified fluctuation-dissipation theorem [229]

$$\langle A^\dagger B \rangle = -\frac{1}{2\pi i} \int d\omega \mathcal{F}(\omega) \left(\langle\!\langle B, A^\dagger \rangle\!\rangle^r - \langle\!\langle B, A^\dagger \rangle\!\rangle^a \right) \;, \tag{5.66}$$

where $\mathcal{F}(\omega)$ is denoted as a nonequilibrium distribution function which reads

$$\mathcal{F}(\omega) = \sum_\alpha \frac{\Gamma_\alpha f_\alpha(\omega)}{\Gamma} \;. \tag{5.67}$$

Here, we have taken $\Gamma = \sum_\alpha \Gamma_\alpha$. Before dealing with the general expression, we focus on the case of $U \to \infty$. Therefore, Eq. (5.62) becomes

$$G^r_{\sigma,\sigma}(\omega) = \frac{1 - \tilde{n}_{\bar\sigma}}{\omega - \varepsilon_d - \Sigma_0 - \Sigma_1} \;, \tag{5.68}$$

whose parameters also take a simpler form

$$\Sigma_1 = \sum_{\alpha k} \frac{\mathcal{V}^*_{\alpha k\bar\sigma}}{\omega - \varepsilon_{\alpha k\bar\sigma}} \left[\sum_{\beta q} (\mathcal{V}_{\beta q\bar\sigma} \langle C^\dagger_{\beta q\bar\sigma} C_{\alpha k\bar\sigma} \rangle - \Sigma_0 \langle d^\dagger_{\bar\sigma} C_{\alpha k\bar\sigma} \rangle) \right] , \tag{5.69}$$

$$\tilde{n}_{\bar\sigma} = \bar{n}_{\bar\sigma} + \sum_{\alpha k} \frac{\mathcal{V}^*_{\alpha k\bar\sigma}}{\omega - \varepsilon_{\alpha k\bar\sigma}} \langle d^\dagger_{\bar\sigma} C_{\alpha k\bar\sigma} \rangle \;. \tag{5.70}$$

At this stage, employing Eq. (5.66) and following the procedure of Entin-Wohlman *et al.* [230], Eqs. (5.69) and (5.70) turn into

$$\begin{aligned}\Sigma_1(\omega) &= -i\frac{\Gamma}{4} + \mathcal{X}(\omega)\left[1 + i\Gamma G^a_{\bar{\sigma},\bar{\sigma}}(\omega)\right]\frac{\Gamma}{2}\,, && (5.71)\\ \tilde{n}_{\bar{\sigma}} &= \bar{n}_{\bar{\sigma}} + \frac{\Gamma}{2} G^a_{\bar{\sigma},\bar{\sigma}}(\omega)\mathcal{X}(\omega) && (5.72)\end{aligned}$$

where $\mathcal{X}(\omega)$ is the solution of the integral of the nonequilibrium distribution function expressed by

$$\begin{aligned}\mathcal{X}(\omega) &= \sum_\alpha \frac{\Gamma_\alpha}{\Gamma}\int_{-D}^{D}\frac{d\omega'}{\pi}\frac{f_\alpha(\omega') - 1/2}{\omega - \omega' + i0^+}\\ &= \sum_\alpha \frac{\Gamma_\alpha}{\pi\Gamma}\left[\frac{1}{2}\ln\frac{D^2 - \omega^2}{2\pi k_B T_\alpha^2} - \psi\left(\frac{1}{2} - i\frac{\omega - \mu_\alpha}{2\pi k_B T_\alpha}\right)\right]\,, && (5.73)\end{aligned}$$

where $\psi(\ldots)$ is the digamma function, responsible for the logarithmic divergences of the Kondo effect. The solution of such integral is discussed in detail in App. C. The final expression of the QD Green's function is

$$G^r_{\sigma,\sigma}(\omega) = g(\omega)\left[\bar{p}_\sigma + i\frac{P(\omega)}{\mathcal{X}^*(\omega)}\right]\,, \tag{5.74}$$

with

$$\begin{aligned}g(\omega) &= \frac{1}{\omega - \varepsilon_d - \Lambda + i3\Gamma/4}\,, && (5.75)\\ P(\omega) &= S(\omega) - \sqrt{S^2(\omega) + |\mathcal{X}(\omega)|^2\left(\frac{3}{2}\bar{p}_\sigma - \bar{p}_\sigma^2\right)}\,, && (5.76)\\ S(\omega) &= z^2 + \frac{9}{16} - z\mathrm{Re}[\mathcal{X}(\omega)] + \left(\bar{p}_\sigma - \frac{3}{4}\right)\mathrm{Im}[\mathcal{X}(\omega)] && (5.77)\end{aligned}$$

where $\bar{p}_\sigma = 1 - \bar{n}_\sigma$ and $z = (\omega - \varepsilon_d - \Lambda)/\Gamma$. We identify two different terms in Eq. (5.74): A Lorentzian-like function located approximately at the mean-field resonance $\omega \approx \varepsilon_d$ and an additional term which is in charge of the emergence of the Abrikosov-Suhl resonance (more details given in Sec. 7.3).

When we assume a finite Coulomb interaction U, the calculation becomes more cumbersome. After employing the same mathematical procedure as with Eqs. (5.71) and (5.72) with all components of the retarded Green's function [Eqs. (5.63)] we obtain

$$\begin{aligned}\Sigma_1 &= \frac{\Gamma}{2}\left(-i + \mathcal{X}(\omega)[1 + i\Gamma G^a_{\bar{\sigma},\bar{\sigma}}(\omega)] - \mathcal{X}^*(\omega)[1 + i\Gamma G^r_{\bar{\sigma},\bar{\sigma}}(\omega_1)]\right)\,, && (5.78)\\ \Sigma_3 &= \Lambda(\omega) - \Lambda(\omega_1) - i\Gamma\,, && (5.79)\\ \tilde{n}_{\bar{\sigma}} &= \bar{n}_{\bar{\sigma}} + \frac{\Gamma}{2}\left[G^a_{\bar{\sigma},\bar{\sigma}}(\omega)\mathcal{X}(\omega) - G^r_{\bar{\sigma},\bar{\sigma}}(\omega_1)\mathcal{X}(\omega_1)\right]\,, && (5.80)\end{aligned}$$

where $\omega_1 = -\omega + 2\varepsilon_d + U$. We highlight that now the retarded Green's function depends recursively on itself in a nontrivial way. For instance, we observe that Σ_1 from Eq. (5.62) depends on $G^a_{\bar{\sigma},\bar{\sigma}}(\omega)$ and $G^r_{\bar{\sigma},\bar{\sigma}}(\omega_1)$. Therefore, we consider an approach which simplifies the problem: for a large, but finite, Coulomb interaction we are allowed to safely neglect the $G^r_{\bar{\sigma},\bar{\sigma}}(\omega_1)$ terms leading to the expression

$$G^r_{\sigma,\sigma}(\omega) = g_u(\omega)\left[p_{u,\sigma} + i\frac{P_u(\omega)}{\mathcal{X}^*_u(\omega)}\right] , \tag{5.81}$$

which is similar to Eq. (5.74) with the difference that now each component depends on $u(\omega)$

$$u(\omega) = \frac{U}{\varepsilon_d + U + \Sigma_0 + \Sigma_3 - \omega} , \tag{5.82}$$

following

$$\begin{aligned}
\mathcal{X}_u(\omega) &= u(\omega)\mathcal{X}(\omega) , && (5.83)\\
g_u(\omega) &= \frac{1}{\Gamma(z + i(1+u)/2 + \bar{\mathcal{X}}_u)} , && (5.84)\\
Q_u(\omega) &= S_u - \left(S_u^2 - \left|\bar{\mathcal{X}}^*_u p_{u,\sigma}\right|^2 + \left|\mathcal{X}_u\right|^2 h_1(\omega)\right)^{1/2} , && (5.85)\\
S_u(\omega) &= z^2 + \frac{|1+u|^2}{4} - \frac{\mathrm{Im}[\bar{\mathcal{X}}_u(1+u)]}{2} + \frac{|\bar{\mathcal{X}}_u|^2}{4} - z\mathrm{Re}[\mathcal{X}_u] \\
&\quad - \frac{\mathrm{Im}[\mathcal{X}_u(1+u^*)]}{2} - \frac{\mathrm{Re}[\mathcal{X}_u\bar{\mathcal{X}}_u]}{2} + \mathrm{Im}[\mathcal{X}_u p_{u,\sigma}] \\
&\quad - z\mathrm{Im}[u] + z\mathrm{Re}[\bar{\mathcal{X}}_u] , && (5.86)
\end{aligned}$$

with $\bar{\mathcal{X}}_u = \mathcal{X}_u(\omega_1)$ and

$$\begin{aligned}
h_1(\omega) &= \left(1 + \mathrm{Re}[u] - \mathrm{Im}[\bar{\mathcal{X}}_u]\right) p_{u,\sigma} \\
&\quad -2\left(z + i\frac{1+u}{2} + \frac{\bar{\mathcal{X}}^*}{2}\right)\mathrm{Im}[p_{u,\sigma}] , && (5.87)\\
p_{u,\sigma} &= 1 - u(\omega)\bar{n}_\sigma . && (5.88)
\end{aligned}$$

Despite the amount of terms in the Green's function, we emphasize that the only self-consistent calculation is inside $\bar{n}_\sigma$. Therefore, the numerical calculation can be computed straightforwardly giving good qualitative results. These theoretical results will be used to investigate the transport across an artificial Kondo impurity in Sec. 7.3 for infinite and finite values of the Coulomb interactions obtaining intriguing nonlinear results.

5.3 Slave-boson formalism

In this section we return to the slave-boson Hamiltonian (Sec. 5.1.2). The presence of the boson field b makes the EOM technique of the previous sections partially inapplicable, at least for the theory explained in this thesis. Nevertheless, it is still possible to use the EOM technique if we move to the SBMFT. In this approach, the boson operator is replaced by its mean-field expected value $b \to \langle b_\mu \rangle \equiv \sqrt{N_s}\tilde{b}_\alpha$, which in general is a complex number. Under this approach, charge fluctuations are totally neglected because we restrict to single-occupied QDs following Eq. (5.14). Now, the aim is to evaluate $\tilde{b}_\mu$ and λ_μ solving mean-field equations. First, we determine the equation of motion of the boson operator b_μ.

$$i\hbar \frac{db_\mu}{dt} = -\lambda_\mu b_\mu - \frac{1}{N}\sum_{\alpha k\sigma} \mathcal{V}_{\alpha k\sigma,\mu} C^\dagger_{\alpha k\sigma} f_{\mu\sigma} \ . \tag{5.89}$$

We assume that Eq. (5.89) is in the stationary limit meaning that $i\hbar d_t b_\mu = 0$. In the following step, we will compute the expected value to Eq. (5.89) considering the mean-field approach. Multiplying the Eq. (5.89) by $\tilde{b}^*_\mu$ and using the definition of Eq. (4.20) we find

$$\sum_{\alpha k\sigma} \tilde{\mathcal{V}}_{\alpha k\sigma,\mu} G^<_{f\mu\sigma,\alpha k\sigma}(t,t) = -\frac{i}{\hbar} N\lambda_\mu |\tilde{b}_\mu|^2 \ , \tag{5.90}$$

where $\tilde{\mathcal{V}}_{\alpha k\sigma,\mu} = \tilde{b}^*_\mu \mathcal{V}_{\alpha k\sigma,\mu}$ is the renormalized tunneling amplitude and f in $G^<_{f\mu\sigma,\alpha k\sigma}(t,t)$ denotes the pseudofermion $f_{\mu\sigma}$ subspace. The second equation corresponds to the expected value of the Lagrange condition [Eq. (5.14)]

$$\sum_\sigma G^<_{f\mu\sigma,f\mu\sigma}(t,t) = \frac{i}{\hbar}(1 - N|\tilde{b}_\mu|^2) \ . \tag{5.91}$$

Hence, $\tilde{b}_\mu$ and λ_μ will be found after solving Eqs. (5.90) and (5.91). For the sake of simplicity, we renormalize the level position $\tilde{\varepsilon}_\mu$ and the hybridization constant $\tilde{\Gamma}_\mu$ in terms of these unknown quantities

$$\tilde{\varepsilon}_\mu = \varepsilon_\mu + \lambda_\mu \ , \ \tilde{\Gamma}_\mu = |\tilde{b}_\mu|^2 \Gamma_\mu \ , \tag{5.92}$$

which represent the position and width of the Kondo resonance of the μ artificial impurity, respectively. Concerning the local DOS, $\rho_{\mu\sigma}(\omega)$ also contains a term due to the boson field

$$\rho_{\mu\sigma}(\omega) = -\frac{|\tilde{b}_\mu|^2}{\pi} \mathrm{Im}\big[G^r_{f\mu\sigma,f\mu\sigma}\big] \ . \tag{5.93}$$

Although Eq. (5.93) obeys the relation $\pi\tilde{\Gamma}\rho_{d\mu\sigma}(\tilde{\varepsilon}_\alpha) = 1$, it does not satisfy completely the Friedel sum rule [Eq. (4.28)] because the SBMFT is unable to capture the single-particle peaks. Nevertheless, it accurately describes the Abrikosov-Suhl resonances and is a good approach to investigate the Kondo effect in the Fermi liquid regime ($T \ll T_K$).

5.3.1 Mean-field equations in single quantum dots

We continue with the development of the mean-field equations for the case of a single impurity in order to obtain a self-consistent expression to find the unknown parameters of the system. We highlight that the slave-boson Hamiltonian in the SBMFT has the form of a noninteracting Anderson Hamiltonian with renormalized parameters $\varepsilon_d \to \tilde{\varepsilon}_d$ and $\Gamma \to \tilde{\Gamma}$. Accordingly, it yields Eq. (5.41) as the retarded Green's function.

Using the effective fluctuation-dissipation relation [Eq. (5.66)] into the Green's function of Eq. (5.91) and resorting to Fourier, Eq. (5.91) reads

$$\sum_\sigma \frac{1}{2\pi} \int_{-D}^{D} d\omega \frac{\tilde{\Gamma}\mathcal{F}(\omega)}{(\omega - \tilde{\varepsilon}_d)^2 + \frac{\tilde{\Gamma}^2}{4}} = 1 - N\frac{\tilde{\Gamma}}{\Gamma} \,. \tag{5.94}$$

On the other hand, Eq. (5.90), after applying Eq. (5.66) and Eq. (5.36), reads

$$\sum_\sigma \frac{1}{\pi} \int_{-D}^{D} d\omega \frac{(\omega - \tilde{\varepsilon}_d)\mathcal{F}(\omega)}{(\omega - \tilde{\varepsilon}_d)^2 + \frac{\tilde{\Gamma}^2}{4}} = (\varepsilon_d - \tilde{\varepsilon}_d)\frac{2N}{\Gamma} \,. \tag{5.95}$$

Both mean-field equations can be combined to a complex integral equation.

$$\sum_\sigma \frac{1}{\pi} \int_{-D}^{D} d\omega \frac{\mathcal{F}(\omega)}{\omega - \tilde{\varepsilon}_d + i\frac{\tilde{\Gamma}}{2}} = \tilde{w} \,, \tag{5.96}$$

where

$$\tilde{w} = (\varepsilon_d - \tilde{\varepsilon}_d)\frac{2N}{\Gamma} \,. \tag{5.97}$$

The integral inside Eq. (5.96) was already solved in App. C. As a result, the mean-field parameters will be obtained by solving following equation

$$\sum_{\alpha\sigma} \frac{\Gamma_\alpha}{\pi\Gamma} \left[\ln\left|\frac{2\pi k_B T_\alpha}{D}\right| + \psi\left(\frac{1}{2} + \frac{i(\tilde{\varepsilon}_d - \mu_\alpha) + \tilde{\Gamma}/2}{2\pi k_B T_\alpha}\right)\right] = \tilde{w} \,. \tag{5.98}$$

Applying Eq. (5.98), we will discuss how the mean-field parameters get altered under the influence of voltage or temperature biases in Sec. 7.3.2. Additionally, we will examine the transport through the impurity to qualitatively describe the behavior of the system.

5.3.2 Mean-field equations in double quantum dots

For a two-impurity slave-boson Hamiltonian, the calculation is slightly more demanding. Nevertheless, we can obtain quite straightforwardly the mean-field equations. In this particular case, the retarded Green's function takes the form of a noninteracting DQD system [Eq. (5.40)]. Applying again Eq. (5.66), Eqs. (5.89) and (5.91) assuming that each QD is attached to only one reservoir $\alpha = \mu = \{L, R\}$ read

$$\frac{1}{\pi}\int_{-D}^{D} d\omega \frac{\tilde{\tau}_\alpha \tilde{\tau}_{\bar{\alpha}} \tilde{\Gamma}_{\bar{\alpha}} f_{\bar{\alpha}}(\omega) + \tilde{\Gamma}_\alpha f_\alpha(\omega) M(\omega)}{\left|(\omega - \tilde{\varepsilon}_\alpha + i\tilde{\Gamma}_\alpha/2)(\omega - \tilde{\varepsilon}_{\bar{\alpha}} + i\tilde{\Gamma}_{\bar{\alpha}}/2) - \tilde{\tau}_\alpha \tilde{\tau}_{\bar{\alpha}}\right|^2} = 1 - N\frac{\tilde{\Gamma}_\alpha}{\Gamma_\alpha}\,, \tag{5.99a}$$

$$\frac{1}{\pi}\int_{-D}^{D} d\omega \frac{(\omega - \tilde{\varepsilon}_\alpha)\left(\tilde{\tau}_\alpha \tilde{\tau}_{\bar{\alpha}} \tilde{\Gamma}_{\bar{\alpha}} f_{\bar{\alpha}}(\omega) + \tilde{\Gamma}_\alpha f_\alpha(\omega) M(\omega)\right)}{\left|(\omega - \tilde{\varepsilon}_\alpha + i\tilde{\Gamma}_\alpha/2)(\omega - \tilde{\varepsilon}_{\bar{\alpha}} + i\tilde{\Gamma}_{\bar{\alpha}}/2) - \tilde{\tau}_\alpha \tilde{\tau}_{\bar{\alpha}}\right|^2} = (\tilde{\varepsilon}_\alpha - \varepsilon_\alpha)N\frac{\tilde{\Gamma}_\alpha}{\Gamma_\alpha}\,, \tag{5.99b}$$

where $M(\omega) = (\omega - \tilde{\varepsilon}_{\bar{\alpha}})^2 + \tilde{\Gamma}_{\bar{\alpha}}^2/4$. We note that the tunnel coupling between dots follows $\tilde{\tau}_\alpha = \tau|\tilde{b}_\alpha|^2$. Nevertheless, Eq. (5.99) depends only on the product of both $\tilde{\tau}_\alpha \tilde{\tau}_{\bar{\alpha}}$ meaning that no approximation has been made for the decoupling of the slave-bosons. We perform several manipulations to split Eq. (5.99) into integrals of the type

$$J_\alpha(\omega_i) = \int_{-D}^{D} d\omega \frac{f_\alpha(\omega)}{\omega - \omega_i}\,, \tag{5.100}$$

whose solution is computed in App. C and ω_i ($i = 1, \ldots, 4$) correspond to the poles of the integrals

$$\omega_{1,2} = \omega_{3,4}^* = \frac{2(\tilde{\varepsilon}_\alpha + \tilde{\varepsilon}_{\bar{\alpha}}) - i\tilde{\Gamma}}{4} \pm \sqrt{\left(\frac{2(\tilde{\varepsilon}_\alpha + \tilde{\varepsilon}_{\bar{\alpha}}) - i\delta\tilde{\Gamma}}{4} - |\tilde{\tau}|^2\right)}\,, \tag{5.101}$$

where $\delta\tilde{\Gamma} = \tilde{\Gamma}_\alpha - \tilde{\Gamma}_{\bar{\alpha}}$ and $|\tilde{\tau}|^2 = \tau|\tilde{b}_\alpha|^2|\tilde{b}_{\bar{\alpha}}|^2$. Hence, the mean-field equations now read

$$\sum_i A_{i\alpha} J_\alpha(\omega_i) + B_{i\alpha} J_{\bar{\alpha}}(\omega_i) = 1 - N\frac{\tilde{\Gamma}_\alpha}{\Gamma_\alpha}\,, \tag{5.102}$$

$$\sum_i C_{i\alpha} J_\alpha(\omega_i) + D_{i\alpha} J_{\bar{\alpha}}(\omega_i) = (\tilde{\varepsilon}_\alpha - \varepsilon_\alpha)N\frac{\tilde{\Gamma}_\alpha}{\Gamma_\alpha}\,, \tag{5.103}$$

with

$$A_{i\alpha} = \frac{1}{\pi}\frac{\tilde{\Gamma}_\alpha M(\omega_i)}{\prod_{j\neq i}(\omega_i - \omega_j)}\,,\quad B_{i\alpha} = \frac{1}{\pi}\frac{|\tilde{\tau}|^2\tilde{\Gamma}_{\bar{\alpha}}}{\prod_{j\neq i}(\omega_i - \omega_j)}\,, \tag{5.104}$$

and $C_{i\alpha} = (\omega - \tilde{\varepsilon}_\alpha)A_{i\alpha}$, $D_{i\alpha} = (\omega - \tilde{\varepsilon}_\alpha)B_{i\alpha}$. Using the solution given by Eqs. (5.102) and (5.103), we discuss in detail the quantum transport under voltage and thermal biases through a two-impurity Kondo system in Sec. 8.3.

6. Transport

In previous chapters, we have shown that the Keldysh NEGF formalism is a powerful tool to compute the response of nanoscale systems far from equilibrium. In fact, we have found theoretical expressions for the local DOS of QD systems modeled with the Anderson Hamiltonian at different regimes. Notwithstanding, we have not yet explained the theoretical connection with the measurable variables such as the currents and conductances. The description of the electronic transport across QD setups is essential to obtain the results of this thesis and, consequently, we fill the gap in this chapter.

We develop the quantum transport theory by defining the electric and heat currents operators:

$$\begin{aligned} \hat{I}_{\alpha\sigma} &= -e\frac{dn_{\alpha\sigma}}{dt} \,, && (6.1) \\ \hat{Q}_{\alpha} &= -\frac{d\mathcal{H}^{\alpha}_{\text{leads}}}{dt} - \frac{\mu_\alpha}{e}\hat{I}_{\alpha} \,, && (6.2) \end{aligned}$$

where $I_\alpha = \sum_\sigma I_{\alpha\sigma}$ and

$$\begin{aligned} n_{\alpha\sigma} &= \sum_k C^\dagger_{\alpha k\sigma} C_{\alpha k\sigma} \,. && (6.3) \\ \mathcal{H}^{\alpha}_{\text{leads}} &= \sum_{k\sigma} \varepsilon_{\alpha k\sigma} C^\dagger_{\alpha k\sigma} C_{\alpha k\sigma} \,. && (6.4) \end{aligned}$$

Eq. (6.1) represents the flow of electrons with spin σ measured at the reservoir α while Eq. (6.2) describes the heat flow at the lead α. As is usual in mesoscopics, positive flows are taken from the reservoirs to the sample. As explained in Sec. 3.1.3, we point out that Q_α has two components: the energy flux $Q_{E,\alpha} = -d\mathcal{H}^{\alpha}_{\text{leads}}/dt$ and the Joule heating term $Q_{I,\alpha} \equiv -V_\alpha I_\alpha$. In addition, we recall that both $I_{\alpha\sigma}$ and Q_α must obey the conservation laws expressed as Eqs. (3.19) and (3.20).

We divide the chapter in two sections: First, we calculate the electrical and heat currents finding expressions dependent of the QD Green's functions in Sec. 6.1. We will discuss the properties of the transmission function and conductances in Secs. 6.1.1 and 6.1.2, respectively. Second, we will perform the perturbation expansion of the electrical current in terms of the Kondo Hamiltonian in Sec. 6.2 with the goal of finding the linear electrical conductance (Sec. 6.2.3) which allows us to obtain its logarithmic dependence and, consequently, the effective Kondo temperature of an artificial impurity.

6.1 Currents in non-perturbative approaches

This section explains the calculation which leads to the currents as a function of the dot Green's functions. We note that this section gives formal results which can be found in Haug and Jauho [213] and Meir and Wingreen [231]. We start by applying the Heisenberg equation [Eq. (4.4)] to Eq. (6.1) and $\hat{Q}_{E,\alpha}$ [first term of Eq. (6.2)] using the Hamiltonian given by Eq (5.2). Thus,

$$I_{\alpha\sigma} = -\frac{ei}{\hbar}\sum_{\mu k}\left[\mathcal{V}^*_{\alpha k\sigma,\mu}\langle d^\dagger_{\mu\sigma}C_{\alpha k\sigma}\rangle - \mathcal{V}_{\alpha k\sigma,\mu}\langle C^\dagger_{\alpha k\sigma}d_{\mu\sigma}\rangle\right] , \tag{6.5a}$$

$$Q_{E,\alpha} = -\frac{i}{\hbar}\sum_{\mu k\sigma}\varepsilon_{\alpha k\sigma}\left[\mathcal{V}^*_{\alpha k\sigma,\mu}\langle d^\dagger_{\mu\sigma}C_{\alpha k\sigma}\rangle - \mathcal{V}_{\alpha k\sigma,\mu}\langle C^\dagger_{\alpha k\sigma}d_{\mu\sigma}\rangle\right] , \tag{6.5b}$$

where $I_{\alpha\sigma} = \langle\hat{I}_{\alpha\sigma}\rangle$ and $Q_{E,\alpha} = \langle\hat{Q}_{E,\alpha}\rangle$. We replace the expected values with the Green's function definition [Eq.(4.20)] and turn to Fourier space

$$I_{\alpha\sigma} = \frac{e}{2\pi\hbar}\sum_{\mu k}\int d\omega\left[\mathcal{V}_{\alpha k\sigma,\mu}G^<_{\mu\sigma,\alpha k\sigma}(\omega) - \mathcal{V}^*_{\alpha k\sigma,\mu}G^<_{\alpha k\sigma,\mu\sigma}(\omega)\right] , \tag{6.6a}$$

$$Q_{E,\alpha} = \frac{1}{2\pi\hbar}\sum_{\mu k\sigma}\int d\omega\varepsilon_{\alpha k\sigma}\left[\mathcal{V}_{\alpha k\sigma,\mu}G^<_{\mu\sigma,\alpha k\sigma}(\omega) - \mathcal{V}^*_{\alpha k\sigma,\mu}G^<_{\alpha k\sigma,\mu\sigma}(\omega)\right] . \tag{6.6b}$$

The next step is to transform Eq. (6.6) such that we find a dependence on the dot Green's functions. However, finding the relation between both tunneling and dot Green's functions is also needed. To do so, we employ Eq. (5.36) and follow the Langreth rules [Eqs. (4.37) and (4.38)]

$$G^<_{\alpha k\sigma,\nu\sigma}(\omega) = \sum_{\mu}\mathcal{V}_{\alpha k\sigma,\mu}[g^r_{\alpha k\sigma}(\omega)G^<_{\mu\sigma,\nu\sigma}(\omega) + g^<_{\alpha k\sigma}(\omega)G^a_{\mu\sigma,\nu\sigma}(\omega)] , \tag{6.7}$$

where $g^{r,a,<}_{\alpha k\sigma}(\omega)$ are the unperturbed Green's functions which can be found in App. A. A similar procedure may be realized for $G^<_{\mu\sigma,\alpha k\sigma}(\omega)$. Therefore, employing the Langreth rules into Eqs. (6.6), we obtain

$$\begin{aligned}I_{\alpha\sigma} &= \frac{e}{h}\sum_{\mu\nu k}\mathcal{V}_{\alpha k\sigma,\mu}\mathcal{V}^*_{\alpha k\sigma,\nu}\int d\omega\left([G^r_{\mu\sigma,\nu\sigma}(\omega) - G^a_{\mu\sigma,\nu\sigma}(\omega)]g^<_{\alpha k\sigma}(\omega)\right.\\ &\left.+G^<_{\mu\sigma,\nu\sigma}(\omega)[g^a_{\alpha k\sigma}(\omega) - g^r_{\alpha k\sigma}(\omega)]\right) ,\end{aligned} \tag{6.8a}$$

$$Q_{E,\alpha} = \frac{1}{h}\sum_{\mu\nu k\sigma} \mathcal{V}_{\alpha k\sigma,\mu}\mathcal{V}^{*}_{\alpha k\sigma,\nu} \int d\omega \big([G^{r}_{\mu\sigma,\nu\sigma}(\omega) - G^{a}_{\mu\sigma,\nu\sigma}(\omega)] g^{<}_{\alpha k\sigma}(\omega) + G^{<}_{\mu\sigma,\nu\sigma}(\omega)[g^{a}_{\alpha k\sigma}(\omega) - g^{r}_{\alpha k\sigma}(\omega)]\big)\, \varepsilon_{\alpha k\sigma} \; . \tag{6.8b}$$

We now replace the tunneling amplitude by its self-energies Σ_{tun} given by Eq. (5.38) and

$$\Sigma^{<}_{\mu\sigma,\nu\sigma} \approx i\sum_{\alpha}\Gamma_{\alpha;\mu\sigma,\nu\sigma} f_{\alpha}(\omega) \; , \tag{6.9a}$$

$$\Sigma^{>}_{\mu\sigma,\nu\sigma} \approx -i\sum_{\alpha}\Gamma_{\alpha;\mu\sigma,\nu\sigma}[1 - f_{\alpha}(\omega)] \; , \tag{6.9b}$$

as the retarded, less and greater tunnel self-energies. Here, we have included the subindex α in Γ denoting the hybridization function of the reservoir. Hence, following the definitions of App. A we transform Eq. (6.8) into

$$I_{\alpha\sigma} = \frac{e}{h}\int d\omega \text{Tr}\big[(\mathbf{G}^{r}_{\sigma,\sigma} - \mathbf{G}^{a}_{\sigma,\sigma})\mathbf{\Sigma}^{<}_{\text{tun},\alpha\sigma} + \mathbf{G}^{<}_{\sigma,\sigma}(\mathbf{\Sigma}^{a}_{\text{tun},\alpha\sigma} - \mathbf{\Sigma}^{r}_{\text{tun},\alpha\sigma})\big] \; , \tag{6.10a}$$

$$Q_{E,\alpha} = \frac{1}{h}\sum_{\sigma}\int d\omega\omega \text{Tr}\big[(\mathbf{G}^{r}_{\sigma,\sigma} - \mathbf{G}^{a}_{\sigma,\sigma})\mathbf{\Sigma}^{<}_{\text{tun},\alpha\sigma} + \mathbf{G}^{<}_{\sigma,\sigma}(\mathbf{\Sigma}^{a}_{\text{tun},\alpha\sigma} - \mathbf{\Sigma}^{r}_{\text{tun},\alpha\sigma})\big] \; , \tag{6.10b}$$

where $\text{Tr}[\mathbf{AB}] = \sum_{\mu\nu} A_{\mu\nu}B_{\nu\mu}$ denotes the trace in the dot-dot subspace. We would like to emphasize that the self-energies appearing in Eq. (6.10) come from the tunneling Hamiltonian. This will lead to important consequences for the expression of the current, which will be crucial to model Coulomb drag systems (Sec. 8.2). In order to obtain general expressions for the currents, we rewrite them in terms of lesser and greater Green's functions following Eq. (4.25) (also valid for $\mathbf{\Sigma}_{\text{tun},\alpha\sigma}$) [213]:

$$I_{\alpha\sigma} = \frac{e}{h}\int d\omega \text{Tr}\big[\mathbf{G}^{>}_{\sigma,\sigma}\mathbf{\Sigma}^{<}_{\text{tun},\alpha\sigma} - \mathbf{G}^{<}_{\sigma,\sigma}\mathbf{\Sigma}^{>}_{\text{tun},\alpha\sigma}\big] \; , \tag{6.11a}$$

$$Q_{E,\alpha} = \frac{1}{h}\sum_{\sigma}\int d\omega\omega \text{Tr}\big[\mathbf{G}^{>}_{\sigma,\sigma}\mathbf{\Sigma}^{<}_{\text{tun},\alpha\sigma} - \mathbf{G}^{<}_{\sigma,\sigma}\mathbf{\Sigma}^{>}_{\text{tun},\alpha\sigma}\big] \; . \tag{6.11b}$$

We calculate $\mathbf{G}^{<}_{\sigma,\sigma}$ and $\mathbf{G}^{>}_{\sigma,\sigma}$ following Eq. (4.44) neglecting the transient component. Then,

$$I_{\alpha\sigma} = \frac{e}{h}\int d\omega \text{Tr}\big[\mathbf{G}^{r}_{\sigma,\sigma}\mathbf{\Sigma}^{>}_{\text{tot},\sigma}\mathbf{G}^{a}_{\sigma,\sigma}\mathbf{\Sigma}^{<}_{\text{tun},\alpha\sigma} - \mathbf{G}^{r}_{\sigma,\sigma}\mathbf{\Sigma}^{<}_{\text{tot},\sigma}\mathbf{G}^{a}_{\sigma,\sigma}\mathbf{\Sigma}^{>}_{\text{tun},\alpha\sigma}\big] \; , \tag{6.12a}$$

$$Q_{E,\alpha} = \frac{1}{h}\sum_{\sigma}\int d\omega\omega \text{Tr}\big[\mathbf{G}^{r}_{\sigma,\sigma}\mathbf{\Sigma}^{>}_{\text{tot},\sigma}\mathbf{G}^{a}_{\sigma,\sigma}\mathbf{\Sigma}^{<}_{\text{tun},\alpha\sigma} - \mathbf{G}^{r}_{\sigma,\sigma}\mathbf{\Sigma}^{<}_{\text{tot},\sigma}\mathbf{G}^{a}_{\sigma,\sigma}\mathbf{\Sigma}^{>}_{\text{tun},\alpha\sigma}\big] \; , \tag{6.12b}$$

where $\mathbf{\Sigma}^<_{\mathrm{tot},\sigma}$ is the lesser self-energy which accounts for every perturbation of the Anderson Hamiltonian, i. e., tunneling, $\mathbf{\Sigma}^<_{\mathrm{tun},\sigma}$, and electron-electron interactions inside the QD system, $\mathbf{\Sigma}^<_{\mathrm{int},\sigma}$. Each self-energy should be computed by evaluating all possible Feynman diagrams. In the case of a noninteracting single level, this can be exactly solved [213]. However, in the case of interactions, we still approximate $\mathbf{\Sigma}^<_{\mathrm{tot},\sigma}$ with Eq. (6.9) but considering the interactions inside the Green's functions as computed in Sec. 5.2. Therefore, we neglect the contribution of interactions in $\mathbf{\Sigma}^<$ in the reminder of this thesis because they are of a higher order than $\mathbf{\Sigma}^<_{\mathrm{tun},\sigma}$ [213, 231]. An exception will be treated in Sec. 8.2 owing to the fact that the drag system is at equilibrium giving zero net current if we only consider the tunneling contribution.

Hence, applying $\mathbf{\Sigma}^{<,>}_\sigma \equiv \mathbf{\Sigma}^{<,>}_{\mathrm{tot},\sigma} \approx \mathbf{\Sigma}^{<,>}_{\mathrm{tun},\sigma}$ and Eqs. (6.9), we find

$$I_{\alpha\sigma} = \frac{e}{h}\sum_\beta \int d\omega [f_\alpha(\omega) - f_\beta(\omega)] \mathrm{Tr}\left[\mathbf{G}^r_{\sigma,\sigma}\mathbf{\Gamma}_{\beta\sigma}\mathbf{G}^a_{\sigma,\sigma}\mathbf{\Gamma}_{\alpha\sigma}\right], \tag{6.13a}$$

$$Q_{E,\alpha} = \frac{1}{h}\sum_{\beta\sigma} \int d\omega\omega [f_\alpha(\omega) - f_\beta(\omega)] \mathrm{Tr}\left[\mathbf{G}^r_{\sigma,\sigma}\mathbf{\Gamma}_{\beta\sigma}\mathbf{G}^a_{\sigma,\sigma}\mathbf{\Gamma}_{\alpha\sigma}\right]. \tag{6.13b}$$

This is a general expression which can be found in Meir and Wingreen [231]. They identify Eq. (6.13) as the current in the noninteracting case. This statement means that the interacting self-energy is neglected as we explained above. Another important feature of Eq. (6.13) is the dependence on the difference between the Fermi distributions of the reservoirs. This is a nice property that leads to a carrier flow only when there exists a bias between reservoirs (θ or V).

Now, we restrict ourselves to the single QD configuration. The matrices of Eq. (6.13) will become scalar functions which, after some algebra, yield the currents

$$I_{\alpha\sigma} = -\frac{2e}{h}\sum_\beta \int d\omega [f_\alpha(\omega) - f_\beta(\omega)] \frac{\Gamma_{\alpha\sigma}\Gamma_{\beta\sigma}}{\Gamma_\sigma} \mathrm{Im}\left[G^r_{\sigma,\sigma}\right], \tag{6.14a}$$

$$Q_{E,\alpha} = -\frac{2}{h}\sum_{\beta\sigma} \int d\omega\omega [f_\alpha(\omega) - f_\beta(\omega)] \frac{\Gamma_{\alpha\sigma}\Gamma_{\beta\sigma}}{\Gamma_\sigma} \mathrm{Im}\left[G^r_{\sigma,\sigma}\right], \tag{6.14b}$$

where $\Gamma_\sigma = \sum_\lambda \Gamma_{\lambda\sigma}$. Eqs. (6.14) directly depend on the local DOS of the QD [Eq. (4.27)]. This property is lost for multiple QD systems.

6.1.1 The transmission function

In comparison with the Landauer formalism, Eqs. (6.13) and (6.14) suggest that the currents depend on a transmission function

$$\mathcal{T}_{\alpha\sigma,\beta\sigma}(\omega) = \mathrm{Tr}\left[\mathbf{G}^r_{\sigma,\sigma}\mathbf{\Gamma}_{\beta\sigma}\mathbf{G}^a_{\sigma,\sigma}\mathbf{\Gamma}_{\alpha\sigma}\right], \tag{6.15}$$

which allows us to rewrite the electric I and heat current Q as

$$I_{\alpha\sigma} = \frac{e}{h}\sum_{\beta}\int d\omega[f_\alpha(\omega) - f_\beta(\omega)]\mathcal{T}_{\alpha\sigma,\beta\sigma}(\omega)\ , \tag{6.16}$$

$$Q_\alpha = \frac{1}{h}\sum_{\beta\sigma}\int d\omega[f_\alpha(\omega) - f_\beta(\omega)](\omega - \mu_\alpha)\mathcal{T}_{\alpha\sigma,\beta\sigma}(\omega)\ . \tag{6.17}$$

Eqs. (6.16) and (6.17) are of the Landauer type since the transmission $\mathcal{T}$ ranges between 0 and 1 for each transport channel. In any case, the Fermi distribution functions inside Eqs. (6.13) are known [the reservoirs are considered to be in local equilibrium following Eq. (5.1)] and, consequently, the transmission becomes a very interesting function since it offers relevant information about the transport along the systems we consider. For instance, in the single QD case we observe that the transmission is proportional to the local DOS. Therefore, one may infer the spectroscopic properties of the QD by analyzing the electric current.

6.1.2 Conductances

This section discusses the relevant properties of the conductances obtained from Eqs. (6.16) and (6.17) and their connection with the transmission. Here, we consider the two-terminal configuration characterized by $V_L = -V_R = V/2$ and $T_L = T + \theta$, $T_R = T$ for $\theta > 0$ (we set the Fermi energy $\varepsilon_F = 0$). Therefore, the total currents read

$$I = \frac{2e}{h}\int d\omega\,[f_L(\omega) - f_R(\omega)]\,\mathcal{T}(\omega, V, \theta)\ , \tag{6.18}$$

$$Q = \frac{2}{h}\int d\omega\,[f_L(\omega) - f_R(\omega)]\,(\omega - V/2)\mathcal{T}(\omega, V, \theta)\ , \tag{6.19}$$

where $\mathcal{T}(\omega, V, \theta)$ is the spin-independent transmission $\mathcal{T}_{L\sigma,R\sigma}$ in the two-terminal configuration. Notice that now the transmission depends on the external biases since Eq. (6.15) is a function of the dot NEGFs, which are also bias-dependent. Now, we follow Eq. (3.17) in order to find the differential conductances

$$\mathcal{G} = \frac{2e}{h}\int d\omega\left(-\frac{e}{2}\frac{\partial}{\partial\omega}[f_L + f_R]\mathcal{T} + [f_L - f_R]\frac{\partial\mathcal{T}}{\partial V}\right)\ , \tag{6.20a}$$

$$\mathcal{L} = \frac{2e}{h}\int d\omega\left(\frac{\omega - V/2}{T_L}\left[-\frac{\partial f_L}{\partial\omega}\right]\mathcal{T} + [f_L - f_R]\frac{\partial\mathcal{T}}{\partial\theta}\right)\ , \tag{6.20b}$$

$$\mathcal{R} = \frac{2}{h}\sum_{\sigma}\int d\omega\left(-\frac{e}{2}\frac{\partial}{\partial\omega}[f_L + f_R]\tilde{\mathcal{T}} + [f_L - f_R]\frac{\partial\tilde{\mathcal{T}}}{\partial V}\right)\ , \tag{6.20c}$$

$$\mathcal{K} = \frac{2}{h}\sum_{\sigma}\int d\omega\left(\frac{\omega - V/2}{T_L}\left[-\frac{\partial f_L}{\partial\omega}\right]\tilde{\mathcal{T}} + [f_L - f_R]\frac{\partial\tilde{\mathcal{T}}}{\partial\theta}\right)\ , \tag{6.20d}$$

where $\tilde{\mathcal{T}} = (\omega - V/2)\mathcal{T}(\omega, V, \theta)$. We identify two components in all conductances: First, a term which depends on the energy derivatives of the Fermi functions, which yield the linear conductances when applying $V \to 0$ and $\theta \to 0$:

$$\mathcal{G}_0 = \frac{e^2}{h}\int d\omega\left[-\frac{\partial f}{\partial\omega}\right]\mathcal{T}(\omega)\,, \tag{6.21a}$$

$$\mathcal{L}_0 = \frac{e}{h}\int d\omega\left[-\frac{\omega}{T}\frac{\partial f}{\partial\omega}\right]\mathcal{T}(\omega)\,, \tag{6.21b}$$

$$\mathcal{R}_0 = \frac{e}{h}\int d\omega\left[-\omega\frac{\partial f}{\partial\omega}\right]\mathcal{T}(\omega)\,, \tag{6.21c}$$

$$\mathcal{K}_0 = \frac{1}{h}\int d\omega\left[-\frac{\omega^2}{T}\frac{\partial f}{\partial\omega}\right]\mathcal{T}(\omega)\,. \tag{6.21d}$$

The second term corresponds to the nonequilibrium response of the QD system. Notice that for a transmission function independent of V and θ, this second term vanishes with the exception of $\mathcal{R}_\alpha$ due to the Joule term component. This is important because transmissions highly-dependent on V and θ can significantly modify the behavior of the differential conductances yielding nontrivial results.

Another important feature is the symmetry of $\mathcal{T}$. For an even transmission function such that $\mathcal{T}(\omega, V, \theta) = \mathcal{T}(-\omega, V, \theta)$, the first term in $\mathcal{L}$ disappears yielding a thermoelectric conductance highly dependent on the thermal derivative of $\mathcal{T}$ [232]. In fact, the off-diagonal linear conductances nullify in this concrete case and the linear transport is thus governed by $\mathcal{G}_0$ and $\mathcal{K}_0$.

Finally, at $T \to 0$ the linear conductances exhibit simplified relations with the transmission which are helpful to measure the internal properties of QD setups in experiments. Applying the Sommerfeld expansion to Eqs. (6.21) [168, 179], we obtain

$$\mathcal{G}_0 = \frac{e^2}{h}\mathcal{T}(\varepsilon_F)\,, \tag{6.22a}$$

$$\mathcal{L}_0 = \frac{e\pi^2}{3h}k_B^2 T\mathcal{T}'(\varepsilon_F)\,, \tag{6.22b}$$

$$\mathcal{R}_0 = \frac{e\pi^2}{3h}k_B^2 T^2\mathcal{T}'(\varepsilon_F)\,, \tag{6.22c}$$

$$\mathcal{K}_0 = \frac{\pi^2}{3h}k_B^2 T\mathcal{T}(\varepsilon_F)\,. \tag{6.22d}$$

We remind that these expressions are only valid at very low temperatures. Hence, in Eq. (6.22), $\mathcal{G}_0$ and $\mathcal{K}_0$ are proportional to the transmission function evaluated at the Fermi energy ε_F. The prefactors are indeed the electric $\tilde{g}_0 = e^2/h = 77.5\ \mu\mathrm{S}$ and thermal quantum of conductance $\kappa_0 = 3.35\ \mathrm{pW/K}$ [Eq. (3.15)], respectively. On the other hand,

$\mathcal{L}_0$ and $\mathcal{R}_0$ are proportional to $\mathcal{T}'(\varepsilon_F)$ becoming functions sensitive to changes in the transmission. This will be useful for the dectection of narrow resonances [233]. Additionally, one can immediately notice that the WF law is satisfied for Eqs. (6.22).

Such properties will be revisited in the numerical results of Chs. 7 and 8 in which the expressions of the currents and conductances will be used to investigate the quantum transport of QD systems.

6.2 Electrical current in the pertubative approach

When instead of using the Anderson Hamiltonian we employ the Kondo Hamiltonian (Sec. 5.1.3), the expressions of the previous section are not valid and they should be recalculated. Therefore, we start the procedure treating Eqs. (5.27) and (5.29) as perturbations. Here, we extend the procedure given by Kaminski *et al.* [105] to spin-dependent amplitudes and also taking into account the potential scattering term First, we apply the Heisenberg equation [Eq. (4.4)] to find the current of Eq. (6.1) as a function of the exchange parameters of the Kondo Hamiltonian

$$\begin{aligned}\hat{I}_{\alpha\sigma} &= -\frac{ei}{\hbar}\sum_{\beta k_\alpha k_\beta}\left(\bar{\mathcal{K}}_{\beta\sigma,\alpha\sigma}C^\dagger_{\beta k_\beta\sigma}C_{\alpha k_\alpha\sigma} - \text{H.c.}\right)\\ &\quad -\frac{ei}{\hbar}\sum_{\beta k_\alpha k_\beta\sigma_\beta}\left(\mathcal{J}_{\beta\sigma_\beta,\alpha\sigma}\hat{S}_l s^l_{\sigma_\beta\sigma}C^\dagger_{\beta k_\beta\sigma_\beta}C_{\alpha k_\alpha\sigma} - \text{H.c.}\right)\ . \end{aligned} \tag{6.23}$$

In the case of Eq. (5.29) as the perturbation Hamiltonian we find

$$\hat{I}_{\alpha\sigma} = -\frac{ei}{\hbar}\sum_{\beta k_\alpha k_\beta\sigma_\beta}\left(\mathcal{J}_{\beta\sigma_\beta,\alpha\sigma}\tilde{x}_{\sigma_\beta\sigma}C^\dagger_{\beta k_\beta\sigma_\beta}C_{\alpha k_\alpha\sigma} - \text{H.c.}\right)\ , \tag{6.24}$$

where $\tilde{x}_{\sigma_1\sigma_2} = \delta_{\sigma_1\sigma_2}/4 + \hat{S}_l s^l_{\sigma_1\sigma_2}$. These operators are the starting point for acquiring an expression of the electric conductance by expanding their expected values in terms of the perturbation ($\mathcal{H}_{\text{Kon}}$ or $\mathcal{H}_{\text{Kam}}$) in the interaction picture.

Before proceeding with the calculation, we would like to pay attention to the charge conservation law given by Eqs. (6.23) and (6.24). Notice that Eq. (3.19) is not accomplished per spin. The reason is that the Kondo Hamiltonian includes simultaneous spin-flip transitions in the QD meaning that $\langle\dot{S}_z\rangle$, where $\dot{S} = dS/dt$, can not be neglected. Therefore, the conservation law can be now generalized by

$$\sum_\alpha I_{\alpha\sigma} = e\sigma\langle\dot{S}_z\rangle\ , \tag{6.25}$$

where $\sigma = \{1, -1\}$ for $\sigma = \{\uparrow, \downarrow\}$. Therefore, the final expressions obtained in this section must satisfy Eq. (6.25). Nonetheless, if we sum over spins, we recover Eq. (3.19) for the full current $I_\alpha = \sum_\sigma I_{\alpha\sigma}$.

6.2.1 First order

We follow with the perturbation expansion. We evaluate the expected value of the electric current defined as

$$I_{\alpha\sigma} \quad = \quad \langle S(-\infty, 0)\hat{I}_{\alpha\sigma}S(0, -\infty)\rangle \; , \tag{6.26}$$

where $S(t, t')$ is the S-matrix [Eq. (4.10)] in which $\mathcal{W}$ is the Kondo Hamiltonian. For the sake of completeness, we will consider in this section that the Fermi functions will also depend on the spin σ via the electrochemical potential $\mu_{\alpha\sigma} = \varepsilon_F + eV_{\alpha\sigma}$ yielding $f_\alpha(\omega) \to f_{\alpha\sigma}(\omega)$. This will be relevant for the Coulomb drag system of Sec. 8.2. Additionally, we will employ a simplified expression when we move to the s-d Hamiltonian of Eq. (5.29). Particularly, we will consider $\mathcal{J}_{\alpha\sigma_\alpha,\beta\sigma_\beta} \to \mathcal{J}_{\alpha\beta}$ and we will calculate the total current $I_\alpha = \sum_\sigma I_{\alpha\sigma}$.

Now, we evaluate the first nonzero term in the current by expanding the S-matrix up to the first order

$$S(t, t') \quad \approx \quad 1 - \frac{i}{\hbar}\int_t^{t'} \mathcal{H}_{\text{Kon}}(t_1)dt_1 \; . \tag{6.27}$$

Following the straightforward calculation of App. D, the current reads

$$\begin{aligned} I_{\alpha\sigma} \quad = \quad & \frac{2\pi e}{\hbar}\sum_\beta \int d\omega \rho_{\alpha\sigma}\rho_{\beta\sigma}\left|\bar{\mathcal{K}}_{\beta\sigma,\alpha\sigma}\right|^2 [f_{\alpha\sigma}(\omega) - f_{\beta\sigma}(\omega)] \\ & + \frac{\pi e}{4\hbar}\sum_\beta \int d\omega \rho_{\alpha\sigma}\rho_{\beta\bar{\sigma}}\left|\mathcal{J}_{\alpha\sigma,\beta\bar{\sigma}}\right|^2 [f_{\alpha\sigma}(\omega) - f_{\beta\bar{\sigma}}(\omega)] \\ & \frac{\pi e}{8\hbar}\sum_\beta \int d\omega \rho_{\alpha\sigma}\rho_{\beta\sigma}\left|\mathcal{J}_{\alpha\sigma,\beta\sigma}\right|^2 [f_{\alpha\sigma}(\omega) - f_{\beta\sigma}(\omega)] \; . \end{aligned} \tag{6.28}$$

We identify three different components in Eq. (6.28): The transport induced by the potential scattering term when an external bias is applied between leads (first line), the transport induced by spin-flip processes (second line) and a spin-conserved charge flow (third line).

It will be useful to consider the particle-hole symmetry point ($\varepsilon_d = -U/2$). After replacing the spin-coupling terms with their definitions in Eqs. (5.21) and (5.28), the electric current becomes

$$\begin{aligned} I_{\alpha\sigma} \quad = \quad & \frac{e}{2h}\sum_\beta \int_{-D}^{D} d\omega \Gamma_{\alpha\sigma}\Gamma_{\beta\bar{\sigma}}\left|-\frac{1}{\omega - U/2} + \frac{1}{\omega + U/2}\right|^2 [f_{\alpha\sigma}(\omega) - f_{\beta\bar{\sigma}}(\omega)] \\ & + \frac{e}{2h}\sum_\beta \int_{-D}^{D} d\omega \Gamma_{\alpha\sigma}\Gamma_{\beta\sigma}\left[\left|\frac{1}{\omega - U/2}\right|^2 + \left|\frac{1}{\omega + U/2}\right|^2\right] \\ & \times [f_{\alpha\sigma}(\omega) - f_{\beta\sigma}(\omega)] \; , \end{aligned} \tag{6.29}$$

which is valid for $U \gg V, D$, in which case the divergences in the integral are avoided. Eq. (6.29) agrees with the results obtained using a master equation approach. We recall that Eq. (6.29) is still not valid in the deep Kondo regime since it does not carry the logarithmic divergences characteristic from the Kondo effect. Nevertheless, it correctly estimates the first order cotunnel transitions of the system. Such situation will be investigated in the Coulomb drag system in Sec. 8.2.

Now, we transform Eq. (6.28) considering the Hamiltonian of Eq. (5.29)

$$I_{\alpha\sigma} = \frac{\pi e}{2\hbar} \sum_{\beta} \rho_\alpha \rho_\beta \left|\mathcal{J}_{\alpha\beta}\right|^2 \int d\omega [f_\alpha(\omega) - f_\beta(\omega)] \, . \tag{6.30}$$

Here, we have assumed energy-independent DOS at the leads and $\varepsilon_d + U, \varepsilon_d \gg D$ such that

$$\mathcal{J}_{\alpha\beta} \approx -\frac{2\mathcal{V}_\alpha \mathcal{V}_\beta U}{\varepsilon_d(\varepsilon_d + U)} \, , \tag{6.31}$$

where we have neglected the dependence in k. For $T = 0$ and a two-terminal configuration with $\rho_L = \rho_R = \rho$, the total current reads

$$I_\alpha = \frac{\pi e^2}{2\hbar} \rho^2 \left|\mathcal{J}_{LR}\right|^2 V \, . \tag{6.32}$$

Eq. (6.32) describes the regular cotunneling (order Γ^2) of an artificial impurity which will be necessary to obtain a formula for the effective Kondo temperature in Sec. 7.3.1.

6.2.2 Second order

In order to recover the logarithmic divergences of the Kondo resonance, we calculate the next order in the perturbation expansion. Therefore, the S-matrix is expanded to second order

$$S(t,t') \approx 1 - \frac{i}{\hbar} \int_t^{t'} \mathcal{H}_{\text{Kon}}(t_1) dt_1 + \left(\frac{i}{\hbar}\right)^2 \int_t^{t'} \hat{\tilde{T}} \mathcal{H}_{\text{Kon}}(t_1) \mathcal{H}_{\text{Kon}}(t_2) dt_1 dt_2 \, . \tag{6.33}$$

We perform the calculation described in App. D which is also explained in [233]

$$I_\alpha^{(3)} = -\frac{3e\pi^3}{4\hbar^2} \rho^3 \left|\mathcal{J}_{LR}\right|^2 (\mathcal{J}_{LL} + \mathcal{J}_{RR}) \int_{-\infty}^{0} dt \frac{k_B^2 T_L T_R \sin(eVt/\hbar)}{\sinh \frac{k_B T_L \pi t}{\hbar} \sinh \frac{k_B T_R \pi t}{\hbar}} \, . \tag{6.34}$$

Eq. (6.34) represents exchange cotunneling which leads to the Kondo logarithmic divergences. In contrast with Kaminski *et al.* [105], we have distinguished when the reservoirs are held with different temperatures. Therefore, Eq. (6.34) is subject to simultaneous voltage and thermal biases.

6.2.3 Electrical conductance

Finally, we combine Eqs. (6.32) and (6.34) to write the differential conductance at $V = 0$.

$$\begin{aligned}\mathcal{G}(V=0,T_L,T_R) &= \frac{\pi e^2}{2\hbar}\rho^2\left|\mathcal{J}_{LR}\right|^2 - \frac{3e^2\pi^3}{4\hbar^3}\rho^3\left|\mathcal{J}_{LR}\right|^2\left(\mathcal{J}_{LL}+\mathcal{J}_{RR}\right)\\ &\times\int_{-\tau_0}^{0} dt\frac{k_B^2 T_L T_R t}{\sinh\frac{k_B T_L \pi t}{\hbar}\sinh\frac{k_B T_R \pi t}{\hbar} + D_0^2}\,, \qquad (6.35)\end{aligned}$$

where, in order to avoid divergences, we have included an energy bandwidth $D_0 = \sqrt{-\varepsilon_d(U+\varepsilon_d)}$ at the denominator of the integral and we have replaced the lower limit of integration to $\tau_0 = \hbar/\sqrt{k_B^2 T_L T_R}$. The solution, assuming $t/\hbar \ll k_B T$, is

$$\begin{aligned}\mathcal{G} &= \frac{3e^2\pi}{4\hbar}\rho^2\left|\mathcal{J}_{LR}\right|^2\left(1-\frac{\rho}{2}\left(\mathcal{J}_{LL}+\mathcal{J}_{RR}\right)\ln\left|\frac{k_B^2 T_L T_R}{D_0^2}\right|\right)\\ &+\frac{e^2\pi}{4\hbar}\rho^2\left|\mathcal{J}_{LR}\right|^2\,. \qquad (6.36)\end{aligned}$$

This formula gives the height of the ZBA due to the Kondo correlations and will be relevant for the description of the effective Kondo temperature under thermal differences in Sec. 7.3.1.

III

Results and discussion

7. Single Dot structures

We have introduced so far all the necessary concepts and performed the theoretical calculations in order to obtain and understand the results of this thesis. Now we begin the discussion of our results with the simplest configuration: a QD with a single level ε_d attached to two reservoirs $\alpha = \{L, R\}$ as sketched in Fig. 3.1. As explained in Sec. 3.1, we consider that each reservoir is characterized by an electrochemical potential $\mu_\alpha = \varepsilon_F + eV_\alpha$, where the Fermi level is set as the energy origin $\varepsilon_F = 0$. The voltage is applied symmetrically $V_L = -V_R = V/2$ and the reservoir temperature is given by $T_\alpha = T + \theta_\alpha$ where $\theta = \theta_L - \theta_R$ denotes the thermal bias of the system taking into account that for $\theta > 0$, $\theta_R = 0$ and for $\theta < 0$, $\theta_L = 0$.

This chapter analyzes the results for a single QD setup as reported in Refs. [202, 233, 234, 235, 236]. We will consider different regimes such as the CB or the Kondo regime. Particularly, we study the quantum transport across a Coulomb-blockaded QD in Sec. 7.1 finding a nonlinear response for both voltage and thermal biases. Later, we analyze theoretically the thermal effects of a molecular junction, which can also be modelled as a single energy level plus interaction, and we fit our results to the measured current across a Ferrocene molecule. Finally, we compare our results with a noninteracting model and propose a method to distinguish between both cases (interacting and noninteracting). In Sec. 7.3 we discuss the internal characteristics of an artificial Kondo impurity due to voltage and thermal biases, but focusing on the latter. We show results obtained using three different approaches which cover different temperature regimes. Additionally, we also analyze the intriguing behavior of the emergence of several nontrivial zeros in the thermocurrent associated to the Kondo resonance and the single-particle peaks in the transmission.

7.1 Coulomb blockade

First, we consider the CB regime of a single QD. This regime is characterized with large temperatures which allows us to neglect Kondo correlations ($T \gg T_K$), but smaller than Coulomb repulsion $U \gg k_B T, \Gamma$. The system is described by the Anderson Hamiltonian of Eq. (5.2) in which Eq. (5.6) represents the single-level QD. The retarded Green's function which satisfies this regime of energies is expressed in Eq. (5.56) :

$$G^{r}_{\sigma,\sigma} = \frac{1-\bar{n}_{\bar{\sigma}}}{\omega - \varepsilon_d - \Sigma^{r}_{\sigma,\sigma}} + \frac{\bar{n}_{\bar{\sigma}}}{\omega - \varepsilon_d - U - \Sigma^{r}_{\sigma,\sigma}} \, . \tag{5.56}$$

In this case, the local DOS exhibits two resonances centered at $\omega = \varepsilon_d$ and $\omega = \varepsilon_d + U$ weighted by the mean occupation $\bar{n}_\sigma$. With the goal of solving the self-consistent calculation, we manipulate Eq. (4.26) using Eq. (4.44) obtaining

$$\bar{n}_\sigma = \frac{1}{2\pi i}\int d\omega \mathcal{F}_\sigma(\omega)\rho_{d\sigma}(\omega) \, , \tag{7.1}$$

where $\mathcal{F}_\sigma(\omega)$ is the effective distribution function written in Eq. (5.67) in which $\Gamma_\alpha \to \Gamma_{\alpha\sigma}$ is the spin-dependent broadening. Additionally, the term $\rho_{d\sigma}(\omega)$ is the local DOS [Eq. (4.27)]. Eq. (5.56) permits us to avoid the self-consistent calculation separating the integrals transforming Eq. (7.1) into an algebraical equation for the occupation whose solution is

$$\bar{n}_\sigma = \frac{A_{\bar{\sigma}} - A_\sigma(A_{\bar{\sigma}} - B_{\bar{\sigma}})}{1-(A_\sigma - B_\sigma)(A_{\bar{\sigma}} - B_{\bar{\sigma}})} \, , \tag{7.2}$$

where

$$A_\sigma = \frac{1}{2\pi}\int d\omega \frac{\Gamma_\sigma \mathcal{F}_\sigma(\omega)}{(\omega - \varepsilon_{d\sigma})^2 + \Gamma_\sigma^2/4} \, , \tag{7.3a}$$

$$B_\sigma = \frac{1}{2\pi}\int d\omega \frac{\Gamma_\sigma \mathcal{F}_\sigma(\omega)}{(\omega - \varepsilon_{d\sigma} - U)^2 + \Gamma_\sigma^2/4} \, . \tag{7.3b}$$

Furthermore, we can observe that the current [Eq. (6.14)] can be also split in two integrals. Following App. C, $I \equiv \sum_\sigma I_{L\sigma}$ reads

$$I = \frac{2e}{h}\frac{\Gamma_L\Gamma_R}{\Gamma}\left[C_1(1-\bar{n})\right] + C_2\bar{n} \, . \tag{7.4}$$

Here, we have assumed that the QD does not present any Zeeman splitting yielding $\varepsilon_{d\sigma} \to \varepsilon_d$ and the leads are not ferromagnetic $\Gamma_{\alpha\sigma} \to \Gamma_\alpha$. Hence, the occupation becomes spin-independent $\bar{n}_\uparrow = \bar{n}_\downarrow \equiv \bar{n}$. Therefore, the coefficients of Eq. (7.4) read

$$C_1 = \sum_\alpha (1-2\delta_{\alpha R})\mathrm{Im}\left[\psi\left(\frac{1}{2} + \frac{\Gamma}{4\pi k_B T_\alpha} + i\frac{\varepsilon_d - \mu_\alpha}{2\pi k_B T_\alpha}\right)\right] , \tag{7.5a}$$

$$C_2 = \sum_\alpha (1-2\delta_{\alpha R})\mathrm{Im}\left[\psi\left(\frac{1}{2} + \frac{\Gamma}{4\pi k_B T_\alpha} + i\frac{\varepsilon_d + U - \mu_\alpha}{2\pi k_B T_\alpha}\right)\right] . \tag{7.5b}$$

Following Eqs. (7.4), (7.2) and (6.19) we proceed with the numerical results of the transport across the Coulomb-blockaded QD.

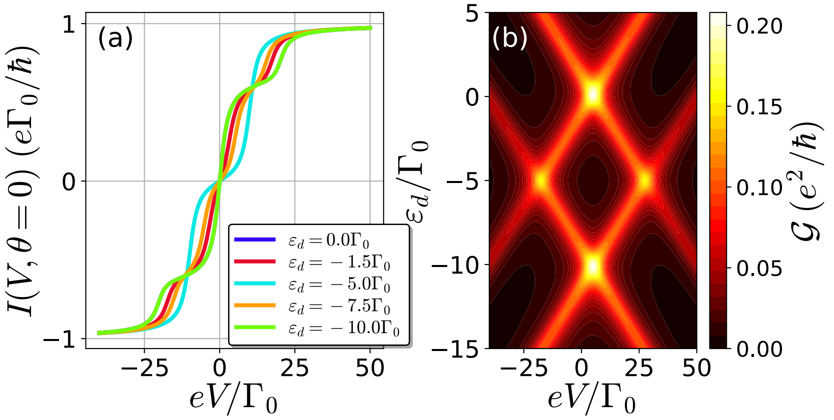

Fig. 7.1. (a) Electric current I vs applied voltage V for a single-level QD with different energies ε_d and a charging energy $U = 10\Gamma_0$. $\varepsilon_d = 0$ and $\varepsilon_d = -10.0\Gamma_0$ curves are overlapped. (b) Differential electrical conductance $\mathcal{G}$ as a function of the voltage bias V and the level position ε_d. Parameters: the background temperature is set at $k_B T = 0.1\Gamma_0$ and $\Gamma_0 \equiv \Gamma_L = \Gamma_R = \Gamma/2$.

7.1.1 Electric and thermoelectric transport

First, we analyze the electric current I due to a voltage bias V or a temperature bias θ. The results of this section corresponds to Sierra and Sanchez [202]. Although the paper is not part of this thesis, we summarize it in order to give a complete picture of the system.

Fig. 7.1a shows the $I-V$ characteristic curves for different level positions ε_d of the QD. In the linear regime $V \to 0$, we find an ohmic behavior $I \approx \mathcal{G}_0 V$, as expected. The maximum values of $\mathcal{G}_0$ correspond to the cases when the single-particle peaks are at resonance with the Fermi energy ($\varepsilon_d = 0$ or $\varepsilon_d + U = 0$). At higher voltages, the current reaches a plateau and increases again when the electrochemical potential realigns with the single-particle resonances [$V = 2\varepsilon_d$ and $V = 2(\varepsilon_d + U)$]. For this reason, in the particle-hole symmetry point $\varepsilon_d = -U/2$ we do not find a second plateau at higher voltages. Finally, at large voltages, the current saturates.

As expected, we observe a diamond structure in the differential conductance $\mathcal{G}$ in Fig. 7.1b. This result is in agreement with the phenomenological CB models of Meir *et al.* [14] and Beenakker [13]. Additionally, we want to emphasize that $\mathcal{G}$ in Fig. 7.1 is a symmetric function with respect to $V = 0$ since we are considering equal hybridization constants $\Gamma_L = \Gamma_R = \Gamma_0$. As a consequence, the current is antisymmetric as seen in Fig. 7.1a. However, we have checked that this symmetry is lost when $\Gamma_L \neq \Gamma_R$. Only when $\varepsilon_d = -U/2$ the symmetry persists because the DOS respects particle-hole symmetry.

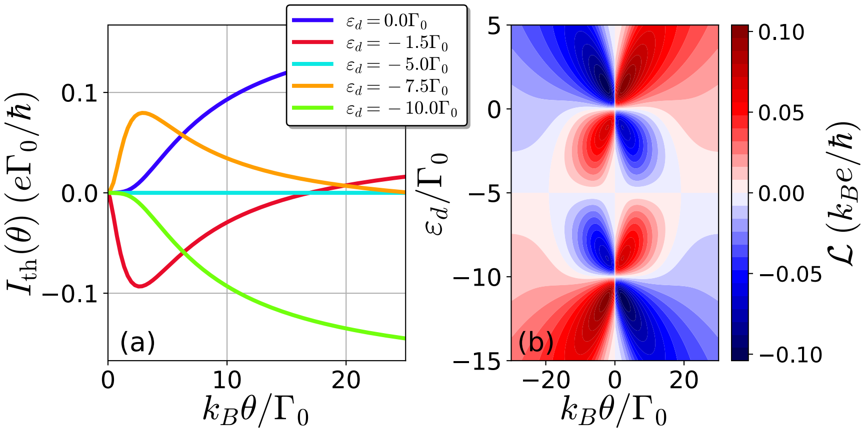

Fig. 7.2. (a) Thermoelectric current I_{th} vs thermal bias θ for a single-level QD with different energies ε_d and a charging energy $U = 10\Gamma_0$. (b) Differential thermoelectrical conductance $\mathcal{L}$ as a function of the temperature bias θ and the level position ε_d. Parameters: the background temperature is set at $k_B T = 0.1\Gamma_0$ and $\Gamma_0 \equiv \Gamma_L = \Gamma_R = \Gamma/2$.

On the other hand, the electrical response of the QD due to thermal biases (Fig. 7.2) shows different features than the voltage bias case of Fig. 7.1. For instance, we observe in Fig. 7.2a that the thermocurrent does not exhibit Coulomb staircases. For $\varepsilon_d = -U/2$, I_{th} is exactly zero since the transmission function is symmetric around ε_F yielding equal electron and hole fluxes nullifying the charge transport. When the system is at resonance ($\varepsilon_d = 0$ and $\varepsilon_d = -10\Gamma$ in Fig. 7.2a), transport is dominated by carriers crossing the non-resonant peak ($I_{\mathrm{th}} > 0$ for $\varepsilon_d = 0$ and $I_{\mathrm{th}} < 0$ for $\varepsilon_d = -U$). For single-level energies $\varepsilon_d \in (\varepsilon_F - U, \varepsilon_F)$ the system responds in a counter-intuitive way yielding dramatic changes at large θ. For instance, for $\varepsilon_d = -3U/4$, at low thermal bias the thermocurrent increases quite rapidly. However, further increasing of θ gives rise to a maximum followed by a decrease of the thermocurrent which, at some point, crosses the θ axis. In other words, the electronic flow has reversed its sign by only heating one reservoir. Hence, we are dealing with a purely nonlinear property of thermoelectric transport which is in agreement with recent experiments [201, 205].

In Fig. 7.2b we depict the differential thermoelectric conductance $\mathcal{L}$, which, for a sign convention, is now defined as $\mathcal{L} = dI/d|\theta|$. We observe a butterfly structure with changes of sign across the resonance points at $\varepsilon_d = 0$ and $\varepsilon_d = -U$ instead of the Coulomb diamonds of Fig. 7.1b. Nevertheless, the butterfly structure in $\mathcal{L}$ is not a general pattern since it gets deformed when including additional QDs as will be explained in Ch. 8. As expected, $\mathcal{L} = 0$ for the particle-hole symmetry point $\varepsilon_d = -U/2$. Outside this symmetry, $\mathcal{L}$ is positive (negative) because electrons (holes)

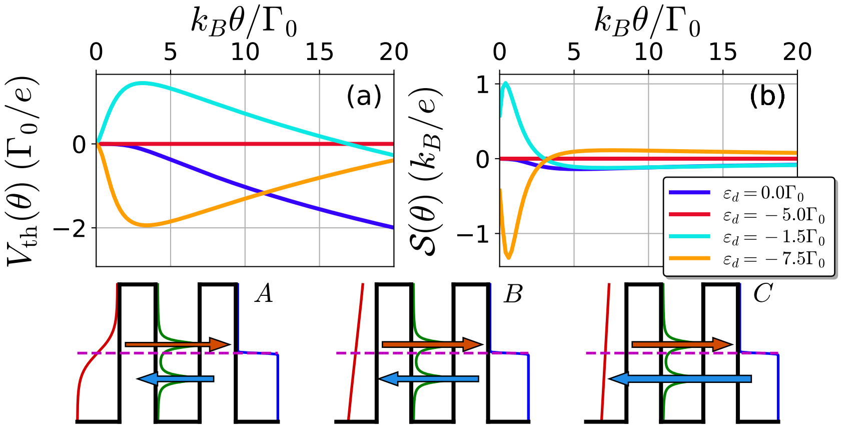

Fig. 7.3. (a) Thermovoltage $V_{\rm th}$ vs thermal bias V for a QD with a single level ε_d and a charging energy $U = 10\Gamma_0$. (b) Differential thermopower $\mathcal{S}$ as a function of the temperature bias θ. The sketches A, B and C denote the energy diagrams describing the electric transport across a QD system with $\varepsilon_d = -3U/4$ at a thermal bias of $k_B\theta = 3\Gamma_0$, $25\Gamma_0$ and $50\Gamma_0$, respectively. Parameters: the background temperature is set at $k_BT = 0.1\Gamma_0$ and $\Gamma_0 \equiv \Gamma_L = \Gamma_R = \Gamma/2$.

dominate the transport depending on the regime of θ and the position of ε_d.

The nonlinear behavior of $I_{\rm th}$ and $\mathcal{L}$ can be easily understood with the energy diagrams of the A, B and C panels of Fig. 7.3. These diagrams represent the energy distribution of particles in the system in which the left reservoir (left red curve) is heated at different temperatures $T_L = T + \theta$ whereas the right reservoir (right blue reservoir) remains cold at the background temperature T. The level position of the QD is located at $\varepsilon_d = -3U/4$ (orange curve in Fig. 7.2a) and the charging energy is set at $U = 10\Gamma_0$. Therefore, we observe that the lower-energy resonance is located below the Fermi energy ($\omega = -3U/4$) while the second resonance is above ($\omega = U/4$). At $k_B\theta = 3\Gamma_0$ (panel A in Fig. 7.3), the Fermi distribution function of the left reservoir is a smoothed step function allowing transport for carriers with energies around the Fermi energy. In this case, the closest resonance of the local DOS to the Fermi energy ($\omega = U/4$) determines the transport, which is now dominated by electrons. Increasing θ the left Fermi function becomes flat in such a way that the second resonance starts to contribute to the transport allowing a hole flow which exactly counterbalances the electron flux at $k_B\theta = 25\Gamma_0$ (panel B) and gives rise to a nontrivial zero for the current. Further increasing of θ favors the hole flux and $I_{\rm th}$ becomes negative as sketched in panel C for $k_B\theta = 50\Gamma_0$.

Another interesting thermoelectric magnitude is the thermovoltage,

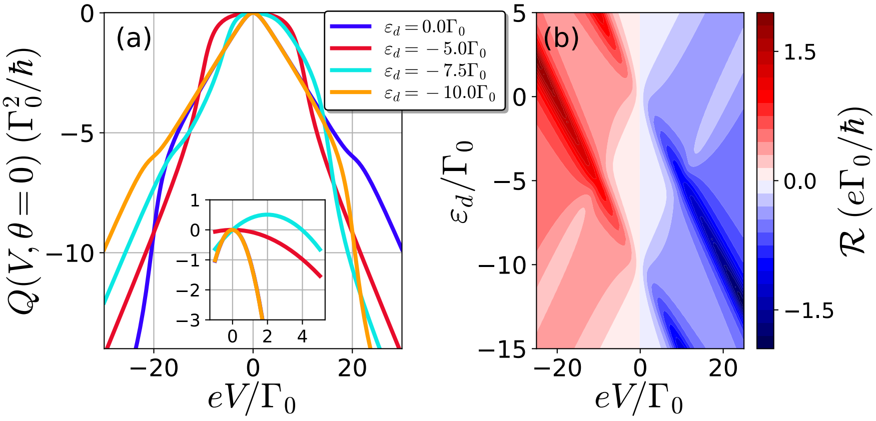

Fig. 7.4. (a) Heat current Q as a function of the applied voltage V of a QD with a single level located at different energies ε_d. Inset: Detail of the heat current showing the Peltier effect at low V. For clarity, we scale the heat current with a factor 10^{-5} and the applied voltage with 10^{-2}. (b) Differential electrothermal conductance $\mathcal{R}$ versus the applied voltage V and the single-level energy ε_d. Parameters: the background temperature is set at $k_B T = 0.1\Gamma_0$, $U = 10\Gamma_0$ and $\Gamma_0 \equiv \Gamma_L = \Gamma_R = \Gamma/2$.

which is determined at open circuit conditions $I(V_{\rm th}, \theta) = 0$ as defined in Ch. 3. We depict the numerical results for $V_{\rm th}$ in Fig. 7.3a and the differential thermopower $\mathcal{S}$ in Fig. 7.3b. At low thermal bias θ, the thermovoltage displays a linear behavior which results in a constant thermopower. However, at larger temperature differences the thermovoltage becomes nonlinear and nontrivial zeros $V_{\rm th}(\theta \neq 0) = 0$ also appear for $\varepsilon_d \in (\varepsilon_F - U, \varepsilon_F)$. Therefore, one can easily observe a nice correlation with the thermocurrent (Fig. 7.2a) because for the thermocurrent to vanish a voltage which favors the flow of carriers in the opposite direction is needed. In the limit of large θ, the Seebeck becomes constant yielding a linear $V_{\rm th}$.

7.1.2 Heat conduction and Peltier effect

Once we have studied the electric current, we also investigate the heat transport due to applied voltage and thermal differences [234]. Now we follow Eq. (6.19) in order to find the numerical results for the heat flux.

The response of the heat current Q due to a voltage bias is depicted in Fig. 7.4 for several values of ε_d. Quite generally, Q exhibits a linear behavior at low bias V characteristic from the Peltier effect. This coincides with the Seebeck effect of Fig. 7.3b due to the Onsager reciprocity relation as explained in Sec. 3.1.1. Note that the Peltier effect does not appear when the QD levels are at resonance with the Fermi energy ($\varepsilon_d = 0$ or $\varepsilon_d = -10\Gamma_0$ in Fig. 7.4a) and in the particle-hole symme-

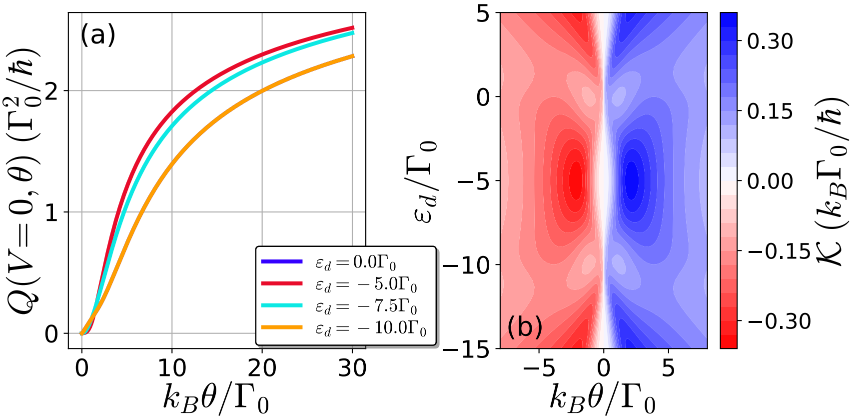

Fig. 7.5. (a) Heat current Q as a function of the thermal bias θ for a QD with a single level located at different energies ε_d. (b) Thermal conductance versus the thermal bias θ and the single-level energy ε_d. Parameters: the background temperature is set at $k_BT = 0.1\Gamma_0$, $U = 10\Gamma_0$ and $\Gamma_0 \equiv \Gamma_L = \Gamma_R = \Gamma/2$.

try point ($\varepsilon_d = -5\Gamma_0$). When voltage increases, the Joule and higher order effects quickly dominate the transport. Therefore, we identify the reversible heat of the Peltier effect at low voltage bias and the irreversible heat due to the Joule term at large voltage bias. Additionally, Q is asymmetric with respect to V except at the particle-hole symmetry point ($\varepsilon_d = -U/2$). This asymmetry appears when, at a given V, the dot resonances align with the electrochemical potentials leading to drastic changes in transport. Besides, we find that Q is invariant under the change $\varepsilon_d \to -\varepsilon_d - U$ and $V \to -V$.

The changes of curvature which are responsible for the asymmetries of Q are related to the maximum and minimum of the differential eletrothermal conductance $\mathcal{R}$ (Fig. 7.4b). In fact, when the QD resonances and the electrochemical potential of the right lead ($\varepsilon_d = -V/2$ and $\varepsilon_d = -V/2 - U$) aligns, $\mathcal{R}$ becomes extremal. This occurs because the energy current at $V < 0$ has the same sign as the dissipation term and therefore, the heat current will be increased when the QD is at resonance. On the other hand, the energy current counteracts the dissipation term when $V > 0$ and the heat current does not decrease rapidly. We observe that there is a sign change of $\mathcal{R}$ which occurs at low values of V, but not exactly at $V = 0$. For instance, the maximum of Q when $\varepsilon_d = -3U/4$ (see inset of Fig. 7.4a) is located at $eV \approx 0.2\Gamma_0$. In addition, we demonstrate that for large voltages the electrothermal conductance follows the electrical current $\mathcal{R}(V \to \infty) = -I/2$. In order to explain this phenomenon, we differentiate Eq. (3.16) :

$$Q = Q_E + IV\,, \tag{3.16}$$

taking into account that the transport flows across the $\alpha = L$ lead:

$$\mathcal{R} = \mathcal{R}_E - \mathcal{G}\frac{V}{2} - \frac{I}{2}\,, \tag{7.6}$$

where $\mathcal{R}_E = dQ_E/dV$. Notice that at high voltages the conductances $\mathcal{R}_E \to 0$ and $\mathcal{G} \to 0$ vanish whereas the electric current reaches a constant value (Fig. 7.1a).

We now show the heat current as a function of temperature differences in Fig. 7.5a. We observe that Q is a monotonic function of θ independently of ε_d. As expected, the linear behavior follows the Fourier's law, but higher-order terms quickly dominate when $\theta > T$. However, when the QD is at resonance the linear response is preserved in a longer θ range. For large θ, the current increases in a logarithmic trend. This is better observed in the thermal conductance $\mathcal{K}$ (Fig. 7.5b) which decays as $\mathcal{K} \to 1/\theta$ at high thermal biases. Additionally, $\mathcal{K}$ is antisymmetric under reversal of θ meaning that the hotter lead determines the direction of the heat flow. When the QD is at resonance, we find that $\mathcal{K}$ reaches two small maxima (for $\theta > 0$) while around the particle-hole symmetry point the thermal conductance presents one high maximum before the power-law decay. Hence, we have numerically tested that the heat transport driven by thermal biases is sensitive to variations of the external gate potential.

Now, we focus our attention on the heat rectification effects presented in Sec. 3.1.3 and the Kelvin-Onsager relation of Eq. (3.6). We first investigate the rectification of Q plotting Δ_C and Δ_E versus V in Fig. 7.6a. Notice that $\Delta_C = \Delta_E$ owing to the form of Eq. (6.19) and the fact that the DOS is symmetric under V reversal. At resonance ($\varepsilon_d = 0$ and $\varepsilon_d + U = 0$), we find that the rectification does not take place until $V \approx U$ and then increases or decreases monotonously. The reason is that $\Delta_{C,E}$ only has the contribution of the energy current due to the fact that the dissipation term IV is symmetrical with respect to V. Consequently, the energy current will flow in the direction determined by the sign of V. In this case, a resonance is located at the Fermi energy. Therefore, $Q(V)$ and $Q(-V)$ will be similar yielding zero rectification. However, at higher voltages the second resonance contributes to the heat transport whose energy position (for instance $\omega = U$ when $\varepsilon_d = 0$) favors the energy transport in a given direction. This picture changes when we deal with levels $\varepsilon_d \in (\varepsilon_F - U, \varepsilon_F)$. We observe that the curves quickly depart from $\Delta_{C,E} \approx 0$ because the energy transport will flow through

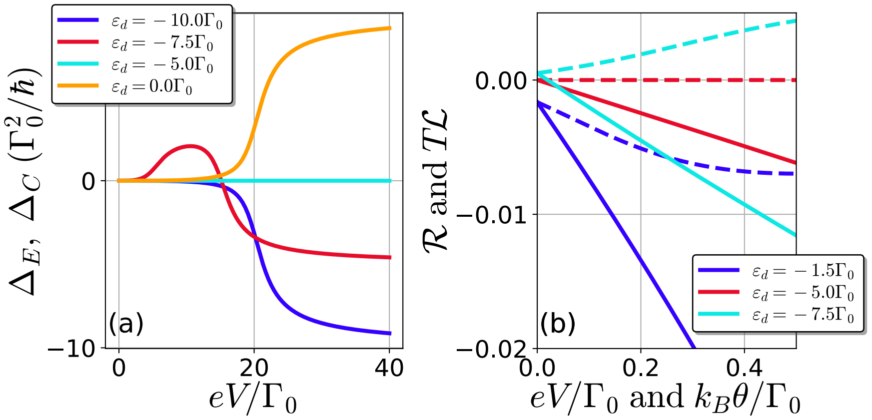

Fig. 7.6. (a) Electric Δ_E and contact Δ_C asymmetries as a function of the voltage bias V of a QD system at energy levels ε_d. Both asymmetries exhibit the same curves such that $\Delta_E = \Delta_C$. (b) Comparison between the differential electrothermal $\mathcal{R}$ (solid curves) and thermoelectric $\mathcal{L}$ (dashed curves) as a function of the voltage V and thermal θ biases, respectively. Departures are observed for values away from the linear regime. Parameters: the background temperature is set at $k_BT = 0.1\Gamma_0$ and $\Gamma_0 \equiv \Gamma_L = \Gamma_R = \Gamma/2$.

the closest resonance to the Fermi energy whose position determines the sign of the rectification ($\Delta_{C,E} > 0$ for $\varepsilon_d = -3U/4$ in Fig. 7.6a because the resonance above ε_F favors energy flow from the left to the right reservoir). When the voltage is increased, the second resonance plays a role and the rectification changes its sign. In contrast, the rectification is absent for $\varepsilon_d = -U/2$ because the DOS is symmetric yielding $Q_E(V) = Q_E(-V)$. Surprisingly, these findings are similar to the ones found in the thermoelectric transport of the QD. Hence, the shape of the transmission function $\mathcal{T}(\omega)$ is a powerful tool which determines both nontrivial thermoelectric transport and heat rectification.

Finally, we briefly discuss the Kelvin-Onsager relation. In Fig. 7.6b we plot $\mathcal{R}(V)$ and $T\mathcal{L}(\theta)$ as a function of the voltage and thermal biases, respectively. At equilibrium, we observe that both functions are equal obeying Eq. (3.6). This was expected because this linear-response property has an universal character. Notwithstanding, the relation is broken when a bias is applied [237]. Therefore, the differential conductances deviate from Kelvin-Onsager relation although it is satisfied in the limit $V \to 0$ and $\theta \to 0$.

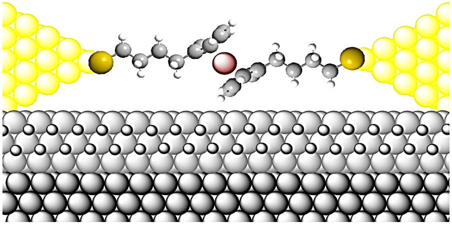

Fig. 7.7. (a) Schematic of the S-$(CH_2)_4$-ferrocenyl-$(CH_2)_4$-S molecular junction system considered in Garrigues *et al.* [41].

7.2 Coulomb blockade in molecular junctions

In Sec. 1.2, we have argued that molecular junctions can be theoretically modelled by a QD system. Therefore, we devote this section to the study of one of these molecules applying the theory of Sec. 7.1 to the experimental results of Garrigues *et al.* [41]. This section focuses on the results obtained in Sierra *et al.* [236] and it is a part of the thesis which extends the theory of the previous section.

7.2.1 The experiment. Thermal effects in Ferrocene.

First, let us summarize the work reported by Garrigues *et al.* [41], which is the starting point of our results. They studied the thermally-dependent charge transport through the molecule S-$(CH_2)_4$-ferrocenyl-$(CH_2)_4$-S (see Fig. 7.7) forming a molecular transistor. Particularly, they measured the electric current across such molecule shifting its levels with a gate (bottom layer in Fig. 7.7) and applying a source-drain voltage bias with two gold contacts (yellow parts). Finally, the data of the experiment was taken at different background temperatures allowing them to study the temperature-dependent behavior.

They found that $\mathcal{G}$ shows a diamond shape (Fig. 7.8a) when plotted as a function of the applied V and gate V_g voltages and, for the $T = 80$ K case, they found that the current showed two peaks when tuning V_g (Fig. 7.8b). Furthermore, they also studied the electric response with increasing temperatures T as shown Fig. 7.8c. They observed that the peaks maxima decrease with T while the valleys increase and at some points the electric current remains approximately constant with T. They compared their measurements with a model based on Eq. (6.18) assuming that the transmission $\mathcal{T}$ is a combination of Breit-Wigner resonances. They found good agreement between the model and the experiment.

We highlight that in the transmission, although there exists good agreement between the model and the experiment, there are some features that may suggest that the system is indeed behaving as an interacting impurity such as the diamond structure of Fig. 7.8a or the double

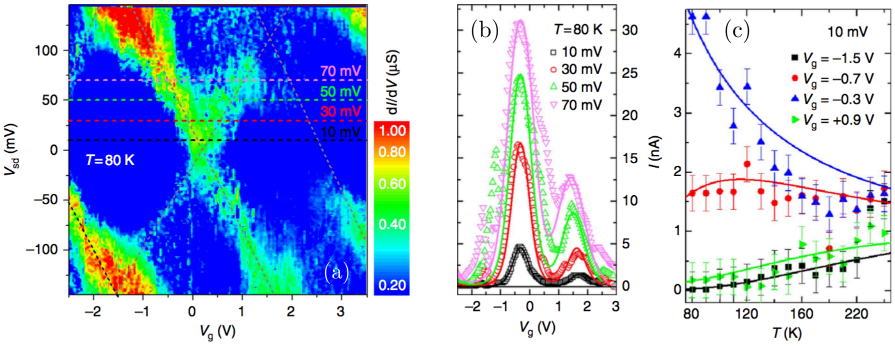

Fig. 7.8. Transport measurements of a Ferrocene molecular junction performed by Garrigues *et al.* [41] (a) Differential conductance as a function of the applied and gate voltages. (b) Electric current as a function of the gate voltage V_g which controls the DOS of the molecule for several source-drain voltages. The points indicate the experimental measurements while the solid line denotes a theoretical model. (c) Electric current versus the background temperature T for the molecular junctions at different gate voltages and a bias voltage of $V = 10$ mV. As in (b), the points denote experimental data whereas the solid lines show the results of a theoretical model.

resonance appearing in the current. Therefore, we begin our work by trying to model the transport through the molecule using the system and the theory discussed in Sec. 7.1.

7.2.2 Interacting model interpretation

We employ again the CB model of Sec. 7.1 and consider Eq. (5.56) as the molecule retarded Green's function. However, the energy level will be now controlled with a gate voltage following Eq. (5.7) which we now quote for clarity

$$\varepsilon_d = \varepsilon_N - \frac{C_L V_L + C_R V_R + C_g V_g}{C} e \,, \tag{5.7}$$

where ε_N and C_α are determined from the experimental measurements (Table 7.1). On the other hand, we slightly modify the broadening function transforming it into

$$\Gamma_\alpha(\omega) = \begin{cases} \gamma_{\alpha 1} & \text{if } \omega < \varepsilon_d + U/2 \\ \gamma_{\alpha 2} & \text{if } \omega > \varepsilon_d + U/2 \end{cases} , \tag{7.7}$$

where j in $\gamma_{\alpha j}$ denotes the hybridization constant around the level resonance ($j = 1$) or the CB resonance ($j = 2$). Therefore, Γ_α is now a step function which takes on a different constant depending on the energy region. In general, the hybridization is a function of energy $\Gamma_\alpha(\omega)$ and, hence, the step function of Eq. (7.7) gives a more appropiate description

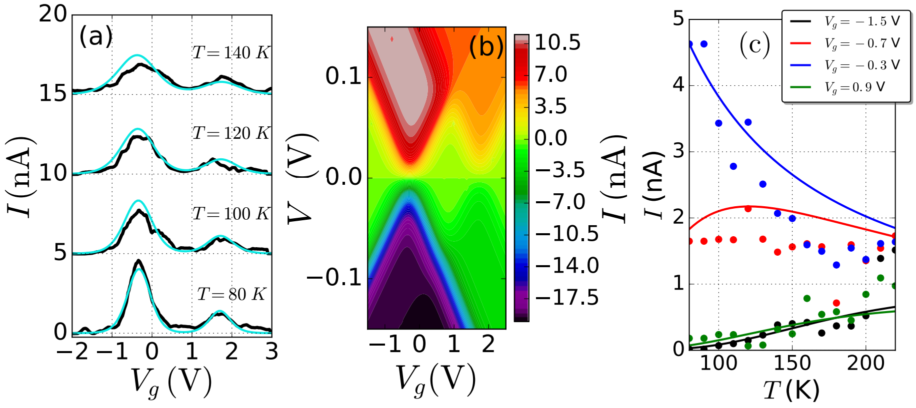

Fig. 7.9. (a) Experimental data of the electric current across a ferrocene-like molecule as a function of the gate voltage and the theoretical curves using the parameters of Table 7.1 for different background temperatures T. The curves at different temperatures are vertically shifted in order to give a clearer view (offset: 5 nA). (b) Electrical current calculated theoretically as a function of the gate and applied voltages for a temperature of $T = 80$ K. The plot clearly shows the Coulomb diamond structure. (c) Electrical current as a function of the temperature T for different gate voltages. The data points show the experimental results given by Garrigues *et al.* [41] while the solid lines denote the theoretical curves of the CB model.

of the tunneling process between the molecule and the reservoirs. In the noninteracting model of Garrigues *et al.* [41], they take $\gamma_{\alpha j}$ as the hybridization constant of the resonance j with energy ε_j. In comparison with our model, the resonances of both theories are located at the same energy positions such that $\varepsilon_1 = \varepsilon_d$ and $\varepsilon_2 = \varepsilon_d + U$. In addition, $\gamma_{\alpha j}$ are fitted with the experimental measurements (see Table 7.1).

U	ε_N	γ_{L1}	γ_{L2}	γ_{R1}
76 meV	27 meV	0.4 meV	0.4 meV	0.05 meV

γ_{R2}	C_g	C_L	C_R	V
0.01 meV	0.525 e/V	5.78 e/V	6.83 e/V	10 mV

Table. 7.1. Parameters of the molecular junction system used in our theoretical model fitting the experimental results of Garrigues *et al.* [41].

In Fig. 7.9a we show the measurements of the electric current for the ferrocene molecule as a function of the gate voltage V_g (black curves). We also include the calculations based on our theoretical model (blue curves). We observe two resonances: one arises when the electrochemical potential of the leads aligns with the level of the molecule $\mu_\alpha = \varepsilon_d$ and the second appears due to charging energy U. This fact suggests that the molecular junction is influenced by Coulomb repulsion in the regime $k_B T < U$. The numerical current as a function of the gate and applied voltages is depicted in Fig. 7.9b. Clearly, the diamond signature of CB is also present. The current is approximately constant inside the diamond meaning that the transport is blockaded. When the energy level ε_d, which is tuned with V_g, aligns with the electrochemical potential of the dot the current increases until it saturates yielding again zero electric conductance $\mathcal{G}$.

The experimental data and theoretical curves of the electric current due to variations of the background temperature is depicted in Fig. 7.9c. We find different behaviors depending on the gate voltage: At the low-energy peak (V_g = -0.3 V in Fig. 7.9c) we observe that the current decreases with T. On the other hand, the electric current is rather insensitive to the background temperature when V_g = -0.7 V, which corresponds when the resonance is at half-maximum. Lastly, we find an enhancement of the current with T around the CB valleys (V_g = -1.5 V and V_g = 0.9 V). Comparing experimental data and theory, we find good agreement in all cases (within the error bars, which are not shown here). However, we would like to point out that at high temperatures our theory breaks down since dephasing and inelastic scattering are expected to occur. On the other hand, the model may also fail at very low temperatures because cotunnel processes may appear yielding, for instance, Kondo correlations when the molecule is strongly hybridized with the electrodes.

7.2.3 Differences between interacting and non-interacting molecular junctions

By taking a quick glance at Figs. 7.8 and 7.9, one identifies two competing models which correctly describe the experimental results. The main difference between these models is the nature behind the appearance of the two resonances. In our theory, the double resonance is due to a splitting of the molecular level due to electron-electron interactions (Fig. 7.10b). In contrast, the noninteracting model attributes the resonances to two different independent molecular levels (Fig. 7.10a). This leads to the following question: How can we distinguish between these two explanations in a real experiment?

We propose the application of an external magnetic field B to the molecules inducing a Zeeman spliting in the levels as a tool to distinguish between both models. In principle, we expect a splitting of the resonance in the noninteracting case (Fig. 7.10a) while in the interacting case the resonances shift in opposite directions (see right panel of Fig 7.10). Let us return to the electrostatic model introduced in Sec. 1.1,

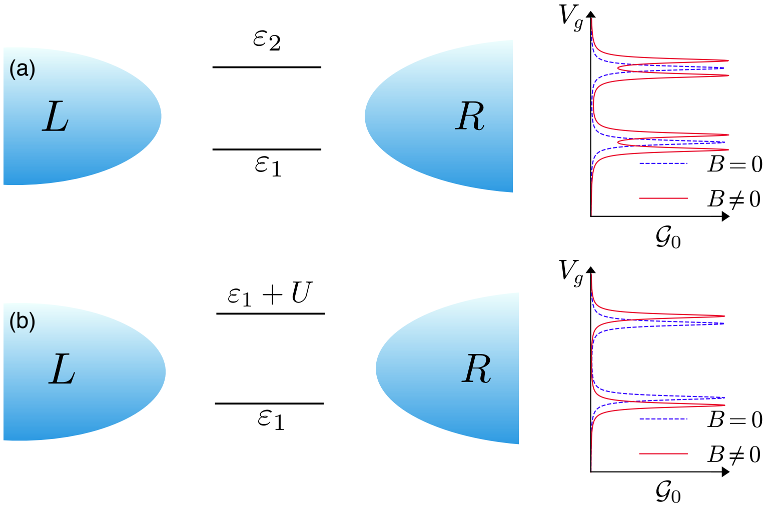

Fig. 7.10. Sketch of the molecular junction showing our proposal to evaluate the relevance of electron-electron interactions in a molecular junction. (a) In the noninteracting case the molecule contains two energy levels ε_1 and ε_2 which lead to two resonances in the electrical conductance $\mathcal{G}_0$ (dashed blue lines). (b) The interacting model consists of a single level ε_d and a charging energy U which also induce two resonances. Importantly, a magnetic field B yields two different responses in $\mathcal{G}_0$ (red solid lines): the noninteracting peaks split at increasing B while the interacting resonances shift. Therefore, this is helpful for characterizing the transport mechanism in molecular junctions.

but now insert the Zeeman term into Eq. (1.6):

$$\mu_d(N) = \varepsilon_N + \frac{(2N-1)e^2}{2C} + \frac{C_L V_L + C_R V_R + C_g V_g}{C} e + \Delta_S \Delta_B \,, \qquad (7.8)$$

where $\Delta_B = g\mu_B B$ is the Zeeman splitting energy and $\Delta_S = S_z^N - S_z^{N-1}$ with S_z^N being the total spin of the molecule. If the spin is augmented after adding an electron to the level ($\Delta_S > 0$), a negative voltage shift is needed for the electrochemical level to remain constant. However, if the spin lowers ($\Delta_S < 0$), the gate voltage must shift to higher values. Therefore, using this argument we are able to discuss the mechanism between two consecutive conductance peaks: We expect an attraction or a repulsion between each other. In fact, the energy separation between two interacting resonances is $U + 2\Delta_B$ and, in contrast, for different energy levels the separation shrinks with $\Delta + U - 2\Delta_B$ where $\Delta = \varepsilon_2 - \varepsilon_1$ is the energy separation between two noninteracting levels at zero magnetic field. In contrast, in the noninteracting model, where each peak corresponds to an energy level, the resonances split symmetrically due to Zeeman splitting generated by the magnetic field .

Now, we show the conductance for both cases illustrating the expla-

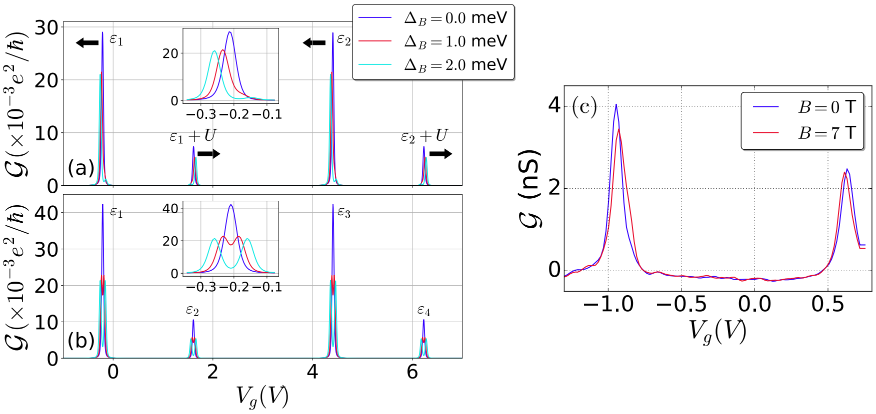

Fig. 7.11. (a) Conductance $\mathcal{G}$ as a function of the gate voltage V_g at a background temperature of $T = 4$ K for different values of the Zeeman splitting Δ_B in the CB model. In this case we consider two molecular levels with a spacing of $\Delta = 140$ meV, each of them is also split due to the Coulomb repulsion. The black arrows at the top of the resonances indicate how the peaks shift when Δ_B is increased. (b) Same as (a) but considering the noninteracting model with four single particle resonances located at the same positions as the resonances of the interacting model. In this case, the resonances split as Δ_B enhances. Insets: Zoom of the conductance peak corresponding to ε_1 for a better visualization of the behavior of the main panel. Parameters taken from Table 7.1.

nation given by the electrostatic model in Fig. 7.11. In this case we consider two different levels ε_μ in the molecule with a charging energy U for the interacting model while in the noninteracting model we consider four single-particle resonances. Since there exists no interlevel transitions, we obtain a diagonal retarded Green's function $G^r_{\mu\sigma,\nu\sigma}$. We include in both models a Zeeman term $\varepsilon_{\mu\sigma} = \varepsilon_\mu + \sigma\Delta_B$ where $\sigma = +\,(-)$ for spins ↑ (↓). Finally, we assume that Γ_α follows Eq. (7.7).

After increasing the magnetic field and, consequently, the Zeeman strength Δ_B we encounter the expected physics. The peak separation for two interacting particles (Fig. 7.11a) expands for ε_j and $\varepsilon_j + U$ and shrinks for $\varepsilon_j + U$ and ε_{j+1}. The reason behind this effect is that the level is already split due to the CB effect and, thus, the resonances only shift in their appropriate direction. On the other hand, the noninteracting model leads to peak splitting for each of the levels ε_j when the magnetic field is increased for $\Delta_B > \Gamma$.

In order to test the previous arguments, we depict the results obtained from an experiment in Fig. 7.11c. Here, a magnetic field is applied to a single-electron molecular junction with a similar Ferrocene molecule at low temperature. In Fig. 7.11c we depict the electrical conductance as a function of the gate voltage for vanishing magnetic field (blue curve) and for $B = 7$ T (red curve). This experiment is performed at $T = 4$ K with a bias voltage of $V = 80$ mV at $B = 0$ T. We observe two peaks at $V_g = -0.95$ V and 0.65 V. Both resonances approach to each other when the magnetic field is applied. One could argue that a drag of the molecule is induced by a magnetic field. This would distort the molecule and the couplings between electrodes and the gate would change. Nonetheless, this effect would also change the transport excitation slopes meaning that a large variation in potential energy is very unlikely. Besides, alterations due to strain in the electrostatic coupling do not take into account the spin value. Therefore, we rule out this explanation.

We return to our previous theoretical predictions. We notice that the peaks in Fig. 7.11c do not split due to the Zeeman effect under the appearance of a magnetic field. This is consistent with the Coulomb blockade behavior appearing at large charging energies U as explained above. We find similar shifts for both peaks: The peak located at $V_g = -0.95$ V is displaced $+18$ mV while the second peak is shifted -19 mV. Accordingly, by applying Eq. (7.8) for the parameters of this experiment we find that the difference in spin is $\Delta_S = -1/2$ for the left peak in Fig. 7.11c and $\Delta_S = +1/2$ for the right peak. This results from the addition of one electron to the molecule. Nevertheless, for this particular case, the distance between peaks shrinks unlike the case of a single Coulomb-blockaded level. The reason is that each level belongs to two different interacting energy levels, whose corresponding levels lie beyond the gate voltage window of this measurement. In other words, Fig 7.11c is equivalent to Fig. 7.11a in a range which only comprises the central resonances. Hence, this experimental observation allows the unequivocal association of the peaks in $\mathcal{G}$ to charging effects in the molecule and confirms that the magnetic field is a powerful tool to determine the nature of the transport conductance peaks in molecular junctions.

7.3 Kondo effect

For the moment, we have investigated the CB properties of single level QD systems or molecular junctions applying the Anderson model. Nevertheless, we have also shown in Ch. 5 that the Anderson Hamiltonian is also able to describe well the physics of artificial magnetic impurities leading to the Kondo effect as discussed in Ch. 2. This would be visible at low temperatures in the localized moment regime explained in Sec. 2.1.3. Although the Kondo effect is broadly studied in the literature, this section includes the results of Refs. [233] and [235] which intend to deepen our theoretical understanding of the thermally-biased effects and thermoelectric transport properties of single artificial magnetic impurities.

For the sake of completeness, we take three different approaches in order to cover all temperature ranges. With this goal we consider three different Hamiltonians: The Kondo Hamiltonian of Eq. (5.29), valid in the localized moment regime and high temperatures $T \geq T_K$ (Sec. 7.3.1); the slave-boson mean-field theory (SBMFT) described in Sec. 5.1.2, which is valid in the Fermi liquid regime meaning $T \ll T_K$ (Sec. 7.3.2) and the single-impurity Anderson Hamiltonian of Eq. (5.2) with Eq. (5.6) for describing qualitatively the local DOS and the conductance when $T \gg T_K$ (Sec. 7.3.3).

7.3.1 The thermally-dependent Kondo temperature

We consider the Kondo Hamiltonian $\mathcal{H}_{\text{Kam}}$ taking the coupling $\mathcal{J}$ as denoted in Eq. (6.31). This approach is only valid at $T > T_K$, because at low temperatures the logarithmic dependence dominates and diverges. In the absence of thermal and voltage bias, Eq. (6.36) allows us to recover the intrinsic Kondo temperature T_K of Eq. (2.5):

$$k_B T_K = D_0 \exp\left[\frac{\pi\varepsilon_d(U+\varepsilon_d)}{U\Gamma}\right], \tag{7.9}$$

with the difference of $\Gamma \to 2\Gamma$ due to our definition of Γ in Eq. (5.15) and $\sqrt{U\Gamma} \to D_0$ because we truncate the perturbation expansion to third order in $\mathcal{J}$ and higher orders are needed [105]. For finite temperature bias ($T_L = T + \theta$ and $T_R = T$), one can transform T_K in an effective Kondo temperature $\tilde{T}_K(\theta)$

$$\tilde{T}_K(\theta) = \sqrt{\left(\frac{\theta}{2}\right)^2 + {T_K}^2} - \frac{\theta}{2}\,. \tag{7.10}$$

This is a central result of our work [233]. We understand $\tilde{T}_K$ as the energy scale when the perturbation expansion made in Sec. 6.2 fails in the presence of a thermal bias. Although $\tilde{T}_K$ becomes T_K when $\theta = 0$, both scales should not be confused because T_K only depends on intrinsic parameters of the QD system, i. e., the charging energy U, the energy level ε_d or the hybridization constant Γ whereas $\tilde{T}_K$ also depends on θ, which is a tunable parameter.

In Fig. 7.12 we illustrate the normalized Kondo temperature $\tilde{T}_K/T_K$ (blue curve for this approach) as a function of θ from Eq. (7.10) in a logarithmic scale for clarity. As expected, $\tilde{T}_K = T_K$ when the system is at equilibrium and remains almost constant at low thermal biases indicating that the system stays in the Kondo regime. When θ approaches the intrinsic Kondo temperature T_K, $\tilde{T}_K$ decreases (scaling region) and vanishes at large thermal bias (Kondo quench). In contrast, for a DQD

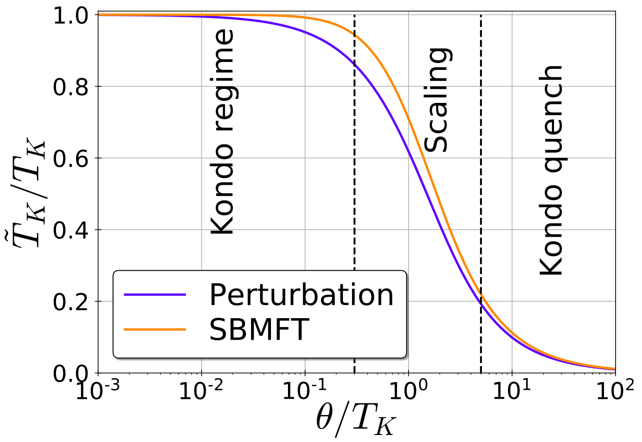

Fig. 7.12. (a) Normalized Kondo temperature $\tilde{T}_K/T_K$ as a function of the thermal bias applied by heating the left reservoir ($T_L = T + \theta$ and $T_R = T$). Blue line corresponds to the result from the perturbation analysis of Sec. 6.2 whereas orange line exhibits the effective Kondo temperature as the width of the Kondo resonance [$\tilde{T}_K \equiv \tilde{\Gamma}$ derived from Eq. (5.98)] in the SBMFT. In both approaches, the intrinsic Kondo temperature can be obtained by $T_K = \tilde{T}_K(\theta = 0)$.

system, the Kondo temperature survives at large θ as will be discussed in Sec. 8.3.

7.3.2 Transport in the Fermi liquid regime

Here, we analyze the Kondo effect in the Fermi liquid regime, meaning $T < T_K$. We will employ the SBMFT solving Eq. (5.98) for the mean-field parameters $\tilde{\Gamma}$ and $\tilde{\varepsilon}_d$. We recall that the former represents the width of the Kondo resonance while the latter is its renormalized position. Certainly, there exist different approaches that are able to describe Kondo physics in the Fermi liquid regime such as the renormalized perturbation theory [238, 239]. Nonetheless, the SBMFT gives accurate results in the limit $T \to 0$ and is thus an interesting approach to apply.

First, we analyze the resonances studying $\tilde{\Gamma}$ and $\tilde{\varepsilon}_d$ due to electrical and thermal biases determining how the Abrikosov-Suhl resonance is modified. Our analytical results are obtained in the deep Kondo or localized moment regime ($|\varepsilon_d| \gg |\tilde{\varepsilon}_d|$) and, at the same time, the Fermi liquid regime $|\tilde{b}|^2 \approx 1$. In addition, from now on, we consider $\Gamma_\alpha = \pi\rho|\mathcal{V}_\alpha|^2$ (notice that this is a slightly modified convention of $\Gamma \to 2\Gamma$ as with Eq. (7.9)). Performing these approximations and also applying the sum over σ, Eq. (5.96) turns into

$$\int_{-D}^{D} d\omega \frac{\mathcal{F}(\omega)}{\omega - \tilde{\varepsilon}_d + i\tilde{\Gamma}} = \frac{\pi N \varepsilon_d}{2\Gamma} \; . \tag{7.11}$$

Although in the previous approach we here defined the effective Kondo temperature as the energy scale where the perturbation theory breaks down due to the presence of θ, in this formalism the effective Kondo temperature is defined as the width of the Kondo resonance $k_B T_K \equiv \tilde{\Gamma}$.

Assuming that the system is in equilibrium at $T = 0$ and $\tilde{\varepsilon}_d \to 0$ in Eq. (7.11), we recover the intrinsic Kondo temperature for $U \to \infty$ [101]

$$k_B T_K \equiv \tilde{\Gamma}(\theta = 0) = D \exp\left[-\frac{\pi|\varepsilon_d|}{\Gamma}\right] , \tag{7.12}$$

where D is the energy bandwidth of the system.

We proceed with the analytical calculation of the mean-field parameters when the system is electrically biased. In this configuration, we consider the limit $T \to 0$ which ensures that the approach taken is valid. The advantage of this limit is that the nonequilibrium distribution function $\mathcal{F}(\omega)$ becomes a doubly-stepped function following $f_\alpha(\omega) \to \theta(\mu_\alpha - \omega)$ where $\theta(x)$ is the Heaviside function. Solving Eq. (7.11) we obtain the following equations

$$\tilde{\Gamma}(V)\tilde{\varepsilon}_d = 0 \; , \tag{7.13a}$$

$$\tilde{\varepsilon}_d^2 - \left(\frac{eV}{2}\right)^2 - \left[\tilde{\Gamma}(V)\right]^2 = -\left(k_B T_K\right)^2 \; . \tag{7.13b}$$

Therefore, for small voltages eV approaching $2k_B T_K$, the width of the Kondo peak drops to zero whereas its location is $\tilde{\varepsilon}_d \approx 0$ yielding $\tilde{b} \to 0$ and $\lambda = -\varepsilon_d$. Once $eV = 2k_B T_K$, the level position undergoes a bifurcation giving rise to a phase transition. In this transition, the Kondo resonance splits in two resonances located at symmetric positions with respect to $\varepsilon_F = 0$. Nevertheless, the width of the resonances follows $\tilde{\Gamma} \to 0$. Our result is consistent with the calculations of Coleman *et al.* [240] and Lopez *et al.* [241] and with the experiments reported in De Francesci *et al.* [113]. Additionally, we recall that these calculations are obtained in the limit of $T = 0$ whereas the SBMFT gives accurate results for $eV < 2k_B T_K$, otherwise the phase transition is actually a crossover.

The numerical results corresponding to the voltage-driven case are depicted in Fig. 7.13a and Fig. 7.13b for $T = 0$. We emphasize that these results are presented without taking any of the approximations of the analytical calculation. Even so, we find good agreement between the analytical and numerical results, especially for the deep Kondo regime

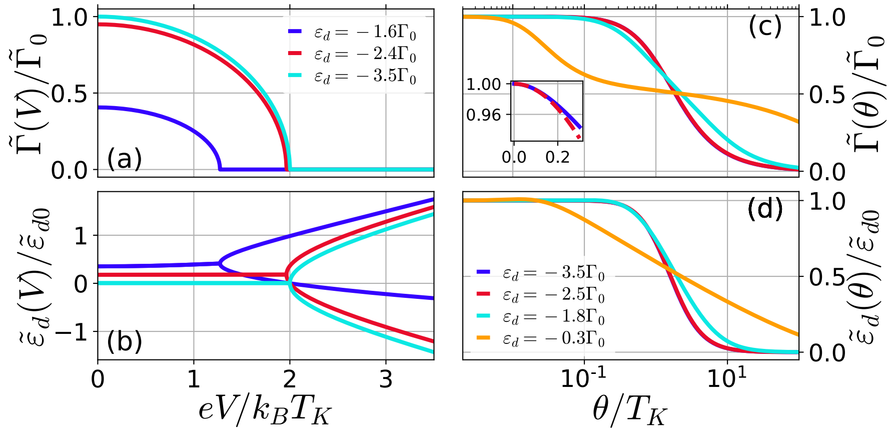

Fig. 7.13. (a) Width of the Kondo resonance following the SBMFT as a function of the applied voltage at different single-level energies ε_d. (b) Same as (a) but for the position of the Kondo peak. (c) Width of the Kondo resonance as a function of the thermal bias between reservoirs for different values of ε_d. (d) Same as (c) but for the position of the Kondo peak. In this case we take $\tilde{\varepsilon}_{d0} = \tilde{\varepsilon}_d(V = 0)$. Inset: Renormalized width versus thermal bias at $\varepsilon_d = -3.5\Gamma_0$ following the numerical calculation (solid line) and the analytical expression given by Eq. (7.14). Parameters: $D = 100\Gamma_0$, $k_BT = 0$ and $\Gamma_0 \equiv \Gamma_L = \Gamma_R = \Gamma/2$.

($\varepsilon_d = -3.5\Gamma_0$). We observe a transition at $eV = 2k_BT_K$ yielding the Kondo resonance splitting [Fig. 7.13b]. When the QD is near the mixed valence regime ($\varepsilon_d \approx -\Gamma$), charge fluctuations take place and the transition arises at lower voltage bias. On the other hand, Fig. 7.13a shows that the Kondo resonance gets narrower for increasing V and becoming zero after the transition.

For the analytical calculation of $\tilde{\Gamma}$ and $\tilde{\varepsilon}_d$ in the thermally-biased case, we apply a Sommerfeld expansion in the integral of Eq. (5.96):

$$\sum_\sigma \frac{1}{\pi}\int_{-D}^{D} d\omega \frac{\mathcal{F}(\omega)}{\omega - \tilde{\varepsilon}_d + i\frac{\tilde{\Gamma}}{2}} = \tilde{w}\,. \tag{5.96}$$

The leading order contribution yields Eq. (7.12), which is already known. Hence, we need to calculate the second-order term to obtain the dependence on θ:

$$\begin{aligned} \tilde{\varepsilon}_d &= 0\,, && (7.14a)\\ \tilde{\Gamma} &= k_BT_K \exp\left[-\frac{\pi^2}{12}\frac{T_L^2 + T_R^2}{{T_K}^2}\right]. && (7.14b) \end{aligned}$$

Eq. (7.14) states that no splitting appears when a thermal bias is applied. Instead, it renormalizes the width $\tilde{\Gamma}$, which drops for high values of θ. In comparison with the numerical results (inset of Fig. 7.13c), this approximation is valid only for $T_L, T_R \ll T_K$, which is the regime where the SBMFT can be applied. Anyway, we arrive at the same conclusion as in the perturbation expansion of Sec. 7.3.1: the Kondo resonance vanishes at large temperature biases.

The numerical calculations of Fig. 7.13c and Fig. 7.13d also agree with the analytical results, mostly in the deep Kondo regime ($\varepsilon_d = -3.5\Gamma$). Nevertheless, departures from the analytical calculation are found as ε_d approaches the mixed-valence regime. Three different regions are visible for $\tilde{\Gamma}(\theta)$ in Fig. 7.13c: A constant width in the low temperature range $\theta \ll 0.1T_K$, an exponential decrease when the thermal bias is near the intrinsic Kondo temperature $\theta \approx T_K$ and a decay to zero at $\theta \gg T_K$. Remarkably, this nicely agrees with our perturbative analysis as illustrated in Fig. 7.12. Both models predict a decrease of the effective Kondo temperature when the thermal bias increases. We highlight that both approaches agree even for values of θ away from the range of validity of the SBMFT. Therefore, this fact reinforces the main result of this work.

Electric transport

Once we understand the out-of-equilibrium response of the Abrikosov-Suhl resonance, we now turn to the electric and thermoelectric transport. We employ Eq. (6.14) taking into account that the transmission function is a Lorentzian peak located at $\tilde{\varepsilon}_d$ with width $\tilde{\Gamma}$. The electric current thus become

$$I = I_0 \mathrm{Im}\left[\psi\left(\frac{1}{2} + \frac{i(\tilde{\varepsilon}_d - \mu_R) + \tilde{\Gamma}}{2\pi k_B T_R}\right) - \psi\left(\frac{1}{2} + \frac{i(\tilde{\varepsilon}_d - \mu_L) + \tilde{\Gamma}}{2\pi k_B T_L}\right)\right], \quad (7.15)$$

where $I_0 = (8e\Gamma_L\Gamma_R)/(h\Gamma)$. Notice that Eq. (7.15) also depends on V and θ via $\tilde{\varepsilon}_d$ and $\tilde{\Gamma}$. Therefore, the transport properties of the QD are not strictly those of the noninteracting single level case.

In Fig. 7.14a we plot the electrical current across the artificial impurity driven by an applied voltage for several gate positions. We observe an ohmic response at low voltages as expected. The differential conductance (inset of Fig. 7.14) is obtained from the results of the electrical current. It exhibits at zero bias its maximum value which corresponds to twice the quantum of conductance $\tilde{g}_0$ due to the fact the artificial impurity is spin degenerate yielding two spin channels.

In comparison with Fig. 7.14a, the thermocurrent shown in Fig. 7.14b has a very different behavior. First, the thermocurrent is more intense for values approaching the mixed-valence regime, a regime in which electron-hole symmetry breaking is more prominent. Second, I lacks the linear response to a thermal bias. The reason is that there exists a particle-hole symmetry which nullifies the current to lowest order ($\mathcal{L}_0 \approx$

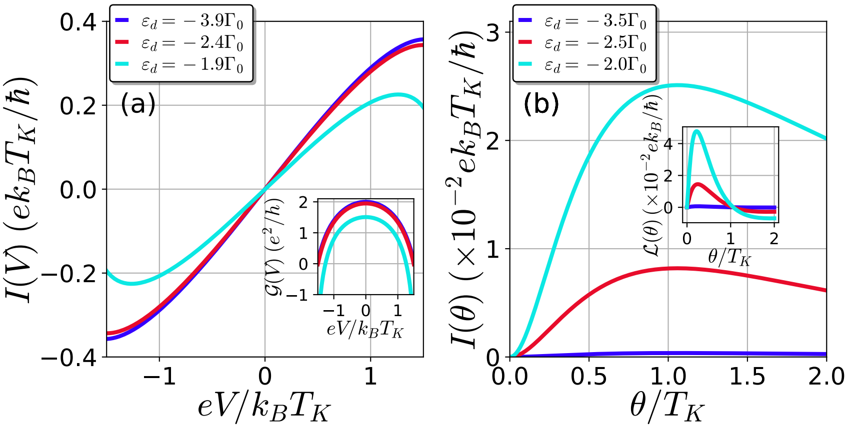

Fig. 7.14. (a) Electric current I versus the applied voltage V for different values of the energy level ε_d of an artificial Kondo impurity in the Fermi liquid regime following the SBMFT. Inset: Differential electric conductance of the artificial impurity as a function of the applied voltage. (b) Thermocurrent I_{th} versus the thermal bias θ between reservoirs in the system of (a) for several values of ε_d. Inset: Differential thermoelectric conductance of the artificial impurity as a function of the thermal bias. Parameters: $D = 100\Gamma_0$, $k_BT = 0$ and $\Gamma_0 = \Gamma_L = \Gamma_R = \Gamma/2$.

0). Therefore, at low temperature differences the current follows $I \approx \mathcal{L}_1\theta^2$ whose leading order is

$$\mathcal{L}_1 = \frac{4\pi^2 e k_B^2}{3h}\tilde{\Gamma}_L\tilde{\Gamma}_R\frac{\tilde{\varepsilon}_d}{\tilde{\varepsilon}_d^2 + \tilde{\Gamma}^2}\ . \tag{7.16}$$

We point out that the sign of $\mathcal{L}_1$ in Eq. (7.16), and consequently I_{th}, depends on the renormalized level position $\tilde{\Gamma}_\alpha$. In addition, we observe that in the deep Kondo regime $\mathcal{L}_1 \approx 0$ since the Kondo resonance is located at the Fermi energy. This effect is illustrated in the inset of Fig. 7.14b where we plot the differential thermoelectric conductance. When the system is in the localized moment regime $\varepsilon_d = -3.5\Gamma_0$, $\mathcal{L}$ deviates little from the $\theta = 0$ axis. However, as the energy level approaches the Fermi energy, the thermoelectric conductance becomes larger. Interestingly, $\mathcal{L}$ exhibits a maximum at small values of θ followed with a decrease and then a change of sign. This maximum grows as the dot gate position enters the mixed-valence regime characterized by the lack of electron-hole symmetry ($\tilde{\varepsilon}_d \neq 0$). In addition, the sign reversal indicates whether the flow is electron-like or hole-like determining the thermocurrent direction at large thermal biases. Besides, the position of this sign reversal occurs at $\theta \approx T_K$ because the quench of the Kondo resonance starts to be visible and the electron flow is thus less intense.

Heat transport

In this part we study the heat transport and Peltier effect of an artificial impurity in the Fermi liquid regime. Following the results shown in Fig. 7.13, we plot in Fig. 7.15 the numerical result of Eq. (6.19) for an artificial Kondo impurity with a level located at $\varepsilon_d = -2.5\Gamma_0$. We recall that the heat current is separated in two terms according to which, following Eq. (6.2), Eq. (6.19) can be separated in

$$\begin{aligned} Q_E &= \frac{2}{h}\int d\omega\,[f_L(\omega) - f_R(\omega)]\,\omega\mathcal{T}(\omega, V, \theta)\,, \qquad (7.17)\\ Q_I &= \frac{eV}{h}\int d\omega\,[f_L(\omega) - f_R(\omega)]\,\mathcal{T}(\omega, V, \theta)\,, \qquad (7.18) \end{aligned}$$

where Q_E and Q_I are the energy current and Joule term, respectively. In Fig. 7.15a we depict both contributions to the heat current finding different behaviors. First, the energy current Q_E is an increasing function of V. Particularly, for $V > 0$ the energy flows from the left lead increasing with V and Q_E is thus positive. However, for $V < 0$ carriers are injected from the right lead yielding negative energy currents. In addition, Q_E presents an antisymmetric shape around $V = 0$. In contrast, the Joule term Q_I is symmetric with $V = 0$ and always takes negative values which means, in our sign convention, that the system suffers dissipation. In order to deeply understand the physics inside these symmetries, we focus our attention on each term in Eqs. (7.17) and (7.18). First, the difference of Fermi functions $f_L - f_R$ is an odd function of V if no thermal bias is applied between the reservoirs. On the other hand, the transmission function is an even function of V such that $\mathcal{T}(\omega, V) = \mathcal{T}(\omega, -V)$ since the mean-field parameters are also even functions of the voltage (Fig. 7.13a and Fig. 7.13b are invariant under $V \to -V$). This is an expected result because the renormalized width has a non-preferential direction given by the voltage bias whereas $\tilde{\Gamma}$ is a function which weakly depends on V. As a consequence, Q_E in Eq. (7.17) is formed from the integral of an odd and an even functions yielding an antisymemtric energy current. Nonetheless, Q_I in Eq. (7.18) is a symmetric function.

Fig. 7.15b illustrates the total current arising from the combination of both Q_E and Q_I. First, the energy current dominates the heat transport at low V causing a linear dependence (dashed line in Fig. 7.15b): the distinctive feature of the Peltier effect. Therefore, the total current in this regime obeys Eq. (3.5b) for $\theta = 0$ with a positive $\mathcal{R}_0 > 0$. The reason behind this fact is that the Kondo peak is not exactly located at the Fermi energy. In fact, the peak is slightly centered at positive energies. This leads to an asymmetric transmission function $\mathcal{T}(\omega, V) \neq \mathcal{T}(-\omega, V)$ from which, taking into account Eq. (6.21c), we obtain a positive linear electrothermal conductance. Thus, the artificial Kondo impurity may be

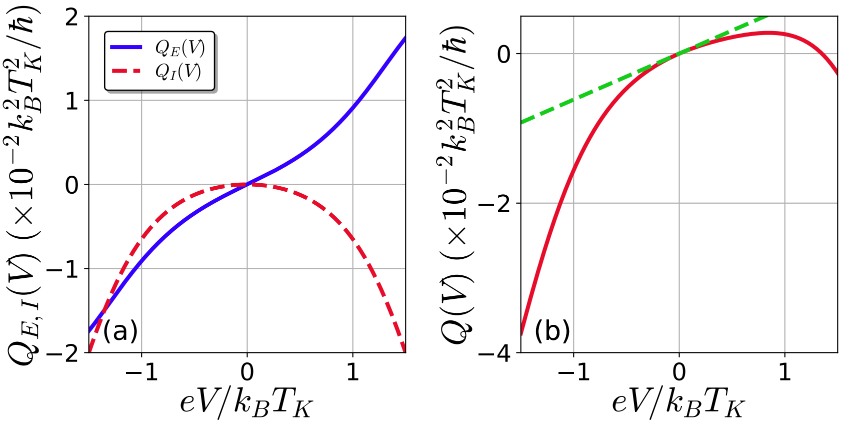

Fig. 7.15. (a) Energy current Q_E (blue solid line) and Joule term Q_I (red dashed line) as a function of the voltage bias V of a QD acting as an artificial Kondo impurity with $\varepsilon_d = -2.5\Gamma_0$. We remark that Q_E also describes the contact Δ_C and electric Δ_E asymmetries of the heat current. (b) Heat current Q versus the voltage bias for the same system as (a). The green dashed line shows the Peltier contribution $Q \approx \mathcal{R}_0 V$ to the heat current. The parameters are the same as Fig. 7.14.

used as a cooler at low $V > 0$. Nevertheless, this effect is lost at higher voltages since Joule dissipation quickly dominates the heat transport yielding a negative flow. Finally, we want to remark that now $Q(V)$ is also asymmetric under the transformation $V \to -V$ because Q arises from the addition of symmetric and antisymmetric functions.

Now, we briefly discuss the asymmetries of Eq. (3.22) involving Δ_C and Δ_E. The symmetry properties of $Q_E(V)$ and $Q_I(V)$ shown in Fig. 7.15a provide interesting physics. Straightforwardly, the contact asymmetry obeys the relation $\Delta_C = 2Q_E(V)$. As a consequence, the behavior of Δ_C is also described by the blue curve of Fig. 7.15a. Remarkably, the electric asymmetry is also proportional to the energy current in the same way $\Delta_E = 2Q_E(V)$. This is a general result [181] which is satisfied always for a system in a two-terminal configuration with a symmetric applied voltage $V_L = -V_R = V/2$ characterized by a symmetric transmission $\mathcal{T}(\omega, V) = \mathcal{T}(\omega, -V)$. In our case, namely, an artificial Kondo impurity in the Fermi liquid regime, such conditions are met as explained above. Importantly, we expect that this result would facilitate the experimental detection of the energy current by measuring either the heat current for different signs of the voltage or the heat current at different reservoirs with a constant V.

7.3.3 Transport at high temperature gradients

So far, we have investigated the Kondo effect by applying two different approaches: the perturbation approach and the SBMFT. Although these models gives intriguing results on the behavior of the Kondo resonance, they are not able to capture the transport properties at all energies. Actually, the electric and heat currents calculated in the SBMFT only considers energies around the Abrikosov-Suhl resonance. For this reason, we now employ the EOM technique to find a local DOS which takes into account the single-particle peaks in addition to the Kondo resonance. This approach allows us to investigate qualitatively the dynamical quantities of an artificial impurity and its transport properties in the case of moderate temperatures.

Density of States

We remind that the local DOS [Eq. (4.27)] requires the computation of the retarded Green's function as observed. Unfortunately, the Green's function used in Secs. 7.1 and 7.2 are not enough to describe the expected physics since Eq. (5.56) was obtained by neglecting spin-flip correlations. Therefore, in this section we consider Eqs. (5.74) [for $U \to \infty$] and (5.81) [for a finite but large U] as the Green's function describing our system.

We begin considering the case when electron-electron interactions are strong ($U \to \infty$). In this model, we estimate the intrinsic Kondo temperature from Haldane's formula [101]

$$k_B T_K = \sqrt{D\Gamma} \exp\left[-\frac{\pi|\varepsilon_d|}{2\Gamma}\right]. \tag{7.19}$$

In this section, we keep the definition of Γ taken in the previous section. Hence, we now calculate the local DOS of the impurity and study how the Abrikosov-Suhl resonance is modified with the application of a voltage and thermal bias. In Fig. 7.16a we present the voltage-driven case. As expected, the Kondo resonance splits symmetrically in two resonances located at $\omega \approx \pm eV/2$ (see inset of Fig. 7.16 for a clearer view). Unfortunately, no dephasing effect is considered within the EOM technique although it should be actually present in the Abrikosov-Suhl resonance [241]. Several proposals has been realized to amend the lack of dephasing by combining EOMs using a dot occupation computed with the noncrossing approximation [115, 116, 229].

The thermally-driven case is depicted in Fig. 7.16b. We observe that the Kondo peak is smeared out. However, the singularity does not disappear for $T \gg T_K$ as discussed previously. The explanation of such

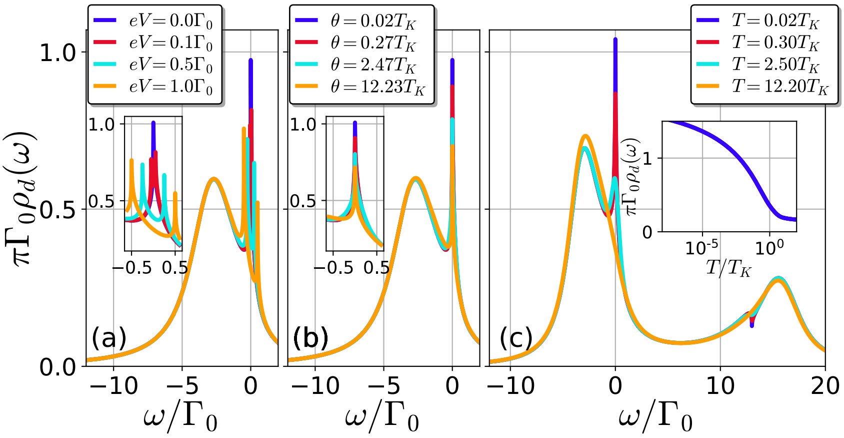

Fig. 7.16. (a) Spectral DOS of a system consisting of an artificial magnetic impurity with a single level with energy $\varepsilon_d = -3.5\Gamma_0$ in the infinite-U case for different values of eV. Inset: Detail of the DOS around the Fermi energy $\varepsilon_F = 0$ for a clearer view of the Abrikosov-Suhl resonance. (b) Spectral DOS for the same system as (a) for different thermal bias θ. Inset: Detail of the DOS around the Fermi energy ($\varepsilon_F = 0$). (c) Spectral DOS of an artificial impurity system with a single level with energy $\varepsilon_d = -3.5\Gamma_0$ and a finite charging energy $U = 20\Gamma_0$ for different temperatures T. Inset: Height of the Kondo resonance as a function of the background temperature. Parameters: $D = 100\Gamma_0$, $\Gamma_0 = 2\Gamma_L = 2\Gamma_R$ and $T = 0.024T_K$ in (a) and (b).

behavior can be found at Eq. (5.81) whose expression was

$$G^r_{\sigma,\sigma}(\omega) = g_u(\omega)\left[p_{u,\sigma} + i\frac{P_u(\omega)}{\mathcal{X}^*_u(\omega)}\right]. \tag{5.81}$$

The sharp peak arises from $\mathcal{X}(\omega)$, which contains the integral of the Fermi functions of the leads [see Eqs. (5.73) and (5.67)]. When a reservoir is heated, its Fermi function stops contributing to the Kondo resonance. However, the second reservoir remains cold and the resonance persists at high temperature biases. This effect is an artifact of the EOM technique. Despite this, the method gives a correct behavior at low θ: The Abrikosov-Suhl resonance is gradually destroyed by a thermal bias, in agreement with both the perturbative approach and the SBMFT.

When Eq. (5.81) is considered instead, we recover the second single-particle peak as illustrated in Fig. 7.16c. We observe that the DOS has the single-particle peaks centered at $\omega \approx \varepsilon_d$ and $\omega \approx \varepsilon_d + U$ and the Kondo singularity at $\omega \approx 0$. In this model we also determine the Kondo temperature using the Haldane's formula for a finite U system [101]

$$k_B T_K = \sqrt{2\Gamma U}\exp\left[-\frac{\pi|\varepsilon_d|(U+\varepsilon_d)}{2\Gamma U}\right]. \tag{7.20}$$

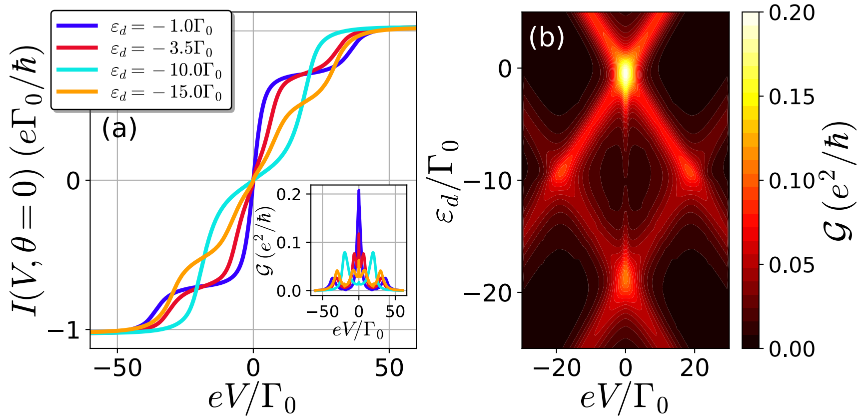

Fig. 7.17. (a) Electric current as a function of the applied voltage of an artificial Kondo impurity at different level positions ε_d. Inset: Differential electric conductance as a function of the applied voltage for different level positions. (b) Differential electric conductance versus energy level ε_d and bias voltage V showing the Coulomb diamond with the ZBA. Parameters: $D = 100\Gamma_0$, $T = 0.0001\Gamma_0$, $U = 20\Gamma_0$ and $\Gamma_0 = 2\Gamma_L = 2\Gamma_R$.

The effect given by an increase of the background temperature is visible in Fig. 7.16c. As explained in Ch. 2, we find that the Kondo singularity disappears at temperatures above T_K. The inset of Fig. 7.16c exhibits the height of the Kondo resonance as a function of T demonstrating how the Kondo peak is gradually destroyed. Therefore, the Kondo peak also vanishes for a finite charging energy. Concerning voltage and temperature biases, we obtain the same tendencies as shown in Fig. 7.16a and Fig. 7.16b: A voltage generates a splitting of the Kondo peak while the thermal bias smears out the Kondo singularity. Similarly, the finite U case also lacks dephasing at large V and the Kondo quenching for $\theta > T_K$.

Electric Current

The DOS calculation explained in the last section can be used in Eq. (6.15) to investigate the electric and thermoelectric transport features of the system. First, we examine the voltage-driven response of the electric current in Fig. 7.17a. The electric current shows a stair-like shape in which, in comparison with Fig. 7.1a, a small change of slope appears around $V = 0$. This is more clearly seen in the inset of Fig. 7.17a where we compute the numerical derivative of I yielding $\mathcal{G}$. We observe at $V = 0$ a very narrow peak: The ZBA which characterizes the Kondo effect. Basically, we distinguish five different peaks in $\mathcal{G}$: The resonance due to the alignment of the single-particle peaks with the electrochemical potential of the fermionic reservoirs [$eV \approx \pm 2\varepsilon_d$ and $eV \approx \pm 2(\varepsilon_d + U)$]

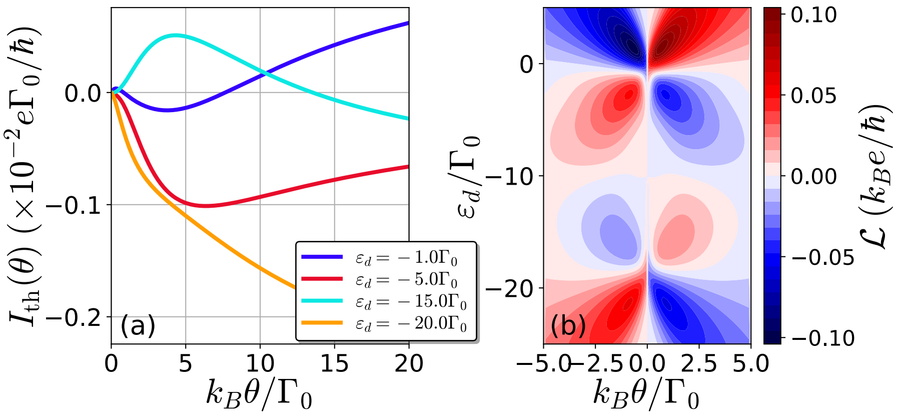

Fig. 7.18. (a) Thermocurrent as a function of the thermal bias θ of an artificial Kondo impurity at different level positions ε_d. (b) Differential thermoelectric conductance versus energy level ε_d and the thermal bias θ. Parameters: $D = 100\Gamma_0$, $T = 0.0001\Gamma_0$, $U = 20\Gamma_0$ and $\Gamma_0 = 2\Gamma_L = 2\Gamma_R$.

and the ZBA at $V = 0$. The electrical conductance $\mathcal{G}$ is also plotted as a function of the dot level ε_d and the applied voltage V in Fig. 7.17b. We observe differences with respect to the Coulomb diamond of Fig. 7.1b. Around $V = 0$ a high conductance line appears as a consequence of the ZBA. This is consistent with the explanation given in Sec. 2.2. Clearly, our approach fails around the particle-hole symmetry point $\varepsilon_d \approx -U/2$ and the effect of the Kondo resonance is barely visible.

Now, we proceed with the thermally-driven response of the Kondo impurity system. The thermocurrent I_{th} when the left reservoir is heated is shown in Fig. 7.18a. Each position of the single level ε_d shows the behavior of the thermocurrent for several regions: For $\varepsilon_d > 0$ and $\varepsilon_d + U < 0$ the system works in the empty orbital or in the full orbital regime as defined in Sec. 2.1.3. Such regions represent a system with a monotonic behavior of I_{th} which either increases or decreases depending on whether both resonances are located above or below the Fermi level. Otherwise, when $0 > \varepsilon_d > -U$, I_{th} changes its sign at a given θ. This is not surprising because it was already found in the CB results discussed in Sec. 7.1. In addition to this, the nontrivial zero can also occur due to Kondo correlations. For instance, the case $\varepsilon_d = -\Gamma_0$ gives a thermocurrent with a nontrivial zero for $k_B\theta \approx \Gamma_0$ and another zero at $k_B\theta \approx 7.5\Gamma_0$. Such finding is lost for $T \gg T_K$ since the Kondo correlations are no longer a dominant contribution to the quantum transport. The thermoelectric conductance $\mathcal{L}$ of the Kondo system is shown in Fig. 7.18b. We observe a similar butterfly structure as Fig. 7.2b. However, below $\varepsilon_d = 0$ and above $\varepsilon_d = -U$ we find a region at small θ in which $\mathcal{L}$ changes sign once before the sign

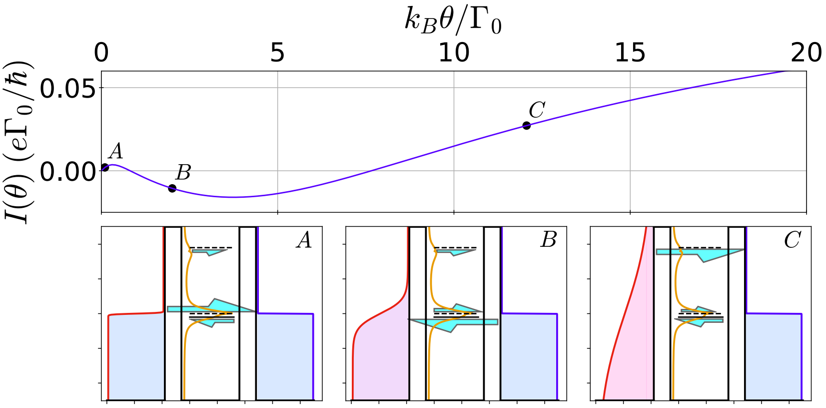

Fig. 7.19. (a) Thermocurrent as a function of the thermal bias for $\varepsilon_d = -\Gamma_0$ as taken from Fig. 7.18. Panels A, B and C are the energy diagrams corresponding to the current states marked in the upper panel. Red (blue) line shows the Fermi-Dirac function of the left (right) reservoir while the orange curve indicates the local DOS of the artificial Kondo impurity in the cases of the three points of the top panel. The position of ε_d is denoted with a solid line whereas the dashed lines indicate the energies $\omega = \varepsilon_F = 0$ and $\omega = \varepsilon_d + U$ which correspond to the Kondo singularity and the single-particle resonance positions, respectively. Finally, the arrows indicate the direction and the strength of the electronic flow through the corresponding resonance.

reversal at larger θ. This first nontrivial zero in the thermocurrent is attributed to the Kondo resonance. We suspect that such sign reversal of $\mathcal{L}$ would occur for $\varepsilon_d \in [0, -U]$ but it is not shown in Fig. 7.18b because of the breakdown of this model at the particle-symmetry point.

The mechanism behind the generation of the nontrivial zeros can be explained with an energy diagram as in Sec. 7.1. In the top panel of Fig. 7.19 $I_{\text{th}}(\theta)$ is reproduced for $\varepsilon_d \approx -\Gamma$ whereas in the bottom panel we plot the configuration of system for the three thermal biases indicated above. As explained before, the local DOS comprises three resonances: The single particle peaks centered at $\omega = \varepsilon_d$ and $\omega = \varepsilon_d + U$ and the Kondo resonance at $\omega \approx 0$. When the left reservoir is slightly heated (case A of Fig. 7.19), the transport window is open around the Fermi energy $\varepsilon_F = 0$ and the Abrikosov-Suhl resonance is the only peak which plays a role in the transport. This peak is slightly located above the Fermi energy since the system is away from the particle-hole symmetry point and electrons will thus flow from the left to the right reservoir leading to $I_{\text{th}} > 0$. If we increase θ, the difference between Fermi functions enhances the transport window and the single-particle resonance at ε_d, which is located below the Fermi energy, starts to contribute to the electric current in opposite direction. At some point, the hole flow of the single-particle peak compensates the electron flow generated by the Kondo resonance giving rise to a vanishing current and for higher thermal biases, $I_{\text{th}} < 0$ (case B). Finally, the electron current crossing the single-particle resonance at $\varepsilon_d + U$ flows when further increasing θ. This favors the current with opposite direction and, hence, the current is again reversed at large thermal bias (case C).

8. Double Dot structures

Although a single QD system shows interesting physics, DQD structures also give intriguing and rich phenomena that should be understood. New tunable parameters such as the tunneling between QDs (denoted by τ) or the additional gate (which modifies the level detuning between the dots) increase the complexity of the system. Additionally, several DQD configurations can be produced taking into account how the electronic reservoirs and the QDs are coupled (see Sec. 1.3). As a consequence, we deal with different transport behaviors worth to be studied.

This chapter analyzes transport through double dot structures as reported in Refs. [232, 242, 243]. Particularly, we study the local DOS and quantum transport across a parallel-coupled DQD with a finite intradot interaction U in which each dot is attached to two fermionic reservoirs in Sec. 8.1. Such system generates BICs when the dot energy levels align. This fact leads to important consequences in the electric and thermoelectric transport. Later, we consider a different double-dot configuration in Sec. 8.2: the Coulomb drag system. In this case we discuss a parallel DQD whose dots are coupled with an interdot interaction energy $\tilde{U}$. This system requires to take into account the interacting self-energy Σ_{int} neglected in Sec. 6.1 in order to study the transport through an unbiased QD at equilibrium due to voltage bias in the second dot. Finally, we analyze the role of the Kondo resonances arisen in a serially-coupled two-impurity system in the presence of a thermal bias (Sec. 8.3). We observe different regimes depending on the tunneling between QDs and find a decoupling of the double impurity at large temperature bias.

8.1 BIC in parallel-coupled quantum dots

First, we focus on the parallel DQD sketched in Fig. 1.6a. In this configuration, we assume that the fermonic reservoirs are attached to both dots. We consider negligible tunnel $\tau \approx 0$ and capacitive coupling $\tilde{U} \approx 0$ between the dots. Hence, the QDs can only feel each other indirectly via the leads. As in previous works, the reservoirs may be subjected to a symmetric voltage bias $V_L = -V_R = V/2$ and a thermal bias θ obtained by heating one reservoir ($T_L = T + \theta$ when $\theta > 0$ and $T_R = T - \theta$ for $\theta < 0$).

This section summarizes the results obtained in Sierra *et al.* [232].

We model the system with the Anderson Hamiltonian of Eq. (5.2) and take $\tau = 0$ and $\tilde{U} = 0$ in the DQD Hamiltonian [Eq. (5.4)]. In addition, we consider intradot Coulomb interactions U and we thus take Eq. (5.57) as the retarded Green's function which reads

$$G^r_{\mu\sigma,\nu\sigma} = h_{\mu\nu}\left[\frac{1-\bar{n}_{\mu\bar{\sigma}}}{\omega-\varepsilon_\mu-\tilde{\Sigma}^r_{\mu\sigma}\left(1-\frac{U_\mu\bar{n}_{\mu\bar{\sigma}}}{\omega-\varepsilon_\mu-U_\mu}\right)}\right. \\ \left. +\frac{\bar{n}_{\mu\bar{\sigma}}}{\omega-\varepsilon_\mu-U_\mu-\tilde{\Sigma}^r_{\mu\sigma}\left(1-\frac{U_\mu(1-\bar{n}_{\mu\bar{\sigma}})}{\omega-\varepsilon_\mu}\right)}\right]. \tag{5.57}$$

We recall that $G^r_{\mu\sigma,\nu\sigma}$ is a matrix whose coefficients $\mu,\nu = \{1,2\}$ denote the QDs whereas σ represents the spin. Therefore, the occupation [Eq. (4.26)], following Eqs. (4.44) and (6.9), reads

$$\bar{n}_{\mu\sigma} = \int\frac{d\omega}{2\pi}\sum_{\alpha\lambda_1\lambda_2} f_\alpha(\omega)G^r_{\mu\sigma,\lambda_1\sigma}(\omega)\Gamma_{\alpha;\lambda_1\sigma,\lambda_2\sigma}G^a_{\lambda_2\sigma,\nu\sigma}(\omega)\,, \tag{8.1}$$

where the hybridization matrices take the form

$$\mathbf{\Gamma}_L = \Gamma_0\begin{pmatrix} 1 & \sqrt{a} \\ \sqrt{a} & a\end{pmatrix}\,,\ \mathbf{\Gamma}_R = \Gamma_0\begin{pmatrix} a & \sqrt{a} \\ \sqrt{a} & 1\end{pmatrix}\,. \tag{8.2}$$

We can control the coupling between dots and leads with a tuning of the parameters Γ_0 and a. This expression of $\mathbf{\Gamma}_\alpha$ was already employed by Hewson [225] and a is useful to parametrize the transition from the fully decoupled ($a = 0$) to the symmetrically coupled case ($a = 1$).

8.1.1 Spectral and transmission functions

We begin our discussion analyzing the local DOS. In this case, Eq. (4.27) is generalized

$$\rho(\omega) = -\frac{1}{\pi}\mathrm{Im}\mathrm{Tr}[\mathbf{G}^r]\,, \tag{8.3}$$

where $\mathrm{Tr}[\mathbf{A}]$ denotes the trace of the matrix $\mathbf{A}$ over spin σ and QDs indices μ. Now, we substitute Eq. (5.57) into Eq. (8.3) in order to understand the emergence of BICs. For the sake of simplicity, we consider the noninteracting case $U = 0$ with symmetrically-located energy levels $\varepsilon_1 = -\varepsilon_2 = \varepsilon$. Therefore, we end up with the following expression

$$\rho(\omega) = \frac{(1+a)\Gamma_0}{\pi\mathcal{D}(\omega)}\left[\omega^2+\varepsilon^2+\frac{1}{4}(1+a)^2\Gamma^2\right]\,, \tag{8.4a}$$

$$\mathcal{D}(\omega) = (\omega^2-\varepsilon^2)^2+\left[\frac{\Gamma_0}{2}(1+a)\right]^4+\frac{\Gamma_0^2}{2}\left[\omega^2(1+6a+a^2)+\varepsilon^2(1-a)^2\right]\,. \tag{8.4b}$$

With the goal of finding a simplified expression, we substitute $a = 1$ and consider energies around the Fermi level ($|\omega| < \varepsilon < \Gamma_0$). Thus, Eq. (8.4) turns into

$$\rho(\omega) = \frac{1}{\pi}\frac{2\Gamma_0}{\omega^2 + 4\Gamma^2} + \frac{1}{\pi}\frac{\varepsilon^2/(2\Gamma_0)}{\omega^2 + [\varepsilon^2/(2\Gamma_0)]^2} \ . \tag{8.5}$$

Therefore, the spectral function now is a sum of two Lorentzian functions centered at $\omega = 0$. This means that the system consists of a superposition of two different states: a state strongly coupled to the continuum [first term in the right hand side of Eq. (8.5)] and a second state which depends on the distance between energy levels [second term in the right hand side of Eq. (8.5)]. For $\varepsilon < 2\Gamma_0$, the resonance is weakly coupled to the continuum and, actually, the peak becomes a bound state when $\varepsilon \to 0$:

$$\rho(\omega) = \frac{1}{\pi}\frac{2\Gamma_0}{\omega^2 + 4\Gamma^2} + \delta(\omega) \ . \tag{8.6}$$

This bound state is effectively decoupled only for $a \to 1$ and when the dot levels are met $\varepsilon_1 \to \varepsilon_2$ and lies at the center of such levels. Therefore, BICs may arise in a noninteracting DQD system [244, 245]. We highlight that for a nonsymmetric tunneling to the leads ($a \neq 1$) the delta function in Eq. (8.6) smears out with a finite width $\gamma(a)$ for aligned levels ($\varepsilon \to 0$). Therefore, when $|\omega| < \Gamma_0$, the DOS reads

$$\rho(\omega) \sim \frac{1}{\pi}\frac{\gamma(a)}{\omega^2 + \gamma^2(a)} \ , \tag{8.7}$$

where $\gamma(a) = \Gamma_0(1-a)^2\sqrt{8(1+6a+a^2)}$ is the width of the resonance which vanishes for $a \to 1$, as expected. The noninteracting behavior of the local DOS at $T = 0$ is illustrated in Fig. 8.1a for different energy levels ε and lead-dot coupling symmetries a. We recall that a self-consistent calculation has to be performed using Eqs. (5.57) and (8.1). When the distance between levels is large in the symmetric case $a = 1$ (red solid curve) we find a resonance centered at $\omega = 0$. Both Lorentzians in Eq. (8.5) overlap yielding a single resonance. In fact, in such case ($\varepsilon = 1\Gamma_0$) the width of the resonances take similar values and the resonances can not be resolved. As we move away from the symmetrically case by taking $a = 0.5$ (red dashed curve), two peaks located at ε_1 and ε_2 can be distinguished in the local DOS. More interesting is the case when $\varepsilon = 0.05\Gamma_0$ (blue curves), a narrow peak is visible at $\omega = 0$ which comes from the second resonance in Eq. (8.5) and will be transformed to a dirac delta if $\varepsilon \to 0$ indicating that a BIC is formed. Furthermore, the bound state is also smeared out in the nonsymmetrical configuration (blue dashed curve).

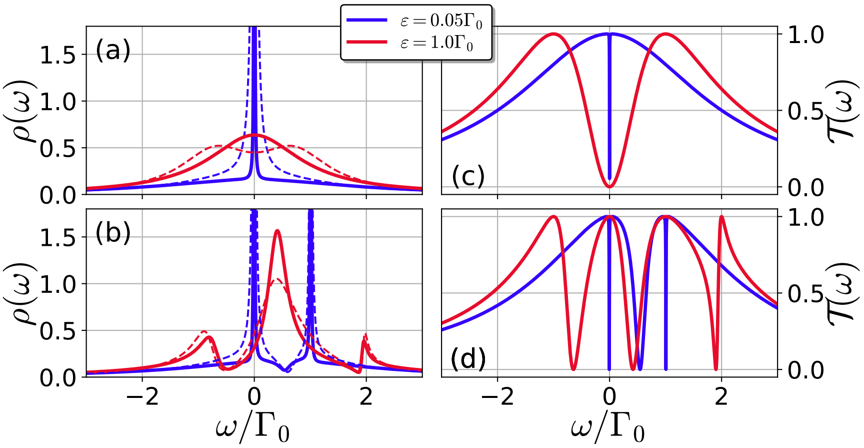

Fig. 8.1. (a) Local DOS of a noninteracting DQD coupled to leads at $T = 0$ for different level positions $\varepsilon_1 = -\varepsilon_2 = \varepsilon$. The solid lines represent symmetrical coupling to the leads $a = 1$ whereas the dashed lines denote the nonsymmetrical coupling with $a = 0.5$. (b) Local DOS of a DQD with intradot Coulomb interactions $U_1 = U_2 = U = 1.0\Gamma_0$. As in (a), solid and dashed curves represent symmetrical and nonsymmetrical coupling to the leads, respectively. (c) Transmission of the same noninteracting DQD in (a) for the case of a symmetrical coupling $a = 1$. (d) Same as (c) but for the interacting case taking $U = 1.0\Gamma_0$.

We now discuss the interacting case shown in Fig. 8.1b assuming $U_1 = U_2 = U$. In comparison with $U = 0$, the spectral function exhibits several resonances instead of the single peak in the symmetric configuration. The reason behind this phenomenon is that virtual levels appear at $\varepsilon_\mu + U$ and, consequently, we find four resonances located at $\pm\varepsilon$ and $\pm\varepsilon + U$. When $\varepsilon = 0.05\Gamma_0$ we still observe the resonance of the BIC of the noninteracting case but, remarkably, a replica comes out at $\omega = U$. This can be found analytically operating Eq. (5.57) in the case of equal occupations $\bar{n}_{1\bar{\sigma}} = \bar{n}_{2\bar{\sigma}} \equiv \bar{n}$ and symmetric coupling to the leads $a = 1$. Assuming negligible contribution of the resonant states strongly coupled to the continuum ($|\omega|, |\omega - U| \ll \Gamma_0$) two poles appear in the spectral function, weighted by the occupations, which in the limit $\varepsilon \to 0$ becomes

$$\rho(\omega) = (1 - \bar{n})\delta(\omega) + \bar{n}\delta(\omega - U) \ . \tag{8.8}$$

This is in agreement with the numerical results: a replica of the BIC emerges at $\omega = U$. Eq. (8.8) represents two BICs weighted by the relative occupations. An important statement we make is that the BICs are preserved even in the presence of Coulomb interactions ($U \neq 0$). Again, an asymmetric configuration (dashed curves) only smears out the resonances and BICs.

We proceed with the analysis of the transmission function defined in

Eq. (6.15). Again, a self-consistent calculation is needed to evaluate $\bar{n}_{\mu\sigma}$. Additionally, we still restrict ourselves to equilibrium conditions $V = 0$ and $T_\alpha = T$. With a similar calculation as with the DOS, the transmission function becomes [245]

$$\mathcal{T}(\omega) = \frac{4a\Gamma_0^2\omega^2}{\mathcal{D}(\omega)} . \tag{8.9}$$

Clearly, Eq. (8.9) vanishes at $\omega = 0$ for $\mathcal{D}(\omega = 0) \neq 0$. After some algebra, one may obtain an equivalent expression to Eq. (8.5) for a system with symmetric coupling with the leads $a = 1$ and detuned energy levels $\varepsilon \neq 0$:

$$\mathcal{T}(\omega) \approx \frac{\omega^2}{\omega^2 + \varepsilon^4/(4\Gamma_0^2)} . \tag{8.10}$$

Here, we have considered $|\omega| < \varepsilon$ and negligible intradot interactions. In comparison with Eq. (1.8), we notice that the transmission follows a Fano resonance for the case of $q = 0$. The mechanism behind this transmission shape is the coexistence of two different paths which give rise to quantum interference. The first path crosses the DQD via the strongly coupled state whereas the second path includes transitions in and out the BIC. A destructive interference between both paths leads to a Fano antiresonance. An illustrative example of this phenomenon can be found in Fig. 8.1c where the transmission of the DQD is displayed in the noninteracting case. We observe two resonances located at $\omega = \pm\varepsilon$ with an antiresonance at $\omega = 0$ which is generated due to the Fano effect.

For asymmetric coupling to the leads $a \neq 1$ and aligned energy levels $\varepsilon = 0$, the transmission also shows a Fano antiresonance with a shape dependent on a:

$$\mathcal{T}(\omega) \approx \frac{\omega^2}{\omega^2 + \gamma^2(a)} . \tag{8.11}$$

Despite the fact that $\mathcal{T}$ can exhibit strong resonances at some energies, the DQD system never reaches full transparency for $a \neq 1$. In addition, when the QD levels approach to each other, the Fano antiresonance becomes narrower as shown in Fig. 8.1c for $\varepsilon = 0.05\Gamma_0$ (blue curve). When $\varepsilon \to 0$, such antiresonance disappears yielding a transmission with a Lorentzian shape:

$$\mathcal{T}(\omega) = \frac{4\Gamma_0^2}{\omega^2 + 4\Gamma_0^2} . \tag{8.12}$$

In general, for a finely tuned system ($\varepsilon = 0$ and $a = 1$), the transmission still shows a marked dip at $\omega = 0$ due to the BIC.

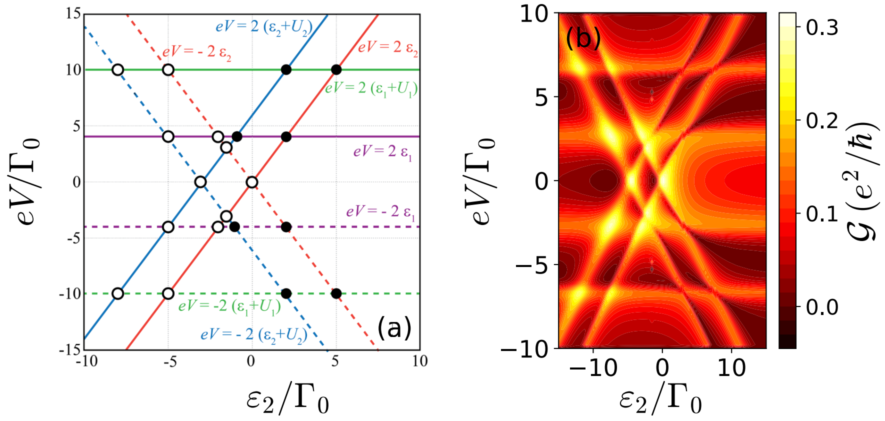

Fig. 8.2. (a) Diagram of energy levels showing the resonance lines corresponding to the conditions $eV = \pm 2\varepsilon_\mu$ and $eV = \pm 2(\varepsilon_\mu + U_\mu)$. Solid lines indicate the alignment with the left resonance ($\mu_L = +eV/2$) while the dashed lines represent crossings with the right reservoir ($\mu_R = -eV/2$). Additionally, the markers denote a crossing of lines leading to maxima (open circles) and minima (solid circles). (b) Differential electric conductances versus the voltage bias between reservoirs V and one of the QD levels ε_2. One may observe that the results agree with the diagram plotted in (a). Parameters: $\varepsilon_1 = 2\Gamma_0$, $U_1 = U_2 = 3\Gamma_0$, $\theta = 0$, $k_B T = 10^{-3}\Gamma_0$ and $a = 1$.

Finally, the transmission presents additional Fano antiresonances as seen in Fig. 8.1d for $\varepsilon = \Gamma_0$. In this case, the maximum values are located at $\omega = \pm\varepsilon$ and $\omega = \pm\varepsilon + U$. For this reason, when $\varepsilon = \Gamma_0$ the system shows a total transparency at $\omega = 0$ instead of an antiresonance like the nontinteracting DQD. Therefore, the number of antiresonances and resonances are increased in the interacting case. Furthermore, for approaching levels $\varepsilon \to 0$, a very narrow antiresonance appears around $\omega = U$ in addition to the antiresonance of the noninteracting case at $\omega = 0$. As expected, these positions correspond to the locations of the BICs shown in Fig. 8.1b. Therefore, this is consistent with the results of the DOS and confirms the robustness of BICs under Coulomb interactions. As a final remark, we would like to emphasize that the replica of the BIC as well as this second narrow antiresonance arise for equal charging energies $U_1 = U_2$. When the intradot charging energies differ, the system will only present the BIC around $\omega = 0$. Nevertheless, it is possible to find a new set of parameters where the BIC may emerge.

8.1.2 Electric transport

Here, we briefly discuss the impact of BICs on the electric response of the DQD system. We follow Eq. (6.16) together with Eqs. (6.15) and (5.57) in order to evaluate the electric current across the system. We remark that this system involves crossing of four resonances: ε_μ and $\varepsilon_\mu + U_\mu$ with $\mu = \{1, 2\}$. This will lead to important consequences in the transport since any level alignment generates narrow antiresonances in the transmission as a result of the BICs. Hence, we display the differential conductance $\mathcal{G}$ as a function of the voltage bias V and a gate of one ε_2 in Fig. 8.2b for a given set of parameters ($\varepsilon_1 = 2\Gamma_0$, $U = 3\Gamma_0$ and $T_L = T_R = T = 10^{-3}\Gamma_0$). As expected, when one of these four resonances aligns with the electrochemical potential of a fermionic reservoir the conductance is maximal. Nevertheless, the alignment between two resonances crossing $\pm eV/2$ simultaneously causes $\mathcal{G}$ to abruptly drop and, consequently, a minimum arises. This can be understood easily with the diagram of Fig. 8.2a. Here, we plot the lines corresponding to the resonant conditions $eV = \pm 2\varepsilon_\mu$ and $eV = \pm 2(\varepsilon_\mu + U_\mu)$. Solid lines denote a crossing of a resonance with $+eV/2$ whereas dashed lines denote alignment with $-eV/2$. Therefore, when two of these lines cross, a maximum will be generated if the QD resonances are not aligned (open circles). On the other hand, if the QD resonances are located at the same position, a BIC emerges and, consequently, the conductance presents a local minimum (solid circles). As observed in Fig. 8.2, the diagram agrees with the numerical results of the differential conductance.

8.1.3 Thermoelectric transport

We now proceed to the thermoelectric transport response of the system. We first analyze the linear thermoelectric conductance $\mathcal{L}_0$ computed from Eq. (6.21b) when tuning the Fermi energy ε_F. We recall that at low voltage $\mathcal{L}_0$ depends on the derivative of the transmission [Eq. (6.22b)]. Hence, $\mathcal{L}_0$ is a magnitude sensitive to changes in the transmission, which helps with the detection of narrow resonances.

First, we plot $\mathcal{L}_0$ for a DQD with close energy levels ($\varepsilon = 0.05\Gamma_0$) in Fig. 8.3a. The thermoelectric conductance exhibits asymmetric resonances around $\varepsilon_F = 0$ and $\varepsilon_F = \Gamma_0$ and a smooth variation at $\varepsilon = 0.5\Gamma_0$. Each of these asymmetric resonances is caused by the antiresonances of the transmission (blue curve in Fig. 8.1d). Therefore, the narrow asymmetric resonances are attributed to the Fano antiresonances generated by the BICs and the resonance at $\varepsilon_F = 0.5\Gamma_0$ is due to the central antiresonance in $\mathcal{T}(\omega)$. Besides, $\mathcal{L}_0$ reverses its sign each time that ε_F aligns with an extremum of $\mathcal{T}(\omega)$. Nevertheless, the contribution of the maxima is not noticeable in Fig. 8.3a since the minima, in comparison, induce sharper variations. In contrast, we illustrate the case of $\varepsilon = \Gamma_0$ in Fig. 8.3b. Since the resonances and antiresonances of the transmission (red curve in Fig. 8.1d) have comparable widths, all changes of sign in $\mathcal{L}_0$ are visible. Another important fact is that $\mathcal{L}_0$ reaches values

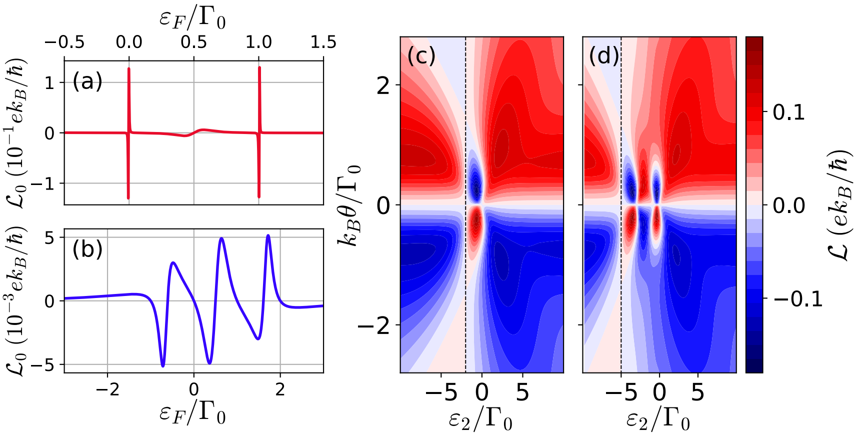

Fig. 8.3. (a) Linear thermoconductance $\mathcal{L}_0$ versus the Fermi energy ε_F of a DQD system with energy levels $\varepsilon_1 = -\varepsilon_2 \equiv \varepsilon = 0.05\Gamma_0$. The intradot charging energies of the QDs are $U_1 = U_2 = U = \Gamma_0$ and the background temperature is $k_BT = 0.001\Gamma_0$. (b) Same as (a) but for $\varepsilon = \Gamma_0$. (c) Differential thermoconductance $\mathcal{L}$ as a function of the thermal bias θ and the level position ε_2 for $\varepsilon_1 = 2\Gamma_0$ in the noninteracting case $U = 0$ with a background temperature $k_BT = 0.001\Gamma_0$. The black dashed line denotes the case of $\varepsilon_2 = -\varepsilon_1$ which yields $\mathcal{L}(\theta) = 0$. (d) Same as (c) but for interacting QDs with intradot charging energy $U = 3\Gamma_0$. Here, the dashed line represents the case $\varepsilon_2 = -(\varepsilon_1 + U)$ which also yields $\mathcal{L}(\theta) = 0$.

of 0.12 $ek_B/\hbar$ (20 nA/K) when the BICs is present. Therefore, systems with BICs are interesting devices for their thermoelectric applications.

More appealing results can be found when we compute the differential conductance $\mathcal{L}$ [Fig. 8.3c and Fig. 8.3d]. In comparison with Secs. 7.1 and 7.3, the DQD system may show more complex and diverse patterns of $\mathcal{L}$. The reason is that the tuning of any parameter can modify the transmission function giving new thermoelectric behavior of the system. Therefore, we expect strong departures from Fig. 7.2b and Fig. 7.9b. In fact, Fig. 8.3c and Fig. 8.3d confirm our expectations by showing a different pattern for a thermoelectric conductance as a function of the thermal bias θ and the energy level of one dot ε_2. In these plots we fix $\varepsilon_1 = 2\Gamma_0$ and consider both noninteracting $U_1 = U_2 = 0$ (Fig. 8.3c) and interacting $U_1 = U_2 \equiv U = 3\Gamma_0$ (Fig. 8.3d) QDs. For the noninteracting system, we recall the configuration $\varepsilon_1 = -\varepsilon_2$ leads to a symmetric transmission such that $\mathcal{T}(\omega) = \mathcal{T}(-\omega)$ (see Fig. 8.1c as an example). Consequently, $\mathcal{L} = 0$ for all values of $k_B\theta$ because both terms appearing in Eq. (6.20b) are integrals of a combination of even and odd functions. In the regime when $\varepsilon_2 = -\varepsilon_1$ and $\varepsilon_2 = 0$, we find a nonlinear behavior of $\mathcal{L}$ as a function of θ in which a change of sign can also occur. Such regime may be understood in the same way as with the thermocurrent in Secs. 7.1.1 and

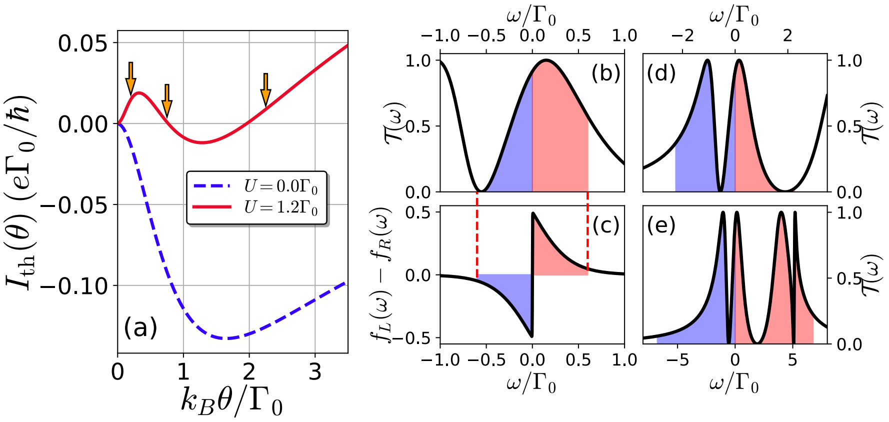

Fig. 8.4. (a) Thermocurrent versus the thermal bias θ of a DQD system with level positions $\varepsilon_1 = 4\Gamma_0$ and $\varepsilon_2 = -1.05\Gamma_0$ in the noninteracting and interacting case. The background temperature is $k_BT = 0.001\Gamma_0$. The arrows show the points of the thermocurrent in which the transmission function is displayed in (b), (d) and (e) for thermal biases $\theta = 0.2\Gamma_0,\ 0.75\Gamma_0$ and $2.25\Gamma_0$, respectively. The color filling in the transmission denotes the part of the transmission which contributes to the electric transport at the given θ. The salmon (purple) color indicates electron (hole) flux around the DQD as observed by the difference of Fermi functions in (b). The boundaries where the electron or hole flux becomes negligible are given by the red dashed lines delimiting the range of energies that should be considered.

7.3.3. The transmission has an asymmetric shape with two resonances centered at $\omega = \varepsilon_1$ and $\omega = \varepsilon_2$, where the latter is closer to the Fermi energy ε_F. Therefore, a small heating of the left reservoir causes an electron flow from the right reservoir yielding a negative $\mathcal{L}$. When we further increase T_L, the thermally excited electrons flow from the left reservoir through the second resonance. Thereupon, transport in the opposite direction is favored yielding a sign reversal. Since a negative θ means a heating of the right reservoir, the thermoelectric transport is reversed but giving the same physics. In contrast, the pattern of the interacting system shown in Fig. 8.3d exhibits several sign reversals of $\mathcal{L}$. As observed in Fig. 8.1d, the transmission involves multiple resonances around ε_F which appears to be a condition to find nonlinear effects in the thermoelectric transport. Additionally, the case $\varepsilon_2 = -\varepsilon_1$ which induces $\mathcal{L} = 0$ gets slightly deformed and, the transmission function is now exactly symmetric for $\varepsilon_2 = -5\Gamma_0$ $[\varepsilon_2 = -(\varepsilon_1 + U)]$ also leading to zero thermoelectrical conductance.

As in previous sections, the patterns found in the thermoelectric conductance suggest that the thermocurrent may exhibit several nontrivial zeros. A representative result of the thermocurrent is given in Fig. 8.4a for the noninteracting and interacting cases. Interestingly, the thermocurrent displays two sign reversals in the interacting case (solid curve). On the contrary, I_{th} does not cross the θ-axis in the noninteracting case. In comparison with a voltage-driven case, we observe that the current here presents a region of negative thermoelectric conductance which would be comparable with the current-voltage characteristics of Esaki diodes [246]. In this case, we obtain a peak-to-valley ratio (the distance between the maximum and minimum of the currents divided by the current peak) of the order of 1.7.

The mechanism which induces the nontrivial zeros of $I_{\mathrm{th}}(\theta)$ is equivalent to the previous sections. Nevertheless, we give an alternative scheme in Figs. 8.4b-e which may give a clearer understanding. From Eq. (6.18) we identify two different terms: the transmission function $\mathcal{T}(\omega)$ and the difference of Fermi functions $f_L(\omega) - f_R(\omega)$. The temperature difference induces large changes to $f_L - f_R$ which, as θ is increased, has a larger effective energy range (filled areas in Fig. 8.4c). It ranges approximately between $\pm 3k_B\theta$. Additionally, $f_L - f_R$ is an antisymmetric function of the energy ω which is positive (negative) for energies above (below) the Fermi energy. Since this term is multiplied by the transmission function, the shape of $\mathcal{T}(\omega)$ would strongly influence the carrier transport. When $k_B\theta = 0.2\Gamma_0$, the electron contribution (salmon color) is stronger than the holes (purple color). Therefore, the net current is positive (first arrow in Fig. 8.4a). If θ increases, the window of energies opens and the shape of the transmission becomes more complex (Fig. 8.4d). Clearly, the hole transport surpasses the electron flow inducing a reversal of the net current. Finally, at larger thermal biases the effective energy area enhances and the transmission has a different shape which now favors the electronic flow in the opposite direction inducing an additional change of sign for I_{th}. In general, we believe that the sign reversal of the thermocurrent is a generic phenomenon which appears for systems characterized by a transmission function with more than one resonance at opposite energy positions with respect to the Fermi energy.

8.2 Coulomb drag and orbital Kondo effects

The parallel configuration can be used for investigating different intriguing phenomena. Previous section focused on the role of BICs to the electronic transport and the influence of intradot interactions. Instead, we now study the Coulomb drag effect presented in Sec. 1.3.2. We recall that the system (see Fig. 8.5) consists of two QDs, each of them with an energy level ε_μ, where $\mu = 1, 2$, assuming large intradot Coulomb interactions such a way that each dot can only be occupied by one electron. Additionally, each dot is connected to two different fermionic reservoirs

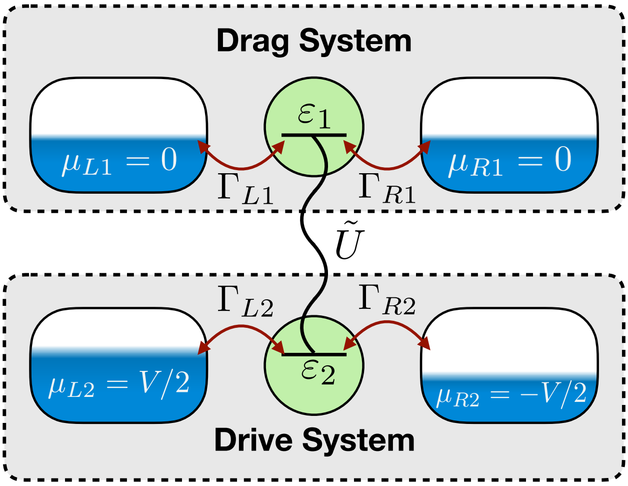

Fig. 8.5. Scheme illustrating a Coulomb-coupled DQD setup consisting of (1) a QD attached to two reservoirs at equilibrium (drag system) and (2) another QD connected to two reservoirs biased with an applied voltage V (drive system). Both systems interact with each other electrostatically with $\tilde{U}$ being the interdot charging energy. No tunnel coupling between the dots is considered in the setup.

whose hybridization matrices will be defined as

$$\mathbf{\Gamma}_{L1} = \begin{pmatrix} \Gamma_{L1} & 0 \\ 0 & 0 \end{pmatrix}, \ \mathbf{\Gamma}_{L2} = \begin{pmatrix} 0 & 0 \\ 0 & \Gamma_{L2} \end{pmatrix}, \tag{8.13}$$

$$\mathbf{\Gamma}_{R1} = \begin{pmatrix} \Gamma_{R1} & 0 \\ 0 & 0 \end{pmatrix}, \ \mathbf{\Gamma}_{R2} = \begin{pmatrix} 0 & 0 \\ 0 & \Gamma_{R2} \end{pmatrix}. \tag{8.14}$$

Instead of using the matrix notation, we will employ the coefficients $\Gamma_{\alpha\mu}$ with $\alpha = \{L, R\}$. Here, we deal with two almost isolated systems: a drive system (bottom panel of Fig. 8.5) where a voltage bias V is applied symmetrically to the reservoirs and a drag system (top panel of Fig. 8.5) which is at equilibrium. Both systems feel each other via an interdot Coulomb interaction $\tilde{U}$ which appears when both levels are occupied. This interaction will be responsible for inducing a current across the unbiased drag system just due to the application of a voltage bias in the drive system.

We consider the Anderson Model for a DQD [Eq. (5.2)] with single levels neglecting the spin degree of freedom. Experimentally, a large magnetic field B can be applied to obtain such setup. On the other hand, the interdot Coulomb interaction is still present in the Hamiltonian. This allows us to view the DQD as a single QD where μ now plays the role of a pseudospin operator following the change of notation $\sigma \to \mu$. Additionally, the reservoirs are dependent of the pseudospin which implies a change of notation of the lead subindex $\alpha \to \alpha\mu$. Therefore, we can still use the results given in Sec. 5.2 and employ Eq. (5.45) as the retarded Green's function of the system. The occupation $\bar{n}_\mu$ will be also obtained by solving Eq. (7.1). Within this scheme, the stability diagram shows regions characterized by different number of electrons occupying the QDs. This can be seen in Fig. 8.6a where we plot the charge susceptibility defined as

$$\delta_\varepsilon \bar{n} = \sum_\mu \frac{d\bar{n}_\mu}{d\varepsilon_\mu} \,. \tag{8.15}$$

When we tune the energy levels ε_μ when $\tilde{U} > \Gamma_0$, we distinguish lines separating four different regions of $(\bar{n}_1, \bar{n}_2)$ and in the intersection of these lines ($\varepsilon_1 = \varepsilon_2 = 0$ and $\varepsilon_1 = \varepsilon_2 = -\tilde{U}$) we find the triple points forming the shape of a honeycomb diagram as in Fig. 1.7a.

In order to study the transport flowing through both systems we define the drag $I_{\text{dg}} = (I_{L1} - I_{R1})/2$ and drive $I_{\text{dv}} = (I_{L2} - I_{R2})/2$ currents. Due to the charge conservation law of Eq. (3.19), the current remains unaltered and also follows Eq. (6.18) for both systems in Fig. 8.5. This leads to dramatic consequences because I_{dg} depends only on the difference between the Fermi functions of the drag system $f_{L1} - f_{R1}$ and, since the drag system is at equilibrium, I_{dg} vanishes completely for any Green's function inserted in $\mathcal{T}$. Thus, the Green's function approach seems to predict the absence of drag effect in DQDs, which is wrong. The origin of the nonexisting current takes place in Eq. (6.12) which for our configuration becomes

$$I_{\alpha\mu} = \frac{e}{h} \int d\omega \left| G^r_{\mu,\mu} \right|^2 \left[\Sigma^>_{\text{tot},\mu} \Sigma^<_{\text{tun},\alpha\mu} - \Sigma^<_{\text{tot},\mu} \Sigma^>_{\text{tun},\alpha\mu} \right] . \tag{8.16}$$

When we assume that the total self-energy only has the contribution of the tunneling processes ($\Sigma^{</>}_{\text{tot},\mu} \approx \Sigma^{</>}_{\text{tun},\mu}$), the terms in brackets of Eq. (8.16) are nullified. This means that the tunneling transitions in and out the reservoir $\alpha\mu$ are equally likely yielding a zero drag current. Hence, as explained in Sec. 6.1, the self-energy of the interacting Hamiltonian $\Sigma_{\text{int},\mu}$ should also be considered.

8.2.1 The interacting self-energy

The aim of this section is to analyze the interacting self-energy $\Sigma_{\text{int},\mu}$ and its influence in the drag current. We apply a perturbation expansion for $\mathcal{H}_{\text{inter}}$ [Eq. (5.4)] using Feynman diagrams. The lowest order in the expansion gives the Hartree approach characterized by $\Sigma^r_{\text{int},\mu} = \tilde{U}\bar{n}_{\bar{\mu}}$ where $\bar{\mu} = \{2,1\}$ for $\mu = \{1,2\}$. However, the lesser and greater self-energies are zero in this case $\Sigma^{<,>}_{\text{int},\mu} = 0$ and the drag current is still absent.

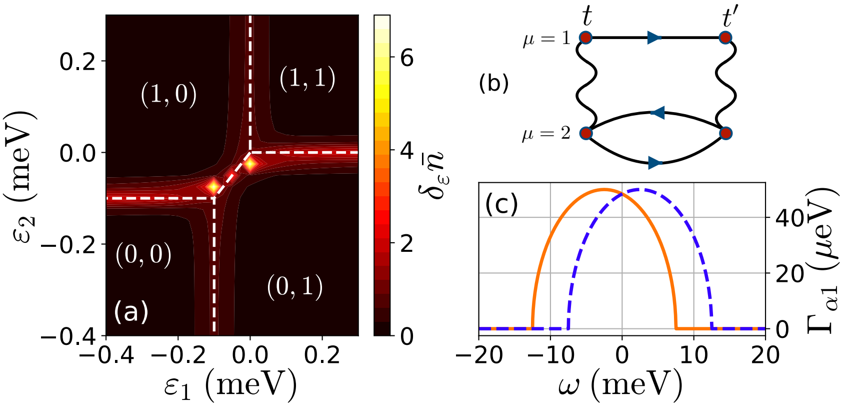

Fig. 8.6. (a) Stability diagram of the whole system indicating the most favorable dot occupations (n_1,n_2) when tuning the level positions ε_μ. The bright colors indicate the regions where the occupation varies given by Eq. (8.15). The honeycomb vertex formed by the connection between the triple points is due to the interdot Coulomb interactions $\tilde{U}$ between QDs. (b) Lowest order nonzero Feynman diagram for the interacting self-energy $\Sigma_{\text{int},\mu}(t,t')$. The solid straight lines indicate the Green's function of the μ layer. The arrow denotes whether the Green's function is time-ordered ($t \to t'$) or anti-time-ordered ($t' \to t$). The sinusoidal lines denote the interdot charging energy $\tilde{U}$. (c) Hybridization function $\Gamma_{\alpha 1}$ of the drag system versus the energy. The solid (dashed) line indicates the connection of the QD to the left (right) reservoir. We take realistic parameters [72]: $\tilde{U} = 0.1$ meV, $\gamma_{L1} = \gamma_{R1} = 7$ μeV, $\gamma_{L2} = \gamma_{R2} = 25$ μeV, $\Lambda = 10$ meV, $T = 21$ mK, $\tilde{\varepsilon}_1 = 2.5$ meV and $\tilde{\varepsilon}_2 = 0$.

Consequently, we include the next-order Feynman diagram sketched in Fig. 8.6b. Each line of the diagram denotes the Green's function which goes from time t to t' or viceversa, following their corresponding arrows. Additionally, the diagram represents three propagators, one in the drag ($\mu = 1$) and two in the drive ($\mu = 2$) QDs. The layers denoted by μ are connected with each other via the interdot interaction energy $\tilde{U}$ represented with sinusoidal lines. Reading off the diagram, the interacting self-energy at this order can be extracted:

$$\Sigma_{\text{int},\mu}(t,t') \approx \tilde{U}^2 G_{\mu,\mu}(t,t') G_{\bar{\mu},\bar{\mu}}(t,t') G_{\bar{\mu},\bar{\mu}}(t',t) \ . \tag{8.17}$$

Note that now Eq. (8.17) comprises the contribution of both systems. This is important for obtaining a nonzero drag because I_{dg} should depend on the applied voltage of the drive system and Eq. (8.17) fulfills this requirement. Remarkably, the product of Green's functions of the $\bar{\mu}$ system can be understood as a polarizability function $P_{\bar{\mu}}(t,t') = G_{\bar{\mu},\bar{\mu}}(t,t') G_{\bar{\mu},\bar{\mu}}(t',t)$. Actually, this function gives the leading-order contribution of the fluctuations in the occupation of the $\bar{\mu}$ system which at all orders in the Fourier space is defined as

$$P_{\bar{\mu}}(\omega) = \int d\omega e^{-i\omega t}\langle n_{\bar{\mu}}(0) n_{\bar{\mu}}(t)\rangle \ , \tag{8.18}$$

which corresponds to the case where all possible intermediate transitions in the bubble of Fig. 8.6 are considered. For simplicity, we restrict ourselves to the solution of Eq. (8.17) which already gives appropriate results. The lesser and greater Green's functions are found by applying Langreth rules [Eq. (4.41)]. An important feature of this interacting self-energy is that it is also able to exhibit an Abrikosov-Suhl resonance in the local DOS giving rise to an orbital Kondo system at low temperatures when a voltage is applied both subsystems (drag and drive). Replacing Eq. (8.17) into Eq. (8.16) and resorting to the Fourier space, the drag current can be split into $I_{\mathrm{dg}} = I^{+}_{\mathrm{dg}} + I^{-}_{\mathrm{dg}}$ obtaining

$$I^{\pm}_{\mathrm{dg}} = \pm\frac{e\tilde{U}}{2h}\int d\omega\frac{d\omega_1}{2\pi}\frac{\Delta\Gamma_1(\omega)}{\Gamma_1(\omega)}\rho_1(\omega)\rho_1(\omega-\omega_1)f^{+}_1(\omega)f^{-}_1(\omega-\omega_1)P^{\pm}(\omega_1) \ , \tag{8.19}$$

where $f^{+}_{\alpha\mu}(\omega) = f_{\alpha\mu}(\omega)$, $f^{-}_{\alpha\mu}(\omega) = 1 - f_{\alpha\mu}(\omega)$, $P^{+}(\omega) = P^{>}(\omega)$, $P^{-}(\omega) = P^{<}(\omega)$ and $\Delta\Gamma_1(\omega) = \Gamma_{L1}(\omega) - \Gamma_{R1}(\omega)$. Eq. (8.19) provides intriguing features about how the drag current is generated. In principle, one condition to find drag current is to have different hybridization constants $\Gamma_{L1} \neq \Gamma_{R1}$. However, the condition is actually more restrictive. A manipulation of Eq. (8.19) taking into account that $P^{<}_2(\omega) = P^{>}_2(-\omega)$ gives the following condition

$$\Gamma_{L1}(\omega)\Gamma_{R1}(\omega') - \Gamma_{R1}(\omega)\Gamma_{L1}(\omega') \neq 0 \ . \tag{8.20}$$

This expression gives the condition for the coupling between dots and fermionic reservoirs. We would like to emphasize that constant hybridization functions do not obey Eq. (8.20) and $\Gamma_{\alpha 1}$ must hence be energy dependent. In fact, we need nonproportional hybridization functions ($\Gamma_{L1}(\omega) \neq C\Gamma_{R1}(\omega)$ with C being a proportionality constant) in order to guarantee a nonzero drag current. For this reason, we now consider tight-binding tunnel self-energies defined by

$$\begin{aligned}\Sigma_{\alpha\mu}(\omega) \quad &= \quad \gamma_{\alpha\mu}\left(\omega_2 + \mathrm{sgn}(\omega_2)\theta(\Lambda_{\alpha\mu}[|\omega_2| - 1])\sqrt{\omega_2^2 - 1}\right) \\ &\qquad + i\gamma_{\alpha\mu}\theta(\Lambda_{\alpha\mu}[1 - |\omega_2|])\sqrt{1 - \omega_2^2} \ , \end{aligned} \tag{8.21}$$

where $\omega_2 = (\omega - \tilde{\varepsilon}_{\alpha\mu})/\Lambda_{\alpha\mu}$. Here, $\gamma_{\alpha\mu}$ is the amplitude of the tunneling self-energy. Additionally, $\tilde{\varepsilon}_{\alpha\mu}$ and $\Lambda_{\alpha\mu}$ are its position and its bandwidth, respectively. As explained previously, the hybridization function is defined as $\Gamma_{\alpha\mu}(\omega) = -2\mathrm{Im}[\Sigma_{\alpha\mu}]$. This definition for tunnel self-energies corresponds to the so-called Newns-Anderson model with shifted bands [247]. A tuning of the parameters involving Eq. (8.21) gives us

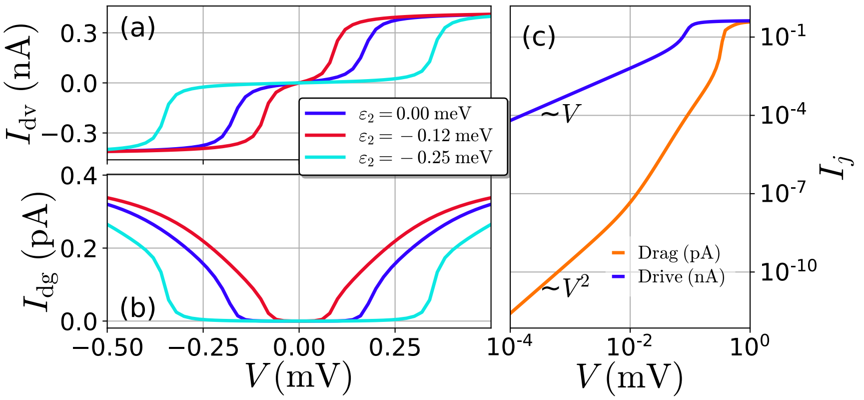

Fig. 8.7. (a) Drive current as a function of the voltage V applied to the drive system for different values of ε_2. (b) Drag current as a function of the voltage bias V applied to the drive system for different values of ε_2. (c) Drive and drag currents as a function of the voltage bias in a logarithmic scale showing that the currents follow $I_{\mathrm{dg}} \propto V^2$ and $I_{\mathrm{dv}} \propto V$. All panels are taken following the hybridization function and parameters of Fig. 8.6.

a setup where Eq. (8.20) is fulfilled. At this stage, we consider that the left and right hybridization functions of the drag system are centered symmetrically with respect to the Fermi energy such as $\tilde{\varepsilon}_{L1} = -\tilde{\varepsilon}_{R1} = \tilde{\varepsilon}_1$ whereas the remaining parameters are equal in both leads meaning that $\gamma_{L1} = \gamma_{R1}$ and $\Lambda_{L1} = \Lambda_{R1} \equiv \Lambda$. As a result, $\Gamma_{\alpha 1}$ becomes shifted semiellipses (see Fig. 8.6c) with equal width and height.

When Eq. (8.20) is satisfied, we are able to encounter a nonzero current flowing through the drag system. One should notice that the voltage dependence of Eq. (8.19) is totally given by the polarizability term $P_2^{>,<}(\omega)$. In addition to Eq. (8.19), we calculate the drive current using Eq. (6.16) because when the system has a voltage or thermal bias, the effect of the interacting self-energy is negligible over the tunneling self-energy. Then, we depict the drive and drag currents driven by the voltage applied to the drive system in Fig. 8.7a and Fig. 8.7b, respectively. For low voltages, we observe that both currents are almost zero until the resonance of the drive system aligns with the electrochemical potentials of the reservoirs $\mu_{\alpha 2}$ and this level starts to play a role in the quantum transport. As expected, we found that the drive current is antisymmetric with V and at low voltages the system exhibits ohmic response (blue line in Fig. 8.7c). In contrast, the drag current is symmetric with V following a parabolic shape at lowest order (orange line in Fig. 8.7c) with a sign denoted by $\Delta\Gamma_1$. This happens for our set of parameters because the drive system does not obey Eq. (8.20) replacing $1 \to 2$ and the linear term vanishes when $\Gamma_{L2} \propto \Gamma_{R2}$. When this condition is satisfied, we

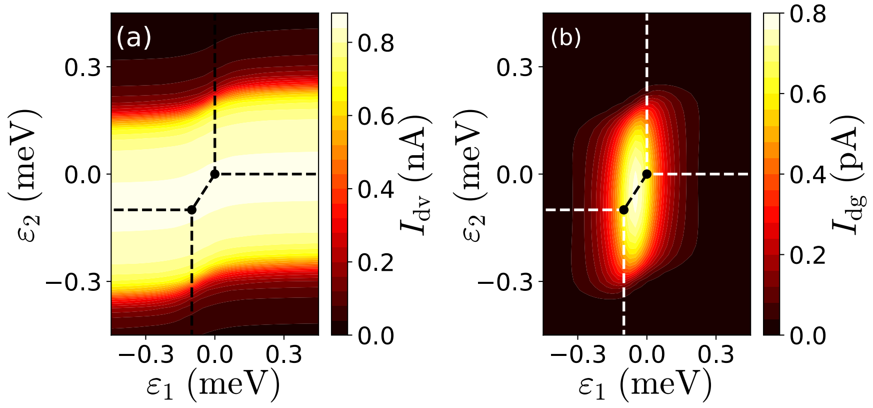

Fig. 8.8. (a) Drive current as a function of the energy levels ε_1 and ε_2 when a voltage of $V = 0.5$ meV is applied to the drive system. (b) Drag current as a function of the energy levels ε_1 and ε_2 when a voltage of $V = 0.5$ meV is applied to the drive system. In both panels, the dashed lines indicate the change of occupation in the stability diagram of Fig. 8.6 whereas the solid dots represent the triple points. Same parameters as in Fig. 8.6.

also find a linear regime and a broken symmetry in the drag current.

More information can be extracted by analyzing the current with a tuning of the energy levels of both QDs at a given voltage (Fig. 8.8). The results of the drive system (Fig. 8.8a) are expected. When the energy level is between the electrochemical potential of the reservoirs such as $|V| > |\varepsilon_2|$, electrons flow through the system giving rise to a drive current. Additionally, the drive current remains almost unaltered when ε_1 is tuned except a shift of the transport window around the triple points. Nevertheless, the drag current is sensitive for both energy levels. $I_{\rm dg}$ depends on ε_2 because a current in the drive system is needed to generate drag meaning that the condition $|V| > |\varepsilon_2|$ has to be also satisfied. On the other hand, the drag current will only be visible around the triple points because the transport in the drag system depends on the fluctuations in the occupation of the dot of the drive system. This means that cotunnel transitions involving both QDs govern the drag current. These results are in agreement with recent experiments [71, 72].

8.3 Two-impurity Kondo model

Contrary to the previous sections, we will now discuss a different system which involves Kondo correlations. We return to the two-terminal configuration, but now the DQD will be serially-coupled to the leads as sketched in Fig. 8.9. Each QD will play the role of an artificial magnetic impurity in the Fermi liquid regime $T < T_K$ with infinite intradot charg-

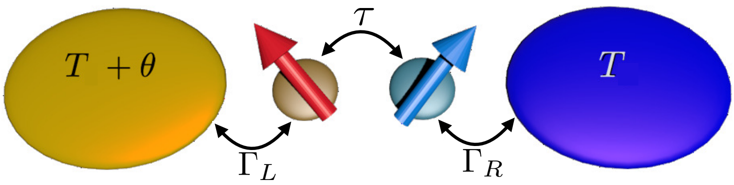

Fig. 8.9. Sketch of the two-impurity Kondo system. The setup consists of two QDs acting as artificial impurities connected to each other with a tunnel coupling of amplitude τ. Each dot is also attached to a reservoir whose hybridization constant is denoted as Γ_α where $\alpha = L$ (R) for the left (right) reservoir. The left reservoir is heated at a temperature $T_L = T + \theta$ whereas the right reservoir remains at background temperature $T_R = T$ yielding a thermal bias in the system.

ing energy $U \to \infty$. Here, we neglect the interdot Coulomb interactions $\tilde{U} \to 0$ and we consider a finite tunnel coupling τ between QDs, which is necessary for obtaining nonzero current in this system. Therefore, this section discusses the thermally-driven transport generated across a two-impurity Kondo system in the Fermi liquid regime and comprises the results obtained in Sierra *et al.* [242]. This is relevant for characterizing the response of two coupled Kondo impurities under thermal biases.

In this section, we recover the SBMFT for the U-infinite slave-boson Hamiltonian of a DQD [Eqs. (5.12), (5.13) and (5.14) taking $\mu = \{L, R\}$]. We want to emphasize that now the hybridization matrix takes the following form:

$$\mathbf{\Gamma}_L = \begin{pmatrix} \Gamma_L & 0 \\ 0 & 0 \end{pmatrix} , \ \mathbf{\Gamma}_R = \begin{pmatrix} 0 & 0 \\ 0 & \Gamma_R \end{pmatrix} , \tag{8.22}$$

which means that each dot is only connected with one reservoir. For this reason, from now on we change the notation $\alpha \equiv \mu = \{L, R\}$. This configuration leads to the retarded Green's function of a noninteracting DQD given by Eq. (5.40) but for the renormalized parameters $\Gamma_\alpha \to \tilde{\Gamma}_\alpha = |b_\alpha|^2 \Gamma_\alpha$ and $\varepsilon_\alpha \to \tilde{\varepsilon}_\alpha = \lambda_\mu + \varepsilon_\alpha$. Thus, we have a new set of mean-field parameters which can be evaluated solving Eqs. (5.102) and (5.103) which they read

$$\sum_i A_{i\alpha} J_\alpha(\omega_i) + B_{i\alpha} J_{\bar{\alpha}}(\omega_i) = 1 - N \frac{\tilde{\Gamma}_\alpha}{\Gamma_\alpha} , \tag{5.102}$$

$$\sum_i C_{i\alpha} J_\alpha(\omega_i) + D_{i\alpha} J_{\bar{\alpha}}(\omega_i) = (\tilde{\varepsilon}_\alpha - \varepsilon_\alpha) N \frac{\tilde{\Gamma}_\alpha}{\Gamma_\alpha} , \tag{5.103}$$

where the coefficients were expressed as

$$A_{i\alpha} = \frac{1}{\pi} \frac{\tilde{\Gamma}_\alpha M(\omega_i)}{\prod_{j \neq i} (\omega_i - \omega_j)} , \ B_{i\alpha} = \frac{1}{\pi} \frac{|\tilde{\tau}|^2 \tilde{\Gamma}_{\bar{\alpha}}}{\prod_{j \neq i} (\omega_i - \omega_j)} , \tag{5.104}$$

8.3.1 Kondo temperature

First, we discuss the response of the width of both Kondo resonances under the application of a thermal bias. We restrict ourselves to the deep Kondo regime by setting the energy levels at $\varepsilon_L = \varepsilon_R = -3.5\Gamma_0$ where $\Gamma_0 \equiv \Gamma_L = \Gamma_R$, which is the range of parameters where the SBMFT is valid. Following Eq. (7.12) and assuming $D = 100\Gamma_0$, the Kondo temperature for a single dot is $T_K = 0.0016\Gamma_0$. Nevertheless, we should consider a global Kondo temperature of the system which takes into account the tunnel coupling between artificial impurities [139]:

$$T_K(\tau) = \frac{T_K}{\sqrt{1+\left(\frac{\tau}{\Gamma_0}\right)^2}} \exp\left[\frac{\tau}{\Gamma_0}\tan^{-1}\left(\frac{\tau}{\Gamma_0}\right)\right]. \tag{8.23}$$

For simplicity, we denote $T_K \equiv T_K(\tau)$ for the remaining of this section. Now, we study the Kondo resonance width $\tilde{\Gamma}_\alpha$ due to a thermal bias by solving Eqs. (5.102) and (5.103). As in Sec. 7.3.2, $\tilde{\Gamma}_\alpha$ can be interpreted as the effective Kondo temperature of the α Abrikosov-Suhl resonance. Therefore, we can study the response of each Kondo impurity individually. In Fig. 8.10 we depict the width of the Kondo resonances for three different τ. We distinguish three scenarios where $\tilde{\Gamma}_\alpha$ behaves differently, namely, (a) the weak coupling regime $\tau/\Gamma_0 < 1$, (b) the intermediate regime $\tau/\Gamma_0 \approx 1$ and (c) the strong coupling regime $\tau/\Gamma_0 > 1$.

In the weak coupling regime (Fig. 8.10a) each Kondo resonance shows a different behavior. The Kondo temperature of the hot reservoir ($\tilde{\Gamma}_L$) at low thermal bias remains almost constant as expected from the Kondo regime. When $\theta \approx T_K$, $\tilde{\Gamma}_L$ drops abruptly following the scaling regime and then, at higher temperature differences, the left Kondo resonance is totally quenched. However, $\tilde{\Gamma}_R$ is almost unaltered when heating the left reservoir and, at large θ, behaves as an independent single impurity system. In contrast, both $\tilde{\Gamma}_L$ and $\tilde{\Gamma}_R$ are affected by the thermal bias in the intermediate regime (Fig. 8.10b). In the scaling regime of temperatures ($\theta \approx T_K$), both widths decay with the thermal bias. Nevertheless, the impurity connected to the cold reservoir has a Kondo temperature that decays slower than the second one. In the end, $\tilde{\Gamma}_R$ reaches a constant value whereas $\tilde{\Gamma}_L$ is quenched at large θ. Finally, the two-impurity system behaves as a single dot at low thermal biases in the strong coupling regime as sketched in Fig. 8.10c. Both Kondo temperatures follow the same drop as θ is increased. Nevertheless, this does not hinder the dot of the cold reservoir to fully decouple from the QD of the hot reservoir at very large θ. Therefore, $\tilde{\Gamma}_R$ reaches a constant Kondo temperature (dashed line in Fig. 8.10c) yielding a single-impurity system and $\tilde{\Gamma}_L$

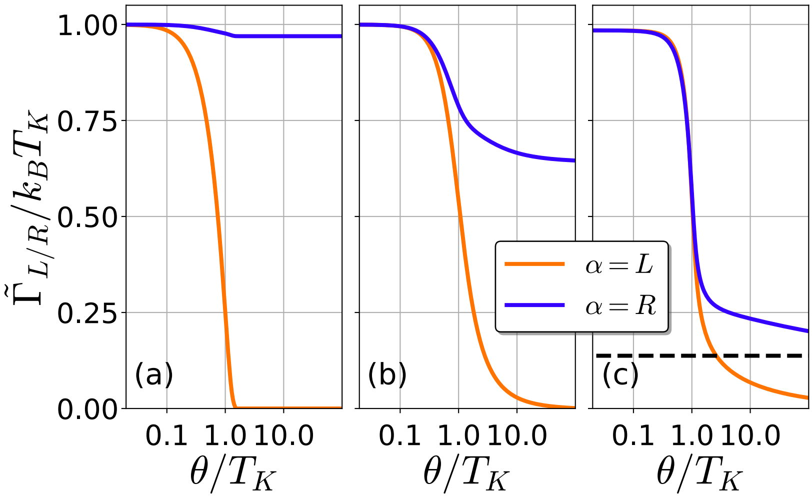

Fig. 8.10. Renormalized hybridization constant Γ_α as a function of the thermal bias θ for the three values of τ/Γ_0 showing different parameter regimes: (a) weekly coupling ($\tau = 0.25\Gamma_0$), (b) intermediate ($\tau = \Gamma_0$) and (c) strong coupling ($\tau = 2.5\Gamma_0$) regimes. The subindex $\alpha = \{L, R\}$ denotes the left L and right R artificial impurity. We highlight that Γ_α can be understood as effective Kondo temperatures $T_{K\alpha}$ of the α impurity. Parameters: $\varepsilon_L = \varepsilon_R = -3.5\Gamma_0$, $k_BT = 10^{-5}\Gamma_0$, $D = 100\Gamma_0$, $\mu_\alpha = \varepsilon_F = 0$ and $\Gamma_L = \Gamma_R = \Gamma_0$.

decays to zero. Therefore, the decoupling of the two-impurity system is always present at large θ for all orders of τ/Γ_0 obtaining a Kondo resonance induced by the cold reservoir, in contrast to Sec. 7.3 where the Kondo resonance of the single impurity fully quenches although the dot is also attached to the cold reservoir.

8.3.2 Thermoelectric and thermal transport

We now proceed to the quantum transport response of the two-impurity system driven by a thermal bias. The results are computed following Eqs. (6.16) and (6.17) considering the retarded Green's function given by Eq. (5.40) for the renormarlized parameters ($\tau \to \tilde{\tau}$, $\Gamma_\alpha \to \tilde{\Gamma}_\alpha$ and $\varepsilon_\mu \to \tilde{\varepsilon}_\mu$). Remarkably, the thermocurrent $I(\theta)$ behaves differently for each of the regimes explained above (Fig. 8.11a). In the weak coupling regime $\tilde{\tau}/\tilde{\Gamma} < 1$ the transmission exhibits a single resonance partially located at positive frequencies (see Fig. 8.11c). Therefore, an electron flow is induced in the system and, at a given thermal bias, the thermocurrent reaches a maximum and then quickly vanishes due to the fact that the dots decouple at such values of θ. When the system is in the intermediate regime, the system still contains a single resonance but reaching total transparency $\mathcal{T} = 1$. This leads to a thermocurrent which gradu-

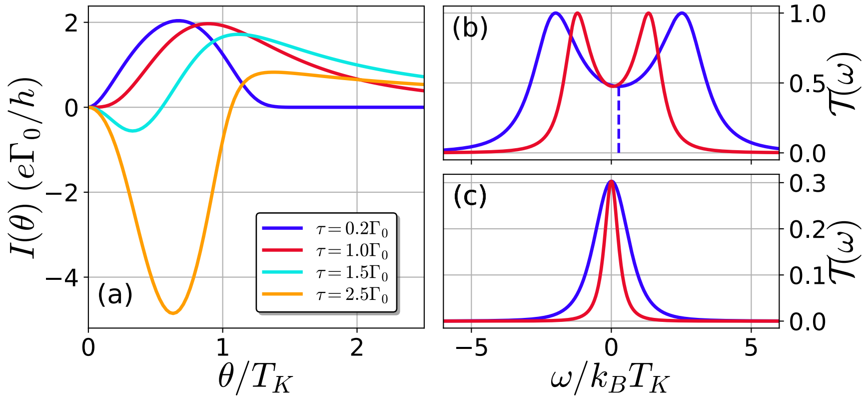

Fig. 8.11. (a) Thermoelectric current $I(\theta)$ versus the thermal bias for different values of the interdot tunnel coupling τ. For clarity, the curves are rescaled with the factors 10^{-6}, 10^{-5}, 2×10^{-5} and 10^{-4} for $\tau = 0.25\Gamma_0$, Γ_0, $1.5\Gamma_0$ and $2.5\Gamma_0$, respectively. (b) and (c) show the transmission function $\mathcal{T}(\omega)$ at two different thermal bias θ for the cases of $\tau > \Gamma_0$ and $\tau < \Gamma_0$, respectively. Same parameters as Fig. 8.10.

ally decays to zero. Nevertheless, we find intriguing differences in the strong coupling regime $\tau/\Gamma_0 > 1$. Now, the transmission function exhibits a combination of bonding and antibonding states (see Fig. 8.11b). We highlight that $\mathcal{T}(\omega)$ is not symmetric as observed from the position of the minimum denoted as a dashed line in Fig. 8.11b. As a consequence, we obtain a nontrivial behavior similar to the results discussed in Secs. 7.1.1, 7.3.3 and 8.1.3. The peak closest to the Fermi level is located at negative energies which induces a negative current. Increasing the thermal bias favors the contribution of the resonance at positive energies yielding electron flow such that, at a given θ, generates a nontrivial zero. After this point, the thermocurrent reverses its sign becoming positive. Finally, the dots decouple at large thermal biases in which $I(\theta)$ vanishes. We would like to note that each thermocurrent curve in Fig. 8.11a has a different scaling. This scaling shows that larger currents are found in the strongly coupled regime. This is an expected result because high values of the tunnel coupling between dots τ are required for an electron to cross the whole DQD system.

In comparison with $I(\theta)$, the heat current $Q(\theta)$ does not vary significantly its shape when tuning θ at every coupling regime as observed in Fig. 8.12a. The only difference is the magnitude of the current which increases with the tunnel coupling τ/Γ_0 giving high values of Q in the strong coupling regime, as in the electric current. Generally, the thermal bias causes two different and opposite effects in the heat transport. On the first hand, the Fourier's law plays a role and the heat current increases with θ. On the other hand, the decoupling of the system at large

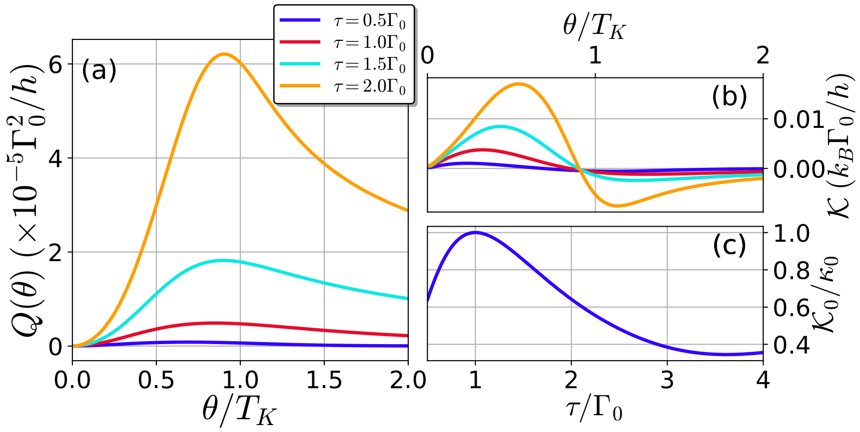

Fig. 8.12. (a) Heat current $Q(\theta)$ versus the thermal bias for different values of the interdot tunnel coupling τ. (b) Differential thermal conductance $\mathcal{K}$ as a function of the thermal bias for several values of τ. (c) Linear thermal conductance $\mathcal{K}_0$ normalized with the thermal quantum conductance κ_0 as a function of the interdot tunnel coupling. This result coincides with the transmission function at the Fermi level such as $\mathcal{K}_0 = \kappa_0 \mathcal{T}(0)$. Same parameters as in Fig. 8.10.

temperatures decreases the heat current. This is also reflected in the sign of the differential thermal conductance $\mathcal{K}$ shown in Fig. 8.12b. At low temperatures, $\mathcal{K}$ increases linearly given by second and higher orders of the current. Eventually, the thermal conductance inverts its sign indicating that the decoupling dominates at large θ impeding transport since the setup turns into two totally disconnected artificial impurity systems. Therefore, the decoupling of the two-impurity system induces a region of negative thermal conductance. Additionally, the linear conductance $\mathcal{K}_0$ describes the behavior of the transmission function $\mathcal{T}(\omega = \varepsilon_F, \tau)$ at very low temperatures $T \to 0$ as observed from Eq. (6.22d). In Fig. 8.12c we depict $\mathcal{K}_0$ renormalized with the thermal quantum conductance κ_0. As expected from Eq. (6.22d) $\mathcal{K}_0$ completely coincides with $\mathcal{T}(0, \tau)$. We find a nonlinear behavior which can be understood as follows: in the weak coupling regime the transmission shows a single peak (Fig. 8.11c) which becomes larger until it shows total transparency in the intermediate coupling regime τ/Γ_0 (maximum in Fig. 8.12b). At higher couplings the peak splits in the bonding and antibonding states yielding a minimum around $\omega = 0$ (Fig. 8.11b) which becomes deeper as τ/Γ_0 increases. At larger couplings, $\mathcal{K}_0$ slightly increases because the minimum of $\mathcal{T}$ shifts.

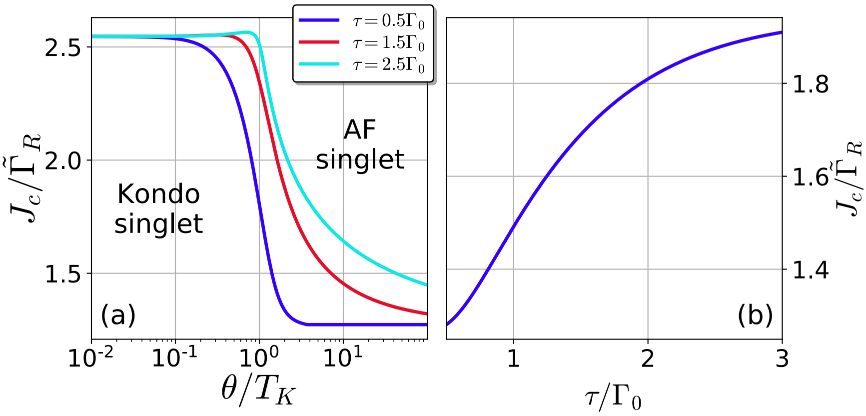

Fig. 8.13. (a) Critical superexchange interaction J_c as a function of the thermal bias θ for different tunnel couplings. The curve indicates the regions where the Kondo singlets or the antiferromagnetic singlets dominate. (b) Critical superexchange interaction J_c as a function of the tunnel coupling τ at a thermal bias of $\theta = 3.1 T_K$. Same parameters as in Fig. 8.10

8.3.3 Antiferromagnetic coupling

In Sec. 1.3.3 we explained that high intradot Coulomb interactions U may lead to a superexchange interaction $J_{\text{ex}} = \tau^2/U$ between the spin states of the QDs. This is important when considering systems of two artificial impurities because at $T = 0$ a QPT can occur at a critical value of the superexchange interacation J_c, as explained in Sec. 2.3.2. This phase transition connects the state which generates two coupled Kondo singlets at $J_{\text{ex}} < J_c$, which is the case studied above for $J_{\text{ex}} = 0$, and the emergence of an antiferromagnetic singlet between the artificial impurities at $J_{\text{ex}} > J_c$. When the system is at a finite temperature $T \neq 0$ the QPT is transformed into a crossover. In our model, we obtain such transition including to the Hamiltonian of Eqs. (5.12), (5.13) and (5.14) an additional term:

$$\mathcal{H} = J_{\text{ex}} \hat{S}_L \cdot \hat{S}_R \,, \tag{8.24}$$

where $\hat{S}_L$ ($\hat{S}_R$) is the spin state of the left (right) QD. At this stage, although one can study the phase transition by solving an additional mean-field equation. We are only interested in how the critical value of this crossover is modified with the temperature difference where the only individual Kondo temperatures are required. In order to study such phenomenon, we refer to Simon *et al.* [248]. They demonstrated that the critical value of the superexchange interaction depends on the Kondo temperatures of both artificial impurities

$$\frac{J_c}{k_B T_{KR}} \approx \frac{4}{\pi}\left(1 + \frac{T_{KL}}{T_{KR}}\right) \,, \tag{8.25}$$

for $T_{KR} > T_{KL}$. Therefore, we apply Eq. (8.25) considering that the width of the Abrikosov-Suhl resonances may be understood as Kondo temperatures $\tilde{\Gamma}_\alpha \equiv k_B T_{K\alpha}$ as above. Accordingly, we can study the effects of the thermal bias to J_c taking into account the results of Fig. 8.10. Therefore, we plot in Fig. 8.13a the behavior of J_c as a function of θ for different τ/Γ_0 considering all coupling regimes. We observe a tendency from $J_c/k_B T_{KR} \approx 8/\pi$ to $J_c/k_B T_{KR} = 4/\pi$. This means that the crossover occurs sooner in the two-impurity system when one reservoir is heated. An explanation to this phenomenon is that at large θ the Kondo correlations of the left QD disappear making the transition to the antiferromagnetic singlet more favorable. Additionally, we observe that the Kondo correlations reinforce as τ/Γ_0 increases. The reason is that the Kondo resonances prevail for a longer regime of temperature differences. Therefore, a high tunnel coupling requires a stronger antiferromagnetic coupling in order to suppress Kondo correlations.

9. Conclusions

The main topic of this thesis has been the investigation of the electric, thermoelectric and thermal transport of QD systems out of equilibrium by the generation of a voltage or thermal bias. A QD consists of a small region in space where electrons are quantum confined yielding a 0-dimensional nanodevice. In the case of semiconductor QDs, they are usually fabricated in the interface between two semiconductors where a 2DEG is formed and, via voltages applied at electrodes, electrons get trapped electrostatically. Nevertheless, the QD is not fully isolated because electrons can hop in and out of the electronic reservoirs allowing transport across the nanodevice. Currents can be induced upon application of thermal or voltage differences. The thermoelectric response of a QD is interesting because these nanodevices are good candidates to be efficient waste-heat-to-electricity converters. Hence, a deep theoretical study of the thermoelectric effects of these systems is needed. In addition, this thesis has been also concerned with the thermal response of Kondo-correlated QDs. The Kondo effect arises when a spin-singlet is created between an electron occupying the QD and the delocalized electrons of the reservoirs. This is a paradigmatic phenomenon which is worth to be studied due to the manifestation at low temperatures of the ZBA in the differential electric conductance. Therefore, Kondo artificial impurities attached to a cold and a hot reservoir could lead to unexpected consequences.

The theoretical techniques of this thesis have been based on the non-equilibrium Green's function formalism (Ch. 4), which is a quite powerful theoretical framework for studying strongly correlated systems such as an artificial Kondo impurity. The Hamiltonian which describes the QD has been basically the Anderson Model (Ch. 5). However, several transformations can be applied to obtain different Hamiltonians like the slave-boson or the Kondo Hamiltonian, which have been also relevant in this thesis. The main methods have been the perturbation expansion of the current using the Kondo Hamiltonian (Sec. 6.2), the evaluation of the mean-field equations of the slave-boson Hamiltonian (SBMFT) or the self-consistent resolution of a truncated set of EOMs. The two latter provide a Green's function as a solution which has to be included in the current expressions, which are obtained using the same formalism

(Sec. 6.1), in order to study the quantum transport. Each of these approaches are useful in different temperature regimes and offer relevant information about several effects as the quench of the Kondo resonances or the generation of nontrivial zeros in the thermocurrent.

Particularly, in Ch. 7 we have discussed the thermoelectric transport through three different single-dot structures: a QD in the Coulomb-blockade regime (Sec. 7.1), a molecular junction (Sec. 7.2) and an artificial magnetic impurity (Sec. 7.3). First, we have observed that the Coulomb-blockaded QD shows a diamond structure in the differential electrical conductance, as expected. More interestingly, a proper tuning of the dot level gives rise to nonlinear behavior of the thermocurrent which leads to nontrivial zeros. This phenomenon can be understood with a change of flow between electrons and holes hopping across different resonances of the local DOS of the system. In addition, the heat transport shows asymmetries when a voltage is applied because the energy current has a sign dependent on the position of the resonances in contrast to the Joule dissipation which does not change sign. Surprisingly, the rectification as a function of voltage shows a similar pattern as the thermocurrent when tuning the thermal bias, suggesting that both behaviors may come from the same origin: The existence of more than one resonance in the DOS. Finally, we observe departures from the WF law at out of equilibrium conditions.

Second, we have studied the thermal effects of a molecular junction and have compared the results with the experimental measurements of a Ferrocene molecule connected to gold contacts. We have applied the theory of a single-level Coulomb-blockaded QD to describe the physics of the molecular junction at different background temperatures. The theoretical results nicely agree with the experiment. Nevertheless, Garrigues *et. al.* [41] also found agreement by applying a noninteracting model where each resonance in the molecular junction is given by a different energy level. For this reason, we have proposed the application of a magnetic field in order to know if the resonances in the molecule arise from different energy levels or are created by the Coulomb blockade effect. By analyzing the differential conductance we have observed that each resonance in the noninteracting case splits into two different peaks as expected from the Zeeman effect whereas the resonances in the interacting case shift in different directions depending on the spin difference of the resonances of the molecule. The experimentally observed shift of conductance peaks of a Ferrocene molecule is consistent with the fact that the resonances are generated from charging effects.

Third, we have investigated the response of the Kondo resonance of an artificial magnetic impurity due to voltage and thermal bias by employing three different techniques which cover all temperature regimes.

With the perturbation expansion of the Kondo Hamiltonian ($T > T_K$) we extract an effective Kondo temperature which shows that the Kondo resonance reaches a scaling regime followed with a quench at large thermal biases. We have also discussed the voltage-driven effects with the SBMFT ($T < T_K$). We have observed a smearing of the Kondo resonance at low voltages which leads into a splitting in two different resonances at larger biases. Remarkably, in the thermally-biased response we have found a trend in the effective Kondo resonance similarly to the perturbation approach: The Kondo resonance decreases with increasing thermal bias obeying a scaling regime and finally vanishes at large bias. Furthermore, we have studied the electric and heat transport within this approach. We have found an ohmic behavior at low voltage bias and a maximum of thermocurrent which finally decays to zero due to the vanishing of the Kondo resonance. In the heat current we have observed the Peltier effect induced by the energy current, which is finally dominated by the dissipation of the Joule term. Within this approach, we have also discussed the heat asymmetries finding a way to obtain experimentally the energy current by measuring the heat current at different leads or different sign of the voltage. We have also employed the EOM technique which is able to recover the single-particle peaks as well as the Kondo resonance although it lacks the behavior exhibited in the previous approaches at large bias. Nevertheless, inside the Coulomb diamond the ZBA at $V = 0$ emerges in the Kondo regime despite the drawback of the model at the particle-hole symmetry point. Additionally, the thermocurrent may present two different nontrivial zeros, one due to the Abrikosov-Suhl resonance and one due to the second single-particle peak.

Then, in Ch. 8, we have exploited the versatility of the DQD by considering three different configurations: a parallel-coupled DQD with negligible Coulomb interaction and tunnel hopping energies (Sec. 8.1), a parallel-coupled DQD with an interdot Coulomb interaction (Sec. 8.2) and a serially-coupled two-impurity system (Sec. 8.3). In the first work we have studied the emergence of BIC in a DQD with each dot attached to two leads. We have observed that the BIC induces a narrow antiresonance in the transmission function of the DQD. Additionally, we have found that the BIC is not destroyed in the presence of intradot Coulomb interactions. Instead it is replicated, at least, in the case of equal charging energies. Regarding the electric transport, the BIC nullifies the differential electric conductance when aligns the BIC with the eletrochemical potential of one reservoir. Additionally, the thermoelectric response becomes highly nonlinear yielding large variations of the linear thermoelectric conductance around the BICs. These findings could be useful for experimental detection of such states. On the other hand, the differential thermoelectric conductance presents complex patterns which lead to several nontrivial zeros in the thermoelectric current caused by different resonances in the transmission function.

The Coulomb drag effect has been studied in a parallel-coupled DQD where each dot is coupled with an interdot charging energy (Sec. 8.2). In addition, each dot is connected to two different terminals, one of these dots is under the application of a voltage bias (drive system) whereas the second dot stays at equilibrium (drag system). We have found that the drag current can only appear theoretically in the Green's function formalism if we consider the first nonzero order of the interacting self-energy. In fact, the drag current seems to depend on the fluctuations of the occupation in the QDs. Furthermore, we have also found that nonproportional energy-dependent hybridization functions for each lead are needed. Using a tight-binding model to obtain shifted hybridization functions between reservoirs, a drag current is induced when a voltage bias is applied to the second system. The drag current shows a parabolic behavior at low bias in contrast to the linear behavior of the drive current. Nevertheless, the linear behavior can be also found in the drag current if we consider nonproportional hybridization functions in the drive system. Finally, we have observed that the drag occurs around the triple points of the stability diagram meaning that the transport in the drag system is generated by high-order cotunnel processes.

The thermal and thermoelectric responses have been analyzed in a serially-coupled DQD acting as an artificial two-impurity system in the Fermi liquid regime $T < T_K$. First, we have investigated how the Kondo resonances of each QD are altered due to a thermal difference between reservoirs. We have distinguished three different regimes depending on the ratio between the dot-dot and lead-dot tunnel couplings: the weakly coupling regime in which the system is almost decoupled since the hot reservoir causes a vanishing of the left Kondo resonance, the intermediate coupling regime where the dot connected to the cold reservoir partially feels the heating of the hot reservoir, and the strong coupling regime in which both dots behave as a single system. Nevertheless, the system is always decoupled at large thermal biases independently of the dot-dot tunnel coupling. These three regimes can be observed in the behavior of the thermocurrent which is also able to exhibit nontrivial zeros in the strong coupling regime. On the other hand, the heat current shows a region of negative thermal conductance which arises from the decoupling of the system at large thermal bias. Finally, we have analyzed the Kondo-to-antiferromagnetic crossover observing that the critical superexchange shifts in response of the temperature difference.

All these systems seem to exhibit similar physics despite the different configurations. An important common characteristic is the appearance of nontrivial zeros in the thermocurrent (see Secs. 7.1, 7.3, 8.1 and 8.3). The explanation given for each nontrivial zero is essentially the same. This effect occurs for an asymmetric transmission function which contains at least two resonances: one located below the Fermi level and another located above. The shape of the transmission function produces a flow of electrons and holes when a temperature difference is applied. First, a flow in one direction will occur due to the first resonance and, as the thermal bias increases, the flow of the second contributes to the transport yielding a reversal of the current. Therefore, we can conclude that this thermoelectric phenomenon is rather general and can appear for any system which accomplishes the previous conditions for the transmission function. In addition, another important feature is the quench of the Kondo resonance at large temperature gradients (see Sec. 7.3). Remarkably, the system with two QDs (see Sec. 8.3) does not show such a global quench because we would need the disappearance of both Kondo resonances, instead of only one resonance vanishing. This is a good example of a complexity enhancement when the number of QDs is increased in the system. We believe that the parallel-coupled DQD would exhibit a different behavior more similar to Sec. 7.3 because this configuration is characterized by both QDs attached to both reservoirs, a more similar scenario to the single QD case.

Let us now discuss the benefits and drawbacks of the mathematical techniques explained in Chs. 4, 5 and 6. On the one hand, the EOM technique offers good and reliable results in the Coulomb blockade regime. Nevertheless, this technique lies in the truncation of a system of differential equations. Physical assumptions have been made in order to guarantee a correct solution, but we should take into account that it does not consist of an expansion in terms of a parameter. Consequently, this technique is not well controlled and may fail at some parameter regimes. An example can be found in Sec. 7.1, which correctly describes the transport of a QD in the Coulomb blockade regime. However, the approximation is not valid to describe Kondo physics at $T < T_K$ because such correlations have been neglected in the truncation. In fact, in Sec. 5.2.4 the system of equations is extended with a truncation able to recover the Kondo resonance yielding good qualitative results. Nonetheless, the result still fails describing dephasing and the Kondo quench at large thermal biases. Additionally, the slave-boson model introduced in Sec. 5.1.2 provides a nice representation of a Kondo system at $T < T_K$ (see Secs. 7.3 and 8.3), but the approach is made for $U \to \infty$ and, consequently, does not give information about the effects at finite charging energies. To solve this issue, a slave-boson Hamiltonian can be obtained with finite U [249, 250]. Hence, a solution of the system considering this new Hamiltonian may be a nice extension of this thesis.

However, we do not expect large variations from the results discussed in Secs. 7.3.2 and 8.3 because strong charging energies are needed to find Kondo correlations in the system. Another important drawback of the SBMFT is that it is unable to show the single-particle peaks relevant to the mixed valence regime. This could be important for characterizing transport because at large enough biases the system activates such resonances and the SBMFT may fail. Nevertheless, the model can offer good results in the particle-hole symmetry point since the energy level is located in the deep Kondo regime. Furthermore, the perturbation approach of the Kondo Hamiltonian has offered us intriguing analytical results like the effective Kondo temperature which is consistent with previously discussed methods. Finally, we would like to emphasize that a large amount of the results of this thesis has been achieved by applying a self-consistent calculation. This, in principle, is not important for understanding the physics. However, one should know that an increase of the number of unknown variables, which can be made by going beyond in our calculations of the EOM technique or increasing the number of QDs in the system, requires more sophisticated tools to solve the set of equations.

Further work could be the investigation of these systems by applying techniques different to the ones employed in this thesis. The scattering approach [211] can offer interesting physics for QDs comparable to the Green's function formalism, even in the nonlinear transport regime [176, 177, 204]. However, an important drawback is its inability to handle strong Coulomb interactions. Another possible approach for obtaining straightforward qualitative results of the quantum transport is by means of quantum master equations [251]. Although the results of this technique can be easy to interpret, the approach has a difficult extension beyond cotunneling. Regarding the Kondo effect, renormalization group approaches [93, 252] are very interesting because their results of the ZBA are valid at any regime of temperature. However, the implementation of voltage or thermal biases is not trivial [110, 253]. Additionally, the noncrossing approximation seems to provide valid results of the Kondo resonance which even exhibits dephasing effects [116, 254]. Interesingly, an analysis of the validity of these previous models with the SBMFT has been reported previously [255]. Another technique would be not to consider the mean-field approach in the slave-boson Hamiltonian [84], but the model would be still valid only for $T < T_K$. The implementation of any of these other methods would extend the validity of the results of this thesis. Finally, we highlight that these are just the most representative extensions of our approaches but do not cover all possible techniques applied in the literature.

Employing an additional approach is not the only way to extend our work. There are still phenomena to investigate in the systems considered in this thesis which can be obtained without using more sophisticated techniques. An open question is the role of magnetic fields in the thermoelectric response of the setups of Chs. 7 and 8. These effects have already been reported in the literature, but for some concrete cases [163, 256]. In particular, for molecular junctions we showed in Sec. 7.2 that magnetic fields determine if the resonances of a molecular junction are due to charging effects. Therefore, a nice extension would be studying the thermoelectric response of molecular junctions. Furthermore, systems with asymmetric tunneling between leads and dots were not considered in this thesis with an exception of Secs. 8.1, 8.2 and a brief discussion in Sec. 7.3. This is important because generally the coupling to the leads is not symmetric in experiments. Another extension would be the study of heat transport in the parallel-coupled DQD of Sec. 8.1. Apparently, the dependence of the heat current on the transmission function can induce new phenomena which would give us extra information about the BICs and maybe it can offer additional ways to detect them. The Coulomb drag system of Sec. 8.2 can be studied in multiple ways. For instance, it would be appealing to study the generation of drag electric current due to thermal differences in the drive system yielding thermoelectric drag. The thermal drag was already analyzed [257] but only in the case of small biases. Therefore, the work can be extended to the nonlinear regime of transport. The investigation of thermal effects on the single-particle peaks in the two-impurity Kondo system of Sec. 8.3 is needed to completely understand the physics beyond the particle-hole symmetry point. Concerning DQDs, Ch. 5 provides the analytical tools to study the case of comparable dot-dot hopping, intra- and interdot charging energies, but we have only restricted ourselves to specific cases. Therefore, the investigation of the most general DQD setup would be a fascinating topic to discuss. Furthermore, we have not given results for the thermovoltage and the differential thermopower in any of the works of this thesis (an exception is Sec. 7.1). Since the thermoelectric conductance and the thermocurrent are partially related to them, we do not believe to find any new physics in their study.

Previously, we have discussed extensions of our work for the same configurations and applying the concepts defined in this thesis. One could think of adding to our setup additional QDs yielding a QD array. Theoretical analysis can be also perfomed using the Anderson Hamiltonian of Ch. 5 and even the Green's function obtained in the Hartree or Hubbard-I approximation. Therefore, the transport response of a QD array can be straightforwardly obtained. Nevertheless, one should take into account that the electrically-driven response is a really well studied topic [258, 259], at least for the case of triple quantum dots [140, 260, 261]. Instead of adding QDs, one can consider to include additional terminals to the system. This was previously discussed as an energy harvester in which the temperature of the third reservoir is able to control the transport between the two additional reservoirs [262]. Furthermore, thermoelectrics was deeply studied in DQDs attached to three terminals [263]. Another additional consideration is the case of a QD attached to different type of reservoirs. In Sec. 8.2 we have considered tight-binding leads, but we can still consider graphene leads [73], which are interesting due to the linear dispersion relation, or superconducting leads, which have been demonstrated theoretically to exhibit intriguing features [208, 264, 265]. The field of spintronics is also interesting to discuss because additional concepts like the spin Seebeck [207, 266, 267] or spin drag effect [268] can be introduced. For large temperatures, we can not avoid the effect of phonons in the system. The thermoelectric effects of a QD including elecron-phonon contributions was investigated recently [206]. A decrease of the lattice thermal conductivity has been also studied due to the phonon contribution in QD superlattices [269]. In general, experiments in QD are performed at temperatures where the effect of phonons is negligible. Nevertheless, one can also find experiments at higher temperatures as shown in Sec. 7.2. The connection between quantum noise and thermoelectric effects would also be a fascinating topic that has been less studied. Several works can be found combining QDs and Kondo correlations with noise [241, 270, 271, 272, 273], but the thermoelectric response is still an unexplored area. Finally, the nonlinear transport of QDs with time-dependent fields such as ac currents is now a very attractive topic because of the recent experiments [274, 275, 276] and theoretical calculations [261, 277, 278, 279].

To conclude, we would like to emphasize that this thesis contributes to the understanding of nonlinear thermoelectrics and Kondo processes in QD systems. We have provided key theoretical predictions which might be experimentally tested in this area of physics. In fact, Sec. 7.2 has already discussed in comparison with experiments. On the other hand, some of our theoretical results agree with experiments perfomed in QDs [72, 111, 133, 201, 205]. We expect that this thesis will inspire the condensed matter community in the realization of future experiments and new theoretical models.

A. Unperturbed Green's functions

The goal of this appendix is to give the expressions of the Green's functions of an unperturbed fermionic reservoir given by the Hamiltonian of Eq. (5.3). These expressions are used in the evaluation of the perturbed Green's function for the QD setups considered in this thesis.

A.1 Lead Green's function

The lead Green's functions are obtained from the definitions of Eqs. (4.18), (4.19), (4.20) and (4.21) for the operators $C^{\dagger}_{\alpha k\sigma}$ and $C_{\alpha k\sigma}$ given from the Hamiltonian of Eq. (5.3). After a straightforward calculation, the Green's functions read

$$g^{t}_{\alpha k\sigma}(t,t') = -\frac{i}{\hbar}e^{-\frac{i}{\hbar}\varepsilon_{\alpha k\sigma}(t-t')}[\theta(t-t')-f_{\alpha}(\varepsilon_{\alpha k\sigma})]\,, \tag{A.1}$$

$$g^{\bar{t}}_{\alpha k\sigma}(t,t') = \frac{i}{\hbar}e^{-\frac{i}{\hbar}\varepsilon_{\alpha k\sigma}(t-t')}[\theta(t'-t)-f_{\alpha}(\varepsilon_{\alpha k\sigma})]\,, \tag{A.2}$$

$$g^{<}_{\alpha k\sigma}(t,t') = \frac{i}{\hbar}e^{-\frac{i}{\hbar}\varepsilon_{\alpha k\sigma}(t-t')}f_{\alpha}(\varepsilon_{\alpha k\sigma})\,, \tag{A.3}$$

$$g^{>}_{\alpha k\sigma}(t,t') = -\frac{i}{\hbar}e^{-\frac{i}{\hbar}\varepsilon_{\alpha k\sigma}(t-t')}[1-f_{\alpha}(\varepsilon_{\alpha k\sigma})]\,, \tag{A.4}$$

Following Eqs. (4.23) and (4.24), we also obtain the expression of the retarded and advanced Green's function

$$g^{r}_{\alpha k\sigma}(t,t') = -\frac{i}{\hbar}e^{-\frac{i}{\hbar}\varepsilon_{\alpha k\sigma}(t-t')}\theta(t-t')\,, \tag{A.5}$$

$$g^{a}_{\alpha k\sigma}(t,t') = \frac{i}{\hbar}e^{-\frac{i}{\hbar}\varepsilon_{\alpha k\sigma}(t-t')}\theta(t'-t)\,, \tag{A.6}$$

In the Fourier space, such functions become

$$g^{t}_{\alpha k\sigma}(\omega) = \frac{1-f_{\alpha}(\omega)}{\omega-\varepsilon_{\alpha k\sigma}+i\eta}+\frac{f_{\alpha}(\omega)}{\omega-\varepsilon_{\alpha k\sigma}-i\eta}\,, \tag{A.7}$$

$$g^{\bar{t}}_{\alpha k\sigma}(\omega) = -\frac{1-f_{\alpha}(\omega)}{\omega-\varepsilon_{\alpha k\sigma}-i\eta}-\frac{f_{\alpha}(\omega)}{\omega-\varepsilon_{\alpha k\sigma}+i\eta}\,, \tag{A.8}$$

$$g^{<}_{\alpha k\sigma}(\omega) = 2\pi i f_{\alpha}(\omega)\delta(\omega-\varepsilon_{\alpha k\sigma})\,, \tag{A.9}$$

$$g^{>}_{\alpha k\sigma}(\omega) = -2\pi i[1-f_{\alpha}(\omega)]\delta(\omega-\varepsilon_{\alpha k\sigma})\,, \tag{A.10}$$

where η indicates a small positive imaginary part. The retarded and advanced Green's functions in the Fourier space read

$$\begin{aligned} g^r_{\alpha k\sigma}(\omega) &= \frac{1}{\omega - \varepsilon_{\alpha k\sigma} + i\eta} \, , \qquad \text{(A.11)} \\ g^a_{\alpha k\sigma}(\omega) &= \frac{1}{\omega - \varepsilon_{\alpha k\sigma} - i\eta} \, , \qquad \text{(A.12)} \end{aligned}$$

which can be split in a principal value and an imaginary part in the limit $\eta \to 0^+$

$$\begin{aligned} g^r_{\alpha k\sigma}(\omega) &= \mathcal{P}\frac{1}{\omega - \varepsilon_{\alpha k\sigma}} - i\pi\delta(\omega - \varepsilon_{\alpha k\sigma}) \, , \qquad \text{(A.13)} \\ g^a_{\alpha k\sigma}(\omega) &= \mathcal{P}\frac{1}{\omega - \varepsilon_{\alpha k\sigma}} + i\pi\delta(\omega - \varepsilon_{\alpha k\sigma}) \, . \qquad \text{(A.14)} \end{aligned}$$

B. Schrieffer-Wolff Transformation

The aim of this appendix is to explain the derivation steps for the transformation of the single-impurity Anderson Hamiltonian [Eq. (5.2)] to the Kondo or s-d Hamiltonian [Eq. (5.1.3)] performed by Schrieffer and Wolff [100]. After this transformation, we obtain a Hamiltonian that only includes cotunneling processes. We recall that we make the assumptions $\varepsilon_d < 0$ and $\varepsilon_d + U > 0$, meaning that the dot is only filled by one electron, and $\Gamma/|\varepsilon_d| \ll 1$ together with $\Gamma/(\varepsilon_d + U) \ll 1$, which provides two narrow resonances.

B.1 The unitary operator

As explained in Sec. 5.1.3, we should apply an unitary transformation $e^{-\bar{\mathcal{S}}}$ which, applied to the total Hamiltonian, leads to the following approximation

$$\bar{\mathcal{H}} \approx \mathcal{H}_0 + \mathcal{H}_{\text{tun}} + [\bar{\mathcal{S}}, \mathcal{H}_0] + [\bar{\mathcal{S}}, \mathcal{H}_{\text{tun}}] + \frac{1}{2}[\bar{\mathcal{S}}, [\bar{\mathcal{S}}, \mathcal{H}_0]] \,. \tag{B.1}$$

In order to eliminate the tunneling term in the total Hamiltonian, Eq. (5.17) needs to be fulfilled. This makes us propose Eq. (5.18) as the unitary operator for the transformation of the Hamiltonian where $w^{(1)}_{\alpha k\sigma}$ and $w^{(2)}_{\alpha k\sigma}$ are the only unknown functions. This section calculates the commutator of Eq. (5.17) and solves the corresponding equation obtaining Eq. (5.19). Hence, the commutator of Eq. (5.17) may be separated in the following commutators

$$\begin{aligned}
\hat{\mathcal{A}}_1 &= \left[\sum_{\vec{\alpha}_1} \varepsilon_{\alpha_1 k_1 \sigma_1} C^\dagger_{\alpha_1 k_1 \sigma_1} C_{\alpha_1 k_1 \sigma_1}, \sum_{\vec{\alpha}_2} w^{\pm}_{\alpha_2 k_2 \sigma_2} n^{\pm}_{\bar{\sigma}_2} C^\dagger_{\alpha_2 k_2 \sigma_2} d_{\sigma_2}\right] \\
&= \sum_{\alpha_1 k_1 \sigma_1} \varepsilon_{\alpha_1 k_1 \sigma_1} w^{\pm}_{\alpha_1 k_1 \sigma_1} n^{\pm}_{\bar{\sigma}_1} C^\dagger_{\alpha_1 k_1 \sigma_1} d_{\sigma_1} \,, && \text{(B.2a)} \\
\hat{\mathcal{A}}_2 &= \left[\sum_{\vec{\alpha}_1} \varepsilon_{d\sigma_1} d^\dagger_{\sigma_1} d_{\sigma_1}, \sum_{\vec{\alpha}_2} w^{\pm}_{\alpha_2 k_2 \sigma_2} n^{\pm}_{\bar{\sigma}_2} C^\dagger_{\alpha_2 k_2 \sigma_2} d_{\sigma_2}\right] \\
&= -\sum_{\alpha_2 k_2 \sigma_1} \varepsilon_{d\sigma_1} w^{\pm}_{\alpha_2 k_2 \sigma_1} n^{\pm}_{\bar{\sigma}_1} C^\dagger_{\alpha_2 k_2 \sigma_1} d_{\sigma_1} \,, && \text{(B.2b)}
\end{aligned}$$

$$\begin{aligned}\hat{\mathcal{A}}_3 &= \Bigl[U n_\uparrow n_\downarrow , \sum_{\vec{\alpha}_2} w^{\pm}_{\alpha_2 k_2 \sigma_2} n^{\pm}_{\bar{\sigma}_2} C^{\dagger}_{\alpha_2 k_2 \sigma_2} d_{\sigma_2}\Bigr] \\ &= - \sum_{\alpha_2 k_2 \sigma_2} U w^{\pm}_{\alpha_2 k_2 \sigma_2} n^{\pm}_{\bar{\sigma}_2} n_{\bar{\sigma}_2} C^{\dagger}_{\alpha_2 k_2 \sigma_2} d_{\sigma_2} \,, \end{aligned} \tag{B.2c}$$

where $w^{+}_{\alpha_2 k_2 \sigma_2} = w^{(1)}_{\alpha_2 k_2 \sigma_2}$, $w^{-}_{\alpha_2 k_2 \sigma_2} = w^{(2)}_{\alpha_2 k_2 \sigma_2}$, $n^{+}_{\bar{\sigma}} = n_{\bar{\sigma}}$ and $n^{-}_{\bar{\sigma}} = 1 - n_{\bar{\sigma}}$. After performing the sum $\sum_i \hat{\mathcal{A}}_i$ and making it equal to Eq. (5.5), we obtain the following equations

$$(\varepsilon_{\alpha k \sigma} - \varepsilon_{d\sigma} - U) w^{(1)}_{\alpha k \sigma} - (\varepsilon_{\alpha k \sigma} - \varepsilon_{d\sigma}) w^{(2)}_{\alpha k \sigma} = 0 \,, \tag{B.3}$$

$$(\varepsilon_{\alpha k \sigma} - \varepsilon_{d\sigma}) w^{(2)}_{\alpha k \sigma} = \mathcal{V}_{\alpha k \sigma} \,, \tag{B.4}$$

whose solutions are found in Eq. (5.19).

B.2 The transformation

Now, applying the condition given by Eq. (5.17), Eq. (B.1) becomes

$$\bar{\mathcal{H}} \approx \mathcal{H}_0 + \frac{1}{2}[\bar{\mathcal{S}}, \mathcal{H}_{\text{tun}}] \,. \tag{B.5}$$

As can be seen from Eq. (B.5), an addtional commutator has to be computed. We will separate such commutator in different components. First, we apply

$$\begin{aligned}\mathcal{H}_{2\text{a}} &= \Bigl[\sum_{\alpha_1 k_1 \sigma_1} w^{\pm}_{\alpha_1 k_1 \sigma_1} n^{\pm}_{\bar{\sigma}_1} C^{\dagger}_{\alpha_1 k_1 \sigma_1} d_{\sigma_1} , \sum_{\alpha_2 k_2 \sigma_2} \mathcal{V}_{\alpha_2 k_2 \sigma_2} C^{\dagger}_{\alpha_2 k_2 \sigma_2} d_{\sigma_2}\Bigr] \\ &= \mp \sum_{\alpha_1 \alpha_2 k_1 k_2 \sigma_1} w^{\pm}_{\alpha_1 k_1 \sigma_1} \mathcal{V}_{\alpha_2 k_2 \bar{\sigma}_1} C^{\dagger}_{\alpha_2 k_2 \bar{\sigma}_1} C^{\dagger}_{\alpha_1 k_1 \sigma_1} d_{\sigma_1} d_{\bar{\sigma}_1} \,. \end{aligned} \tag{B.6}$$

Here, in combination with its Hermitian conjugate, we obtain the Hamiltonian of Eq. (5.22). At this stage, we calculate the commutator

$$\mathcal{H}_3 = \Bigl[\sum_{\vec{\alpha}_1} w^{\pm}_{\alpha_1 k_1 \sigma_1} n^{\pm}_{\bar{\sigma}_1} C^{\dagger}_{\alpha_1 k_1 \sigma_1} d_{\sigma_1} , \sum_{\vec{\alpha}_2} \mathcal{V}^{*}_{\alpha_2 k_2 \sigma_2} d_{\sigma_2} C^{\dagger}_{\alpha_2 k_2 \sigma_2}\Bigr] \tag{B.7}$$

which we split in three terms $\mathcal{H}_3 = \mathcal{H}_{3\text{a}} + \mathcal{H}_{3\text{b}} + \mathcal{H}_{3\text{c}}$:

$$\mathcal{H}_{3\text{a}} = \sum_{\alpha_1 \beta_1 k_1 k_2 \sigma_1} w^{\pm}_{\alpha_1 k_1 \sigma_1} \mathcal{V}^{*}_{\alpha_2 k_2 \sigma_1} n^{\pm}_{\bar{\sigma}_1} C^{\dagger}_{\alpha_1 k_1 \sigma_1} C^{\dagger}_{\alpha_2 k_2 \sigma_1} \tag{B.8}$$

$$\mathcal{H}_{3\text{b}} = - \sum_{\alpha_1 k_1 \sigma_1} w^{\pm}_{\alpha_1 k_1 \sigma_1} \mathcal{V}^{*}_{\alpha_1 k_1 \sigma_1} n^{\pm}_{\bar{\sigma}_1} n_{\sigma} \tag{B.9}$$

$$\mathcal{H}_{3\text{c}} = \mp \sum_{\alpha_1 \beta_1 k_1 k_2 \sigma} w^{\pm}_{\alpha_1 k_1 \sigma_1} \mathcal{V}^{*}_{\alpha_2 k_2 \bar{\sigma}_1} C^{\dagger}_{\alpha_1 k_1 \sigma_1} C_{\alpha_2 k_2 \bar{\sigma}_1} d^{\dagger}_{\bar{\sigma}_1} d_{\sigma_1} \,. \tag{B.10}$$

These different Hamiltonians are combined to obtain the remaining terms of the Schrieffer-Wolff transformations. In order to obtain Eq. (5.24), we add to Eq. (B.8)

$$\mathcal{H}_{3\mathrm{d}} = \sum_{\alpha_1\beta_1 k_1 k_2 \sigma_1} \mathcal{J}_{\alpha_1\sigma_1,\alpha_2\sigma_1} C^\dagger_{\alpha_1 k_1 \sigma_1} C_{\alpha_2 k_2 \sigma_1} n_\sigma \,. \tag{B.11}$$

Additionally, Eq. (B.9) leads to Eq. (5.26). Finally, since we have added Eq. (B.11) to Eq. (B.8), we need to substract the same expression to Eq. (B.10) to keep Eq. (B.7) invariant. After a straightforward calculation $\mathcal{H}_{\mathrm{sd}} = (\mathcal{H}_{3\mathrm{c}} + \mathcal{H}_{3\mathrm{d}})/2$ reads

$$\begin{aligned}\mathcal{H}_{\mathrm{sd}} &= \frac{1}{2} \sum_{\alpha_1 k_1 \alpha_2 k_2 \sigma} \mathcal{J}_{\alpha_1\sigma,\alpha_2\bar{\sigma}} C^\dagger_{\alpha_1 k_1 \sigma} C_{\alpha_2 k_2 \bar{\sigma}} d^\dagger_{\bar{\sigma}} d_\sigma \\ &+ \frac{1}{4} \sum_{\alpha_1 k_1 \alpha_2 k_2 \sigma} \mathcal{J}_{\alpha_1\sigma,\alpha_2\bar{\sigma}} C^\dagger_{\alpha_1 k_1 \sigma} C_{\alpha_2 k_2 \bar{\sigma}} (n_\sigma - n_{\bar{\sigma}}) \,. \end{aligned} \tag{B.12}$$

Now, the next step is to transform the QD subspace into a spin subspace. To do so, we rewrite the dot operators

$$n_\sigma + n_{\bar{\sigma}} = \vec{d}^\dagger \mathbf{1} \vec{d} \,, \tag{B.13}$$

$$d^\dagger_{\bar{\sigma}} d_\sigma = s^x_{\sigma\bar{\sigma}} \vec{d}^\dagger \mathbf{S}_x \vec{d} + s^y_{\sigma\bar{\sigma}} \vec{d}^\dagger \mathbf{S}_y \vec{d} \,, \tag{B.14}$$

$$n_\sigma - n_{\bar{\sigma}} = s^z_{\sigma\sigma} \vec{d}^\dagger \mathbf{S}_z \vec{d} \,, \tag{B.15}$$

where $\mathbf{S}_l$ with $l = \{x, y, z\}$ are the Pauli matrices, $s^l_{\sigma_1\sigma_2}$ denotes its coefficients, $\mathbf{1}$ is the unitary matrix and $\vec{d}$ is the vector operator given by:

$$\vec{d} = \begin{pmatrix} d_\uparrow \\ d_\downarrow \end{pmatrix} \,, \; \vec{d}^\dagger = \begin{pmatrix} d^\dagger_\uparrow & d^\dagger_\downarrow \end{pmatrix} \,. \tag{B.16}$$

We resort to the spin subspace by replacing $\vec{d}^\dagger \mathbf{S}_l \vec{d}$ with the spin operator $\hat{S}_l$. This substitution transforms $\mathcal{H}_{3\mathrm{a}} + \mathcal{H}_{3\mathrm{d}}$ into Eq. (5.24) and Eq. (B.12) into the original s-d Hamiltonian of Eq. (5.20).

C. Fermi function integrals

This thesis concerns transport of electrons, fermionic particles which are distributed following the Fermi function occupation $f(\omega)$ [Eq. (5.1)]. Due to this fact, we may encounter integrals of the form

$$H(z) = \int_{-D}^{D} d\omega \frac{f(\omega - \mu)}{\omega - z} , \tag{C.1}$$

where z is, generally, a complex number and the Fermi function contains the contribution of the electrochemical energy μ of a given reservoir. For simplicity, we will assume that the bandwidth D is the largest energy in the problem. Although Eq. (C.1) can be complicated, it has a straighforward result. First, we rewrite the Fermi function in a more convenient way

$$f(\omega - \mu) = \frac{1}{2}\left[1 - \tanh\frac{\omega - \mu}{2k_B T}\right] . \tag{C.2}$$

This relation allows us to split Eq. (C.1) in two terms $H(z) = G(z) + F(z)$ where

$$G(z) = \frac{1}{2}\int_{-D}^{D} d\omega \frac{1}{\omega - z} , \tag{C.3}$$

$$F(z) = -\frac{1}{2}\int_{-D}^{D} d\omega \frac{\tanh\frac{\omega-\mu}{2k_B T}}{\omega - z} . \tag{C.4}$$

The first integral has a simple solution

$$G(z) = \frac{1}{2}\ln\left|\frac{D - z}{D + z}\right| . \tag{C.5}$$

We should take into account that z is a complex variable. In the case that Im$[z]$ is vanishingly small, Eq. (C.3) has an additional contribution due to the Dirac delta function:

$$G(z) = \varsigma\frac{i\pi}{2} + \frac{1}{2}\ln\left|\frac{D - z}{D + z}\right| . \tag{C.6}$$

Here, we define $\varsigma = \text{sgn}(\text{Im}[z])$, where $\text{sgn}(x)$ denotes the sign of x.

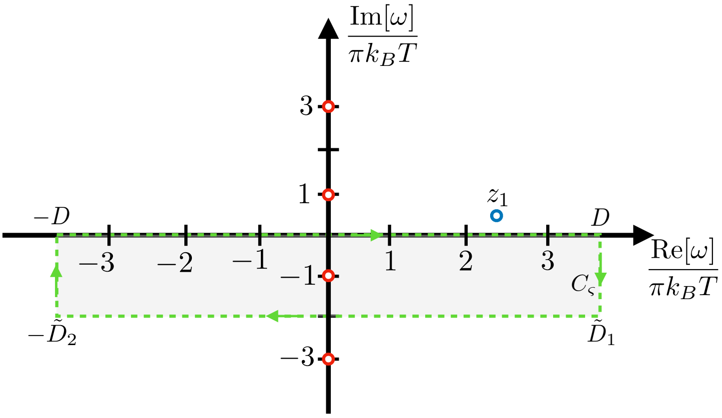

Fig. C.1. Scheme of the complex plane for the complex energy ω. The red points are associated to the poles of the hyperbolic tangent in Eq. (C.7) ($\omega = i(2n+1)\pi k_B T$ with $n = 0, 1, 2\ldots$) whereas the blue point is the pole which comes from the denominator of the integral ($\omega = z_1$). Finally, the square denotes the integration contour C_ς delimited by the vertices $\omega = \pm D$, $\omega = \tilde{D}_1 = D - 2\pi\varsigma i k_B T$ and $\omega = -\tilde{D}_2 = -D - 2\pi\varsigma i k_B T$. One can observe that there is only one pole inside the contour.

C.1 Integral $F(z)$

The integral $F(z)$ is slightly more complicated, but one can still solve it. To do so, we are going to employ complex analysis. Firstly, we change the integration variable $\omega' = \omega - \mu$ in order to eliminate μ from the Fermi function. Additionally, we apply the assumption $D \gg \mu$ obtaining

$$F(z_1) = -\frac{1}{2}\int_{-D}^{D} d\omega \frac{\tanh\frac{\omega}{2k_BT}}{\omega - z_1}, \tag{C.7}$$

where $z_1 = z - \mu$. Now, we notice that $F(z)$ has one pole at $\omega = z_1$ (blue point in Fig. C.1). In addition to z_1, the hyperbolic tangent has an infinite number of poles given by $\omega = i(2n+1)\pi k_B T$ (red points in Fig. C.1). In order to avoid the pole at z_1, we choose a contour C_ς (rectangle in Fig. C.1) that only contains the single pole $\omega = -i\varsigma\pi k_B T$. Then, we separate the contour in four parts denoted by the lines delimiting the contour C_ς

$$\begin{aligned}
-\frac{1}{2}\oint_{C_\varsigma} d\omega \frac{\tanh\frac{\omega}{2k_BT}}{\omega - z_1} = {} & F(z_1) - \frac{1}{2}\int_{D}^{\tilde{D}_1} d\omega \frac{\tanh\frac{\omega}{2k_BT}}{\omega - z} \\
& -\frac{1}{2}\int_{\tilde{D}_1}^{-\tilde{D}_2} d\omega \frac{\tanh\frac{\omega}{2k_BT}}{\omega - z_1} \\
& -\frac{1}{2}\int_{-\tilde{D}_2}^{-D} d\omega \frac{\tanh\frac{\omega}{2k_BT}}{\omega - z_1},
\end{aligned} \tag{C.8}$$

where $\tilde{D}_1 = D - 2\pi\varsigma i k_B T$ and $-\tilde{D}_2 = -D - 2\pi\varsigma i k_B T$. Here, one can easily demonstrate with the change of variables $\omega' = \omega + 2\pi\varsigma k_B T$ that

$$\begin{aligned} -\frac{1}{2}\int_{\tilde{D}_1}^{-\tilde{D}_2} d\omega \frac{\tanh\frac{\omega}{2k_BT}}{\omega - z_1} &= -\frac{1}{2}\int_{D}^{-D} d\omega' \frac{\tanh\frac{\omega'}{2k_BT}}{\omega' - z_1 - i2\pi\varsigma k_B T} \\ &= -F(z_1 + i2\pi\varsigma k_B T)\ . \end{aligned} \tag{C.9}$$

The contour integral can be solved by applying the residue theorem. First, we evaluate the Laurent series of $\tanh s$ around $s_0 = -i\varsigma\pi/2$ (the pole inside C_ς)

$$\tanh s = \frac{1}{s + i\varsigma\frac{\pi}{2}} + \sum_{n=0}^{\infty} c_n \left(s + i\varsigma\frac{\pi}{2}\right)^n . \tag{C.10}$$

Since we only need the expression for $n < 0$, we are not interested in the evaluation of c_n. Next, we proceed with the residue theorem which states that an integral around a closed contour C of a function $g(z)$ which has a pole in z_0 inside the contour can be evaluated as

$$\oint g(z)dz = 2\pi i \mathrm{Res}[g; z_0]\ , \tag{C.11}$$

where $\mathrm{Res}[g; z_0]$ is the coefficient of the s^{-1} term in the Laurent expansion of g. For our case, we obtain the residue of Eq. (C.10). Then,

$$\begin{aligned} \frac{1}{2\pi i}\oint_{C_\varepsilon} d\omega \frac{\tanh\frac{\omega}{2k_BT}}{\omega - z_1} &= \mathrm{Res}[frac\tanh\frac{\omega}{2k_BT}\omega - z_1; \omega_0 = -i\pi k_B T] \\ &= -\frac{\varsigma k_B T}{z_1 + i\pi k_B T\varsigma}\ . \end{aligned} \tag{C.12}$$

Furthermore, we need to evaluate the two remaining integrals, which will be solved in the limit of $D \gg \omega$. Hence, we obtain

$$-\frac{1}{2}\int_{D}^{\tilde{D}_1} d\omega \frac{\tanh\frac{\omega}{2k_BT}}{\omega - z_1} \approx -\frac{1}{2}\int_{D}^{\tilde{D}_1} d\omega \frac{1}{\omega - z_1} \tag{C.13}$$

$$= \frac{1}{2}\ln\left|\frac{D - z_1}{D - z_1 - i2\pi\varsigma k_B T}\right|$$

$$-\frac{1}{2}\int_{-\tilde{D}_2}^{-D} d\omega \frac{\tanh\frac{\omega}{2k_BT}}{\omega - z_1} \approx \frac{1}{2}\int_{-\tilde{D}_2}^{-D} d\omega \frac{1}{\omega - z_1} \tag{C.14}$$

$$= \frac{1}{2}\ln\left|\frac{D + z_1}{D + z_1 + i2\pi\varsigma k_B T}\right|\ . \tag{C.15}$$

We insert the solutions into Eq. (C.8) and, after a little algebra, we find a recurrence equation.

$$\begin{aligned}F(z_1+i2\pi\varsigma k_BT) &= F(z_1)+\frac{2\pi i\varsigma k_BT}{z_1+i\pi\varsigma k_BT}\\ &\quad+\frac{1}{2}\ln\left|\frac{D^2-z_1^2}{D^2-(z_1+i2\pi\varsigma k_BT)^2}\right| \end{aligned}\tag{C.16}$$

We add an additional term in both sides of Eq. (C.16) to have a recurrence relation:

$$\begin{aligned}F(z_1+i2\pi\varsigma k_BT)+\frac{1}{2}\ln\left|\frac{D^2-(z_1+i2\pi\varsigma k_BT)^2}{(i2\pi\varsigma k_BT)^2}\right| =\\ F(z_1)+\frac{2\pi i\varsigma k_BT}{z_1+i\pi\varsigma k_BT}+\frac{1}{2}\ln\left|\frac{D^2-z_1^2}{(i2\pi\varsigma k_BT)^2}\right|. \end{aligned}\tag{C.17}$$

One can realize that $F(z)$ can be written properly as $\tilde{F}(z-\mu)$. If we compare to $\psi(x+1)=\psi(x)+x^{-1}$, which is the recurrence relation of the digamma function with $x=1/2+z_1/(2\pi i\varsigma k_BT)$, the integral $F(z)$ (applying $z\to z_1$) becomes

$$F(z)=\psi\left(\frac{1}{2}-i\varsigma\frac{z-\mu}{2\pi k_BT}\right)-\frac{1}{2}\ln\left|\frac{D^2-(z-\mu)^2}{(2\pi k_BT)^2}\right|. \tag{C.18}$$

We remark that at $D\to\infty$, the logarithm term vanishes in Eq. (C.16) yielding only the digamma function. This solution corresponds to the integral of Eq. (5.73). Additionally, combining Eq. (C.18) with Eq. (C.5) in the limit of negligible $\mathrm{Im}[z]$ we obtain

$$H(z)=\varsigma\frac{i\pi}{2}+\ln\left|\frac{2\pi k_BT}{D+z-\mu}\right|+\psi\left(\frac{1}{2}-i\varsigma\frac{z-\mu}{2\pi k_BT}\right). \tag{C.19}$$

D. Perturbation expansion of $I_{\alpha\sigma}$

This appendix summarizes the calculation concerning the perturbation expansion of the current operator [Eqs. (6.23) and (6.24)]. First, replacing the S-matrix of Eq. (6.26) with the terms Eq. (6.33) the current is expressed

$$\begin{aligned} I_{\alpha\sigma} &= \langle \hat{I}_{\alpha\sigma}\rangle - \frac{2}{\hbar}\mathrm{Im}\Big[\int_{-\infty}^{0} dt \langle \mathcal{H}_K(t)\hat{I}_{\alpha\sigma}(0)\rangle\Big] \\ &+\Big(-\frac{i}{\hbar}\Big)^2 \frac{1}{2}\mathrm{Re}\Big[\int_{-\infty}^{0}\int_{-\infty}^{0} dt_2 dt_1 \langle \hat{T}[\mathcal{H}_K(t_2)\mathcal{H}_K(t_1)\hat{I}_{\alpha\sigma}(0)]\rangle\Big] \\ &+\Big(-\frac{i}{\hbar}\Big)^2 \mathrm{Re}\Big[\int_{-\infty}^{0}\int_{-\infty}^{0} dt_2 dt_1 \langle \mathcal{H}_K(t_2)\hat{I}_{\alpha\sigma}(0)\mathcal{H}_K(t_1)]\rangle\Big] . \end{aligned} \tag{D.1}$$

We identify three different orders in Eq. (D.1): the expected value of the current, which is zero $\langle \hat{I}_{\alpha\sigma}\rangle = 0$, the second order current $I^{(2)}_{\alpha\sigma}$ in the coupling coefficients (second term in first line) and the third order $I^{(3)}_{\alpha\sigma}$ (second and third lines). The solution of the two last components will be found below.

D.1 Second order

Substituting Eq. (6.23) in Eq. (D.1), $I^{(2)}_{\alpha\sigma}$ becomes

$$\begin{aligned} I^{(2)}_{\alpha\sigma} &= \frac{2e}{\hbar^2}\sum_{\vec{v}}\Big(\tilde{\delta}_1 \bar{\mathcal{K}}_{\alpha_1\sigma_1,\beta_1\sigma_1}\bar{\mathcal{K}}_{\beta\sigma,\alpha\sigma} + \tilde{x}_1 \mathcal{J}_{\alpha_1\sigma_1,\beta_1\sigma_{\beta_1}}\mathcal{J}_{\beta\sigma_\beta,\alpha\sigma}\Big) \\ &\quad\times\mathrm{Re}\Big[\int_{-\infty}^{0} dt \langle C^\dagger_{\alpha_1 k_{\alpha_1}\sigma_1} C_{\beta_1 k_{\beta_1}\sigma_{\beta_1}} C^\dagger_{\beta k_\beta \sigma_\beta} C_{\alpha k_\alpha \sigma}\rangle\Big] \\ &\quad-\frac{2e}{\hbar^2}\sum_{\vec{v}}\Big(\tilde{\delta}_1 \bar{\mathcal{K}}_{\alpha_1\sigma_1,\beta_1\sigma_1}\bar{\mathcal{K}}_{\alpha\sigma,\beta\sigma} + \tilde{x}_2 \mathcal{J}_{\alpha_1\sigma_1,\beta_1\sigma_{\beta_1}}\mathcal{J}_{\alpha\sigma,\beta\sigma_\beta}\Big) \\ &\quad\times\mathrm{Re}\Big[\int_{-\infty}^{0} dt \langle C^\dagger_{\alpha_1 k_{\alpha_1}\sigma_1} C_{\beta_1 k_{\beta_1}\sigma_{\beta_1}} C^\dagger_{\alpha k_\alpha \sigma} C_{\beta k_\beta \sigma_\beta}\rangle\Big] , \end{aligned} \tag{D.2}$$

where $\vec{v} = \{\alpha_1, k_{\alpha_1}, \sigma_1, \beta_1, k_{\beta_1}, \sigma_{\beta_1}, \beta, k_\beta, \sigma_\beta, k_\alpha\}$, $\tilde{\delta}_1 = \delta_{\sigma_1\sigma_{\beta_1}}\delta_{\sigma\sigma_\beta}$, $\tilde{x}_1 = \sum_{ll'}\langle S_l S_{l'}\rangle s^l_{\sigma_1\sigma_{\beta_1}} s^{l'}_{\sigma\sigma_\beta}$ and $\tilde{x}_2 = \langle S_l S_{l'}\rangle s^l_{\sigma_1\sigma_{\beta_1}} s^{l'}_{\sigma_\beta\sigma}$. The next step is the assessment of the expected values. First, we apply the Wick theorem to the expected values of the lead operators

$$\langle C^\dagger_{\vec{\alpha}}(t) C_{\vec{\beta}}(t) C^\dagger_{\vec{\gamma}}(0) C_{\vec{\lambda}}(0)\rangle = \delta_{\vec{\beta}\vec{\gamma}}\delta_{\vec{\alpha}\vec{\lambda}}\langle C^\dagger_{\vec{\alpha}}(t) C_{\vec{\lambda}}(0)\rangle\langle C_{\vec{\beta}}(t) C^\dagger_{\vec{\gamma}}(0)\rangle , \tag{D.3}$$

where $\vec{\alpha}, \vec{\beta}, \vec{\gamma}$ and $\vec{\lambda}$ are arbitrary sets of quantum numbers. Replacing the resulting expected values with the unperturbed lead Green's functions of Eqs. (4.20) and (4.21), the current reads

$$\begin{aligned} I^{(2)}_{\alpha\sigma} &= 2e \sum_{\vec{\beta}k_\alpha} \left(\tilde{\delta}_1 \left| \bar{\mathcal{K}}_{\beta\sigma,\alpha\sigma} \right|^2 + \tilde{x}_1 \left| \mathcal{J}_{\beta\sigma_\beta,\alpha\sigma} \right|^2 \right) \\ &\quad \times \mathrm{Re}\Big[\int_{-\infty}^{0} dt g^{>}_{\beta k_\beta \sigma_\beta}(t,0) g^{<}_{\alpha k_\alpha \sigma}(0,t) \Big] \\ &\quad -2e \sum_{\vec{\beta}k_\alpha} \left(\tilde{\delta}_1 \left| \bar{\mathcal{K}}_{\alpha\sigma,\beta\sigma} \right|^2 + \tilde{x}_2 \left| \mathcal{J}_{\alpha\sigma,\beta\sigma_\beta} \right| \right) \\ &\quad \times \mathrm{Re}\Big[\int_{-\infty}^{0} dt g^{>}_{\alpha k_\alpha \sigma}(t,0) g^{<}_{\beta k_\beta \sigma_\beta}(0,t) \Big] , \end{aligned} \tag{D.4}$$

where $\vec{\beta} = \{\beta, k_\beta, \sigma_\beta\}$. Applying $\langle S_l S_{l'} \rangle = \delta_{ll'}/4$, the coefficients $\tilde{x}_{1,2}$ read

$$\tilde{x}_1 = \tilde{x}_2 = \sum_l \frac{1}{4} |s^l_{\sigma\sigma_\beta}|^2 . \tag{D.5}$$

Now, we replace the greater and lesser Green's functions with Eqs. (A.9) and (A.4)

$$\begin{aligned} I^{(2)}_{\alpha\sigma} &= \frac{2e}{\hbar^2} \sum_{\vec{\beta}k_\alpha} \left(\tilde{\delta}_1 \left| \bar{\mathcal{K}}_{\beta\sigma,\alpha\sigma} \right|^2 + \tilde{x}_1 \left| \mathcal{J}_{\beta\sigma_\beta,\alpha\sigma} \right|^2 \right) f_{\alpha\sigma}(\varepsilon_{\alpha k_\alpha \sigma}) \\ &\quad \times [1 - f_{\beta\sigma_\beta}(\varepsilon_{\beta k_\beta \sigma_\beta})] \mathrm{Re}\Big[\int_{-\infty}^{0} dt \exp\Big(-\frac{i}{\hbar} [\varepsilon_{\alpha k_\alpha \sigma} - \varepsilon_{\beta k_\beta \sigma_\beta}] t \Big) \Big] \\ &\quad -\frac{2e}{\hbar^2} \sum_{\vec{\beta}k_\alpha} \left(\tilde{\delta}_1 \left| \bar{\mathcal{K}}_{\alpha\sigma,\beta\sigma} \right|^2 + \tilde{x}_2 \left| \mathcal{J}_{\alpha\sigma,\beta\sigma_\beta} \right|^2 \right) f_{\beta\sigma_\beta}(\varepsilon_{\beta k_\beta \sigma_\beta}) \\ &\quad \times [1 - f_{\alpha\sigma}(\varepsilon_{\alpha k_\alpha \sigma})] \mathrm{Re}\Big[\int_{-\infty}^{0} dt \exp\Big(-\frac{i}{\hbar} [\varepsilon_{\beta k_\beta \sigma_\beta} - \varepsilon_{\alpha k_\alpha \sigma}] t \Big) \Big] . \end{aligned} \tag{D.6}$$

Now, we evaluate the following integral

$$\mathrm{Re}\Big[\int_{-\infty}^{0} dt \exp\Big(-\frac{i}{\hbar} \omega t \Big) \Big] = \pi \delta(\omega) . \tag{D.7}$$

Therefore, Eq. (D.6) becomes

$$\begin{aligned} I^{(2)}_{\alpha\sigma} &= \frac{2\pi e}{\hbar^2} \sum_{\vec{\beta}k_\alpha} \left(\tilde{\delta}_1 \left| \bar{\mathcal{K}}_{\beta\sigma,\alpha\sigma} \right|^2 + \tilde{x}_1 \left| \mathcal{J}_{\beta\sigma_\beta,\alpha\sigma} \right|^2 \right) f_{\alpha\sigma}(\varepsilon_{\alpha k_\alpha}) \\ &\quad \times [1 - f_{\beta\sigma_\beta}(\varepsilon_{\beta k_\beta \sigma_\beta})] \delta\big(\varepsilon_{\alpha k_\alpha \sigma} - \varepsilon_{\beta k_\beta \sigma_\beta} \big) \\ &\quad -\frac{2\pi e}{\hbar^2} \sum_{\vec{\beta}k_\alpha} \left(\tilde{\delta}_1 \left| \bar{\mathcal{K}}_{\alpha\sigma,\beta\sigma} \right|^2 + \tilde{x}_2 \left| \mathcal{J}_{\alpha\sigma,\beta\sigma_\beta} \right|^2 \right) f_{\beta\sigma_\beta}(\varepsilon_{\beta k_\beta \sigma_\beta}) \\ &\quad \times [1 - f_{\alpha k_\alpha \sigma}(\varepsilon_{\alpha k_\alpha \sigma})] \delta\big(\varepsilon_{\beta k_\beta \sigma_\beta} - \varepsilon_{\alpha k_\alpha \sigma} \big) . \end{aligned} \tag{D.8}$$

We transform the sums over k_α and k_β into integrals obtaining

$$\begin{aligned} I^{(2)}_{\alpha\sigma} &= \frac{2\pi e}{\hbar^2}\sum_{\beta\sigma_\beta}\int d\omega\rho_{\alpha\sigma}\rho_{\beta\sigma_\beta}\left(\tilde{\delta}_1\left|\bar{\mathcal{K}}_{\beta\sigma,\alpha\sigma}\right|^2+\tilde{x}_1\left|\mathcal{J}_{\beta\sigma_\beta,\alpha\sigma}\right|^2\right) \\ &\quad\times\left[f_{\alpha\sigma}(\omega)-f_{\beta\sigma_\beta}(\omega)\right]. \end{aligned} \tag{D.9}$$

Taking into account that $s^{x,y}_{\sigma\sigma_\beta}=\delta_{\bar{\sigma}\sigma_\beta}/4$ and $s^{z}_{\sigma\sigma_\beta}=\delta_{\sigma\sigma_\beta}/4$, we find

$$\begin{aligned} I^{(2)}_{\alpha\sigma} &= \frac{e\pi}{4\hbar^2}\sum_{\beta}\int d\omega\rho_{\alpha\sigma}\rho_{\beta\bar{\sigma}}\left|\mathcal{J}_{\beta\bar{\sigma},\alpha\sigma}\right|^2\left[f_{\alpha\sigma}(\omega)-f_{\beta\bar{\sigma}}(\omega)\right] \\ &\quad+\frac{e\pi}{8\hbar^2}\sum_{\beta}\int d\omega\rho_{\alpha\sigma}\rho_{\beta\sigma}\left(16\left|\bar{\mathcal{K}}_{\beta\sigma,\alpha\sigma}\right|^2+\left|\mathcal{J}_{\beta\sigma,\alpha\sigma}\right|^2\right) \\ &\quad\times\left[f_{\alpha\sigma}(\omega)-f_{\beta\sigma}(\omega)\right], \end{aligned} \tag{D.10}$$

The solution of Eq. (D.10) is given by Eq. (6.29).

D.2 Third order

Now, we restrict to the s-d Hamiltonian of Eq. (5.29) considering spin-independent reservoirs. This implies that $V_{\alpha\sigma}\to V_\alpha$ and $\mathcal{J}_{\alpha\sigma_\alpha,\beta\sigma_\beta}\to\mathcal{J}_{\alpha\sigma}$. The third order of the electric current reads

$$\begin{aligned} I^{(3)}_{\alpha} &= -\frac{1}{\hbar^2}\sum_{\vec{v}_2}\mathcal{J}_{\alpha_1\beta_1}\mathcal{J}_{\alpha_1\beta_1}\mathrm{Re}\Big[\int_{-\infty}^{0}dt_1\int_{-\infty}^{0}dt_2 \\ &\quad\times\Big(\langle\hat{\bar{T}}x_{\sigma_{\alpha_1}\sigma_{\beta_1}}C^\dagger_{\vec{\alpha}_1}C_{\vec{\beta}_1}x_{\sigma_{\alpha_2}\sigma_{\beta_2}}C^\dagger_{\vec{\alpha}_2}C_{\vec{\beta}_2}\hat{I}_\alpha(0)\rangle \\ &\quad-\langle x_{\sigma_{\alpha_1}\sigma_{\beta_1}}C^\dagger_{\vec{\alpha}_1}C_{\vec{\beta}_1}\hat{I}_\alpha(0)x_{\sigma_{\alpha_2}\sigma_{\beta_2}}C^\dagger_{\vec{\alpha}_2}C_{\vec{\beta}_2}\rangle\Big)\Big], \end{aligned} \tag{D.11}$$

where $\vec{v}_2=\{\vec{\alpha}_1,\vec{\alpha}_2,\vec{\beta}_1,\vec{\beta}_2\}$ where $\vec{\gamma}_j=\{\gamma_j,k_{\gamma_j},\sigma_{\gamma_i}\}$ for arbitrary γ and j. Now, we replace the current with Eq. (6.24). We employ again the Wick theorem [Eq. (D.3)] and we substitute Eqs. (4.19), (4.20) and (4.21) into Eq. (D.11) obtaining

$$\begin{aligned} I^{(3a)}_{\alpha} &= e\sum_{\alpha\beta}\left|\mathcal{J}_{LR}\right|^2\mathcal{J}_{\alpha\alpha}\zeta_{\beta L}\mathrm{Re}\Big[\int_{-\infty}^{0}dt_1\int_{-\infty}^{0}dt_2 \\ &\quad\times\left(\sum_{\vec{\sigma}}\langle\hat{\bar{T}}x_{\sigma_1\sigma_2}(t_1)x_{\sigma_2\sigma_3}(t_2)x_{\sigma_3\sigma_1}(0)\rangle\right. \\ &\quad\left.+\langle\hat{\bar{T}}x_{\sigma_1\sigma_2}(t_2)x_{\sigma_3\sigma_1}(t_2)x_{\sigma_2\sigma_3}(0)\rangle\right) \\ &\quad\times\left(\sum_{\vec{k}}g^{\bar{t}}_{\beta k_1}(0,t_1)g^{\bar{t}}_{\alpha k_2}(t_1,t_2)g^{\bar{t}}_{\bar{\beta}k_3}(t_2,0)\right)\Big], \end{aligned} \tag{D.12a}$$

$$\begin{aligned} I_\alpha^{(3b)} &= -e\sum_{\alpha\beta}\left|\mathcal{J}_{LR}\right|^2\mathcal{J}_{\alpha\alpha}\zeta_{\beta L}\mathrm{Re}\Big[\int_{-\infty}^{0}dt_1\int_{-\infty}^{0}dt_2 \\ &\quad\times-\left\{\left(\sum_{\vec{\sigma}}\langle x_{\sigma_1\sigma_2}x_{\sigma_2\sigma_3}x_{\sigma_3\sigma_1}\rangle\right)\right. \\ &\quad\times\left(\sum_{\vec{k}}g^{>}_{\beta k_1}(0,t_2)g^{<}_{\alpha k_2}(t_2,t_1)g^{>}_{\bar{\beta}}(t_1,0)\right)\Bigg] \\ &\quad+\left(\sum_{\vec{\sigma}}\langle x_{\sigma_1\sigma_2}x_{\sigma_3\sigma_1}x_{\sigma_2\sigma_3}\rangle\right) \\ &\quad\times\left.\left(\sum_{\vec{k}}g^{<}_{\beta k_1}(0,t_1)g^{>}_{\alpha k_2}(t_1,t_2)g^{<}_{\bar{\beta}k_3}(t_2,0)\right)\right\}\Bigg]\ , \qquad \text{(D.12b)}\end{aligned}$$

where $\vec{\sigma}=\{\sigma_1,\sigma_2,\sigma_3\}$, $\vec{k}=\{k_1,k_2,k_3\}$, $I_\alpha^{(3)}=I_\alpha^{(3a)}+I_\alpha^{(3b)}$ and $\zeta_{\beta L}=1-2\delta_{\beta L}$. Now, we sum over spins

$$\begin{aligned} &\sum_{\vec{\sigma}}\langle\hat{\hat{T}}x_{\sigma_1\sigma_2}(t_1)x_{\sigma_2\sigma_3}(t_2)x_{\sigma_3\sigma_1}(0)\rangle \\ +&\sum_{\vec{\sigma}}\langle\hat{\hat{T}}x_{\sigma_1\sigma_2}(t_2)x_{\sigma_3\sigma_1}(t_2)x_{\sigma_2\sigma_3}(0)\rangle = \frac{5}{8}+\frac{3}{8}\mathrm{sgn}(t_2-t_1)\ , \qquad \text{(D.13)} \\ &\sum_{\vec{\sigma}}\langle x_{\sigma_1\sigma_2}x_{\sigma_2\sigma_3}x_{\sigma_3\sigma_1}\rangle = \frac{1}{8}\ , \qquad \text{(D.14)} \\ &\sum_{\vec{\sigma}}\langle x_{\sigma_1\sigma_2}x_{\sigma_3\sigma_1}x_{\sigma_2\sigma_3}\rangle = \frac{1}{2}\ , \qquad \text{(D.15)}\end{aligned}$$

where $\mathrm{sgn}(t)$ denotes the sign of t.

We continue including the unperturbed Green's function of Eqs. (A.9), (A.4) and (A.1) obtaining

$$\begin{aligned} I_\alpha^{(3)} &= \frac{e}{8\hbar^3}\sum_{\alpha\beta}\left|\mathcal{J}_{LR}\right|^2\mathcal{J}_{\alpha\alpha}\zeta_{\beta L}\mathrm{Im}\Big[\int_{-\infty}^{0}dt_1\int_{-\infty}^{0}dt_2\varrho(t_2-t_1) \\ &\quad\times\exp\left(-\frac{i}{\hbar}[\varepsilon_{\alpha k_2}-\varepsilon_{\beta k_1}]t\right)\exp\left(-\frac{i}{\hbar}[\varepsilon_{\bar{\beta}k_3}-\varepsilon_{\alpha k_2}]t\right) \\ &\quad\times f_\beta(\varepsilon_{\beta k_1})[\theta(t_2-t_1)-f_\alpha(\varepsilon_{\alpha k_2})][1-f_{\bar{\beta}}(\varepsilon_{\bar{\beta}k_3})] \\ &\quad-\exp\left(-\frac{i}{\hbar}[\varepsilon_{\alpha k_2}-\varepsilon_{\beta k_1}]t\right)\exp\left(-\frac{i}{\hbar}[\varepsilon_{\bar{\beta}k_3}-\varepsilon_{\alpha k_2}]t\right) \\ &\quad\times\big\{f_\alpha(\varepsilon_{\alpha k_2})-f_\beta(\varepsilon_{\beta k_1})f_\alpha(\varepsilon_{\alpha k_2})-f_{\bar{\beta}}(\varepsilon_{\bar{\beta}k_3})f_\alpha(\varepsilon_{\alpha k_2}) \\ &\quad-4f_{\bar{\beta}}(\varepsilon_{\bar{\beta}k_3})f_\beta(\varepsilon_{\beta k_1})+5f_{\bar{\beta}}(\varepsilon_{\bar{\beta}k_3})f_\alpha(\varepsilon_{\alpha k_2})f_\beta(\varepsilon_{\beta k_1})\big\}\Big] \qquad \text{(D.16)}\end{aligned}$$

where $\varrho(t_2-t_1)=5-3\mathrm{sgn}(t_2-t_1)$. Here, we convert the sums over k into integrals and perform the Fourier transform

$$\int_{-\infty}^{\infty}d\omega\frac{e^{-i\frac{\omega t}{\hbar}}}{1+e^{\frac{\omega-\mu_\alpha}{k_BT}}}=\frac{\pi i e^{i\frac{\mu_\alpha t}{\hbar}}}{\sinh\frac{\pi k_BTt}{\hbar}}\ . \qquad \text{(D.17)}$$

Therefore, the current becomes

$$\begin{aligned} I_\alpha^{(3)} \quad = \quad & \frac{e\pi^3}{8\hbar^2}\rho\sum_{\alpha\beta}\left|\mathcal{J}_{LR}\right|^2\mathcal{J}_{\alpha\alpha}\zeta_{\beta L}\int_{-\infty}^{0}dt[3\mathrm{Bs}_{\beta\bar{\beta}}(t)-\mathrm{Bs}_{\beta\alpha}(t)+\mathrm{Bs}_{\alpha\bar{\beta}}(t)] \\ & -\frac{e\pi^3}{8\hbar^2}\rho\sum_{\alpha\beta}\left|\mathcal{J}_{LR}\right|^2\mathcal{J}_{\alpha\alpha}\zeta_{\beta L} \\ & \times\mathrm{Re}\left[\int_{-\infty}^{0}dt_2e^{-\frac{ie}{\hbar}(V_{\bar{\beta}}-V_\alpha)t_2}\int_{-\infty}^{0}dt_1e^{-\frac{ie}{\hbar}(V_\alpha-V_\beta)t_2}\mathrm{Ts}_{\beta\alpha\bar{\beta}}(t_1,t_2)\right], \end{aligned} \tag{D.18}$$

where $\rho=\rho_L=\rho_R$ and

$$\mathrm{Bs}_{\alpha\beta} \quad = \quad \frac{k_B^2T_\alpha T_\beta\sin\left[e(V_\alpha-V_\beta)t/\hbar\right]}{\sinh\frac{\pi k_BT_\alpha t}{\hbar}\sinh\frac{\pi k_BT_\beta t}{\hbar}}, \tag{D.19}$$

$$\mathrm{Ts}_{\alpha\beta\gamma} \quad = \quad \frac{k_B^3T_\alpha T_\beta T_\gamma\mathrm{sgn}(t_2-t_1)}{\sinh\frac{\pi k_BT_\alpha t_1}{\hbar}\sinh\frac{\pi k_BT_\beta(t_1-t_2)}{\hbar}\sinh\frac{\pi k_BT_\gamma t_2}{\hbar}}. \tag{D.20}$$

After performing the sum over α and β the third order current reads

$$I_\alpha^{(3)}=\frac{e\pi^3}{8\hbar^2}\rho^3\left|\mathcal{J}_{LR}\right|^2\left(\mathcal{J}_{LL}+\mathcal{J}_{RR}\right)\int_{-\infty}^{0}dt\frac{k_B^2T_LT_R\sin\left(eVt/\hbar\right)}{\sinh\frac{\pi k_BT_Lt}{\hbar}\sinh\frac{\pi k_BT_Rt}{\hbar}}. \tag{D.21}$$

Bibliography

[1] M. A. Kastner, “Artificial Atoms”, Physics Today **46**, 24 (1993).

[2] B. J. Riel, “An introduction to self-assembled quantum dots”, American Journal of Physics **76**, 750 (2008).

[3] S. Bandyopadhyay et al., “Electrochemically assembled quasi-periodic quantum dot arrays”, Nanotechnology **7**, 360 (1996).

[4] M. W. Larsson, J. B. Wagner, M. Wallin, P. Håkansson, L. E. Fröberg, L. Samuelson, and L. R. Wallenberg, “Strain mapping in free-standing heterostructured wurtzite InAs/InP nanowires”, Nanotechnology **18**, 015504 (2007).

[5] D. K. Ferry, S. M. Goodnick, and J. Bird, *Transport in Nanostructures* (Cambridge University Press, Cambridge, 2009).

[6] L. P. Kouwenhoven, C. M. Marcus, P. L. McEuen, S. Tarucha, R. M. Westervelt, and N. S. Wingreen, “Electron Transport in quantum dots”, in *Proceedings of the nato advanced study institute on mesoscopic electron transport* (Kluwer, Dordrecht, 1997), page 105.

[7] D. Goldhaber-Gordon, H. Shtrikman, D. Mahalu, D. Abusch-Magder, U. Meirav, and M. A. Kastner, “Kondo effect in a single-electron transistor”, Nature **391**, 156 (1998).

[8] Y. Imry, *Introduction to Mesoscopic Physics*, 2nd (Oxford University Press, Oxford, 2001), page 252.

[9] S. Datta, *Electronic Transport in Mesoscopic Systems* (Cambridge University Press, Cambridge, 1995).

[10] H. Grabert and M. H. Devoret, editors, *Single Charge Tunneling*, Vol. 294, NATO ASI Series (Springer US, Boston, MA, 1992).

[11] J. H. F. Scott-Thomas, S. B. Field, M. A. Kastner, H. I. Smith, and D. A. Antoniadis, “Conductance Oscillations Periodic in the Density of a One-Dimensional Electron Gas”, Physical Review Letters **62**, 583 (1989).

[12] S. Lindemann, T. Ihn, T. Heinzel, W. Zwerger, K. Ensslin, K. Maranowski, and A. C. Gossard, “Stability of spin states in quantum dots”, Physical Review B **66**, 195314 (2002).

[13] C. W. J. Beenakker, "Theory of Coulomb-blockade oscillations in the conductance of a quantum dot", Physical Review B **44**, 1646 (1991).

[14] Y. Meir, N. S. Wingreen, and P. A. Lee, "Transport through a strongly interacting electron system: Theory of periodic conductance oscillations", Physical Review Letters **66**, 3048 (1991).

[15] U. Meirav, M. A. Kastner, and S. J. Wind, "Single-electron charging and periodic conductance resonances in GaAs nanostructures", Physical Review Letters **65**, 771 (1990).

[16] L. P. Kouwenhoven, N. C. van der Vaart, A. T. Johnson, W. Kool, C. J. P. M. Harmans, J. G. Williamson, A. A. M. Staring, and C. T. Foxon, "Single electron charging effects in semiconductor quantum dots", Zeitschrift für Physik B Condensed Matter **85**, 367 (1991).

[17] Y. Nagamune, H. Sakaki, L. P. Kouwenhoven, L. C. Mur, C. J. P. M. Harmans, J. Motohisa, and H. Noge, "Single electron transport and current quantization in a novel quantum dot structure", Applied Physics Letters **64**, 2379 (1994).

[18] S. Tarucha, D. G. Austing, T. Honda, R. J. van der Hage, and L. P. Kouwenhoven, "Shell Filling and Spin Effects in a Few Electron Quantum Dot", Physical Review Letters **77**, 3613 (1996).

[19] M. Ciorga, A. S. Sachrajda, P. Hawrylak, C. Gould, P. Zawadzki, S. Jullian, Y. Feng, and Z. Wasilewski, "Addition spectrum of a lateral dot from Coulomb and spin-blockade spectroscopy", Physical Review B **61**, R16315 (2000).

[20] J. C. Cuevas and E. Sheer, *Molecular Electronics* (World Scientific Publishing Co., Danvers, 2010).

[21] J. R. Heath and M. A. Ratner, "Molecular Electronics", Physics Today **56**, 43 (2003).

[22] A. von Hippel, "Molecular Engineering", Science **123**, 315 (1956).

[23] A. Aviram and M. A. Ratner, "Molecular rectifiers", Chemical Physics Letters **29**, 277 (1974).

[24] M. Fujihira, K. Nishiyama, and H. Yamada, "Photoelectrochemical responses of optically transparent electrodes modified with Langmuir-Blodgett films consisting of surfactant derivatives of electron donor, acceptor and sensitizer molecules", Thin Solid Films **132**, 77 (1985).

[25] M. A. Reed, C. Zhou, T. Burgin, and J. Tour, "Conductance of a Molecular Junction", Science **278**, 252 (1997).

[26] L. Venkataraman, J. E. Klare, C. Nuckolls, M. S. Hybertsen, and M. L. Steigerwald, "Dependence of single-molecule junction conductance on molecular conformation", Nature **442**, 904 (2006).

[27] I. Díez-Pérez, J. Hihath, Y. Lee, L. Yu, L. Adamska, M. A. Kozhushner, I. I. Oleynik, and N. Tao, "Rectification and stability of a single molecular diode with controlled orientation", Nature Chemistry **1**, 635 (2009).

[28] W. F. Reus, M. M. Thuo, N. D. Shapiro, C. A. Nijhuis, and G. M. Whitesides, "The SAM, Not the Electrodes, Dominates Charge Transport in Metal-Monolayer//Ga2O3/Gallium–Indium Eutectic Junctions", ACS Nano **6**, 4806 (2012).

[29] C. A. Nijhuis, W. F. Reus, J. R. Barber, and G. M. Whitesides, "Comparison of SAM-Based Junctions with Ga2O3 /EGaIn Top Electrodes to Other Large-Area Tunneling Junctions", The Journal of Physical Chemistry C **116**, 14139 (2012).

[30] D. Fracasso, H. Valkenier, J. C. Hummelen, G. C. Solomon, and R. C. Chiechi, "Evidence for Quantum Interference in SAMs of Arylethynylene Thiolates in Tunneling Junctions with Eutectic Ga–In (EGaIn) Top-Contacts", Journal of the American Chemical Society **133**, 9556 (2011).

[31] X. Chen, M. Roemer, L. Yuan, W. Du, D. Thompson, E. del Barco, and C. A. Nijhuis, "Molecular diodes with rectification ratios exceeding 105 driven by electrostatic interactions", Nature Nanotechnology **12**, 797 (2017).

[32] C. M. Bowers, K.-C. Liao, T. Zaba, D. Rappoport, M. Baghbanzadeh, B. Breiten, A. Krzykawska, P. Cyganik, and G. M. Whitesides, "Characterizing the Metal–SAM Interface in Tunneling Junctions", ACS Nano **9**, 1471 (2015).

[33] Y. Zhang, Z. Zhao, D. Fracasso, and R. C. Chiechi, "Bottom-Up Molecular Tunneling Junctions Formed by Self-Assembly", Israel Journal of Chemistry **54**, 513 (2014).

[34] H. Park, J. Park, A. K. L. Lim, E. H. Anderson, A. P. Alivisatos, and P. L. McEuen, "Nanomechanical oscillations in a single-C60 transistor", Nature **407**, 57 (2000).

[35] J. Park et al., "Coulomb blockade and the Kondo effect in single-atom transistors", Nature **417**, 722 (2002).

[36] S. Ho Choi, B. Kim, and C. D. Frisbie, "Electrical Resistance of Long Conjugated Molecular Wires", Science **320**, 1482 (2008).

[37] L. Lafferentz, F. Ample, H. Yu, S. Hecht, C. Joachim, and L. Grill, "Conductance of a Single Conjugated Polymer as a Continuous Function of Its Length", Science **323**, 1193 (2009).

[38] M. Koch, F. Ample, C. Joachim, and L. Grill, “Voltage-dependent conductance of a single graphene nanoribbon”, Nature Nanotechnology **7**, 713 (2012).

[39] G. I. Livshits et al., “Long-range charge transport in single G-quadruplex DNA molecules”, Nature Nanotechnology **9**, 1040 (2014).

[40] L. Yuan, N. Nerngchamnong, L. Cao, H. Hamoudi, E. del Barco, M. Roemer, R. K. Sriramula, D. Thompson, and C. A. Nijhuis, “Controlling the direction of rectification in a molecular diode”, Nature Communications **6**, 6324 (2015).

[41] A. R. Garrigues, L. Wang, E. del Barco, and C. A. Nijhuis, “Electrostatic control over temperature-dependent tunnelling across a single-molecule junction”, Nature Communications **7**, 11595 (2016).

[42] R. L. McCreery and A. J. Bergren, “Progress with Molecular Electronic Junctions: Meeting Experimental Challenges in Design and Fabrication”, Advanced Materials **21**, 4303 (2009).

[43] F. Hofmann, T. Heinzel, D. Wharam, J. P. Kotthaus, G. Böhm, W. Klein, G. Tränkle, and G. Weimann, “Single electron switching in a parallel quantum dot”, Physical Review B **51**, 13872 (1995).

[44] A. Adourian, C. Livermore, R. Westervelt, K. Campman, and A. Gossard, “Single electron charging in parallel coupled quantum dots”, Superlattices and Microstructures **20**, 411 (1996).

[45] A. W. Holleitner, C. R. Decker, H. Qin, K. Eberl, and R. H. Blick, “Coherent Coupling of Two Quantum Dots Embedded in an Aharonov-Bohm Interferometer”, Physical Review Letters **87**, 256802 (2001).

[46] Y. Aharonov and D. Bohm, “Further Considerations on Electromagnetic Potentials in the Quantum Theory”, Physical Review **123**, 1511 (1961).

[47] D. Loss and E. V. Sukhorukov, “Probing Entanglement and Nonlocality of Electrons in a Double-Dot via Transport and Noise”, Physical Review Letters **84**, 1035 (2000).

[48] M. Büttiker, Y. Imry, and M. Y. Azbel, “Quantum oscillations in one-dimensional normal-metal rings”, Physical Review A **30**, 1982 (1984).

[49] Y. Gefen, Y. Imry, and M. Y. Azbel, “Quantum Oscillations and the Aharonov-Bohm Effect for Parallel Resistors”, Physical Review Letters **52**, 129 (1984).

[50] H. Lu, R. Lü, and B.-f. Zhu, “Tunable Fano effect in parallel-coupled double quantum dot system”, Physical Review B **71**, 235320 (2005).

[51] A. E. Miroshnichenko, S. Flach, and Y. S. Kivshar, “Fano resonances in nanoscale structures”, Reviews of Modern Physics **82**, 2257 (2010).

[52] U. Fano, “Effects of Configuration Interaction on Intensities and Phase Shifts”, Physical Review **124**, 1866 (1961).

[53] P. A. Orellana, M. L. Ladrón de Guevara, and F. Claro, “Controlling Fano and Dicke effects via a magnetic flux in a two-site Anderson model”, Physical Review B **70**, 233315 (2004).

[54] R. H. Dicke, “The Effect of Collisions upon the Doppler Width of Spectral Lines”, Physical Review **89**, 472 (1953).

[55] T. V. Shahbazyan and M. E. Raikh, “Two-channel resonant tunneling”, Physical Review B **49**, 17123 (1994).

[56] T. Vorrath and T. Brandes, “Dicke effect in the tunnel current through two double quantum dots”, Physical Review B **68**, 035309 (2003).

[57] A. W. Holleitner, R. H. Blick, A. K. Hüttel, K. Eberl, and J. P. Kotthaus, “Probing and Controlling the Bonds of an Artificial Molecule”, Science **297**, 70 (2002).

[58] A. Fuhrer, P. Brusheim, T. Ihn, M. Sigrist, K. Ensslin, W. Wegscheider, and M. Bichler, “Fano effect in a quantum-ring–quantum-dot system with tunable coupling”, Physical Review B **73**, 205326 (2006).

[59] S. Gustavsson, R. Leturcq, M. Studer, T. Ihn, K. Ensslin, D. C. Driscoll, and A. C. Gossard, “Time-Resolved Detection of Single-Electron Interference”, Nano Letters **8**, 2547 (2008).

[60] D. Loss and D. P. DiVincenzo, “Quantum computation with quantum dots”, Physical Review A **57**, 120 (1998).

[61] X. Hu and S. Das Sarma, “Hilbert-space structure of a solid-state quantum computer: Two-electron states of a double-quantum-dot artificial molecule”, Physical Review A **61**, 062301 (2000).

[62] A. Ramšak, J. Mravlje, R. Žitko, and J. Bonča, “Spin qubits in double quantum dots: Entanglement versus the Kondo effect”, Physical Review B **74**, 241305 (2006).

[63] B. N. Narozhny and A. Levchenko, “Coulomb drag”, Reviews of Modern Physics **88**, 025003 (2016).

[64] T. J. Gramila, J. P. Eisenstein, A. H. MacDonald, L. N. Pfeiffer, and K. W. West, “Evidence for virtual-phonon exchange in semiconductor heterostructures”, Physical Review B **47**, 12957 (1993).

[65] H. Noh, S. Zelakiewicz, X. G. Feng, T. J. Gramila, L. N. Pfeiffer, and K. W. West, “Many-body correlations probed by plasmon-enhanced drag measurements in double-quantum-well structures”, Physical Review B **58**, 12621 (1998).

[66] B. Laikhtman and P. M. Solomon, "Mutual drag of two- and three-dimensional electron gases in heterostuctures", Physical Review B **41**, 9921 (1990).

[67] M. Yamamoto, M. Stopa, Y. Tokura, Y. Hirayama, and S. Tarucha, "Negative Coulomb Drag in a One-Dimensional Wire", Science **313**, 204 (2006).

[68] W.-K. Tse, B. Y.-K. Hu, and S. Das Sarma, "Theory of Coulomb drag in graphene", Physical Review B **76**, 081401 (2007).

[69] R. Sánchez, R. López, D. Sánchez, and M. Büttiker, "Mesoscopic Coulomb Drag, Broken Detailed Balance, and Fluctuation Relations", Physical Review Letters **104**, 076801 (2010).

[70] G. Shinkai, T. Hayashi, T. Ota, K. Muraki, and T. Fujisawa, "Bidirectional Current Drag Induced by Two-Electron Cotunneling in Coupled Double Quantum Dots", Applied Physics Express **2**, 081101 (2009).

[71] D. Bischoff, M. Eich, O. Zilberberg, C. Rössler, T. Ihn, and K. Ensslin, "Measurement Back-Action in Stacked Graphene Quantum Dots", Nano Letters **15**, 6003 (2015).

[72] A. J. Keller, J. S. Lim, D. Sánchez, R. López, S. Amasha, J. A. Katine, H. Shtrikman, and D. Goldhaber-Gordon, "Cotunneling Drag Effect in Coulomb-Coupled Quantum Dots", Physical Review Letters **117**, 066602 (2016).

[73] K. Kaasbjerg and A.-P. Jauho, "Correlated Coulomb Drag in Capacitively Coupled Quantum-Dot Structures", Physical Review Letters **116**, 196801 (2016).

[74] A.-P. Jauho and H. Smith, "Coulomb drag between parallel two-dimensional electron systems", Physical Review B **47**, 4420 (1993).

[75] T. J. Gramila, J. P. Eisenstein, A. H. MacDonald, L. N. Pfeiffer, and K. W. West, "Mutual friction between parallel two-dimensional electron systems", Physical Review Letters **66**, 1216 (1991).

[76] A. Kamenev and Y. Oreg, "Coulomb drag in normal metals and superconductors: Diagrammatic approach", Physical Review B **52**, 7516 (1995).

[77] A. Levchenko and A. Kamenev, "Coulomb Drag in Quantum Circuits", Physical Review Letters **101**, 216806 (2008).

[78] D. Segal, "Heat flow in nonlinear molecular junctions: Master equation analysis", Physical Review B **73**, 205415 (2006).

[79] W. G. van der Wiel, S. De Franceschi, J. M. Elzerman, T. Fujisawa, S. Tarucha, and L. P. Kouwenhoven, "Electron transport through double quantum dots", Reviews of Modern Physics **75**, 1 (2002).

[80] R. Hanson, L. P. Kouwenhoven, J. R. Petta, S. Tarucha, and L. M. K. Vandersypen, “Spins in few-electron quantum dots”, Reviews of Modern Physics **79**, 1217 (2007).

[81] H.-A. Engel, V. N. Golovach, D. Loss, L. M. K. Vandersypen, J. M. Elzerman, R. Hanson, and L. P. Kouwenhoven, “Measurement Efficiency and n-Shot Readout of Spin Qubits”, Physical Review Letters **93**, 106804 (2004).

[82] L. M. K. Vandersypen, H. Bluhm, J. S. Clarke, A. S. Dzurak, R. Ishihara, A. Morello, D. J. Reilly, L. R. Schreiber, and M. Veldhorst, “Interfacing spin qubits in quantum dots and donors—hot, dense, and coherent”, npj Quantum Information **3**, 34 (2017).

[83] D. P. DiVincenzo, “Double Quantum Dot as a Quantum Bit”, Science **309**, 2173 (2005).

[84] A. C. Hewson, *The Kondo Problem to Heavy Fermions* (Cambridge University Press, Cambridge, UK, 1993).

[85] W. de Haas, J. de Boer, and G. van dën Berg, “The electrical resistance of gold, copper and lead at low temperatures”, Physica **1**, 1115 (1934).

[86] J. Kondo, “Theory of Dilute Magnetic Alloys”, in *Solid state physics*, edited by F. Seitz, D. Turnbull, and H. Ehrenreich (New York Academic Press, New York, 1970) Chap. 2, pages 183–281.

[87] L. P. Kouwenhoven and L. I. Glazman, “Revival of the Kondo effect”, Physics World **14**, 33 (2001).

[88] M. P. Sarachik, E. Corenzwit, and L. D. Longinotti, “Resistivity of Mo-Nb and Mo-Re Alloys Containing 1% Fe”, Physical Review **135**, A1041 (1964).

[89] D. K. C. MacDonald, W. B. Pearson, and I. M. Templeton, “Thermo-Electricity at Low Temperatures. IX. The Transition Metals as Solute and Solvent”, Proceedings of the Royal Society A: Mathematical, Physical and Engineering Sciences **266**, 161 (1962).

[90] A. A. Abrikosov, “Electron scattering on magnetic impurities in metals and anomalous resistivity effects”, Physics **2**, 5 (1965).

[91] L. D. Landau, “The theory of a Fermi liquid”, in *Soviet physics jetp*, Vol. 3, 6 (1957), page 920.

[92] P. Phillips, *Advanced Solid State Physics* (Cambridge University Press, Cambridge, 2012), page 413.

[93] K. G. Wilson, “The renormalization group: Critical phenomena and the Kondo problem”, Reviews of Modern Physics **47**, 773 (1975).

[94] B. Horvatić, D. Sokcević, and V. Zlatić, “Finite-temperature spectral density for the Anderson model”, Physical Review B **36**, 675 (1987).

[95] L. I. Glazman and M. E. Raikh, “Resonant Kondo transparency of a barrier with quasilocal impurity states”, Sov. Phys. JETP Lett. **47**, 452 (1988).

[96] J. Friedel, “On some electrical and magnetic properties of metallic solid solutions”, Canadian Journal of Physics **34**, 1190 (1956).

[97] C. Zener, “Interaction Between the d Shells in the Transition Metals”, Physical Review **81**, 440 (1951).

[98] P. W. Anderson, “Localized Magnetic States in Metals”, Physical Review **124**, 41 (1961).

[99] P. W. Anderson, “Ground State of a Magnetic Impurity in a Metal”, Physical Review **164**, 352 (1967).

[100] J. R. Schrieffer and P. A. Wolff, “Relation between the Anderson and Kondo Hamiltonians”, Physical Review **149**, 491 (1966).

[101] F. D. M. Haldane, “Scaling Theory of the Asymmetric Anderson Model”, Physical Review Letters **40**, 416 (1978).

[102] J. Hubbard, “Electron Correlations in Narrow Energy Bands. IV. The Atomic Representation”, Proceedings of the Royal Society A: Mathematical, Physical and Engineering Sciences **285**, 542 (1965).

[103] B. Coqblin and J. R. Schrieffer, “Exchange Interaction in Alloys with Cerium Impurities”, Physical Review **185**, 847 (1969).

[104] T. K. Ng and P. A. Lee, “On-Site Coulomb Repulsion and Resonant Tunneling”, Physical Review Letters **61**, 1768 (1988).

[105] A. Kaminski, Y. V. Nazarov, and L. I. Glazman, “Universality of the Kondo effect in a quantum dot out of equilibrium”, Physical Review B **62**, 8154 (2000).

[106] W. G. van der Wiel, S. De Franceschi, T. Fujisawa, S. Tarucha, and L. P. Kouwenhoven, “The Kondo Effect in the Unitary Limit”, Science **289**, 2105 (2000).

[107] D. C. Ralph and R. A. Buhrman, “Kondo-assisted and resonant tunneling via a single charge trap: A realization of the Anderson model out of equilibrium”, Physical Review Letters **72**, 3401 (1994).

[108] P. San-Jose, J. L. Lado, R. Aguado, F. Guinea, and J. Fernández-Rossier, “Majorana Zero Modes in Graphene”, Physical Review X **5**, 041042 (2015).

[109] M. Z. Hasan and C. L. Kane, “Colloquium : Topological insulators”, Reviews of Modern Physics **82**, 3045 (2010).

[110] A. V. Kretinin, H. Shtrikman, and D. Mahalu, “Universal line shape of the Kondo zero-bias anomaly in a quantum dot”, Physical Review B **85**, 201301 (2012).

[111] A. Svilans, M. Josefsson, A. M. Burke, S. Fahlvik, C. Thelander, H. Linke, and M. Leijnse, “Thermoelectric Characterization of the Kondo Resonance in Nanowire Quantum Dots”, Physical Review Letters **121**, 206801 (2018).

[112] J. M. Thijssen and H. S. J. van der Zant, “Charge transport and single-electron effects in nanoscale systems”, physica status solidi (b) **245**, 1455 (2008).

[113] S. De Franceschi, R. Hanson, W. G. van der Wiel, J. M. Elzerman, J. J. Wijpkema, T. Fujisawa, S. Tarucha, and L. P. Kouwenhoven, “Out-of-Equilibrium Kondo Effect in a Mesoscopic Device”, Physical Review Letters **89**, 156801 (2002).

[114] R. Scheibner, H. Buhmann, D. Reuter, M. N. Kiselev, and L. W. Molenkamp, “Thermopower of a Kondo Spin-Correlated Quantum Dot”, Physical Review Letters **95**, 176602 (2005).

[115] Y. Meir, N. S. Wingreen, and P. A. Lee, “Low-temperature transport through a quantum dot: The Anderson model out of equilibrium”, Physical Review Letters **70**, 2601 (1993).

[116] A. Rosch, J. Kroha, and P. Wölfle, “Kondo Effect in Quantum Dots at High Voltage: Universality and Scaling”, Physical Review Letters **87**, 156802 (2001).

[117] D. Sánchez and R. López, “Three-terminal transport through a quantum dot in the Kondo regime: Conductance, dephasing, and current-current correlations”, Physical Review B **71**, 035315 (2005).

[118] Q.-f. Sun and H. Guo, “Double quantum dots: Kondo resonance induced by an interdot interaction”, Physical Review B **66**, 155308 (2002).

[119] L. Tosi, P. Roura-Bas, and A. A. Aligia, “Orbital Kondo spectroscopy in a double quantum dot system”, Physical Review B **88**, 235427 (2013).

[120] Z.-q. Bao, A.-M. Guo, and Q.-f. Sun, “Orbital Kondo effect in a parallel double quantum dot”, Journal of Physics: Condensed Matter **26**, 435301 (2014).

[121] A. Wong, W. B. Lane, L. G. G. V. Dias da Silva, K. Ingersent, N. Sandler, and S. E. Ulloa, “Signatures of quantum phase transitions in parallel quantum dots: Crossover from local moment to underscreened spin-1 Kondo physics”, Physical Review B **85**, 115316 (2012).

[122] F. W. Jayatilaka, M. R. Galpin, and D. E. Logan, “Two-channel Kondo physics in tunnel-coupled double quantum dots”, Physical Review B **84**, 115111 (2011).

[123] D. Krychowski and S. Lipiński, “Spin-orbital and spin Kondo effects in parallel coupled quantum dots”, Physical Review B **93**, 075416 (2016).

[124] A. N. Pasupathy, R. C. Bialczak, J. Martinek, J. E. Grose, L. A. K. Donev, P. L. McEuen, and D. C. Ralph, “The Kondo Effect in the Presence of Ferromagnetism”, Science **306**, 86 (2004).

[125] J. R. Hauptmann, J. Paaske, and P. E. Lindelof, “Electric-field-controlled spin reversal in a quantum dot with ferromagnetic contacts”, Nature Physics **4**, 373 (2008).

[126] M. R. Calvo, J. Fernández-Rossier, J. J. Palacios, D. Jacob, D. Natelson, and C. Untiedt, “The Kondo effect in ferromagnetic atomic contacts”, Nature **458**, 1150 (2009).

[127] P. Jarillo-Herrero, J. Kong, H. Van Der Zant, C. Dekker, L. P. Kouwenhoven, and S. De Franceschi, “Orbital Kondo effect in carbon nanotubes”, Nature **434**, 484 (2005).

[128] R. López, R. Aguado, and G. Platero, “Nonequilibrium Transport through Double Quantum Dots: Kondo Effect versus Antiferromagnetic Coupling”, Physical Review Letters **89**, 136802 (2002).

[129] N. J. Craig, J. M. Taylor, E. A. Lester, C. M. Marcus, M. P. Hanson, and A. C. Gossard, “Tunable Nonlocal Spin Control in a Coupled-Quantum Dot System”, Science **304**, 565 (2004).

[130] L. Borda, G. Zaránd, W. Hofstetter, B. I. Halperin, and J. von Delft, “SU(4) Fermi Liquid State and Spin Filtering in a Double Quantum Dot System”, Physical Review Letters **90**, 026602 (2003).

[131] K. Le Hur, P. Simon, and L. Borda, “Maximized orbital and spin Kondo effects in a single-electron transistor”, Physical Review B **69**, 045326 (2004).

[132] R. López, D. Sánchez, M. Lee, M.-S. Choi, P. Simon, and K. Le Hur, “Probing spin and orbital Kondo effects with a mesoscopic interferometer”, Physical Review B **71**, 115312 (2005).

[133] S. Amasha, A. J. Keller, I. G. Rau, A. Carmi, J. A. Katine, H. Shtrikman, Y. Oreg, and D. Goldhaber-Gordon, “Pseudospin-Resolved Transport Spectroscopy of the Kondo Effect in a Double Quantum Dot”, Physical Review Letters **110**, 046604 (2013).

[134] D. M. Schröer, A. K. Hüttel, K. Eberl, S. Ludwig, M. N. Kiselev, and B. L. Altshuler, “Kondo effect in a one-electron double quantum dot: Oscillations of the Kondo current in a weak magnetic field”, Physical Review B **74**, 233301 (2006).

[135] M. A. Ruderman and C. Kittel, “Indirect exchange coupling of nuclear magnetic moments by conduction electrons”, Physical Review **96**, 99 (1954).

[136] T. Kasuya, "A Theory of Metallic Ferro- and Antiferromagnetism on Zener's Model", Progress of Theoretical Physics **16**, 45 (1956).

[137] K. Yosida, "Magnetic Properties of Cu-Mn Alloys", Physical Review **106**, 893 (1957).

[138] H. Jeong, A. M. Chang, and M. R. Melloch, "The Kondo Effect in an Artificial Quantum Dot Molecule", Science **293**, 2221 (2001).

[139] T. Aono and M. Eto, "Kondo resonant spectra in coupled quantum dots", Physical Review B **63**, 125327 (2001).

[140] R. Žitko and J. Bonča, "Quantum phase transitions in systems of parallel quantum dots", Physical Review B **76**, 241305 (2007).

[141] S. J. Chorley, M. R. Galpin, F. W. Jayatilaka, C. G. Smith, D. E. Logan, and M. R. Buitelaar, "Tunable Kondo Physics in a Carbon Nanotube Double Quantum Dot", Physical Review Letters **109**, 156804 (2012).

[142] J. C. Chen, A. M. Chang, and M. R. Melloch, "Transition between Quantum States in a Parallel-Coupled Double Quantum Dot", Physical Review Letters **92**, 176801 (2004).

[143] H. Goldsmid, "Conversion Efficiency and Figure-of-Merit", in *Crc handbook of thermoelectrics* (CRC Press, July 1995).

[144] I. Terasaki, *Introduction to thermoelectricity* (2005), pages 339–357.

[145] H. J. Goldsmid, *Introduction to Thermoelectricity*, Vol. 121, Springer Series in Materials Science (Springer, Berlin, 2010).

[146] L. Onsager, "Reciprocal Relations in Irreversible Processes. I.", Physical Review **37**, 405 (1931).

[147] A. F. Joffe and L. S. Stil'bans, "Physical problems of thermoelectricity", Reports on Progress in Physics **22**, 306 (1959).

[148] L. D. Hicks and M. S. Dresselhaus, "Effect of quantum-well structures on the thermoelectric figure of merit", Physical Review B **47**, 12727 (1993).

[149] L. D. Hicks and M. S. Dresselhaus, "Thermoelectric figure of merit of a one-dimensional conductor", Physical Review B **47**, 16631 (1993).

[150] G. D. Mahan and J. O. Sofo, "The best thermoelectric.", Proceedings of the National Academy of Sciences **93**, 7436 (1996).

[151] G. Benenti, G. Casati, K. Saito, and R. S. Whitney, "Fundamental aspects of steady-state conversion of heat to work at the nanoscale", Physics Reports **694**, 1 (2017).

[152] D. Sánchez and H. Linke, "Focus on thermoelectric effects in nanostructures", New Journal of Physics **16**, 110201 (2014).

[153] E. Macia-Barber, *Thermoelectric Materials Advances and Applications* (Pan Stanford Publishing, Stanford, 2015).

[154] R. Franz and G. Wiedemann, “Ueber die Wärme-Leitungsfähigkeit der Metalle”, Annalen der Physik und Chemie **165**, 497–531 (1853).

[155] C. Kittell, *Introduction to Solid State Physics* (John Wiley & Sons, Inc, Berkeley, 1986).

[156] M. Cutler and N. F. Mott, “Observation of Anderson Localization in an Electron Gas”, Physical Review **181**, 1336 (1969).

[157] J. B. Pendry, “Quantum limits to the flow of information and entropy”, Journal of Physics A: Mathematical and General **16**, 2161 (1983).

[158] L. G. C. Rego and G. Kirczenow, “Quantized Thermal Conductance of Dielectric Quantum Wires”, Physical Review Letters **81**, 232 (1998).

[159] K. Schwab, E. A. Henriksen, J. M. Worlock, and M. L. Roukes, “Measurement of the quantum of thermal conductance”, Nature **404**, 974 (2000).

[160] N. W. Ashcroft and N. Mermin, *Solid State Physics* (Hartcourt College Publishers, Harcourt, 1976).

[161] Y. Dubi and M. Di Ventra, “Colloquium : Heat flow and thermoelectricity in atomic and molecular junctions”, Reviews of Modern Physics **83**, 131 (2011).

[162] D. Sánchez and R. López, “Nonlinear phenomena in quantum thermoelectrics and heat”, Comptes Rendus Physique **17**, 1060 (2016).

[163] D. Sánchez and M. Büttiker, “Magnetic-Field Asymmetry of Nonlinear Mesoscopic Transport”, Physical Review Letters **93**, 106802 (2004).

[164] B. Spivak and A. Zyuzin, “Signature of the Electron-Electron Interaction in the Magnetic-Field Dependence of Nonlinear $I-V$ Characteristics in Mesoscopic Systems”, Physical Review Letters **93**, 226801 (2004).

[165] C. A. Marlow, R. P. Taylor, M. Fairbanks, I. Shorubalko, and H. Linke, “Experimental Investigation of the Breakdown of the Onsager-Casimir Relations”, Physical Review Letters **96**, 116801 (2006).

[166] D. M. Zumbühl, C. M. Marcus, M. P. Hanson, and A. C. Gossard, “Asymmetry of Nonlinear Transport and Electron Interactions in Quantum Dots”, Physical Review Letters **96**, 206802 (2006).

[167] R. Leturcq, D. Sánchez, G. Götz, T. Ihn, K. Ensslin, D. C. Driscoll, and A. C. Gossard, “Magnetic Field Symmetry and Phase Rigidity of the Nonlinear Conductance in a Ring”, Physical Review Letters **96**, 126801 (2006).

[168] R. López and D. Sánchez, "Nonlinear heat transport in mesoscopic conductors: Rectification, Peltier effect, and Wiedemann-Franz law", Physical Review B **88**, 045129 (2013).

[169] I. O. Kulik, "Non-linear thermoelectricity and cooling effects in metallic constrictions", Journal of Physics: Condensed Matter **6**, 9737 (1994).

[170] A. S. Dzurak, C. G. Smith, L. Martin-Moreno, M. Pepper, D. A. Ritchie, G. A. C. Jones, and D. G. Hasko, "Thermopower of a one-dimensional ballistic constriction in the non-linear regime", Journal of Physics: Condensed Matter **5**, 8055 (1993).

[171] E. N. Bogachek, A. G. Scherbakov, and U. Landman, "Nonlinear Peltier effect and thermoconductance in nanowires", Physical Review B **60**, 11678 (1999).

[172] M. Terraneo, M. Peyrard, and G. Casati, "Controlling the Energy Flow in Nonlinear Lattices: A Model for a Thermal Rectifier", Physical Review Letters **88**, 094302 (2002).

[173] C. W. Chang, D. Okawa, A. Majumdar, and A. Zettl, "Solid-State Thermal Rectifier", Science **314**, 1121 (2006).

[174] R. Scheibner, M. König, D. Reuter, A. D. Wieck, C. Gould, H. Buhmann, and L. W. Molenkamp, "Quantum dot as thermal rectifier", New Journal of Physics **10**, 083016 (2008).

[175] R. S. Whitney, "Nonlinear thermoelectricity in point contacts at pinch off: A catastrophe aids cooling", Physical Review B **88**, 064302 (2013).

[176] D. Sánchez and R. López, "Scattering Theory of Nonlinear Thermoelectric Transport", Physical Review Letters **110**, 026804 (2013).

[177] J. Meair and P. Jacquod, "Scattering theory of nonlinear thermoelectricity in quantum coherent conductors", Journal of Physics: Condensed Matter **25**, 082201 (2013).

[178] J. Matthews, F. Battista, D. Sánchez, P. Samuelsson, and H. Linke, "Experimental verification of reciprocity relations in quantum thermoelectric transport", Physical Review B **90**, 165428 (2014).

[179] P. N. Butcher, "Thermal and electrical transport formalism for electronic microstructures with many terminals", Journal of Physics: Condensed Matter **2**, 4869–4878 (1990).

[180] W. Lee, K. Kim, W. Jeong, L. A. Zotti, F. Pauly, J. C. Cuevas, and P. Reddy, "Heat dissipation in atomic-scale junctions", Nature **498**, 209 (2013).

[181] J. Argüello-Luengo, D. Sánchez, and R. López, "Heat asymmetries in nanoscale conductors: The role of decoherence and inelasticity", Physical Review B **91**, 165431 (2015).

[182] D. Sánchez and L. Serra, “Thermoelectric transport of mesoscopic conductors coupled to voltage and thermal probes”, Physical Review B **84**, 201307 (2011).

[183] C. W. J. Beenakker and A. A. M. Staring, “Theory of the thermopower of a quantum dot”, Physical Review B **46**, 9667 (1992).

[184] A. A. M. Staring, L. W. Molenkamp, B. W. Alphenaar, H. van Houten, O. J. A. Buyk, M. A. A. Mabesoone, C. W. J. Beenakker, and C. T. Foxon, “Coulomb-Blockade Oscillations in the Thermopower of a Quantum Dot”, Europhysics Letters (EPL) **22**, 57 (1993).

[185] L. W. Molenkamp, A. A. M. Staring, B. W. Alphenaar, H. van Houten, and C. W. J. Beenakker, “Sawtooth-like thermopower oscillations of a quantum dot in the Coulomb blockade regime”, Semiconductor Science and Technology **9**, 903 (1994).

[186] A. S. Dzurak, C. G. Smith, C. H. W. Barnes, M. Pepper, L. Martín-Moreno, C. T. Liang, D. a. Ritchie, and G. a. C. Jones, “Thermoelectric signature of the excitation spectrum of a quantum dot”, Physical Review B **55**, R10197 (1997).

[187] T.-S. Kim and S. Hershfield, “Thermoelectric effects of an Aharonov-Bohm interferometer with an embedded quantum dot in the Kondo regime”, Physical Review B **67**, 165313 (2003).

[188] Y. M. Blanter, C. Bruder, R. Fazio, and H. Schoeller, “Aharonov-Bohm-type oscillations of thermopower in a quantum-dot ring geometry”, Physical Review B **55**, 4069 (1997).

[189] S. F. Godijn, S. Möller, H. Buhmann, L. W. Molenkamp, and S. A. van Langen, “Thermopower of a Chaotic Quantum Dot”, Physical Review Letters **82**, 2927 (1999).

[190] D. Boese and R. Fazio, “Thermoelectric effects in Kondo-correlated quantum dots”, Europhysics Letters (EPL) **56**, 576 (2001).

[191] M. Krawiec and K. I. Wysokiński, “Thermoelectric effects in strongly interacting quantum dot coupled to ferromagnetic leads”, Physical Review B **73**, 075307 (2006).

[192] T. A. Costi and V. Zlatić, “Thermoelectric transport through strongly correlated quantum dots”, Physical Review B **81**, 235127 (2010).

[193] P. Reddy, S.-Y. Jang, R. A. Segalman, and A. Majumdar, “Thermoelectricity in Molecular Junctions”, Science **315**, 1568 (2007).

[194] Y. S. Liu and X. F. Yang, “Enhancement of thermoelectric efficiency in a double-quantum-dot molecular junction”, Journal of Applied Physics **108**, 023710 (2010).

[195] J. Zheng, M.-J. Zhu, and F. Chi, “Fano Effect on the Thermoelectric Efficiency in Parallel-Coupled Double Quantum Dots”, Journal of Low Temperature Physics **166**, 208 (2012).

[196] P. S. Cornaglia, G. Usaj, and C. A. Balseiro, “Tunable charge and spin Seebeck effects in magnetic molecular junctions”, Physical Review B **86**, 041107 (2012).

[197] I. Weymann and J. Barnaś, “Spin thermoelectric effects in Kondo quantum dots coupled to ferromagnetic leads”, Physical Review B **88**, 085313 (2013).

[198] L. Ye, D. Hou, R. Wang, D. Cao, X. Zheng, and Y. Yan, “Thermopower of few-electron quantum dots with Kondo correlations”, Physical Review B **90**, 165116 (2014).

[199] M. Krawiec and K. I. Wysokiński, “Thermoelectric phenomena in a quantum dot asymmetrically coupled to external leads”, Physical Review B **75**, 155330 (2007).

[200] J. Azema, A.-M. Daré, S. Schäfer, and P. Lombardo, “Kondo physics and orbital degeneracy interact to boost thermoelectrics on the nanoscale”, Physical Review B **86**, 075303 (2012).

[201] S. F. Svensson, E. A. Hoffmann, N. Nakpathomkun, P. M. Wu, H. Q. Xu, H. A. Nilsson, D. Sánchez, V. Kashcheyevs, and H. Linke, “Nonlinear thermovoltage and thermocurrent in quantum dots”, New Journal of Physics **15**, 105011 (2013).

[202] M. A. Sierra and D. Sánchez, “Strongly nonlinear thermovoltage and heat dissipation in interacting quantum dots”, Physical Review B **90**, 115313 (2014).

[203] N. A. Zimbovskaya, “The effect of Coulomb interactions on nonlinear thermovoltage and thermocurrent in quantum dots”, The Journal of Chemical Physics **142**, 244310 (2015).

[204] N. A. Zimbovskaya, “Scattering theory of thermocurrent in quantum dots and molecules”, Physica E: Low-dimensional Systems and Nanostructures **74**, 213 (2015).

[205] A. Svilans, A. M. Burke, S. F. Svensson, M. Leijnse, and H. Linke, “Nonlinear thermoelectric response due to energy-dependent transport properties of a quantum dot”, Physica E: Low-dimensional Systems and Nanostructures **82**, 34 (2016).

[206] T. Koch, J. Loos, and H. Fehske, “Thermoelectric effects in molecular quantum dots with contacts”, Physical Review B **89**, 155133 (2014).

[207] S.-Y. Hwang, R. López, M. Lee, and D. Sánchez, “Nonlinear spin-thermoelectric transport in two-dimensional topological insulators”, Physical Review B **90**, 115301 (2014).

[208] S.-Y. Hwang, D. Sánchez, and R. López, “A hybrid superconducting quantum dot acting as an efficient charge and spin Seebeck diode”, New Journal of Physics **18**, 093024 (2016).

[209] Y. Wang, Y. Zhang, C. Huang, and J. Chen, “Performance analysis of an interacting quantum dot heat engine with an external applied magnetic field”, Physica A: Statistical Mechanics and its Applications **438**, 586 (2015).

[210] G. Gómez-Silva, P. A. Orellana, and E. V. Anda, “Enhancement of the thermoelectric efficiency in a T-shaped quantum dot system in the linear and nonlinear regimes”, Journal of Applied Physics **123**, 085706 (2018).

[211] M. Büttiker and M. Moskalets, “Scattering Theory of Dynamic Electrical Transport”, in *Mathematical physics of quantum mechanics* (Springer Berlin Heidelberg, 2006), page 33.

[212] H. Bruus and K. Flensberg, *Many-body quantum theory in condensed matter physics* (Oxford University Press, Copenhagen, 2002), page 464.

[213] H. Haug and A.-P. Jauho, *Quantum Kinetics in Transport and Optics of Semiconductors*, Vol. 123, Solid-State Sciences (Springer, Berlin, 2008).

[214] G. D. Mahan, *Many-Particle Physics* (Springer US, Boston, MA, 2000).

[215] R. D. Mattuck, *A Guide to Feynman Diagrams in the Many-Body Problem*, Courier Co (McGraw-Hill, New York, 1967), page 464.

[216] M. Wagner, “Expansions of nonequilibrium Green’s functions”, Physical Review B **44**, 6104 (1991).

[217] D. C. Langreth, “Linear and Nonlinear Response Theory with Applications”, in *Linear and nonlinear electron transport in solids*, edited by J. T. Devreese and V. E. van Doren (Springer US, Boston, MA, 1976), pages 3–32.

[218] S. Alexander and P. W. Anderson, “Interaction Between Localized States in Metals”, Physical Review **133**, A1594 (1964).

[219] O. Sakai, Y. Shimizu, and T. Kasuya, “Single-Particle and Magnetic Excitation Spectra of Degenerate Anderson Model with Finite f-f Coulomb Interaction”, Journal of the Physical Society of Japan **58**, 3666 (1989).

[220] P. Coleman, “New approach to the mixed-valence problem”, Physical Review B **29**, 3035 (1984).

[221] S. E. Barnes, “New method for the Anderson model”, Journal of Physics F: Metal Physics **6**, 1375 (1976).

[222] S. E. Barnes, “New method for the Anderson model. II. The U=0 limit”, Journal of Physics F: Metal Physics **7**, 2637 (1977).

[223] S. M. Reimann and M. Manninen, “Electronic structure of quantum dots”, Reviews of Modern Physics **74**, 1283 (2002).

[224] T. Ruokola, T. Ojanen, and A.-P. Jauho, “Thermal rectification in nonlinear quantum circuits”, Physical Review B **79**, 144306 (2009).

[225] A. C. Hewson, “Theory of Localized Magnetic States in Metals”, Physical Review **144**, 420 (1966).

[226] C. Lacroix, “Density of states for the Anderson model”, Journal of Physics F: Metal Physics **11**, 2389 (1981).

[227] V. Kashcheyevs, A. Aharony, and O. Entin-Wohlman, “Applicability of the equations-of-motion technique for quantum dots”, Physical Review B **73**, 125338 (2006).

[228] A. Theumann, “Self-Consistent Solution of the Anderson Model”, Physical Review **178**, 978 (1969).

[229] C. A. Balseiro, G. Usaj, and M. J. Sánchez, “Out of equilibrium transport through an Anderson impurity: probing scaling laws within the equation of motion approach”, Journal of Physics: Condensed Matter **22**, 425602 (2010).

[230] O. Entin-Wohlman, A. Aharony, and Y. Meir, “Kondo effect in complex mesoscopic structures”, Physical Review B **71**, 035333 (2005).

[231] Y. Meir and N. S. Wingreen, “Landauer formula for the current through an interacting electron region”, Physical Review Letters **68**, 2512 (1992).

[232] M. A. Sierra, M. Saiz-Bretín, F. Domínguez-Adame, and D. Sánchez, “Interactions and thermoelectric effects in a parallel-coupled double quantum dot”, Physical Review B **93**, 235452 (2016).

[233] M. A. Sierra, R. López, and D. Sánchez, “Fate of the spin-1/2 Kondo effect in the presence of temperature gradients”, Physical Review B **96**, 085416 (2017).

[234] M. A. Sierra and D. Sánchez, “Nonlinear Heat Conduction in Coulomb-blockaded Quantum Dots”, Materials Today: Proceedings **2**, 483 (2015).

[235] M. A. Sierra and D. Sánchez, “Heat current through an artificial Kondo impurity beyond linear response”, Journal of Physics: Conference Series **969**, 012144 (2018).

[236] M. A. Sierra, D. Sánchez, A. R. Garrigues, E. del Barco, L. Wang, and C. A. Nijhuis, “How to distinguish between interacting and noninteracting molecules in tunnel junctions”, Nanoscale **10**, 3904 (2018).

[237] A. Sellitto, “Crossed nonlocal effects and breakdown of the Onsager symmetry relation in a thermodynamic description of thermoelectricity”, Physica D: Nonlinear Phenomena **283**, 56 (2014).

[238] A. C. Hewson, “Renormalized perturbation expansions and Fermi liquid theory”, Physical Review Letters **70**, 4007 (1993).

[239] A. Oguri and A. C. Hewson, “NRG Approach to the Transport through a Finite Hubbard Chain Connected to Reservoirs”, Journal of the Physical Society of Japan **74**, 988–996 (2005).

[240] P. Coleman, C. Hooley, Y. Avishai, Y. Goldin, and A. F. Ho, “Oscillatory instabilities in dc-biased quantum dots”, Journal of Physics: Condensed Matter **14**, L205 (2002).

[241] R. López, R. Aguado, and G. Platero, “Shot noise in strongly correlated double quantum dots”, Physical Review B **69**, 235305 (2004).

[242] M. A. Sierra, R. López, and J. S. Lim, “Thermally Driven Out-of-Equilibrium Two-Impurity Kondo System”, Physical Review Letters **121**, 096801 (2018).

[243] M. A. Sierra, D. Sánchez, K. Kaasbjerg, and A.-P. Jauho, “Coulomb drag in interacting quantum dot systems across coupling regimes”, (unpublished) (2018).

[244] C. González-Santander, P. A. Orellana, and F. Domínguez-Adame, “Bound states in the continuum driven by AC fields”, EPL (Europhysics Letters) **102**, 17012 (2013).

[245] C. Álvarez, F. Domínguez-Adame, P. A. Orellana, and E. Díaz, “Impact of electron–vibron interaction on the bound states in the continuum”, Physics Letters A **379**, 1062 (2015).

[246] L. Esaki, “New Phenomenon in Narrow Germanium p-n Junctions”, Physical Review **109**, 603 (1958).

[247] J. Muscat and D. Newns, “Chemisorption on metals”, Progress in Surface Science **9**, 1 (1978).

[248] P. Simon, R. López, and Y. Oreg, “Ruderman-Kittel-Kasuya-Yosida and Magnetic-Field Interactions in Coupled Kondo Quantum Dots”, Physical Review Letters **94**, 086602 (2005).

[249] R. Yu and Q. Si, “U(1) slave-spin theory and its application to Mott transition in a multiorbital model for iron pnictides”, Physical Review B **86**, 085104 (2012).

[250] A. B. Georgescu and S. Ismail-Beigi, “Generalized slave-particle method for extended Hubbard models”, Physical Review B **92**, 235117 (2015).

[251] C. Timm, “Tunneling through molecules and quantum dots: Master-equation approaches”, Physical Review B **77**, 195416 (2008).

[252] R. Peters, T. Pruschke, and F. B. Anders, “Numerical renormalization group approach to Green’s functions for quantum impurity models”, Physical Review B **74**, 245114 (2006).

[253] M. Grobis, I. G. Rau, R. M. Potok, H. Shtrikman, and D. Goldhaber-Gordon, “Universal Scaling in Nonequilibrium Transport through a Single Channel Kondo Dot”, Physical Review Letters **100**, 246601 (2008).

[254] L. Tosi, P. Roura-Bas, A. Llois, and A. Aligia, “Out of equilibrium Anderson model: Conductance and Kondo temperature”, Physica B: Condensed Matter **407**, 3263 (2012).

[255] P. Roura-Bas, L. Tosi, A. A. Aligia, and P. S. Cornaglia, “Thermopower of an SU(4) Kondo resonance under an SU(2) symmetry-breaking field”, Physical Review B **86**, 165106 (2012).

[256] S.-Y. Hwang, D. Sánchez, M. Lee, and R. López, “Magnetic-field asymmetry of nonlinear thermoelectric and heat transport”, New Journal of Physics **15**, 105012 (2013).

[257] B. Bhandari, G. Chiriacò, P. A. Erdman, R. Fazio, and F. Taddei, “Thermal drag in electronic conductors”, Physical Review B **98**, 035415 (2018).

[258] B. Wang, J. Zhou, R. Yang, and B. Li, “Ballistic thermoelectric transport in structured nanowires”, New Journal of Physics **16**, 065018 (2014).

[259] W. Z. Shangguan, T. C. Au Yeung, Y. B. Yu, and C. H. Kam, “Quantum transport in a one-dimensional quantum dot array”, Physical Review B **63**, 235323 (2001).

[260] W.-P. Xu, Y.-Y. Zhang, Q. Wang, and Y.-H. Nie, “Spin-dependent thermoelectric effect and spin battery mechanism in triple quantum dots with Rashba spin–orbital interaction”, Chinese Physics B **25**, 117307 (2016).

[261] M. Niklas, A. Trottmann, A. Donarini, and M. Grifoni, “Fano stability diagram of a symmetric triple quantum dot”, Physical Review B **95**, 115133 (2017).

[262] H. Thierschmann, R. Sánchez, B. Sothmann, F. Arnold, C. Heyn, W. Hansen, H. Buhmann, and L. W. Molenkamp, “Three-terminal energy harvester with coupled quantum dots”, Nature Nanotechnology **10**, 854 (2015).

[263] J.-H. Jiang, O. Entin-Wohlman, and Y. Imry, “Thermoelectric three-terminal hopping transport through one-dimensional nanosystems”, Physical Review B **85**, 075412 (2012).

[264] D. Futterer, M. Governale, M. G. Pala, and J. König, “Nonlocal Andreev transport through an interacting quantum dot”, Physical Review B **79**, 054505 (2009).

[265] J. Eldridge, M. G. Pala, M. Governale, and J. König, “Superconducting proximity effect in interacting double-dot systems”, Physical Review B **82**, 184507 (2010).

[266] T. Rejec, R. Žitko, J. Mravlje, and A. Ramšak, “Spin thermopower in interacting quantum dots”, Physical Review B **85**, 085117 (2012).

[267] S. Dong and Z. P. Niu, “Thermospin effects in a quantum dot connected to normal leads”, Physics Letters A **379**, 443 (2015).

[268] I. D’Amico and G. Vignale, “Spin Coulomb drag in the two-dimensional electron liquid”, Physical Review B **68**, 045307 (2003).

[269] D. L. Nika, E. P. Pokatilov, A. A. Balandin, V. M. Fomin, A. Rastelli, and O. G. Schmidt, “Reduction of lattice thermal conductivity in one-dimensional quantum-dot superlattices due to phonon filtering”, Physical Review B **84**, 165415 (2011).

[270] M. Büttiker, “Dynamic conductance and quantum noise in mesoscopic conductors”, Journal of Mathematical Physics **37**, 4793 (1996).

[271] B. Dong and X.-L. Lei, “Effect of the Kondo correlation on shot noise in a quantum dot”, Journal of Physics: Condensed Matter **14**, 11747 (2002).

[272] A. A. Clerk, M. H. Devoret, S. M. Girvin, F. Marquardt, and R. J. Schoelkopf, “Introduction to quantum noise, measurement, and amplification”, Reviews of Modern Physics **82**, 1155 (2010).

[273] L. E. Bruhat, J. J. Viennot, M. C. Dartiailh, M. M. Desjardins, T. Kontos, and A. Cottet, “Cavity Photons as a Probe for Charge Relaxation Resistance and Photon Emission in a Quantum Dot Coupled to Normal and Superconducting Continua”, Physical Review X **6**, 021014 (2016).

[274] J. Gabelli, G. Fève, J. M. Berroir, B. Plaçais, A. Cavanna, B. Etienne, Y. Jin, and D. C. Glattli, “Violation of Kirchhoff’s laws for a coherent RC circuit”, Science **313**, 499 (2006).

[275] G. Feve, A. Mahe, J.-M. Berroir, T. Kontos, B. Placais, D. C. Glattli, A. Cavanna, B. Etienne, and Y. Jin, “An On-Demand Coherent Single-Electron Source”, Science **316**, 1169 (2007).

[276] J. Gabelli, G. Fève, J.-M. Berroir, and B. Plaçais, “A coherent RC circuit”, Reports on Progress in Physics **75**, 126504 (2012).

[277] M. Moskalets, P. Samuelsson, and M. Büttiker, “Quantized Dynamics of a Coherent Capacitor”, Physical Review Letters **100**, 086601 (2008).

[278] M. I. Alomar, J. S. Lim, and D. Sánchez, "Coulomb-blockade effect in nonlinear mesoscopic capacitors", Physical Review B **94**, 165425 (2016).

[279] M. F. Ludovico, L. Arrachea, M. Moskalets, and D. Sánchez, "Periodic Energy Transport and Entropy Production in Quantum Electronics", Entropy **18**, 419 (2016).